Near real-time reconciliation of geochemical data acquired with handheld spectroscopic devices : Application to volcanogenic massive sulphide (VMS) deposit from the Iberian Pyrite Belt

Yonghwi Kim

Université de Lorraine, Collégium Sciences et Technologies
Ecole Doctorale SIRENA – Sciences et Ingénierie des Ressources Naturelles

THESE

Présentée pour l'obtention du grade de
Docteur de l'Université de Lorraine
Mention « Géosciences »

par **Yonghwi KIM**

Near real-time reconciliation of geochemical data acquired with handheld spectroscopic devices: Application to volcanogenic massive sulphide (VMS) deposit from the Iberian Pyrite Belt

---

Soutenance publique le 26 Janvier 2022

Membres du jury :

Directeurs de thèse :

Mme. Cécile FABRE	Maîtresse de conférences HDR, Université de Lorraine
M. Jean CAUZID	Maître de conférences, Université de Lorraine

Président de jury :

M. Jan JEHLIČKA	Professeur, Charles University, Czech Republic

Rapporteurs :

Mme. Patricia PATRIER-MAS	Professeure des universités, Université de Poitiers
M. Eric PIRARD	Professeur, Université de Liège, Belgium

Examinateurs :

Mme. Emmanuelle MONTARGES-PELLETIER	Directrice de recherche, LIEC, CNRS
M. Jan JEHLIČKA	Professeur, Charles University, Czech Republic

Membres invités :

Mme. Marie-Camille CAUMON	Ingénieure de recherche, Université de Lorraine
M. Erwan ANDRE	Maître de conférences, Université de Lorraine

Faculté des Sciences et Technologies – Campus des Aiguillettes – 54506 Vandoeuvre-lès-Nancy

Résumé

L'exploration minière axée sur des cibles cachées en profondeur nécessite (i) des techniques efficaces qui sont applicables sur le terrain pour identifier les systèmes minéralisateurs à grande échelle et (ii) des indicateurs pour pouvoir localiser le minerai à plus petite échelle. Avec le développement rapide des équipements portables ces dernières années, l'importance de l'analyse en temps quasi réel sur le terrain a augmenté en aidant à la prise de décision rapide sans attendre le retour des analyses de laboratoire.

Des équipements portatifs ont été largement utilisés dans l'exploration des ressources minérales pour réaliser des analyses spectroscopiques. Cependant, les données obtenues par plusieurs techniques sont rarement appliquées pour caractériser les "vecteurs" qui peuvent fournir des informations intéressantes sur les variations dans la lithologie, la géochimie, la minéralogie et la chimie des minéraux. La combinaison des données spectrales obtenues à partir de divers instruments portables est encore plus rare. L'objectif principal de ce travail de thèse est de concilier les données géochimiques acquises à partir de différents appareils spectroscopiques portables afin de déterminer la meilleure information géochimique de chaque technique appliquée en combinant les informations minéralogiques et élémentaires. Dans cette étude, les données élémentaires et minéralogiques sont fournies par six techniques portables : (i) des analyses élémentaires telles que XRF et LIBS pour les éléments majeurs, les traces et les éléments légers, et (ii) des analyses minéralogiques telles que Raman, VNIR-SWIR, MIR et XRD pour contraindre les minéraux de formation de roche, de minerai et d'altération.

L'objectif final de cette étude est d'identifier les vecteurs pointant vers le minerai en réconciliant les données multispectrales obtenues à partir d'échantillon des encaissants de gisement de sulfure massif volcanogène (SMV) d'Elvira. Pour cela, les étape suivantes ont été réalisées : (i) comprendre la méthodologie applicable à chaque technique, (ii) établir une base de données spectrales composée de monominéraux, (iii) concevoir d'un arbre de décision pour classer par minéral ou classes de minéraux en fonction des bandes diagnostiques, et identifier et quantifier des minéraux naturels (iv) carbonate et (v) phyllosilicate (i.e., chlorites trioctaédriques et micas dioctaédriques), qui sont des indicateurs du gisement cible.

Plusieurs limites de la spectroscopie portable ont été confirmées qui dépendent des appareils ou de l'environnement géologique du gisement d'Elvira. Néanmoins, la spectroscopie portable est efficace pour identifier la présence et les changements de composition de divers minéraux dans des échantillons de roches hétérogènes. Par conséquent, l'analyse spectroscopique sur place peut être l'un des outils de vectorisation pour déterminer l'emplacement de la minéralisation dans les explorations de minerais cachés.

Abstract

Mineral exploration focused on deeply concealed targets at depth requires effective techniques applicable in the field to identify ore-forming systems on a large scale and pathfinders to locate ore on a smaller scale. According to the rapid development of portable equipment in recent years, the importance of near real-time analysis in the field has been increasing by helping fast decision-making support before laboratory requests.

Spectroscopic analysis using individual equipment has been widely used in the exploration of mineral resources, but it is rare to apply integrated data from several techniques to characterize "vectors", which provide variations in lithology, geochemistry, mineralogy, and mineral chemistry. In addition, it is even rarer if the combination of spectral data is obtained from various portable instruments. Therefore, this study aims at reconciling geochemical data acquired from portable spectroscopic devices in order to determine the best geochemical information from each technique applied by combining the mineralogical and elemental information. Elemental and mineralogical data are provided in this study by six portable techniques: (i) elemental analyses such as XRF and LIBS for major, trace, and light elements, and (ii) mineralogical analyses such as Raman, VNIR-SWIR, MIR, and XRD to constrain rock-forming, ore, and alteration minerals.

The final objective of this study is to identify vectors to the ore by applying the reconciled multi-spectral data obtained from the "real" sample in the Elvira volcanogenic massive sulphide (VMS) deposit. To achieve this, step-by-step procedures were carried out: (i) methodological understanding of each technique, (ii) establishment of a spectral database consisting of naturally monomineralic minerals, (iii) design of a decision tree to classify by mineral or mineral classes based on diagnostic bands, and mineral identification and quantification of (iv) carbonate and (v) phyllosilicate minerals (i.e., trioctahedral chlorites and dioctahedral micas), which are indicators of the target deposit.

Several limitations of portable spectroscopy were confirmed based on the device itself and the geological environment in the Elvira deposit. Nevertheless, portable spectroscopy is effective in identifying the presence and compositional changes of various minerals from heterogeneous rock samples. Therefore, spectroscopic analysis on-site can be one of the vectoring tools to determine the implication for ore mineralization in hidden ore explorations.

Acknowledgments

My foremost acknowledgment is to my thesis supervisors, Jean CAUZID and Cécile FABRE, who gave me this great opportunity to participate in this project. During my Ph.D. thesis, they suggested the direction of research for the achievement of the project as supervisors and also informed me of the joy of research as senior researchers walking the path of a scientist. Based on their comprehensive support, I could finish my Ph.D. with the same curiosity and enthusiasm as when I started.

I would like to express my deep gratitude to the lab members at GeoRessources contributed to many aspects of this work. Especially Marie-Camille CAUMON and Odile BARRES, who are involved in the project as experts in Raman and Infrared spectroscopy, have helped me a lot in greatly improving the quality of my thesis. Moreover, their abundant experiences and knowledge of spectroscopic analysis further expanded my knowledge and interest in spectroscopy. Analytical support for electron microprobe and micro-XRF was skilfully provided by Andreï LECOMTE, Olivier ROUER, and Lise SALSI in SCMEM platform, and successful sample preparation for those analyses was aided by Alexandre FLAMMANG in Lithopréparation platform. I also thank Victoria FABERT, Amadou SALL, Ahmed ABOUTAJ, Naila MEZOUED who participated in this project for their collaboration with my studies.

I would like to thank Philippe MARION, Régine MOSSER, Michel CATHELINEAU, Anne-Sylvie ANDRE-MAYER, and Alexandre TARANTOLA from GeoRessources and Emmanuelle PELLETIER from LIEC for providing pure mineral references essential for establishing the spectral database in this study. My sincere thanks to IGEO-CSIC team in Spain (Fernando TORNOS, Guillem GISBERT PINTO, Emma LOSANTOS GUILLEN) for sharing and discussing the geological background of the Elvira deposit. This thesis could be improved by collaborating with the Geological Survey of Finland. In particular, Pertti SARALA and Johanna TORPPA are thanked for their assistance in portable XRD and Self-organizing maps.

I would like to thank all the members of my thesis monitoring committee and the jury members of my thesis defence for evaluating and examining my thesis work: Emmanuelle MONTARGES-PELLETIER, Erwan ANDRE, Patricia PATRIER-MAS, Jan JEHLIČKA, and Eric PIRARD.

Finally, I would like to express my thanks to my international friends who experienced pleasant and healthy life together in Nancy, and my family in Korea who always support me behind. Above all, special gratitude and love to Yujin JEGAL for supporting me as a wife and a Ph.D. candidate in the same geoscience field.

This thesis is part of the NEXT (New Exploration Technologies) project (G.A. No. 776804-H2020-SC5-2017) funded by European Union's Horizon 2020 research and innovation program. I would like to thank all the people who contributed to this project and its progress.

Résumé élargi

Avec le développement rapide des équipements portables au cours des dernières décennies, la spectroscopie de terrain a acquis un rôle clé en tant que moyen d'identifier et de caractériser les matériaux et les sols sur le terrain (Milton et al., 2009). Les technologies portables sur le terrain fournissent en continu des résultats d'analyse in situ, presque en temps réel, en réduisant les délais et les coûts d'analyse. En outre, la plupart des appareils portables ne nécessitent aucun prétraitement des échantillons, ou alors un traitement limité. L'analyse est donc beaucoup plus rapide que les techniques conventionnelles en laboratoire, ce qui permet d'économiser du temps et de la main-d'œuvre. Cette étude vise à réconcilier les données géochimiques acquises par des appareils spectroscopiques portables sur le terrain afin de déterminer la meilleure information géochimique pour chacune des techniques appliquées en combinant les celles provenant de la minéralogique et des données élémentaires. Les données multispectrales réconciliées donnent alors des "vecteurs" fournissant la relation quantitative entre la concentration élémentaire et la minéralogie des minéraux altérés par hydrothermalisme, de la marge distale aux minerais les plus enrichis. Suivant les instruments portables utilisés, l'analyse spectroscopique sur le terrain permet d'obtenir soit la discrimination et la quantification des minéraux dans des roches qui présentent une paragenèse complexe, soit la composition chimique de ces minéraux. Cette thèse s'inscrit dans le cadre du projet NEXT (New Exploration Technologies) (G.A. n° 776804) financé par le programme de recherche et d'innovation Horizon 2020 de l'Union européenne (https://www.new-exploration.tech/). Le projet NEXT vise à développer de nouveaux géomodèles et de nouvelles technologies d'exploration avec une très bonne sensibilité, rapides à mettre en place, peu onéreuses et sans danger pour l'environnement. Dans ce cadre, notre tâche dans ce projet a été d'extraire autant d'informations spectrales que possible à partir d'un nombre limité d'échantillons analysés par un équipement léger (c'est-à-dire portable) existant.

Cette thèse comporte six chapitres détaillant les différentes étapes nécessaires à la réalisation de cet objectif. Les compositions des minéraux présents dans ce système VMS, ainsi que leur composition et leur quantification minéralogique au sein de la roche, ont été obtenus en utilisant les différents outils spectroscopiques. Les données spectrales ont été réalisées en utilisant six appareils portables : (i) analyses élémentaires par les outils XRF et LIBS, et (ii)

analyses minéralogiques pour le Raman, VNIR-SWIR, MIR et XRD.

Le chapitre (I) Méthodologie de la spectroscopie fait le point sur les bases fondamentales nécessaires à la compréhension des six techniques spectroscopiques utilisées ici, soit sept appareils portables. Afin de comprendre correctement toute donnée spectroscopique provenant de différentes techniques (XRF, LIBS, VNIR…) ou acquises sur des espèces minérales/roches différentes, il est d'abord essentiel de maitriser la théorie mais aussi la mise en pratique de chacun des outils. Dans ce chapitre, est présenté un bref aperçu des principales lois qui régissent l'interaction du rayonnement électromagnétique avec la matière, et en particulier en ce qui concerne les six techniques spectroscopiques utilisées.

Le chapitre (II) Création d'une base de données spectrales fournit une collection de données spectrales obtenues sur des mono-minéraux à l'aide des sept outils portables. Cette base de données spectrales pourra être utilisée pour la reconnaissance rapide de minéraux non identifiables à l'œil et les spectres seront utilisés la réconciliation spectrale des différents outils. Ainsi, cette bibliothèque spectrale est le point de départ et le cœur de ce travail de thèse. Un arbre de décision pour la discrimination des minéraux est ensuite construit en combinant les informations spectrales les plus pertinentes qui ont pu être extraites de la bibliothèque. En observant les variations spectrales (par rapport aux gammes spectrales de référence de l'arbre de décision), il est possible de reconnaître des changements de composition au sein d'un même groupe de minéraux tels que les carbonates et les phyllosilicates.

Cette bibliothèque spectrale est composée de spectres de référence de différents groupes de minéraux, qui peuvent être présents dans les gisements de sulfures massifs volcanogènes (VMS). La base de données spectrales a été régulièrement mise à jour au cours de la thèse. Le nombre final de phases minérales étudiées est de 27, pour 52 échantillons reportés dans la bibliothèque. Le jeu de données fourni dans la bibliothèque spectrale contient certes un nombre limité d'espèces minérales par rapport aux bibliothèques existantes, mais les données ont été acquises sur les mêmes échantillons pour les six techniques spectroscopiques ce qui n'avait jamais été fait avant ce travail de thèse. Ces minéraux de référence couvrent presque tous les minéraux cibles du gisement de SMV d'Elvira pour les applications du projet NEXT. Toutes les données spectrales obtenues sur un même minéral, à l'aide des différents outils, pourront être utilisées conjointement pour en tirer les informations nécessaires à la détermination des

minéraux en place.

En plus de cette bibliothèque spectrale, une nouvelle base de données minéralogiques portant sur la composition élémentaire de différents groupes de minéraux a été mise en place. La plupart des minéraux présentent une large gamme de composition chimique et leurs signatures spectrales produisent des bandes caractéristiques qui peuvent varier à la fois en nombres d'onde qu'en longueurs d'onde, en fonction de leur composition élémentaire. Par conséquent, l'analyse spectroscopique associée à la variation de la composition des minéraux en fonction de leur composition minéralogique permet d'obtenir des informations essentielles sur leurs réponses spectrales, qui pourront être utilisées comme diagnostiques lors des analyses de minéraux sur le terrain.

Chapitre (III) La conception d'un arbre de décision, en combinant les informations spectroscopiques des caractéristiques spectrales, fournit des positions de bandes diagnostiques pour tous les minéraux de la base de données spectrales. Ces données spectrales sont disponibles et stockées dans différentes bibliothèques spectrales libres d'accès. Les caractéristiques spectrales de minéraux connus (considérées comme les références) des bibliothèques spectrales aident à l'identification de minéraux (les cibles) pour les différentes techniques spectroscopiques en les comparant à leurs réponses spectrales. Certaines bibliothèques existantes se composent de quelques milliers de spectres de référence avec une large gamme de matériaux, mais le nombre de techniques est limité. Par conséquent, l'incompatibilité et les techniques restreintes peuvent limiter les applications pour les études de terrain, l'identification minérale, l'identification de la couverture végétale et la cartographie géologique. L'arbre de décision de cette étude détermine donc les zones de bandes représentatives des minéraux de chaque technique sur la base d'une analyse non destructive et d'une analyse destructive afin de confirmer la présence/absence de signaux dans la zone analysée. Trois techniques spectroscopiques non-destructives sont utilisées pour l'arbre de décision : Raman, MIR-SR, et VNIR-SWIR. Les six classes suivantes peuvent être identifiées en Raman : (1) les sulfures, (2) les silicates, (3) les phosphates, (4) les sulfates, (5) les carbonates et (6) le graphite. L'IR-SR peut distinguer toutes les classes sauf les sulfures et certains phyllosilicates. Le VNIR-SWIR distingue efficacement les sulfates, phyllosilicates et carbonates contenant de l'OH ou de l'H_2O. L'arbre de décision de l'analyse destructive telle que la XRD et la MIR-ATR commence par l'hypothèse qu'un échantillon qui peut être coupé/broyé

ou réduit en poudre sur place. Pour obtenir des diagrammes XRD, les particules de l'échantillon doivent être inférieures à 150 µm, et la taille minimale de l'échantillon est de 15 mg. Pour la MIR-ATR, un échantillon en poudre de 5 à 10 milligrammes (mg) est placé sur un cristal de diamant et pressé avec une enclume. Alors que la XRD est capable de reconnaître les six classes de minéraux, les caractéristiques spectrales des sulfures ne sont pas actives en MIR-ATR.

La LIBS peut détecter n'importe quel élément du tableau périodique mais elle est particulièrement adaptée à l'analyse des éléments légers à faible potentiel d'ionisation, mal détectés par les rayons X, comme Be, B, C, F, Li et Na. Pour l'analyse quantitative par LIBS, ce chapitre traite de la sélection des meilleures raies d'émission pour Na et Mg et de l'établissement de courbes de calibration univariée en fonction de la teneur en éléments. Ces courbes d'étalonnage peuvent être appliquées à diverses classes de minéraux telles que les silicates et les carbonates. Le résultat des analyses univariées dans cette étude suggère le potentiel de quantifier le lithium et le magnésium dans le matériau et de comparer la concentration élémentaire parmi les minéraux classés par l'arbre de décision. Trois spectres LIBS différents ont été utilisés dans cette étude : i) non normalisé, ii) normalisé par l'aire totale, et iii) normalisation SNV après correction de la ligne de base. Il est souligné que des valeurs de validation croisée (R^2) élevées avec des valeurs MAAPE similaires sont obtenues pour les données LIBS non corrigées et normalisées pour Na (819 nm). Cependant, pour les raies d'émission du magnésium, les modèles univariés des deux données normalisées sont meilleurs que les données non corrigées. Parmi les trois régions des raies d'émission du Mg, la région à privilégier est celle à 880 nm correspondant à la région visible, avec une meilleure précision de prédiction (MAAPE) pour les données normalisées par SNV. Ces résultats indiquent que la normalisation spectrale après correction de la ligne de base est préférable pour une quantification plus précise du sodium et du magnésium en minimisant l'effet de matrice potentiel de chaque échantillon.

Le chapitre (IV) Identification et quantification des minéraux carbonatés se concentre sur l'identification spectrale et la quantification des minéraux carbonatés, l'un des minéraux indicatifs du gisement d'Elvira. Les outils utilisés sont le Raman, MIR, LIBS, XRF, VNIR-SWIR et XRD. Deux articles ont été publiés dans Spectrochimica Acta Part A et B, respectivement : i) l'identification et la détermination de la composition des minéraux carbonatés du groupe de la calcite en utilisant leurs propriétés spectrales dans les spectres

Raman et infrarouge. L'étude systématique comparant les positions des bandes avec les rapports élémentaires se concentre sur la sélection de la région spectrale et du rapport le plus approprié pour la discrimination des carbonates, suggérant la possibilité de combiner les spectroscopies Raman et IR portables sur le terrain. ii) L'applicabilité spectrale pour l'identification et la quantification des minéraux carbonatés naturels Ca-Mg-Fe-Mn en utilisant la LIBS portable. Il est démontré que les informations spectrales des raies d'émission LIBS ont des corrélations élevées avec leur concentration élémentaire (Ca, Mg, Fe et Mn), et les rapports spectraux pour les mélanges de carbonates montrent également une corrélation linéaire avec le contenu minéral.

La discrimination des carbonates composée de 6 minéraux carbonatés a été réalisée par VNIR-SWIR et pXRD. Les bandes d'absorption dans la région SWIR sont situées vers 2300 nm pour la magnésite, 2320 nm pour la dolomite, 2330 nm pour l'ankerite, 2332 nm pour la sidérite et 2340 nm pour la calcite, respectivement. La rhodochrosite présente une absorption diagnostique plus longue à 2365 nm par rapport aux autres minéraux carbonatés, et trois absorptions de Mn de la rhodochrosite sont en outre observées à 408, 448 et 554 nm dans le domaine visible. Il est démontré que la position d'absorption des carbonates pour la magnésite, la dolomite, l'ankerite et la calcite est linéairement corrélée avec leur Mg# avec un coefficient de détermination élevé (R^2 = 0,97). En XRD, les minéraux carbonates dans la structure calcite sont identifiés entre 34° et 39° 2θ CoKα (3.06 à 2.68 Å), intervalle basé sur la position de la réflexion la plus intense (hkl = 104) dans les variétés trigonales. Même si la position du pic de diffraction dans les carbonates n'est pas corrélée avec Mg#, la position du pic est bien alignée pour les carbonates dans l'intervalle de pic (34°-39°).

Les cartes auto-organisées (SOM) sont une méthode de regroupement non supervisée qui créé un ensemble de vecteurs à n dimensions en une trame SOM généralement à une ou trois dimensions, de sorte que les vecteurs similaires soient situés à proximité les uns des autres. Quatre types différents d'instruments portables ont été utilisés : Raman, XRD et MIR avec mode de réflectance totale atténuée (ATR). Les données XRF portables n'ont été utilisées que pour les données quantifiées (interprétées), pas pour les spectres. 11 minéraux carbonatés purs de la bibliothèque spectrale du **chapitre II** sont utilisés en représentant six groupes de carbonates : calcite, ankérite, dolomite, sidérite, rhodochrosite et magnésite. Le résultat a montré que plus le nombre de paramètres appliqués était important, meilleure était la

reconnaissance des différents minéraux. La dolomite et l'ankérite, par exemple, ont été regroupées dans le même groupe en utilisant les données de trois instruments (c'est-à-dire XRF, Raman et XRD), mais ils ont été séparés en ajoutant un quatrième type de données spectrales (MIR) permettant ainsi d'obtenir une carte SOM mieux organisée. Ce résultat prometteur démontre des possibilités d'identification spectrale des minéraux sur la base d'un regroupement non supervisé.

Des mélanges synthétiques entre calcite-ankérite-dolomite ont été analysés pour évaluer la relation quantitative entre les rapports spectraux et les rapports de minéraux dans les systèmes à deux ou trois composants. Les expériences sur les mélanges synthétiques sont réalisées à l'aide de trois instruments portables Raman, MIR-ATR et XRD. Les mélanges ont été préparés en mélangeant différentes proportions, en pondérant 3:1, 1:1 et 1:3 pour le système à deux composants, et 1:1:1 pour le système à trois composants. Toutes les techniques montrent des corrélations linéaires entre les rapports des signaux spectraux et les contenus minéralogiques avec des coefficients de détermination supérieurs à 0,97. L'analyse quantitative des minéraux carbonatés dans un mélange ternaire (rapport massique 1:1:1) contenant de la calcite, de l'ankérite et de la dolomite a été réalisée à l'aide des trois appareils. L'erreur maximale du spectre Raman acquis par un laser vert est de 16,9% (région I), et de 6,2% (région II), respectivement. Le spectre Raman mesuré par un laser rouge-NIR présente une erreur maximale de 2,8 %. L'erreur maximale de la MIR-ATR et de la pXRD est de 4,0 %. Toutes les techniques portables peuvent donc être appliquées aux mélanges ternaires des minéraux carbonatés pour de l'analyse quantitative.

Le chapitre (V) Identification minérale et quantification des minéraux phyllosilicatés se concentre sur les analyses spectroscopiques Raman et VNIR-SWIR pour étudier les caractéristiques spectrales sur une gamme de compositions chimiques pour les chlorites trioctaédriques et les micas dioctaédriques. Les changements de bandes sont ensuite utilisés afin d'estimer la composition chimique des minéraux en se basant sur les informations spectrales obtenues sur le terrain. La composition chimique de chaque minéral entraîne un déplacement des positions des bandes Raman et SWIR correspondantes. Le Fe# ([Fe/(Fe+Mg)]) dans les chlorites et la teneur en Al (c'est-à-dire l'Al total et l'Al octaédrique) dans les micas dioctaédriques sont fortement corrélés avec les positions des bandes des spectres Raman et SWIR. La variation de la composition des chlorites est fortement corrélée aux régions

spectrales en ce qui concerne le mode O-Si-O dans les spectres Raman et la région Fe-OH dans la région SWIR. Les micas dioctaédriques montrent des changements dans la position de la bande en ce qui concerne le mode de stretching O-Al-O dans les spectres Raman et la région Al-OH dans la région SWIR. Le déplacement de la bande peut être expliqué par la substitution de Tschermak, qui est une substitution entre Al^{VI}, Fe et Mg dans les sites octaédriques. Notre étude minéralogique et spectrale détaillée suggère que l'analyse spectrale utilisant des outils portables est effectivement applicable à la détermination des minéraux phyllosilicates sur le terrain.

Trois ensembles de mélanges synthétiques binaires (ankerite-muscovite, ankerite-chlorite, et chlorite-muscovite) ont été étudiés pour la différenciation de leurs mélanges minéraux dans une région de bande spécifique du spectre par Raman portable avec un laser rouge-NIR et des instruments VNIR-SWIR. Dans les mélanges ankerite-muscovite, les rapports spectraux calculés à partir des deux techniques montrent des corrélations élevées avec le changement de contenu minéral en montrant des R^2 de 0,99 et 0,96, respectivement. Les mélanges chlorite-ankérite montrent que les rapports spectraux calculés à partir des spectres Raman présentent une corrélation élevée (R^2 = 0,98) avec le changement de contenu minéral. Dans la région SWIR, le rapport spectral utilisant l'intensité d'absorption à 1392 nm, indiquant la caractéristique d'absorption de OH, et l'absorption du carbonate à 2325 nm montre un coefficient de détermination élevé de 0,99. Néanmoins, il faut faire attention à l'application de ce rapport spectral car la caractéristique d'absorption autour de 1400 nm par OH apparaît non seulement dans la chlorite mais aussi dans d'autres silicates tels que les phyllosilicates et les silicates hydroxylés. Les changements d'intensité du dernier ensemble de mélanges (chlorite-muscovite) dans les spectres Raman sont observés sous la forme d'un épaulement ou d'un pic unique en fonction du rapport de mélange. Le rapport spectral entre l'intensité de Al-OH à 2194 nm et celle de Fe-OH à 2247 nm est utilisé pour une analyse quantitative dans la région SWIR. Les rapports spectraux calculés à partir des deux techniques montrent des corrélations élevées avec le changement de la teneur en minéraux en montrant un R^2 supérieur à 0,99.

Chapitre (VI) Application au gisement de VMS d'Elvira. Le gisement de sulfures massifs polymétalliques (Cu-Zn-Pb) d'Elvira est situé dans la région sud-est de la ceinture de pyrite ibérique (IPB). Le gisement de VMS hébergé par des schistes représente une continuité vers l'est des gisements de sulfures massifs de Sotiel-Migollas. La carotte de forage ELV44,

d'une longueur totale de 358 m, recoupe la marge même du gisement de sulfures massifs par le sud. Partant de la surface, elle traverse 324 m de schiste VSC composé de schistes noirs et de schistes gris/foncés, 2 m de sulfures massifs et 14 m de stockwork riche en carbonates dont la base est définie par une zone de faille. Dans cette étude, des dizaines d'échantillons ont été collectés de manière continue à partir d'une profondeur d'environ 245 m jusqu'au fond de la carotte de forage ELV44, en fonction des diverses lithologies présentes dans la carotte. La comparaison systématique entre les caractéristiques spectrales et la composition chimique des carbonates, chlorites et micas dioctaédriques de la carotte de forage ELV44 est effectuée afin de trouver des vecteurs permettant de se positionner par rapport à la zone enrichie. Des sections minces ont été sélectionnées pour acquérir une chimie minérale précise par EPMA, et les autres parties des sections minces ont été étudiées par les outils portables Raman et VNIR-SWIR. Les phyllosilicates tels que les chlorites et les micas dioctaédriques dans le gisement d'Elvira représentent des quantités plus faibles que les autres minéraux tels que le quartz, le graphite et le carbonate par observation microscopique. Ainsi, les chlorites à grain fin et en petite quantité dans les échantillons ELV44 sont difficiles à détecter par le Raman portable. Aussi, des analyses Micro-Raman en laboratoire, utilisant un laser vert ont été également effectuées pour identifier les caractéristiques spectrales associées à la composition minérale des phyllosilicates dans la carotte de forage ELV44.

On trouve différents types de minéraux carbonatés dans tous les groupes lithologiques de la carotte de forage ELV44, et ils sont bien distingués par l'analyse Raman qui montre des changements continus de composition sur les courbes de corrélation établies au **chapitre IV**. Cependant, la spectroscopie VNIR-SWIR ne permet pas une bonne distinction des carbonates dans les schistes chloritisés, les schistes noirs spéciaux et les sulfures massifs en raison de sa faible proportion en carbonates et de la réflectance extrêmement faible. Les chlorites des schistes réguliers de la carotte de forage ELV44 montrent des couleurs marron à bleu foncé sur les images XPL pour un taux de Fe# élevé. Le schiste chloritisé a un Fe# intermédiaire entre les schistes et le stockwork riche en carbonates et montre différentes couleurs d'interférence du gris au bleu. Dans la région du stockwork riche en carbonates, des chlorites gris pâle sont couramment observées avec un Fe# très faible (0.2-0.5) avec de grands écarts types. Quelques échantillons ne présentent des caractéristiques d'absorption de la chlorite que dans la région visible à SWIR, car la plupart des schistes sombres/noirs ont une réflectance excessivement

faible ne permettant pas la reconnaissance de la chlorite. De plus après observation microscopique, j'ai montré que les chlorites dans la carotte de forage sont beaucoup moins nombreux que d'autres minéraux tels que le quartz, le graphite et le carbonate. La position d'absorption des schistes réguliers, spéciaux et chloritisés est bien située sur la courbe d'étalonnage fournie au **chapitre V**. Les micas dioctaédriques d'Elvira ont une composition muscovitique constante indépendamment des types de schistes. Les échantillons de muscovite situés dans la partie inférieure des schistes réguliers ont des valeurs d'indice de potassium [K# = K/(K+Na)] plus faibles. Les différentes teneurs en potassium affectant les teneurs potassiques et sodiques dans les micas blancs de cette région peuvent être interprétées comme un remplacement par la dickite. En tant que minéral accessoire, le groupe de la kaolinite peut être distingué par l'analyse SWIR et Raman, et les échantillons d'Elvira sont identifiés comme étant de la dickite. Le graphite présente deux pics diagnostiques dans le spectre Raman, et la différence d'intensité entre la bande désordonnée (D) et la bande graphite (G) reflète le degré de métamorphisme.

Le logiciel de réconciliation développé ici permet d'obtenir une composition minéralogique à partir d'une série de mesures spectrales. La force de ce logiciel est que chaque technique spectroscopique peut être appliquée à partir de n'importe quel instrument disponible dans le commerce, qu'il soit de laboratoire ou portable. En outre, la composition minéralogique de l'échantillon est complétée par des informations supplémentaires qui présentent un intérêt pour les géologues.

Table of Content

Introduction

1. General context of the thesis

1.1. Portable spectroscopy and mineral exploration

Field spectroscopy is the term to describe spectroscopy undertaken in the natural environment with respect to objects such as vegetation, soils, rocks, and water bodies in the natural environment (Milton, 2004). The term 'field spectroscopy' was first introduced by Longshaw (1974). Field spectroscopy was used to support remote sensing, yet over the last decades, a key role for field spectroscopy has emerged, as a means of identifying and characterizing materials and surfaces in the field (Milton et al., 2009). As the importance of field spectroscopy has increased, rapid development of portable equipment has also begun accordingly since the first portable field spectroradiometer was described by Goetz et al. (1975). For several years, manufacturers have been designing portable spectrometers for producing chemical analyses out of the lab (Crocombe, 2018). Due to the technical development of portable instruments, the applicable fields of portable spectroscopy have been widely broadened, for example, agriculture, archaeology, astrobiology, chemistry, cultural heritage, **field geology**, food, forensic application, hazardous materials response, law enforcement, military application, pharmaceuticals, safety screening, and smartphone (Crocombe, 2018; Crocombe et al., 2021a).

A portable spectrometer is described by various definitions (Leary et al., 2021). In this thesis, a portable spectrometer should be small and lightweight enough for one person to carry its portable unit, and capable of running on battery power for a reasonable duration of time for fieldwork. These downsized devices, which are autonomous in energy, allow being taken to the sample, as opposed to the sample being taken to the spectrometer, hence moving the laboratory to the location of the sample. Thus, portable instruments dramatically improve the efficiency of the testing process. These tools provide practical information to make informed decisions on the spot. Therefore, the time saved in not having to send samples back to a laboratory is extremely valuable by rapidly delivering those applicative results at the point of need.

A typical portable spectrometer is capable of providing a limited amount of information compared to its laboratory counterpart for three reasons as follows: i) to start with, the use and

operation of the portable devices are simplified to be fit-for-purpose to non-expert operators (Crocombe, 2018). As a consequence, no fine-tuning of the analytical conditions nor extensive signal interpretation are required. ii) It also tends to be specially adapted to field use, being mechanically hardened, optically stable, and producing simplified information such as identity, validity, concentration in which case the reduced spectroscopic performance is fit for purpose. iii) A single tool cannot produce a full characterization of a sample. Even in the laboratory, for example, one has to run several experiments on several devices to obtain comprehensive data.

Nevertheless, these portable instruments present several very interesting features (Crocombe et al., 2021b). They are inexpensive compared to their laboratory-based equivalents; they are designed to be run by non-specialists; and they are producing data of an incredibly good quality. The analysis parameters of these instruments are predesignated by the manufacturer's hardware choices; in some cases, the measurement time is automatically determined as the spectral data are collected, ensuring that the spectrum has a sufficient S/N ratio for the type of analysis selected by the operator. Thus, much more information can be extracted from that data than what is really done. That is not due a lack of effort from manufacturers, it is due to the way there are supposed to be used: by a non-expert, on a large range of possible applications, without input from other techniques.

Core drilling is mainly used in mineral exploration to discover ore deposits by obtaining geologic and stratigraphic properties from the Earth's subsurface, specifically with respect to alteration referred to as metasomatism providing a much larger target for detection and mapping of a hydrothermal system than does a deposit (Ridley, 2013). Alteration facies on the basis of characteristic mineral assemblages in hydrothermally altered rocks are an important indicator of proximity to ore in exploration. However, alteration facies, including mineralogy, mineral abundances, and mineralogical textures, can be difficult to identify with the naked eyes in the field depending on the types of rock such as fine-grained or dark-coloured rocks, for example. In these cases, visual examination even by a field geologist may not give a definite answer. Spectroscopy, however, utilizes the physical and chemical properties of a mineral, thus it does not depend much on optical properties. Furthermore, many portable devices are appropriate for analysing fine-grained minerals due to their small beam sizes ranging from microns (μm) to millimetres (mm).

Preparatory drilling should be undertaken to ascertain the exact location where it becomes economical and commercially viable for the mining operation since mining for the exploitation of mineral resources is a very costly affair. In the long-term trend, exploration efficiency over the last 20 years has been declined based on the total amount of metres drilled in the world (Schodde, 2019). **Fig. 1** shows the amount of drilling required to discover a new deposit was increased by 2.8 times between 2005 and 2017. One of the main factors associated with the recent decline in discovery performance is the progressive move to deep-seated target deposits under-cover (Schodde, 2019). In this reason, the importance of real-time analysis in the field has been increasing by helping fast decision-making support during fieldwork, drilling operations, and sample screening before laboratory requests in mineral/resource exploration (Lemière and Uvarova, 2020).

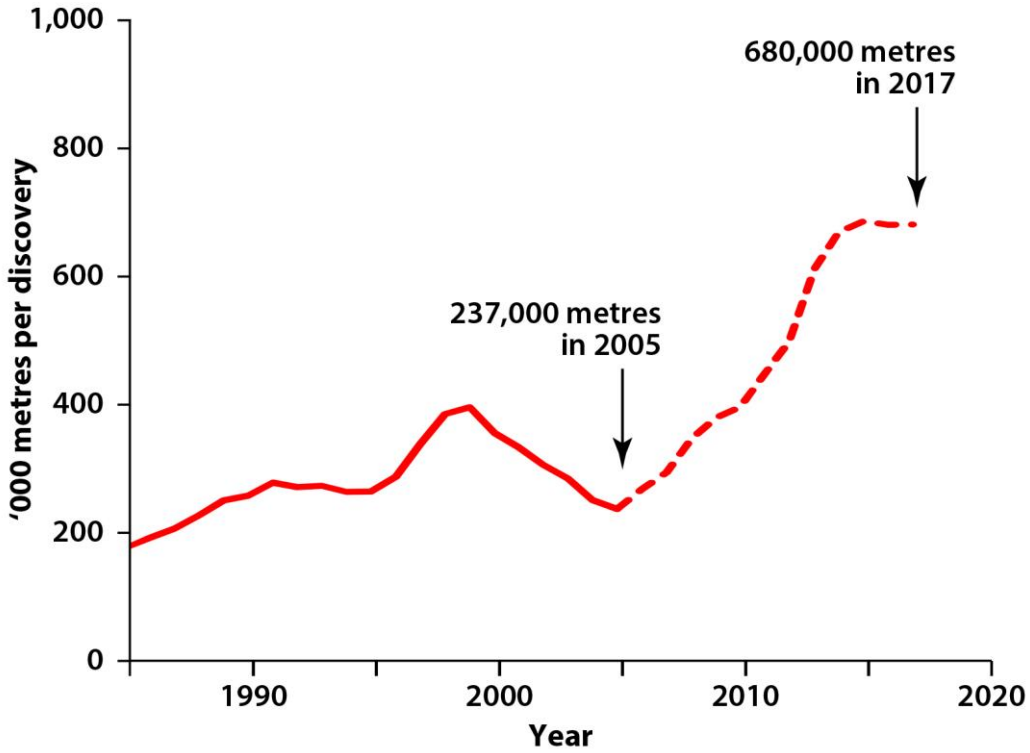

Fig. 1. The total amount of metres drilled to discover a new deposit in the world modified from Schodde (2019). The red dotted line is estimated values including adjustment for unreported discoveries.

Analysis of the obtained drill core samples is traditionally performed through visual inspection and laboratory-based analyses, which are generally time-consuming and expensive. Alternatively, drill core scanners are systems that use single or multi-sensors to gather mineralogical and/or geochemical information on drill core samples at much higher speeds and

lower costs. Although the semi-automatized and non-destructive sensor systems can be applied to real-time spectroscopic analyses, the following major limitations remain compared to portable equipment: i) only applicable to the drill core; ii) less precision of sensors; iii) much expensive cost of instruments; iv) issues associated with handling and/or interpreting large amounts of data. On the other hand, field-portable technologies continuously provide analytical results on the spot in almost real-time by reducing analysis delay and expense. Furthermore, most handheld devices require no or limited sample pre-treatment. This makes it much faster analysis than laboratory-based conventional techniques and thus can save energy and manpower.

1.2. Overview of the Elvira VMS deposit

Volcanogenic Massive Sulphide (VMS) deposits typically consist of stratabound to stratiform massive to semi massive lens-shaped sulphide bodies with an underlying discordant vein-type mineralization called stringer or stockwork zone and are surrounded by an envelope of altered host rock which usually is most developed in the footwall (Franklin et al., 2005). VMS deposits are dominated by pyrite, with lower amounts of other sulphides and accompanying phases, which together represent a major source of base (Cu, Pb, Zn), precious (Ag, Au) and other metals (e.g., Co, Sn, In, Cd, Tl, Ga, Se, Sb, Bi) of economic and industrial importance (Franklin et al., 2005; Large et al., 2001b; Tornos et al., 2015). The Iberian Pyrite Belt (IPB) is an E-W 250 km long by 20-70 km wide VMS district in the southwestern Iberian Peninsula. The Minas de Aguas Teñidas SAU (MATSA) company operates the Sotiel-Migollas VMS deposits, which have been mined since Roman times (**Fig. 2**A). A detailed geophysical exploration led by MATSA in order to increase resources of this ore deposit led to the discovery of a new massive sulphide body called Elvira (Gisbert et al., 2019; Tornos, 2006, **Fig. 2**B). The Elvira deposit represents an eastward continuation of the Sotiel-Migollas massive sulphide deposits cluster due to strong similarities with respect to lithologic and structural settings (Gisbert et al., 2019; Prada et al., 1996; Velasco-Acebes et al., 2019). The Elvira deposit consists of a polymetallic (Cu-Zn-Pb) pyrite-rich massive sulphide body with evidence of having been dominantly deposited in a sub-oxic to anoxic basin and rooted on a large stockwork zone (Gisbert et al., 2019).

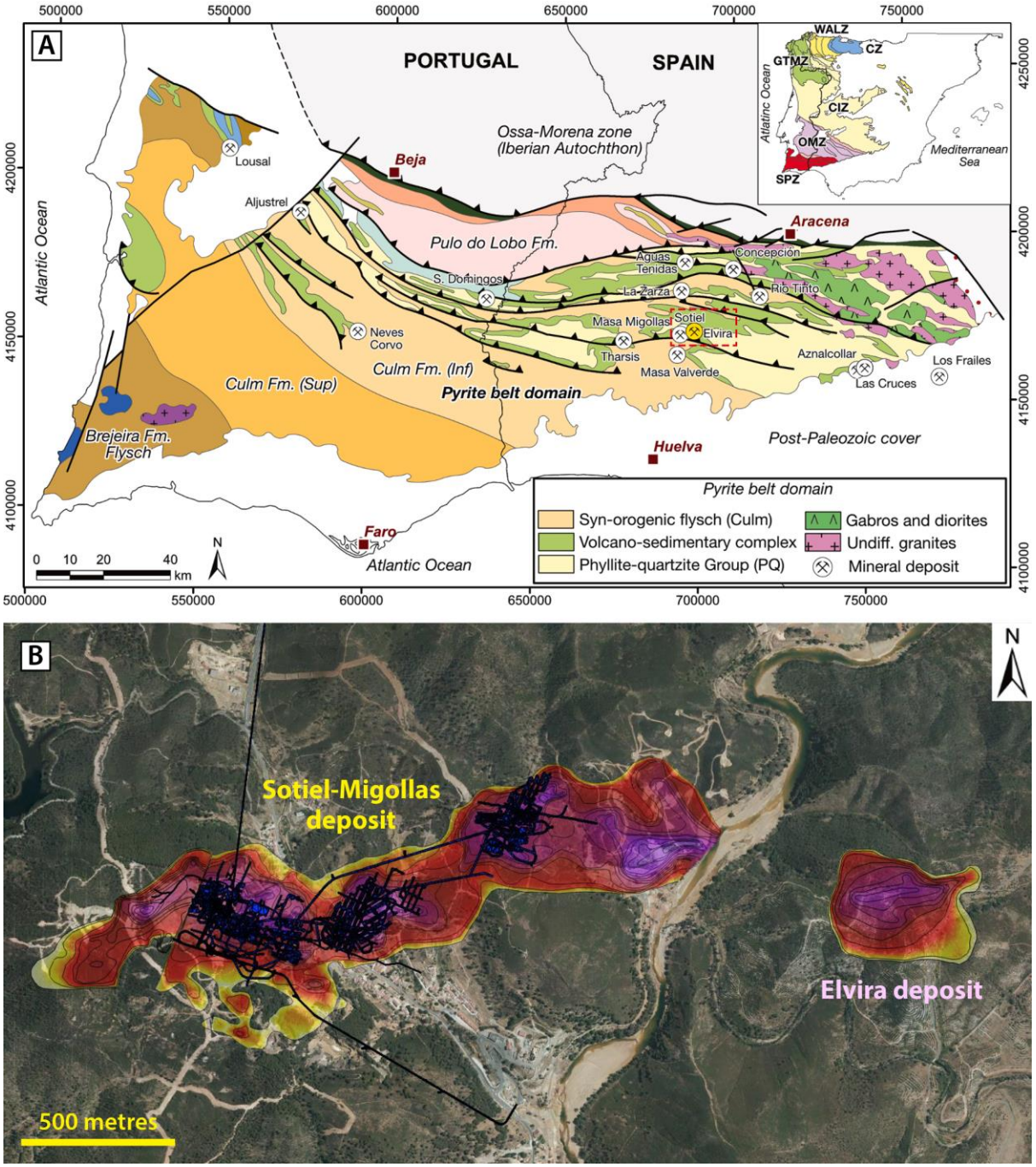

Fig. 2. A) Main stratigraphic units in the Iberian Pyrite Belt. CIZ: Central Iberian Zone, CZ: Cantabrian Zone, GTMZ: Galicia-Trás-os-Montes Zone, OMZ: Ossa-Morena Zone, SPZ: South Portuguese Zone, WALZ: West Asturian-Leonese Zone. The red dotted box indicates the location of the Sotiel-Migollas and Elvira deposits modified from De La Rosa et al., 2021; B) Electromagnetic (VTEM) anomalies in Sotiel-Migollas-Elvira deposits provided by MATSA.

Most of the shale-hosted VMS deposits in the IPB do not display either clear metal zonation or zones of major base metal enrichment (Tornos, 2006). In Sotiel-Migollas, Cu and Zn–Pb rich zones are common, but they do not show a well-defined distribution and neither does Elvira (Prada et al., 1996). The mineralization of the Migollas deposit is mostly massive and with no interbedded shale, and is dominated by a siderite-rich massive sulphide (Velasco-Acebes et al., 2019). The mineral assemblage of the massive sulphides in the Sotiel-Migollas-Elvira area is dominated by massive pyrite with variable amounts of chalcopyrite, sphalerite and galena, lesser amounts of arsenopyrite, pyrrhotite, magnetite and tetrahedrite-tennantite, as well as trace amounts of sulfosalts (boulangerite, bournonite, jaskolkiite and meneghinite), cassiterite, native bismuth and electrum (Velasco-Acebes et al., 2019).

Alteration characteristics in the Sotiel-Migollas area have been described by Velasco-Acebes et al. (2019). The less hydrothermally altered shale mainly consists of a foliated groundmass of fine-grained illite ± muscovite, sparse pyrite, disperse grains of anhedral quartz, carbonates, ilmenite (altered to rutile) and zircon. In areas affected by hydrothermal alteration, chloritic alteration is closely associated to zones of brecciation or veinlets of carbonates and sulphides ± quartz. Primary shale layering was lost during chloritization, and the illite was replaced by massive chlorite. The resulting mineral assemblage contains clinochlore ± chamosite, variable amounts of carbonates, abundant anhedral pyrite (10-30%), and small amounts of disseminated sphalerite, chalcopyrite, galena, monazite, and a significant amount of hydrothermal zircon. In the Migollas area, the shale between the individual lenses and lateral to the mineralization shows irregular chloritization and a subtle carbonate-rich alteration.

2. Subject of the thesis

This thesis is part of the NEXT (New Exploration Technologies) project (G.A. No. 776804) funded by European Union's Horizon 2020 research and innovation program (https://www.new-exploration.tech/). The NEXT project aims at developing new geo-models and novel sensitive exploration technologies, which are rapid, cost-effective, and environmentally safe. Within this frame, therefore, our task in the project is to extract as much spectral information as possible from a limited number of samples analysed by existing lightweight (i.e., portable) equipment. Portable devices are able to measure any type of solid

samples such as drill cores and outcrops, and also powders. Since we focus on data treatment, any spectral data obtained from a laboratory-based or portable instrument can be applied. The subject of this thesis is the spectral characterisation of "**vectors**", which provide the chemical composition/variation in the hydrothermally altered minerals from the distal margin to the high-grade ores, by applying the reconciliation of mineralogical and geochemical data acquired from several portable spectroscopic devices.

The use of vectors to ore focuses on the identification and study of lithogeochemical fingerprints produced by the mineralizing hydrothermal system or by subsequent ore remobilizations within and around ore deposits (Ames et al., 2016; Large et al., 2001b; Madeisky and Stanley, 1993). Vectors to ore have the potential to detect the nearby presence of an ore deposit and to provide information on its likely location or characteristics. The alteration assemblage is controlled by factors such as rock/sediment composition, water/rock ratio, temperature, fluid composition, pH, and redox (Hannington, 2014). In the exploration and characterization of the VMS system, changes in these controlling factors with depth and distance from the centre of the hydrothermal system typically result in distinct mineralogically and geochemically zoned alteration halos, which are the base for most vectoring tools (Gibson et al., 2007; Large et al., 2001b). The main vectors to ore used in the exploration and study of the VMS systems can be grouped into three main categories suggested by Gisbert et al. (2021a): i) mineralogical zoning; ii) related to whole-rock geochemistry; iii) related to mineral chemistry. In this thesis, the main vectors i) and iii) are considered.

3. General problematic of the thesis

Portable spectroscopic techniques have been widely used in mineral exploration based on: X-ray fluorescence (XRF), X-ray diffraction (XRD), Fourier-transform infrared spectroscopy (FTIR), Visible, near-infrared and short-wave infrared (VNIR-SWIR), and Raman spectroscopy (Leary et al., 2021). Furthermore, handheld Laser-induced breakdown spectroscopy (LIBS) is becoming increasingly accepted as important techniques recently (Singh et al., 2011). Despite this fact, only two codes from JORC (the Australasian code for reporting of exploration results, mineral resources, and ore reserves) in 2012, UMREK (Turkey's National Resources and Reserves Reporting Committee) in 2018 explicitly refer to

these tools through handheld XRF instruments only. The Canadian Institute of Mining, Metallurgy and Petroleum (CIM) Mineral Exploration Best Practice Guidelines in 2018 do mention handheld XRF to outline that "these units can help provide rapid information to field geologists, assist in recognizing new or unexpected types of mineralization, and enable on-the-spot decisions to extend or infill drill holes for an exploration-stage property" (Gosson, 2018). For the other techniques, however, no additional systematic quality assurance process was undertaken. Operator skills and knowledge on the analytical side are hence not equivalent in between the field and the laboratory. There is, therefore, a need to promote best practices in applying these analytical techniques and reporting the results they provide. To solve this problem, the methodological knowledge linked to each spectroscopic technique should be first addressed as follows: sample preparation, the definition of analytical conditions, data processing, use of standards, safety issues, reporting, and adding general considerations on applicability and restrictions.

In order to enhance the spectral understanding of each mineral, mineral identification by spectroscopic analyses firstly requires recognition of spectral properties such as band positions with respect to single purified or well-characterized materials. Various spectral libraries based on different spectroscopic techniques currently exist, for example, USGS and ASTER for VNIR-SWIR and MIR, RRUFF for Raman and MIR, and AMCSD for XRD (Baldridge et al., 2009; Downs and Hall-Wallace, 2003; Kokaly et al., 2017; Lafuente et al., 2016). Although these libraries possess a few thousands of reference spectra, it is rare to provide spectrum and interpreted data simultaneously using multiple techniques analysed on the same samples. In this thesis, therefore, a spectral library consisting of spectral data with respect to each mineral acquired from several portable spectroscopic instruments is provided together with compositional data by an electron microprobe.

Many minerals are not restricted to a single chemical composition, yet instead can have a range of composition. These minerals are referred as solid solution which is a single crystalline phase that may be varied in composition within finite limits without the appearance of an additional phase (Neuendorf, 2005). Mineral discrimination in solid solution is always a difficult and complicated challenge due to a continuous variation in terms of chemical compositions. Compositional changes in white mica, carbonate, and chlorite in VMS systems, for example, can help define the alteration halos and therefore have been commonly used as

vectoring tools to ore (Dehnavi et al., 2018; Large et al., 2001a; Lydon, 1988). Therefore, systematic comparison between spectral properties and chemical composition should be preceded before applying to "real" rock samples. In the late 1980s, more than 50 types of spectroscopic techniques already existed, and further developments are constantly leading to new types of measurements and modifications of the older more established spectroscopic methods (Calas and Hawthorne, 1988). The use of various spectroscopic techniques for one mineral or one technique for various minerals is easily accessible. However, it is rare to find a study of diverse spectroscopic methods for various minerals comprehensively addressing the relationship between their spectral properties and compositional changes. For this reason, it is essential to know which spectroscopic technique is most/less sensitive to changes in the chemical composition of which minerals.

Spectral data reconciliation derives from the assumption that the strengths of one technique will address the weaknesses of the others. Furthermore, errors and uncertainties from one analysis can be reduced by the use of accurate values from another. For example, one spectroscopic technique can easily answer these kinds of questions such as i) what the elemental concentration is and ii) which minerals are identified in the analysed area. However, in practice, we could face more detailed questions such as iii) what the mineralogical concentration is and iv) what the chemical composition of selected minerals in the analysed area is. These questions should be much more complicated to answer by using only one technique, but the reconciliation of geochemical data from multiple techniques can provide information to address them. Therefore, several developments in this thesis are carried out: building a procedure to match the elemental and mineralogical information, which corresponds to the reconciliation of the geochemical data, translating it into software that will automatically run this reconciliation method, and extracting the best geochemical information from each technique applied.

4. Objectives and structure of the thesis

Reconciliation of geochemical data acquired from portable spectroscopic devices is the heart of this thesis. The main aim of this thesis is to determine the best geochemical information from each technique applied by combining the mineralogical and elemental information

together. In order to develop the usage of portable spectroscopic devices applied to rock or core samples, both analyses consisting of six portable techniques include: (i) elemental analyses such as XRF and LIBS for major, trace, and light elements, and (ii) mineralogical analyses such as Raman, VNIR-SWIR, MIR, and XRD to constrain rock-forming, ore, and alteration minerals. This Ph.D. thesis aims four main scientific objectives that will be described in the six chapters (**Fig. 3**).

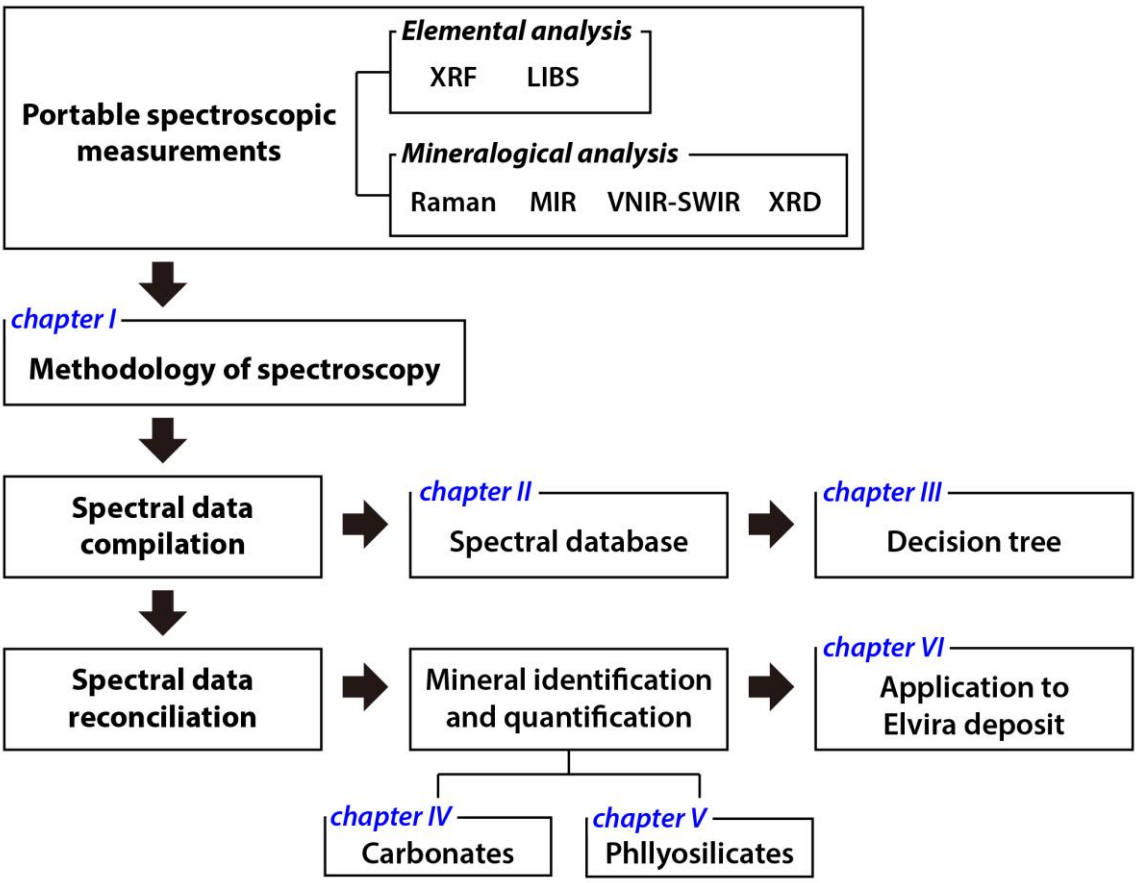

Fig. 3. Structure of the Ph.D. thesis.

Chapter (I) Methodology of spectroscopy. The range of methodologies and the types with respect to spectroscopy is extensive. Therefore, it is first necessary to acquire or broaden the required knowledge for each spectroscopic technique. The spectral knowledge includes theoretical background, and technical information for best practice associated with each portable instrument. This chapter contains some parts of the work done with Task 4.3 team in the NEXT project.

Chapter (II) Establishment of a spectral database. The spectral database gathers the portable spectroscopic data obtained on standard samples: silicates, carbonates, sulphates, and sulphides, which are possibly present in the target ore deposit. In addition, the composition database is made up of the standard samples from the spectral database analysed by laboratory analytical instruments such as Electron probe micro-analyser (EPMA).

Chapter (III) Design of a decision tree. The decision tree for mineralogical analysis provides diagnostic band positions from each technique with respect to all the minerals from the spectral database by combining spectroscopic information of spectral characteristics. The idea is to obtain the right order for presence/absence in the analysed area, and both qualitative and quantitative information on light elements such as sodium (Na) and magnesium (Mg).

Chapter (IV) Mineral identification and quantification of carbonate minerals. Spectroscopic features of carbonates, which are one of the indicative minerals in the Elvira VMS deposit, are identified by comparing the spectral changes based on the compositional variations. Synthetic mixtures among the indicative minerals are analysed to access the quantitative relationship between their spectral changes and mineral concentration.

Chapter (V) Mineral identification and quantification of phyllosilicate minerals. Spectroscopic features of trioctahedral chlorites and dioctahedral micas, which are the other indicative minerals in the Elvira VMS deposit, are identified by comparing the spectral changes based on the compositional variations. Synthetic mixtures among the indicative minerals are analysed to access the quantitative relationship between their spectral changes and mineral concentration.

Chapter (VI) Application to the Elvira VMS deposit. A whole downhole from the Elvira deposit is used as the application of the case study. About 200 points in the ELV-44 drill core are directly measured on the core by each portable spectroscopic device. The bottom part of the core showing diverse lithologies, is analysed intensively. Mineral assemblages and composition are identified from thin sections, and spectral data by the portable devices are measured on the opposite rock chips. Spectral characteristics of accessory minerals in the deposit are additionally identified. Finally, the developed software based on the geochemical data from portable devices is tested by comparing with the mineralogical mapping by scanning electron microscopy (SEM) with energy dispersive X-ray spectrometry (EDS).

Chapter I. Methodology

1. Introduction to spectroscopy

1.1. Introduction

Spectroscopy is the study of the interaction between matter and electromagnetic (EM) radiation, including what is commonly referred to as "light" as well as radiation at shorter and longer wavelengths. Spectroscopy is widely applied as an exploratory tool in the various fields of agriculture, archaeology, art, astronomy, biology, chemistry, **earth science**, ecology, food, forensic science, forestry, historical perspective, medicine, physics, and so forth. (Lindon et al., 2016). It allows the composition, physical structure, and electronic structure of matter to be investigated at the atomic, molecular, and macro scale, and over astronomical distances. In terms of earth science, the solid Earth mostly consists of rocks, which are composed primarily of mineral grains formed from atoms chemically bonded into an orderly structure (Nesse, 2012). The International Mineralogical Association (IMA) established that minerals are naturally occurring solids with well-defined chemical compositions and crystallographic properties, which display a highly ordered internal atomic structure having a regular geometric form (Nickel and Grice, 1998). However, in practice, exceptions and borderline cases inevitably arise, and the IMA Commission dealt with mineral nomenclature with respect to these specified mineral substances. For example, the basis for accepting naturally-occurring amorphous phases as a mineral species could be a series of complete quantitative chemical analyses that are sufficient to reveal the homogeneous chemical composition of a substantial number of grains in the specimen, and physico-chemical data that prove the uniqueness of the phase. In the case of solid solution series, the compositional range of the species is taken to apply from that of the end member to 50 mol % of the series in a continuous binary solid-solution series, and the "50% rule" is interpreted to mean predominant occupancy of a particular structural site in multiple solid-solution series (Nickel and Grice, 1998). In practice, the 50% rule should not be applied too rigorously, and that a certain degree of latitude must be permitted when dealing with complex minerals. Since scientific understanding of fundamental chemical and physical properties of minerals plays an important role in numerous geochemical and geophysical processes, the field of mineralogy and geochemistry has been captivated with investigating the nature of all geomaterials.

Spectroscopy in earth science can provide local and atomistic-level information on a variety of different materials such as gas, liquid, or solid phase, and it produces diverse information, for example, chemical composition, structure, and crystal chemistry as well as dynamics. The conventional methods analysed in a laboratory to characterize a rock or mineral are an optical microscope, a powder X-ray diffractometer, and a couple of different devices for analytical chemistry determinations, such as the electron microprobe or an X-ray fluorescence unit. The development and application of various spectroscopic methods over the last approximately half-century have been most prominent as a result of new approaches and the development of instruments for mineralogy (Geiger, 2004).

Before the beginning of the spectroscopic analysis managing diverse types of spectral data of various mineral/rock species, it is first essential to understand the spectral knowledge such as theoretical background and technical information of each technique. In this part, a brief outlook of the main laws that govern the interaction of electromagnetic radiation with matter, and **six techniques** in which these laws can be applied to the different phenomena that can arise from this interaction. It is noted that the part concerning the fundamentals of spectroscopy is succinctly summarized, and the specific techniques are described in more detail as needed in each of the following.

1.2. Electromagnetic radiation

EM radiation is the simultaneous propagation of both electric and magnetic fields orthogonal to each other, with varying intensity as a function of time and distance (**Fig. 4**). Maxwell's equations lead to the prediction of electromagnetic waves that can travel through space without a material medium, implying a speed of electromagnetic waves equal to the speed of light (Hertz, 1888; Maxwell, 1865).

Furthermore, EM radiation is a form of energy accompanied by both wave-like (i.e., wavelength) and particle-like (i.e., photon) properties, and the EM waves carry their energy in discrete packets called photons (Einstein, 1905; Planck, 1901). The energy of a particular wavelength can be expressed as:

$$E = h\nu = \frac{hc}{\lambda} \quad (1)$$

where E is the energy in kJ/mol, h is 3.99 x 10^{-13} kJ·s·mol^{-1}, a number known as Planck's constant, c is 3.00 x 10^{8} m.s^{-1} (the velocity of light in vacuum), ν is the frequency in s^{-1} (reciprocal second), and λ is the wavelength in meters.

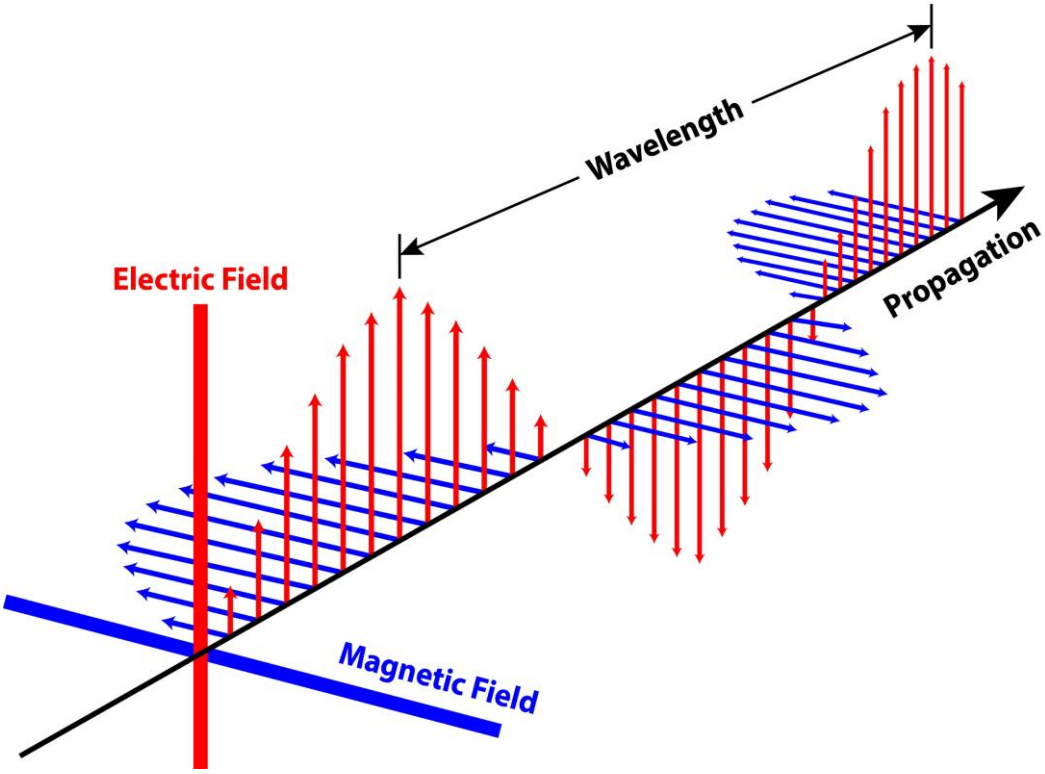

Fig. 4. Schematic of an electromagnetic (EM) wave consisting of an oscillating electric field with an orthogonal oscillating magnetic field.

1.3. Electromagnetic spectrum

The electromagnetic spectrum shows the full range of EM radiation according to their respective wavelengths and frequencies (**Fig. 5**). The visible spectrum, which can be seen with the naked eyes, makes up a small fraction of the different types of radiation that exist (400 nm < λ < 800 nm). For example, X-rays are higher in frequency (and thus lower in wavelength) than visible light whereas infrared (IR) rays are lower-frequency EM waves. It is conventional to convert the frequency, ν, from Hz (s^{-1}) to wavenumbers (cm^{-1}) by dividing ν by the speed of

light c in vacuum. Wavenumbers are defined as the number of wavelengths per unit distance, typically centimetres. Thus, the wavenumber, which is directly proportional to frequency and to photon energy is used as a convenient unit of energy in spectroscopy such as mid-IR (MIR) and Raman spectroscopy.

On the other hand, remote sensing or handheld users in the visible and near infrared region, display spectra as a function of wavelength in micrometres (μm) or nanometres (nm) since absorption features occur at well-defined wavelength positions due to distinct and consistent energy levels as a function of the size of the ionic radii of the cations bonded to different molecules (Hunt, 1977).

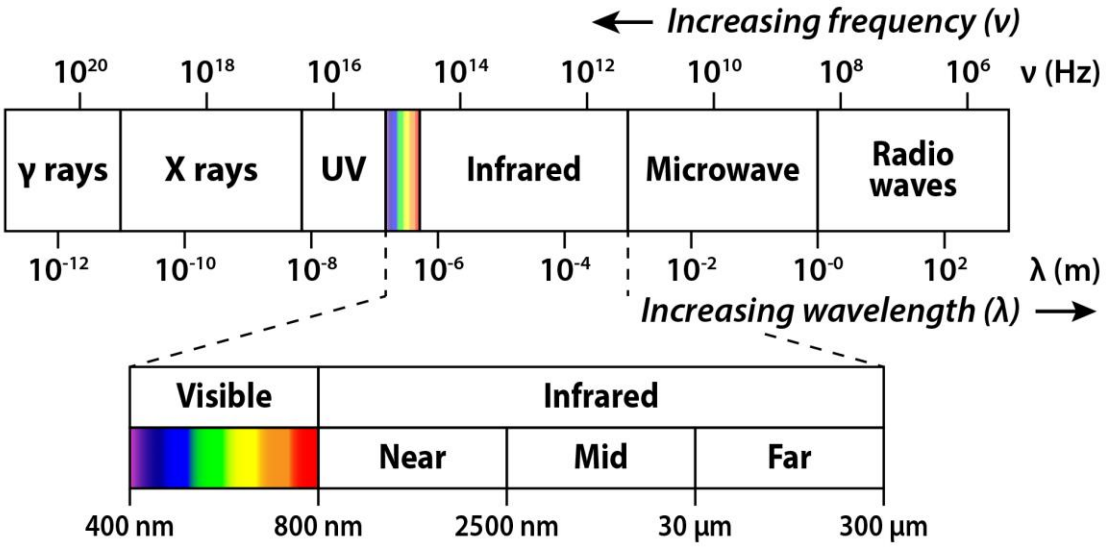

Fig. 5. Schematic of the EM spectrum with the spectral subdivisions of the visible and infrared region.

1.4. Spectroscopy: Interaction between light and matter

The study of spectroscopic methods is based on quantum mechanics concepts (Atkins and Friedman, 2011; Levine et al., 2009; Merkt and Quack, 2011; Sakurai and Commins, 1995). According to Bohr's frequency condition, the absorption or emission of energy can only occur if the energy of the EM radiation corresponds to the difference between two discrete energy levels ($\Delta E_{1\to 2} = E_2 - E_1 = h\nu$) for some state of an atom (Bohr, 1914). Thus, a determination of the magnitude of the energy difference (ΔE) provides a measure or probe of the system under study and it can give chemical and/or structural information.

Spectroscopy is the study of the absorption, emission, reflection or scattering of EM radiation by atoms or molecules (or atomic or molecular ions) to qualitatively or quantitatively study atoms or molecules. The interactions between the photon beam and matter offer insight into a host of fundamental processes and properties of material. The types of spectroscopies can be distinguished by their physical process, which occurs when radiation interacts with an atom (**Fig. 6**).

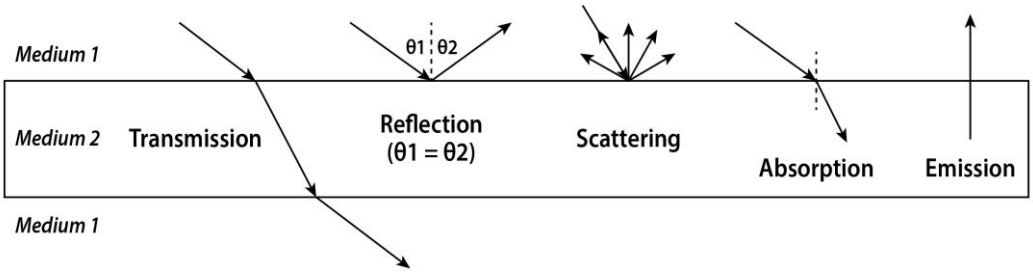

Fig. 6. Schematics of interactions between EM radiation and matter.

Transmission is the refracting process, which EM waves have a modified pathway at the Medium 1/Medium 2 interface, as governed by Snell's Law. In reflection, EM waves are deviated at an angle equal to the angle of incidence from a smooth surface. EM waves may also be scattered at a surface due to roughness, sending the light in all directions. During absorption, EM waves transfer their energy to the material (e.g., vibrations or phonons, electronic excitations). When matter in the excited state returns to the ground state, it emits EM radiation.

2. Spectroscopic techniques

This thesis concentrates on **six techniques** in three spectroscopic methods based on the interactions: i) emission-based methods; ii) absorption-based methods; and iii) scattering and diffraction methods.

i) Emission-based methods. A photon is generated while the energy in the medium (atom, molecule, or material) decreases by hv. For this to happen, atoms or molecules that are excited to high energy levels can decay to lower levels by emitting radiation. Because each element emits a characteristic set of discrete wavelengths according to its electronic structure, the elemental composition of the material can be determined by observing these wavelengths

(Moudgil, 2010). **X-ray fluorescence (XRF)** and **laser-induced breakdown spectroscopy (LIBS)** fall in this classification as an elemental spectroscopy.

ii) Absorption-based methods. A photon is destroyed while the absorbing medium increases its energy by hv. Absorption of photons in different regions of the electromagnetic spectrum leads to transitions between different levels of energy in atoms, molecules, or materials (**Fig. 7**). Infrared spectroscopy is one of the most common and widely used absorption-based techniques, and infrared region is usually divided into three regions: the near-, mid- and far- infrared (**Fig. 5**). **MIR**, approximately 4,000-400 cm^{-1} (2.5-25 μm) is generally used to study the fundamental vibrations and associated rotational–vibrational structure. **NIR**, approximately 14,000-4,000 cm^{-1} (0.7-2.5 μm) can probe overtone or combination modes of molecular vibrations.

iii) Scattering and diffraction methods. Most of the EM radiation passes through the sample unaffected, but a small percentage of the light is scattered in all directions by the particles in the sample. The radiation scattering is divided into elastic or inelastic whether the wavelength of the scattered radiation is the same as the wavelength of the incoming beam (Raman and Krishnan, 1928; Rayleigh, 1899, **Fig. 7**). **Raman spectroscopy** is the one of the most popular among the techniques based in inelastic scattering, and **X-ray diffraction (XRD)** is coherent elastic scattering of X-rays by atoms or ions in a crystal.

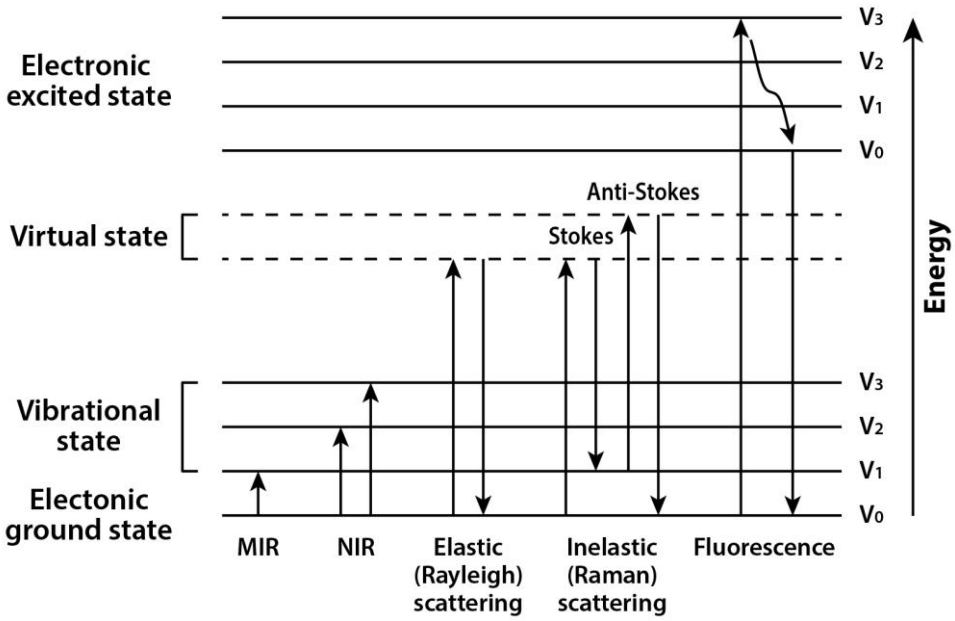

Fig. 7. Schematic representation of energy level diagram related to IR absorption, Raman scattering.

2.1. XRF technique

XRF is to determine chemical elements both qualitatively and quantitatively by measuring their emission of characteristic "secondary" (or fluorescent) X-rays (Bertin, 1975). When materials are excited with the primary X-radiation, ionization consisting of the ejection of one or more electrons from the atom may occur. Electrons from outer electron shells fill the resultant voids emitting fluorescence radiation that is characteristics in its energy distribution for a particular material. The intensity of each characteristic radiation is directly related to the amount of each element in the material. The relation between the emission energy and the atomic number is described by the Moseley's law concerning the characteristic X-rays.

Portable XRF (pXRF) instruments is one of the most widespread techniques available in the raw material sector as a portable tool since the early 1990s (Leary et al., 2021). In particular, since 2010, the performance of portable instruments has been enhanced with improved detection capabilities of lighter elements (i.e., Al, Si, P, S, Cl) (Laperche and Lemière, 2021). Niton XL3t GOLDD+ XRF analyser used in this thesis is optimized for analyse of geological materials, designed for portable use, both in the laboratory and in the field. It provides element identification within a sample as well as quantifies each element from bulk percentages to part per million (**Fig. 8**).

Fig. 8. Thermo Fisher Niton Xl3t GOLDD+ XRF analyser.

2.1.1 Samples and sample preparation

The applicability of pXRF is mainly on solid samples. Some tests have been done on liquids by installing the device in a waterproof container, but the containers themselves absorb some of the signal. Gas analysis is not possible as pXRF safety usually relies partly on a proximity detector, which disables analysis if no dense material (i.e., liquid and solid) is facing the device head. Sample preparation depends on the type of data to be gathered. Quantitative data with limited error bars is possible only under the following conditions for the sample:

i) Flatness. Marked asperities on the sample surface can lead to shadowing effects. That means that X-rays emitted in bottoms of the sample surface will be absorbed by highs of the same surface. That will mainly lead to inaccurate quantification of lighter elements.

ii) Homogeneity. Samples must be homogeneous at the beam scale. Changing the position of the beam on the sample should not change the value of the calculated concentrations. Crushing and mixing the sample is the best way to achieve that purpose.

iii) Dryness. Water is an absorbing medium for X-rays emitted by most elements. Samples must then be dried on all their "infinite thickness" before being analysed.

iv) Thickness. Most quantification programs in pXRF rely on a sample of infinite thickness. That means that no X-ray emitted from behind the sample should reach the detector. That does not mean that the beam is totally absorbed by the sample, and it does not reduce by any means the safety rules. The real size of the infinite thickness depends on the energy of the emitted X-rays. It will be limited to a few micrometres for Mg and reach several millimetres in a quartz matrix for barium (Ba).

Beads, pellets, and powders held in capsules can meet these requirements. Finely grained samples may be homogeneous enough and provide good data but there is no means to exclude a hidden feature below the sample surface that would contribute to the signal. As such, confidence in results from such samples is not at the level as it would be on homogenized ones. Unprepared surfaces on the outcrop or handpieces can lead to indicative values only unless it has been proven applicable in a specific context (e.g., in the case of glacial till), and errors associated with the measurement properly understood as done in Sarala et al., 2015.

2.1.2. Analytical conditions

i) Films. The device operates in direct contact with the sample. Any membrane, film, bag, container, and so forth. in between the sample and the device will act as a filter and absorb part of the X-rays emitted by the elements of the sample. As a consequence, elements with absorbed X-rays will be underestimated. That is particularly critical for elements emitting at lower energies, which includes low-Z elements. The material composition, density, and thickness are of concern. The thin film holding a powder into a container should be as transparent to X-rays as possible. Some films can also contribute to the signal, for example, PVC bags or films contain large amounts of chlorine (Cl).

ii) Beams. A "Beam" or "Filter" corresponds to a voltage in the X-Ray tube and the possible presence of a film of known composition in between the tube and the sample, acting as a secondary source. "Beams" and "Filters" are designed to specifically stimulate the XRF from a series of elements. Most pXRF devices use at least two beams, one for light elements and another for the rest of the periodic table. A single pXRF analysis combines results from up to four Beams. Some pXRF allows the user to design its own beams. The duration of each beam can be modified by the user. The longer the duration, the better the signal to noise and the detection limits.

iii) Number and duration of measurements. Increasing the duration of a single measurement will improve the signal-to-noise ratio in general. That sill in turn lowers the detection limits, measurement accuracy, and precision. Provided that the detection limits are met, repeating measurements can also improve the accuracy of the average value. For some still not fully understood reasons, it appears that multiplying the number of analyses provides a more accurate result than multiplying the acquisition time by the same factor on a single measurement. Hence, once the duration of a beam enables to quantify an element, one would better duplicate or triplicate results rather than going on increasing the duration of the beam. Previous studies found that an average value of triplicate measurements increased the accuracy of the results and by that way provided more comparable results to laboratory analytical methods (Sarala, 2016; Sarala et al., 2015).

2.1.3. Data processing

Data is automatically processed by the pXRF. However, each device usually holds several programs for signal processing. They can be linked to specific analytical conditions or not. Three classes of algorithms are available and a longer presentation of them can be found in (Laperche and Lemière, 2021).

i) User calibration curves. These curves are built by the User from known samples of compositions similar to that of the samples to be analysed. The calibration curve can be implemented into the device so that it will directly provide quantitative results. This method depends on the sample composition and must be checked each time the matrix changes.

ii) Compton Standardization methods (Soil mode). This category of data processing relies on a sample density correction based on the detection of the inelastic scattering of the sample. That method can compensate matrix effects to a certain degree. It is usually designed in pXRF to quantify dilute elements in an Al-Si matrix. This is the reason why it is often referred to as a "Soil" program. Samples consisting of matrices far from that of the reference (e.g., massive oxides or sulphides) will not be properly quantified.

iii) Fundamental Parameters methods (Mining mode). This method takes relies on a proper compensation of absorption and matrix effects from the calculated sample composition. That enables correcting for almost any sample composition, hence increasing accuracy on non-Al-Si-rich matrices, at the cost of some precision. An extensive discussion about the results obtained with "soil" and "mining" modes is available in Hall et al., 2014.

2.1.4. Standards

Most pXRF have a built-in internal standard or a specific external one dedicated to checking the calibration in energy of the detector. Beyond that, these devices do not require a standard in order to obtain a result. However, these devices are known to suffer from temporary and/or short term and/or long-term deviations (Gazley and Fisher, 2014). Operators should therefore always use standards to check the device results before, during and after a series of measurements. These standards should be multi-element ones as deviations do not necessarily affect all the detected elements. Some standards should be common to all experiments so that long term deviations can be monitored.

2.1.5. Applicability and limitations

i) Low Z elements. X-ray emission decreases in energy and efficiency with the atomic number of the elements. H and He do not emit XRF. Li to Ne can only be detected under vacuum. Na can only be detected under vacuum or He atmosphere. Mg is the lightest element detectable under air when running a device equipped with a Silicon Drift Detector (SDD). If running a solid-state detector, the lightest detectable element is Ca; SDDs should then always be preferred for geological applications.

ii) Detection limits. Detection limits depends on the absorption and the emission efficiency. Hence, detection limits improve from Mg (several %) to Nb (~10 ppm). These values remain indicative. They depend on the type of detector, the anode material and voltage during X-ray generation. From that optimum, detection limits become poorer for elements detected on their K lines, up to Ba for tubes operating under a voltage greater than 40kV. For elements heavier than Ba, detection is made on their L-lines with detection limits greater than that of the elements detected on their K-lines of similar energy.

iii) Rare Earth. Rare Earth Elements should be detectable but interfere (see below **v) Interferences**) a lot with each other. Moreover, they are detected with their L-lines which also interfere with K-lines of elements between Ca (Kα: 3.69 keV) and Zn (Kα: 8.64 keV) (Schramm, 2017, **Fig. 9**). That both increases their detection limits and renders their quantification very hard.

iv) Beam size. X-ray cannot be easily focused. Only laboratory devices can be equipped with X-ray optics. The beam is only collimated. Any reduction in the beam size will then decrease the signal. Most devices operate a beam slightly larger or smaller than ~1 cm in diameter. Some devices are equipped with an extra collimator that can further decrease the beam size to a few mm. This size range is often too large to avoid measuring more than one mineral and too small for considering the analysed portion of the sample as homogeneous.

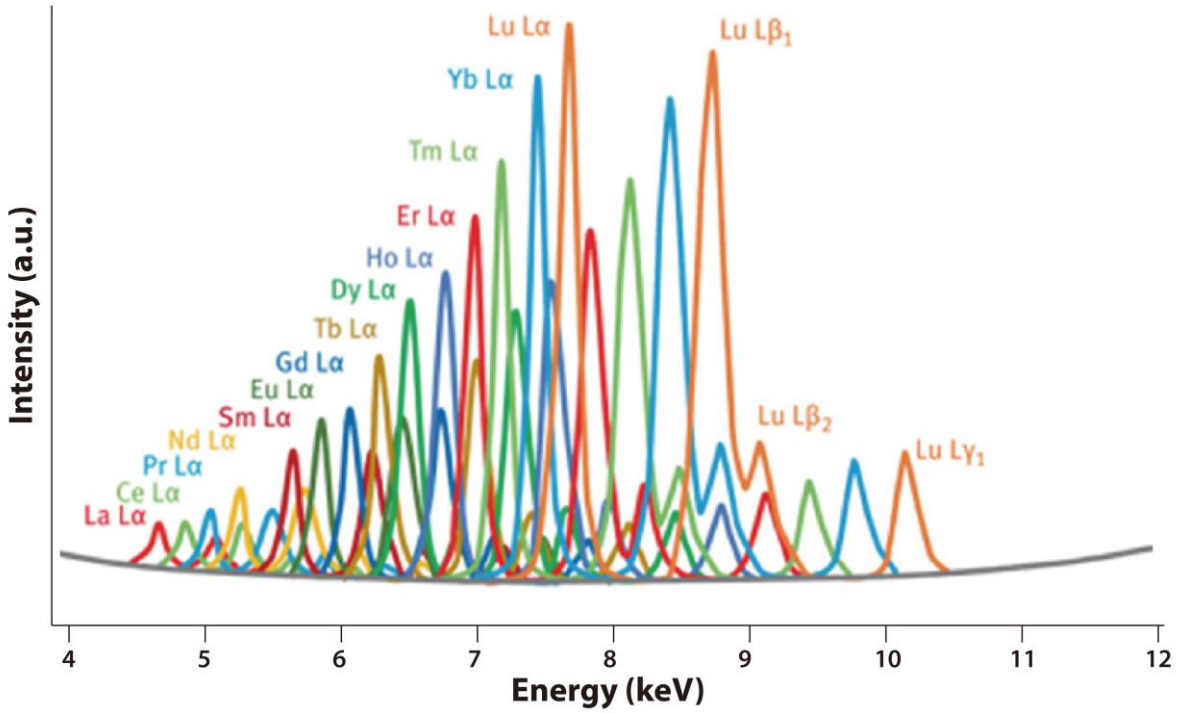

Fig. 9. Overlapped L-line spectra of REE measured at 100 μg/g single element samples from FLUXANA, ED-XRF, W tube, 40 kV, Mo secondary target, SDD modified from Schramm (2017).

v) Interferences. All portable pXRF rely on Energy Dispersive detectors. The aim of any quantification is to calculate the factor between the XRF signal of an element and the concentration of this element in the sample. That factor is unique for each sample and for each element. All portable devices, up to now, rely on evaluating the signal from Regions of Interest (ROI), which corresponds to the integration of the XRF signal over a specific energy window. The energy resolution of detectors is of ~150 eV at the MnKα line. Elements emitting X-rays in an energy window narrower than 150 eV will then interfere with each other. On laboratory devices, this interference is solved by decomposing the spectrum in Gaussian or Voigt functions. Portable spectrometers solve such interferences by applying multilinear corrections to the ROI values. However, the effect of one interfering emission on a detected one correspond to the contribution of a Gaussian (or Lorentzian or Voigt) into another one slightly moved side wise. This is not a linear effect. Hence, ROI based measurements should remain close to the conditions under which the device has been calibrated, which conditions are not well known by the user. If the sample do not correspond to the calibration conditions, the result will suffer from a bias. Testing the device result against data obtained by more reliable techniques is therefore compulsory to ensure that they remain accurate.

vi) Unforeseen interferences. The heaviest detectable element found in natural samples is U, which atomic number is 92. Among the elements from H to U, 11 elements are not detectable at all or not with a handheld (H to Na) and 9 are radioactive elements that are not found in natural samples (Tc, Pm, Po, At, Rn, Fr, Ra, Ac, Pa). Hence 62 elements are possibly present in natural samples while pXRF programs usually hold up to about 40 elements. Even if some of these 22 are often too dilute to be detected (e.g., Pt), some elements that are not included in the quantification program may produce some signal and this signal may interfere with another quantified element. In such case, the signal of the unforeseen element will be taken into account as emitted by the element with which it is interfering. Such situations are not rare, and the user should check the spectrum if some elements appear noticeably overestimated.

2.2. LIBS technique

LIBS is an atomic emission spectrometry technique based on the interaction of a highly energetic pulsed laser as the excitation source with the matter to be analysed (Cremers and Radziemski, 2013). This pulse produces the vaporization of the matter on its surface, then it atomizes and ionizes the vapor and forms a plasma in which atoms and ions are driven to excited states. While expansion and cooling of the plasma, these excited atoms and ions relax to lower energy level by emitting photons of their own specific wavelengths. The wavelengths of the detected atomic lines provide qualitative information on the presence of elements within the laser-induced plasma and consequently on the sample. The intensity of plasma emission lines at specific wavelengths proportional to the elemental abundance as the Boltzmann equation also describes (Radziemski and Cremers, 1989).

LIBS is not a widespread technique applied in various geoscientific fields, yet the emergence of handheld (HH) LIBS such as SciAps Z300 LIBS analyser used in this thesis, occurred in the early 2010s (Crocombe, 2018; Fabre, 2020, **Fig. 10**). The applicable domain has been broadened as follows: i) Handheld LIBS instrument is able to be performed with all-optical systems remotely or under various conditions; ii) The range of potentially detected elements is extensive. In principle, LIBS can detect any element of the periodic table, but for now, light elements are ideally suited (Fabre, 2020; Fabre et al., 2021; Senesi et al., 2021).

Fig. 10. Z300 tool and the interface for element pro identification lines.

2.2.1. Samples and sample preparation

LIBS has the advantage of being able to analyse geomaterials in any state (i.e., solid, liquid, or gas), yet solid samples are more suitable as the necessity of contact makes the liquid analysis hardly accessible using HH LIBS. Gas analysis is not possible as HH LIBS safety usually rely partly on a proximity detector, which disables analysis if no dense material (solid) is facing the device head.

Sample preparation depends on the type of data to be gathered. Quantitative data with limited error bars is possible only under the following conditions for the sample:

i) Flatness. Marked asperities on the sample surface may lead to loss of ablation of problem on the plasma emission. But, for classical element detection, the signal is usually largely sufficient to give good identification even if the sample is not strictly flat (for the scale of the window 3 mm x 4 mm). For quantitative applications, a strict flatness is required.

ii) Homogeneity. If bulk estimation is the aim of the study, samples must be homogeneous at the laser beam scale (or on the area analysed by several laser shots). The granulometry of the rock is the most critical point to be investigated before any interpretation. Multiplying the number of analysis on the rock can lead to a good bulk composition estimation. Crushed and homogenized samples can be investigated by making pressed pellets.

iii) Dryness. Water may lead to a loss of efficiency for the ablation process. The detection can be less effective but if its amount is not too high, qualitative analysis can be done.

iv) Thickness. LIBS analysis is slightly destructive with an ablated layer of ~12 micrometres per laser shot in general, depending on the status of the sample. As a series of laser shots is usually done, the sample thickness should be 40 micrometres at a minimum.

Finely grained samples may be homogeneous enough and provide good data but there is no mean to exclude a hidden feature below the sample surface, shallow enough to contribute to the signal. As such, confidence in results from such samples is not at the level as it would be on homogenized ones.

2.2.2. Analytical conditions

Portable LIBS tools are now largely developed by various companies (SciAps, Bruker, Hitachi, and so forth.). The technical aspects and the analytical conditions of the analysis are thus specific for each portable tool, even if some characteristics are usually identical as the use of pulsed Nd-YAG laser (1064 nm).

i) Laser. The parameters of the laser for portable tool cannot be modified. For this study, the Z300 tool has been used with these characteristics: 5-6 mJ/pulse, 50 Hz repetition rate, 1064 nm pulsed Nd-YAG laser source.

ii) Wavelength range of the detectors. Depending on the portable tools, the wavelength is adapted to a specific range to focus on the user applications (pharmaceutic, alloys, carbon…) and cannot be modified after. The Z300 presents an extended spectrometer range from 190 nm out to 950 nm. The extended range allows emission lines from elements H, C, F, N, O, Br, Cl, Rb, Cs and S to be measured.

iii) Observation of the sample. Most of the devices can provide an image of the sample through a camera, expect for the pharmaceutic applications (use of pellets or liquids). For this study, on-board camera/video for viewing sample before, during analysis, laser spot finder to show where laser strikes sample. The Z includes an illumination fibre which when aligned with the rastering/pointing, illuminates the location where the plasma will be created.

iv) Cleaning. The use of laser ablation permits to "clean" the first micrometres of the surface and LIBS analysis through a depth profile can be done if the spectra can be recorded for each laser shot. The Z300 features novel cleaning mode to provide automated, user-settable surface preparation depending on the type of application. Cleaning mode fires 5-6 mJ/pulse laser shots at 50 Hz, thus 5 cleaning shots every 0.1 sec. Users can choose the number of total cleaning shots, after which the tool will use subsequent shots for spectral data and analysis.

v) Depth profiling. The cleaning shot capability may also be used for depth profiling, for example, monitoring elemental concentrations as functions of depth into the sample. The laser focus is also under software control so that analysis continues into the depth of the material.

vi) Number of measurements. As the laser beam is 100 µm, the final crater is around 100µm-200µm (depending on the softness of the sample). A single measurement can be associated with large errors, and it can be badly representative of the bulk composition. Repeating the measurement can improve the error bars. The Z300 can raster the laser in discreet increments in two dimensions (X-Y) that can be modified by the user. This allows for heat mapping of regions on rocks up to several mm square. We recommend multiplying the number of analyses to increase the liability of the mean results. For bulk samples, the HH LIBS can be set to average results from every raster location for a bulk sample result, similarly handheld XRF analysis.

vii) Atmosphere (argon). LIBS tools are used under ambient air, but some of the tools provide argon purge if necessary. The Z300 is a handheld LIBS with an integrated, user-replaceable argon purge. Operating in an argon environment yields 10x or more boost in signal, particularly for emissions in the deep UV (190 - 300 nm), where many elements are measured. Also available are larger belt-mounted canisters (4x the volume). Users may also connect the tool to industry standard stationary argon tanks with our optional package of bridge regulator and tubing.

2.2.3. Data processing

Data is automatically processed by the HH LIBS. Specific internal programs are included to treat the spectra, detection of the elements, and quantification using internal calibration curves obtained on standards.

i) 2D rasters. Not all HH LIBS do include the 2D raster function. It depends on the applications. For mineral/alloy studies, it is of great importance if the aim of the study is the identification of 'mineral'/'inclusion' in the material. One may suggest the best LIBS precision is obtained when the laser is rastered (10Hz or 50Hz) and results averaged over multiple locations. The Z300 HH LIBS has an integrated XY stage, plus a Z-direction focus adjustment and the user may also setup their own raster pattern. A user can do a line scan, or even single spot analysis on an inclusion or vein of material.

ii) Gating time. Spectral data can be collected in either ungated or gated operation, with user settable gate delays. The temporal resolution (adapting the time after the laser shot and the width of the recording of the plasma emission) of the LIBS analysis is a way to avoid the bremsstrahlung and enhance the elementary emission or the access to recombination of the molecules in the plasma (**Fig. 11**).

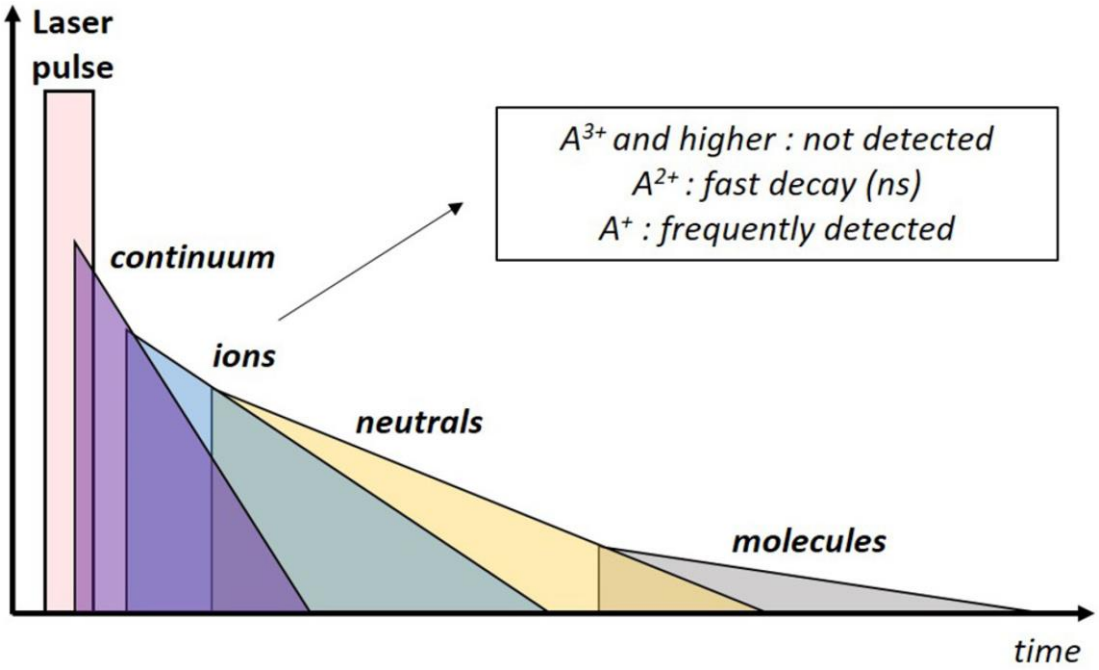

Fig. 11. Schematic observations of ions, atoms and molecules observed on plasma depending on the time delay after laser pulse modified from Fabre (2020).

iii) Acquisition, detection and quantification. For each point of analysis, one or several laser shots can be done, thus several individual spectra can be recorded for each point. The user has the possibility to keep all the spectra or only keep the mean value for each point of the rasters/lines. The included GeoChemPro software makes the element identification automatically, and an estimation of the probability of presence is given, according to the reference emission lines (NIST or Z300). Using a specific internal calibration curve (done with well-known standards), it is possible to obtain quantitative content using internal software and standards previously analysed.

2.2.4. Standards

A self-calibration of the spectrometer for wavelength accuracy is automatically done by firing on the alloy part close the window. This calibration is essential to obtain a good identification of the emission lines, which are sharp in LIBS compared to most analytical techniques. That is critical for element identification. No standards are provided for the quantification. Calibration curves should be designed by the user and should match the sample nature and the range of the expected concentrations.

2.2.5. Applicability and limitations

i) Low Z elements. HH LIBS is the only technique available for direct measurement of light elements directly on the field. The higher or lower ability to detect them depends on the spectral range effectively detected. As such, HH LIBS analyses elements that X-ray cannot, including lithium (Li), beryllium (Be), boron (B), carbon (C), fluorine (F) and sodium (Na).

ii) Detection limits. Detection limits are difficult to provide without sample knowledge. They depend on the matrix composition and the presence and abundance of elements emitting a large number of intense emission lines such as iron or calcium. The detection limits are not linked to the atomic weight as for XRF. That makes the two tools highly complementary.

iii) Sample preparation. For quantification, the form of the sample: powders or solids is of importance as it will have an influence on the laser efficiency. Hence, standards should be in the same form of the samples unless it has been proven that has no impact on quantification.

iv) Rare Earth. Rare Earth Elements are theoretically detectable by LIBS but suffer from poor detection, which prevents their detection in most common rocks.

2.3. MIR technique

Infrared spectroscopy uses molecular absorptions of specific frequencies occurring principally based on a transition between energy levels of molecular vibration. Thus, these absorptions are the frequency of the absorbed radiation matches the frequency of the bond or group that vibrates. The frequency of the vibrations can be associated with a particular bond type. In order to be "infrared active", the dipole moment of the molecule changes during the vibration (Harris and Bertolucci, 1989). A molecule can vibrate in many ways, and each way is called a vibrational mode. Linear molecules have 3N - 5 normal modes of vibration whereas nonlinear molecules have 3N - 6 normal modes of vibration (also called vibrational degrees of freedom) where N is the number of atoms of the molecule.

The most common sample interface for portable FTIR spectrometers is a diamond ATR (Attenuated Total Reflection) for both liquids and solids, and in principle, specular reflectance (SR) would be the straightforward technique concerning a handheld mid-IR instrument (Crocombe, 2018). However, MIR absorption bands are strong and are associated with a large change in refractive index as a function of wavelength. Therefore, SR spectra in MIR can appear distorted by strongly absorbing solids due to anomalous dispersion as compared to transmission spectra (Crocombe, 2018). A portable device, Alpha Bruker used in this thesis, provides three types of modules to measure the interaction of infrared radiation with a sample by reflection: ATR, DRIFT (Diffuse Reflectance Infrared Fourier Transform) and SR (**Fig. 12**).

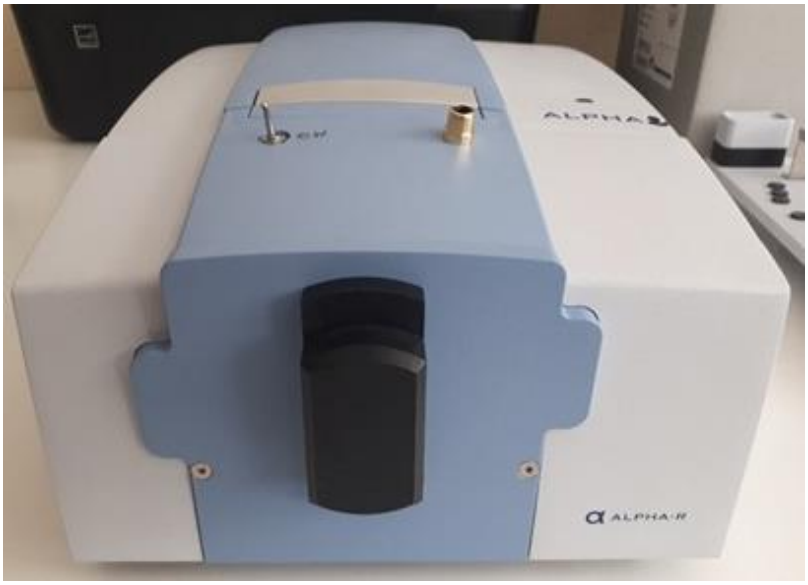

Fig. 12. Bruker Alpha FTIR spectrometer equipped with SR module.

2.3.1. Samples and sample preparation

For infrared analysis, samples can be powders, massive solids, gases or liquids. The sample preparation is depending on the type of module used with the spectrometer. DRIFT module is used for powders. ATR module allows to use different sample types such as powders, small-sized solids and liquids whereas SR module only allows the analysis of solid samples. Two important samples criteria should be taking into account before measurements: surface condition and moisture effect. For surface condition, especially on solid samples used with the SR module, the reflectance used for sample study is sensitive to light variations, thus, the use of flat surface samples is advised to avoid noisy spectrum. About moisture effect, fundamental bonds of liquid water could be seen on the spectrum centred at around 3300 and 1600 cm^{-1}. This phenomenon is important to consider for spectral interpretation.

2.3.2. Analytical conditions

To obtain an infrared spectrum, a background spectrum has to be done before starting the sample measurement. Depending on the reflection technique used, the background is done so as to obtain the maximum reflection with a reference cap, mirror or crystal. The measurements consist of the accumulation of several scans each giving an interferogram. The infrared spectrum is obtained by the Fourier transform of the mean of the interferograms. Theoretically a single scan is sufficient but increasing the number of scans improves the signal to noise ratio. Acquisition time or number of scans are defined before the measurement start.

2.3.3. Data processing

The device allows spectrum observation directly on a computer linked to the device. Each mineral has a specific IR spectrum with characteristic bands of different intensities. All devices are delivered with a software solution for interpreting the spectrum as minerals present in the sample by identifying band position, shape and intensity. Depending on the technique used, transformations can be applied such as the Kramers-Kronig transformation (KKT) for spectra obtained in specular reflection (**Fig. 13**). In practice, the transformed spectra can provide confusing results because most samples will return a mixture of specular and diffuse reflection

radiation (Griffiths and De Haseth, 2007).

Regarding band assignment, the software allows the comparison with a spectral database to help mineral interpretation. This can also be done manually by checking infrared spectra of minerals in the literature. Best matching solutions are also implemented in some software but usually not implemented directly on the portable device.

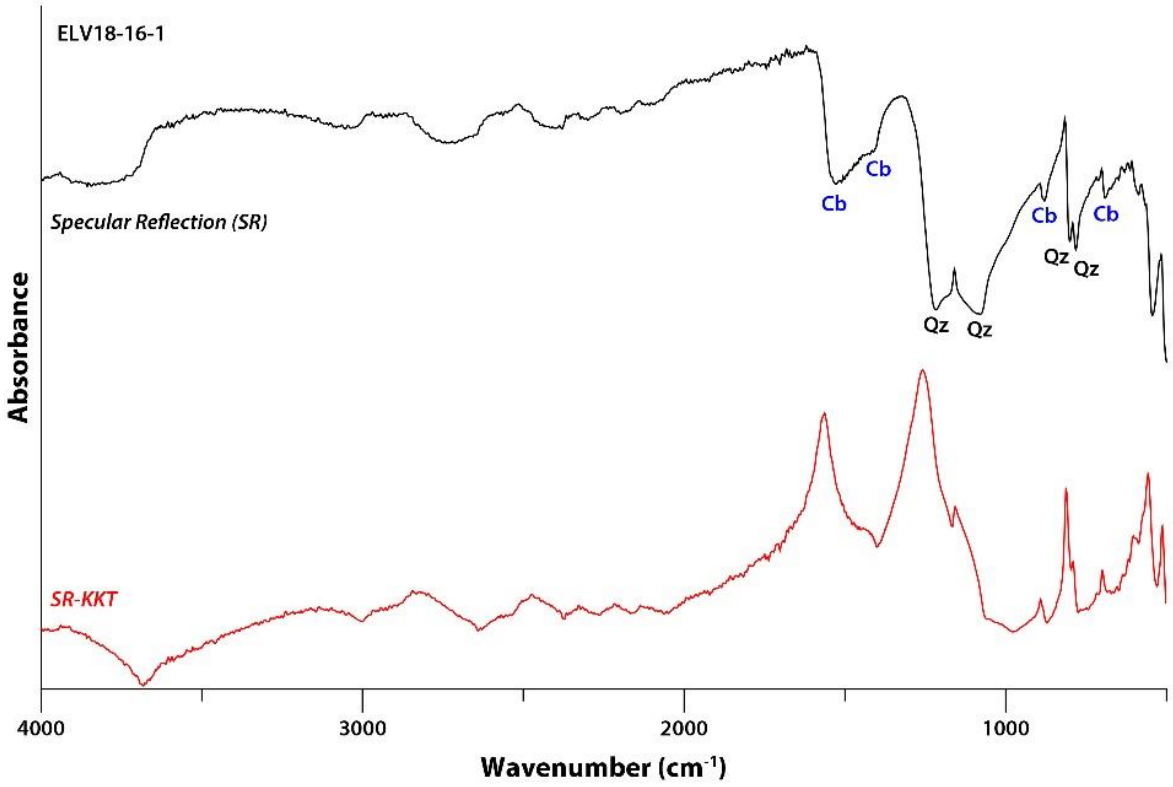

Fig. 13. IR spectrum of the Elvira sample in specular reflexion mode (up) and Kramers-Kroning transformation mode (down). Abbreviations: Cb = carbonate; Qz = quartz.

2.3.4. Standards

No standard is required to perform measurements. However, as for any analytical technique, the regular use of specific samples will help monitoring short- and long-term stability of the device.

2.3.5. Applicability and limitations

Portable infrared spectroscopy is theoretically applicable to any minerals. However, the bands corresponding to the molecular groups present in the samples do not give the same intensities at equal concentration (different molar absorption coefficients). Infrared spectroscopy can provide relative concentrations of minerals. It is commonly feasible with the ATR and DRIFT techniques but more difficult with the SR technique. Limitations of this techniques are mainly due to spot size, sample and mineral types.

i) Spot size. The infrared beam is focused on a spot of a few millimetres diameter and IR is not visible. Devices without a camera to locate it makes things complicated to properly position the sample at a precise given point. This diameter also provides some difficulties while analysing tiny and crystallized samples in which resulting spectra could present mix of several minerals.

ii) Sample surface. Uneven sample surfaces may give rise to low or noisy signal due to light variations. Flat surfaces are to be preferred for better mineral identification.

iii) Mineral types. Infrared spectroscopy shows some signal limitations on specific mineral species. It is the case for graphite mineral or sulphide minerals which give a flat signal and then are poorly detected by this technique.

2.4. VNIR-SWIR technique

VNIR-SWIR spectroscopy is the study of the interaction between energy as EM radiation covering from 350 to 2500 nm, representing visible light (350 to 700 nm), near-infrared (NIR; 700 to 1300 nm) and short-wave infrared (SWIR; 1300 to 2500 nm) region (**Fig. 5**). Whereas the absorptions observed in the visible-NIR are associated with sub-atomic transitions, those observed in the SWIR region are associated with molecular bonds (Pontual, 2008). While absorption bands related to fundamental vibrations such as bending and stretching vibrations occur in the MIR region, SWIR absorptions are mainly related to harmonics of the fundamental vibrations, for example, overtones of stretching vibrations and combinations of stretching and bending vibrations (Laukamp, 2011).

The VNIR-SWIR technique was initially developed for remote sensing, but was able to apply a wider range of geological environments by the addition of internal light sources (Kerr et al., 2011). Since introduced portable infrared mineral analyser (PIMA) in the mid-1980s, portable VNIR-SWIR spectrometers have been improved, and SR-6500 portable spectroradiometer from Spectral Evolution in this thesis can be applied in the field for in situ mineral, vegetation, and soil identification (**Fig. 14**).

Fig. 14. Spectral Evolution SR-6500 VNIR-SWIR spectrometer.

2.4.1. Samples and sample preparation

Most devices designed to contact analysis use a self-illuminated 10 mm-diameter probe to acquire data on solid samples. Other measurement conditions are feasible with handheld devices: radiance from solar illumination and benchtop probe for powders and soils. Sample preparation is not required, but two criteria should be considered before measurement:

i) Surface condition. Since VNIR-SWIR spectroscopy uses an analytical method for measuring the amount of reflected electromagnetic waves on a sample, reflectance changes in wavelength can be expected by the scattering phenomenon depending on the surface condition of the mineral. Kim et al. (2017) demonstrated that the natural and cutting surface have almost similar reflectance, and powder samples have the highest reflectance among them. In the powder condition, the reflectance was increased with decreasing grain sizes from 500 to 45 μm reviewed by Zaini et al. (2012).

ii) Moisture effect. The bonds giving rise to absorption features in the SWIR include those in hydroxyl, water, carbonate and ammonia and between Al-OH, Mg-OH and Fe-OH (Pontual, 2008). The moisture contained in a sample, such as free water and structure water, has a significant effect on the SWIR spectrum. Moisture-induced absorption peaks near 1400 nm and 1900 nm are broad and asymmetrical, resulting in offsetting the characteristic peaks of the target minerals. Therefore, spectroscopic measurement should be conducted on dry samples.

2.4.2. Analytical conditions

i) White calibration. Before the first measurement or at regular intervals, VNIR-SWIR spectrum is provided by normalizing against a reference. That is done by using a specialized ceramic disk, which uniformly reflects the light across the spectral range (350-2500 nm). The reflectance correction is commonly calibrated using a 99% whiteness reference panel, and various reflectance disks ranging from 2% to 99% whiteness are available.

ii) Averaging measurement. VNIR-SWIR instruments allow adjusting the signal-to-noise ratio (SNR) of a spectrum by manually modifying the number of measurements accumulated. The minimum scan speed in SR-6500 is 100 milliseconds. Dark samples require longer acquisitions to discriminate low reflectance from background noise (Kim et al., 2017).

2.4.3. Data processing

All devices come with software dedicated to the basic spectral evaluation and the data format is made compatible with more sophisticated software for detailed spectral investigation. The influence of out-of-range absorptions (i.e., ferrous iron absorptions around 1000 to 1200

nm and strong water and carbonate absorptions around 2700 nm) can affect the overall background shape (or continuum) of the spectrum. This background curvature of the reflectance spectrum is known as the "reflectance hull". Although the reflectance hull contains useful information, the curvature tends to distort the spectral absorption features. This can make the determination of the wavelength positions of the absorptions difficult, particularly those on the steepest parts of the reflectance spectrum, towards longer wavelengths.

Processing the spectra to remove the reflectance hull enhances the spectral absorption features. This enhancement is achieved by applying a baseline correction to the spectral data. The calculation commonly used to correct spectra is known as "hull quotient correction" (**Fig. 15**). The calculation of the hull quotient corrected spectrum involves dividing the reflectance value for each wavelength on the spectrum by the reflectance value for the same wavelength on the calculated hull line, which is calculated to touch the maximum number of points on the spectrum whilst remaining convex and not crossing the spectrum line.

The main advantage of using hull corrected data is that absorption features or minima rarely detectable in the reflectance spectrum become apparent in the hull corrected spectrum. The spectral signatures of specific minerals are also generally more easily identifiable in hull corrected data. This is especially the case for the SWIR spectra of many common minerals with diagnostic features between 2100 and 2400 nm. Furthermore, more accurate band centres can be assigned, allowing the resolution of additional bands near 2400-2500 nm. These bands can be due to OH stretching and bending combinations and also can be associated with tetrahedral substitution of Al or Fe for Si or with bonding between the octahedral cation and the tetrahedral cation (Bishop et al., 2002; Gates, 2005).

However, the main disadvantage is that the effect of ferrous (Fe^{2+}) on a SWIR spectrum is largely removed by a hull correction. For example, the intense charge transfer slope of Fe oxides will be removed by the hull quotient correction and this slope is important in estimating the Fe-oxide concentration in a sample. For this reason, it is essential that spectra are examined in reflectance if the presence of Fe^{2+} bearing minerals is to be recognized, especially when analysing VNIR absorption features. Hence, for practical spectroscopic analysis in the VNIR-SWIR region, both the raw reflectance and hull quotient corrected spectra are commonly used.

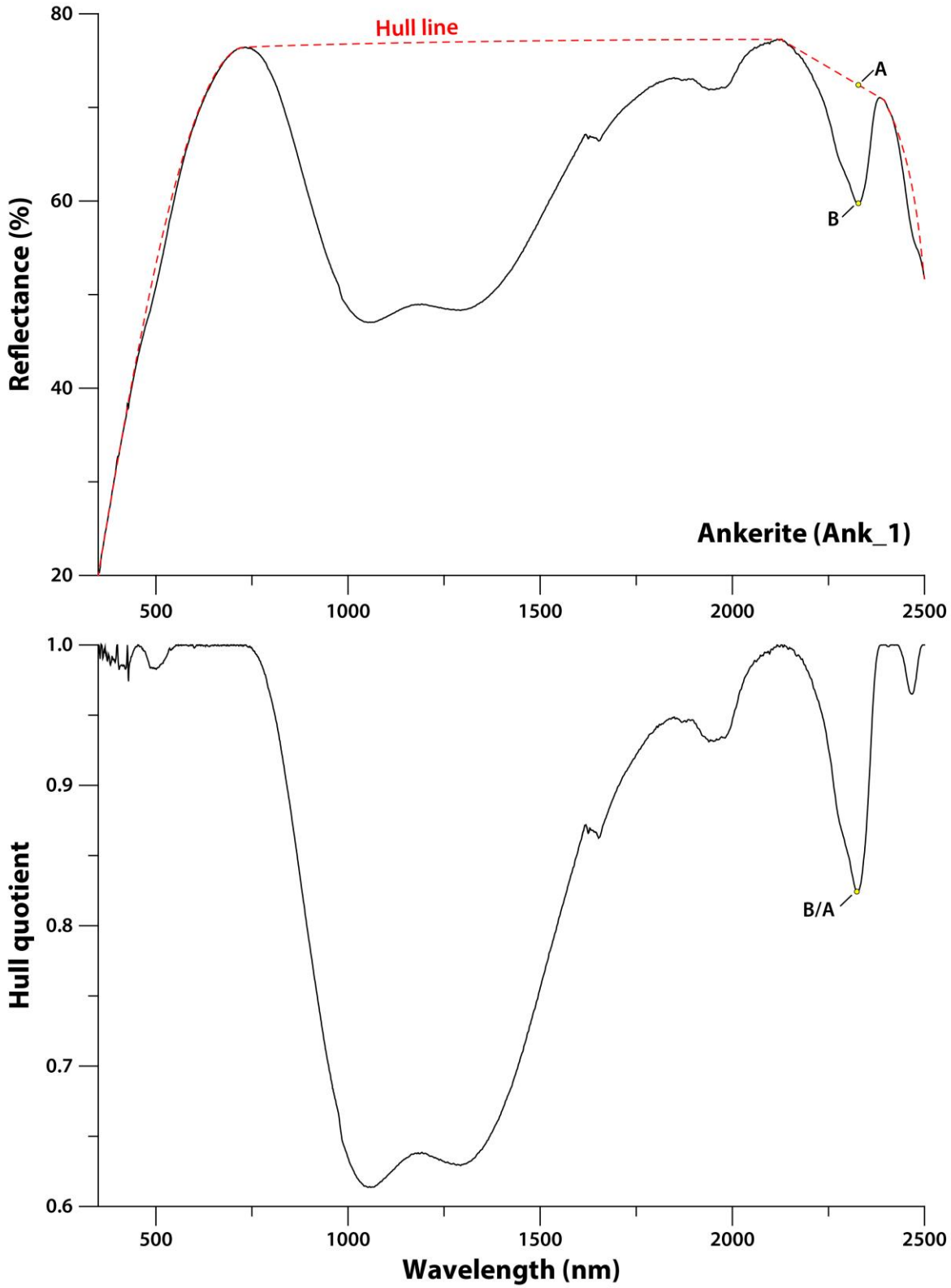

Fig. 15. Reflectance, Hull quotient spectrum and Hull line of ankerite.

2.4.4. Standards

Upon connection to the instrument, a reference scan should be collected first using a standard disk before acquiring the reflectance spectrum of the unknown sample. Various reflectance disks ranging from 2% to 99% are available. Normalization against these disks is compulsory to take into account the non-flat emission spectrum of the bulb included in the device. Reflectance correction should be done regularly during a series of measurements in order to correct for low noises near 1630 nm due to switching between detectors.

2.4.5. Applicability and limitations

The primary objective for portable VNIR-SWIR spectroscopy is the identification of the minerals. In addition, other significant information such as chemical substitution, crystallinity, effects of water, and temperature can be obtained from the spectral data (Hauff, 2008).

i) Mineral identification. Diverse alteration zones distributed extensively in various ore deposits are used as an important technique in resource exploration. Predicting the centre of the ore bodies is eased by recognizing with VNIR-SWIR the spatial distribution characteristics of the alteration zones. Thompson et al. (1996) summarizes the majority of the common infrared-active minerals that can be detected in the SWIR range (**Table 1**). Additionally, Rare Earth Elements (REE) have very distinctive signatures in the visible region.

ii) Chemistry. The ability to discern compositional differences in mineral groups that have solid solution substitution is very useful. Some examples are the carbonates, amphiboles, chlorites, dioctahedral micas, tourmalines, smectites, alunites, all of which exhibit wavelength shifts with cation substitution.

iii) Crystallinity variations associated with kaolinite and illite/sericite group of minerals is significant in term of spectral analysis for alteration and regolith mapping. For example, kaolinite crystallinity is determined near 2160 nm in the SWIR region, and it softens and broadens from a sharp, well-defined minimum to a shoulder as ordering decreases (**Fig. 16**).

Table 1. Summary of SWIR active minerals with absorption features modified from Hauff (2008).

Environment of formation	Standard terminology	SWIR active mineral assemblage (key minerals are in bold)
intrusion-related	Potassic (biotite-rich), K silicates, biotitic	**Biotite (phlogopite), actinolite, sericite, chlorite, epidote,** muscovite, anhydrite
	Sodic, sodic-calcic	**Actinolite,** clinopyroxene (diopside), chlorite, epidote, scapolite
	Phyllic, sericitic	**Sericite** (muscovite-illite), chlorite, anhydrite
	Intermediate argillic, sericite-chlorite-clay (SCC), argillic	**Sericite** (illite-smectite), **chlorite, kaolinite** (dickite), **montmorillonite, calcite,** epidote
	Advanced argillic	**Pyrophyllite, sericite, diaspore, alunite, topaz, tourmaline,** dumortierite, zunyite
	Greisen	**Topaz, muscovite,** tourmaline
	Skarn	**Clinopyroxene, wollastonite,** actinolite-tremolite, vesuvianite, epidote, serpentinite-talc, calcite, chlorite, illite-smectite, nontronite
	Propylitic	**Chlorite, epidote, calcite,** actinolite, sericite, clay
High-sulfidation epithermal	Advanced argillic - acid sulphate	**Kaolinite, dickite, alunite,** diaspore, pyrophyllite, zunyite
	Argillic, intermediate argillic	**Kaolinite, dickite, montmorillonite, illite-smectite**
	Propylitic	**Calcite, chlorite, epidote,** sericite, clay
Low-sulfidation epithermal	"Adularia" - sericite, sericitic, argillic	**Sericite, illite-smectite,** kaolinite, chalcedony, opal, montmorillonite, calcite, dolomite
	Advanced argillic - acid-sulphate (steam-heated)	**Kaolinite, alunite, cristobalite** (opal, chalcedony), jarosite
	Propylitic, zerolitic	**Calcite, epidote, wairakite,** chlorite, illite-smectite, montmorillonite
Mesothermal	Carbonate	**Calcite, ankerite,** dolomite, muscovite (Cr-Ni-rich), chlorite
	Chloritic	**Chlorite,** muscovite, actinolite
	Biotitic	**Biotite,** chlorite
Sediment-hosted gold	Argillic, intermediate argillic	Kaolinite, **dickite,** illite
Volcanogenic massive sulfide	Sericitic	**Sericite,** chlorite, chloritoid
	Chloritic	**Chlorite,** sericite, biotite
	Carbonate	**Dolomite, sericite,** ankerite, calcite, sericite, chlorite
Sediment-hosted massive sulfide	Tourmalinite	**Tourmaline,** muscovite
	Carbonate	**Ankerite, siderite, calcite,** muscovite
	Sericitic	**Sericite, chlorite**
	Albitic	**Chlorite, muscovite,** biotite

iv) Temperature of formation. SWIR spectrum indirectly provides information related to temperature of formation for some minerals. Broad and open absorption features coupled with large water features such as those found in smectites, zeolites, and opaline silica indicate ambient to low temperatures from low energy environments. As the profile sharpens and becomes well defined, such as in muscovite, pyrophyllite, epidote, and dickite, the temperature of formation increases, and the crystal lattice becomes ordered in a high-energy environment.

v) Water. The type of water present also can be tracked relative to profile and wavelength. Different types of water, i.e., channel, structural, interlayer, surface, silica, encapsulated, have different profiles which provide information about how the water was formed and where it resides.

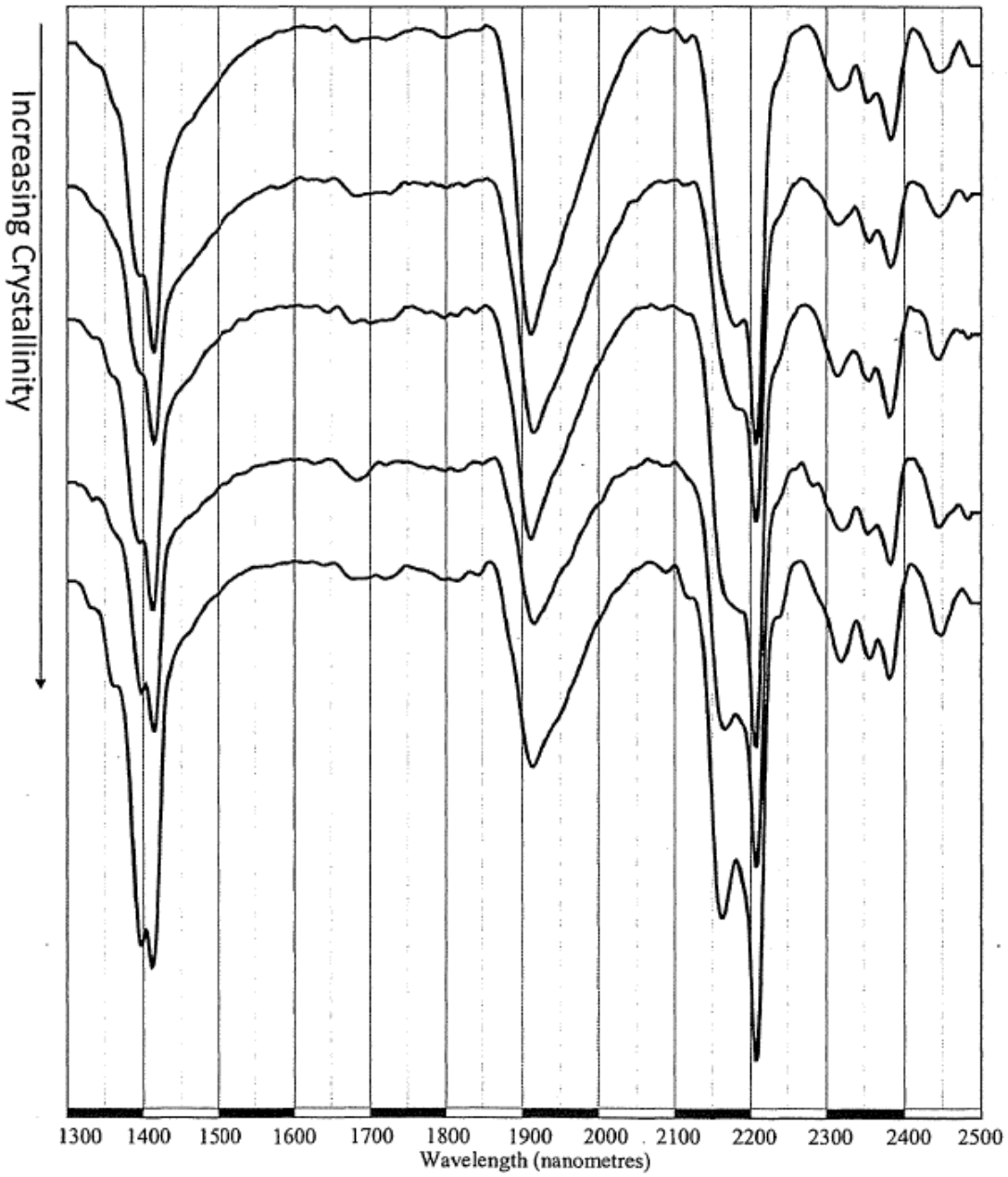

Fig. 16. Kaolinite crystallinity in the SWIR region (Pontual, 2008).

However, VNIR-SWIR spectroscopy has some limitations in qualitative and/or quantitative analysis.

i) Narrow wavelength range. Most minerals have major diagnostic absorption features between 2050-2450 nm. Due to the narrow wavelength range, the absorption features of multiple minerals can overlap each other.

ii) Mixture issues. Opaque minerals, such as magnetite and sulphides, have an adverse effect on the spectrum of a sample if: 1) finely disseminated in the sample; 2) present in proportions > 5-10%. This effect significantly lowers the reflectance or weakens the spectral absorption features of other minerals in the sample. Carbonaceous material in rocks such as black shales will have a similar effect on their spectral responses as that caused by finely disseminated opaque minerals. As a general feature, if a single spectrum can be interpreted by a user as a mineral mixture, unmixing and best matches for mixtures are not yet fully implemented as automatic data interpretation on handheld devices.

iii) Unsuitable mineral groups. Minerals that do not have structural OH, water and CO_3 such as silica/quartz or feldspar do not display any diagnostic absorption features in this wavelength region. The spectra of samples dominated by these other minerals can, however, display absorptions associated with non-diagnostic secondary components. For example, broad water bands associated with fluid inclusions in silica and clay absorptions due to weathering/alteration of felspathic components.

2.5. Raman technique

Raman spectroscopy, as molecular optical spectroscopy, has the ability to rapidly provide unique fingerprints used for the identification of the chemical structure in solids, liquids, and gaseous materials (Dubessy et al., 2012). The incident radiation excites the atoms or molecules in the sample to a virtual state that takes part of the energy of the incoming light (ν_0), and intensity relaxes from this virtual excited state to a second state, higher or lower in energy than the initial state (Rull et al., 2012). The inelastic scattering can be of the Stokes ($\nu_0 - \nu_R$) or anti-Stokes ($\nu_0 + \nu_R$) scattering, where ν_R is the frequency of the molecular or lattice vibration (**Fig. 7**). The frequency change of the incident photon is called the Raman shift. It is noted that while in infrared spectroscopy the signal is due to the vibration of the dipole moment, in Raman spectroscopy it is due to the variation of the polarizability (Lewis and Edwards, 2001; Weber and Merlin, 2013). Raman spectroscopy provides both i) qualitative and ii) quantitative information: i) The Raman shift wavenumbers produce qualitative information on chemical bonds (nature and geometry). ii) Quantitative information can be estimated using the Raman line intensities, or at least their ratio.

Since possibly the first study of mineralogical application was published by Jehlička et al. (2009) in field geology, the technical progress in the field resulted in a much broader selection of portable Raman spectrometers in 2021 (Edwards et al., 2021). In this thesis, two miniaturized Raman spectrometers were performed: one with a 532 nm excitation laser (RaPort from EnSpectr) and the second with a dual excitation option at expected 785 nm and 1064 nm lasers (Bravo from Bruker), respectively (**Fig. 17**).

Fig. 17. EnSPectr RaPort Raman spectrometer (left) and Bruker Bravo Raman spectrometer (right).

2.5.1. Samples and sample preparation

Samples can be powders, massive solid, gases or liquids. No preparation is required. Thin sections cannot be analysed because the thickness is not big enough. The analysis can be done through a container (glass flask, plastic bag, and so forth.) if transparent and not too thick (max. ~1 mm). For liquid and gas samples, the concentration (or pressure) of the investigated species must be large enough because the sensitivity of the techniques is low.

There are several sample holders, one for each kind of sample: for small flasks (1 cm diameter), for direct contact or for measurement through a container. The use of the proper holder ensures that laser is focused on the sample and not on the container.

2.5.2. Analytical conditions

i) Spectrum accumulation. The resulting spectra are always the mean (or the sum) of several spectra (accumulations) of the same duration (acquisition time). Laser power, acquisition time and number of accumulations are usually automatically defined. Some spectrometers allow to manually define these parameters.

ii) Laser power. The highest the laser power is the highest the signal intensity is. However, laser power can be reduced to avoid thermal damage or to limit background fluorescence.

iii) Acquisition time. Signal intensity is proportional to acquisition time and number of accumulations. These parameters are limited by detector saturation, and reasonable total acquisition time (if manually defined).

2.5.3. Data processing

Each mineral has a specific spectrum with usually several peaks of different intensities. The relative intensities of the peaks are always the same for a powder of a given mineral but depend on crystal orientation for single crystal. Data processing aims to identify (and quantify) minerals in the sample by identifying peak position and intensity. It consists in baseline subtraction, recognition of peak position and intensity, and peak assignment.

i) Baseline. Usually, a baseline is automatically subtracted. Another baseline (linear or polynomial) can be manually subtracted if necessary.

ii) Peak position and intensity. the positions and intensity of the peaks can be determined by searching for local maxima. If several peaks are suspected to be superimposed, or to get quantitative information, the bands can be decomposed by fitting using pseudo-Voigt functions (Gaussian-Lorentzian).

iii) Peak assignment. the peak positions (and intensities) are compared to a database to identify the minerals. It can be done manually or automatically. The RRUFF database (ruff.info) is a free database of Raman spectra of several thousands of well-characterized minerals (chemical composition and XRD data provided) and that provides a tool for automatic recognition.

2.5.4. Standards

Raman spectroscopy does not require standardization. Typically, for dispersive instruments, the SNR is estimated by measuring the throughput (i.e., the quantity of the signal read by the CCD) using a suitable standard sample. The throughput is a measure of the absolute Raman signal; thus, it is proportional to the CCD counts. In the presence of a reference sample, it is reasonable to consider a signal (i.e., the intensity or area of a specified band), to measure the noise in a certain spectral range and finally to calculate their ratio. By applying this procedure to the spectra acquired with each technique, it is possible to obtain a sensible value functional to their comparison.

2.5.5. Applicability and limitations

Portable Raman spectroscopy applies to any minerals. **Table 2** shows that the characteristic wavenumber regions of the various characteristic groups. Theo Kloprogge (2017) presents those eight classes can be identified: (1) elements, (2) sulphides and related compounds, (3) halides, (4) oxides and hydroxides, (5) carbonates, nitrates, borates, (6) sulphates, tungstates, chromates, and molybdates, (7) phosphates, arsenates, and vanadates, and (8) silicates. Each of these groups is reflected as specific bands in either or both the IR and Raman spectra and function as fingerprints for specific minerals.

Table 2. Wavenumber regions for various anionic groups modified from Theo Kloprogge (2017).

Anionic group	4000-3000 cm^{-1}	1600-1200 cm^{-1}	1200-800 cm^{-1}	800-600 cm^{-1}	600-400 cm^{-1}	< 400 cm^{-1}
Sulfides					< 500	
Hydroxides	4000-3000		1200-600			
Oxides			< 1200			
Carbonates		1550-1300	890-800	700-670		
Nitrates			1050, 850-800	770-715		
Borates		1350-1250	900-600			
Sulfates			1250-900	680-570		
Tungstates			950-750		450-250	
Chromates			950-800		500-350	
Molybdates			950-750		450-250	
Phosphates			1150-900		600-400	
Arsenates			900-770			400-350
Vanadates			900-700			400-300
Silicates			1200-800			

The green laser (532 nm) can be suitable for inorganic materials due to stronger Raman scattering and better signal-to-noise ratio (SNR), but there is a major challenge to be overcome with the fluorescence emission. A red to near-infrared laser (700–1100 nm) is used for fluorescence suppression but decreased sensitivity can result from near-infrared excitation compared to a green laser.

i) Fluorescence. It is a competing luminescent process. It can be excited if the laser energy of radiation (wavelength) is large enough to induce electronic transition in the sample, in the mineral itself (due to traces of REE or transition metal elements) or external (organic) pollution. The quantum efficiency of fluorescence being generally much larger than the one of Raman scattering, the Raman signal can be hidden by this luminescent emission. This problem can be avoided by (1) cleaning the sample if fluorescence is due to external pollution, (2) by changing laser wavelength to avoid electronic transition (with a red or infrared laser) or to shift the Raman spectrum from fluorescence emission, or (3) by using a spectrometer equipped with Sequentially Shifted Excitation (SSETM) system.

ii) Crystallinity. Any solid can provide a Raman signal but peaks are more intense and thinner for solids of high crystallinity. They are therefore easily detected.

iii) Spot size. The laser beam is focused on a spot of about 15-30 µm diameter. It is difficult to manually position the spectrometer with an accuracy better than cm scale. Therefore, for finely dispersed minerals (< 30 µm), the spectrometer provides a spectrum that is the sum of the signals from several minerals. For grains between 30 µm and ~1 cm, it is also difficult to position the spectrometer exactly on the target position.

iv) Detection limit. Raman scattering is a light emission process of low probability (low quantum efficiency). It is usually difficult to detect phases at a proportion below 1%. However, this efficiency depends among others on the chemical nature of the molecular bond and crystal symmetry. Though all minerals have not the same detection limits. It can vary by several orders of magnitude for some specific cases. For example, carbonaceous matter yields resonance Raman signal, increasing signal intensity by 100 or 1000. On the contrary, clay minerals are generally poorly detected.

2.6. XRD technique

X-ray diffraction (XRD) by matter, one of the conventional and rapid techniques for mineralogical research, arises from the combination of two different phenomena: scattering by each individual atom of a crystal by virtue of its uniform spacing, and interference between the X-ray waves scattered by these atoms (Guinier, 1994). Diffraction methods, thus, are based on the wave behaviour of radiation or on the wavelike properties of particles. Crystal atoms scatter the incident X-rays, primarily through interaction with the atoms' electrons. The atomic planes of the crystal act on the X-rays in the same manners as does a uniformly ruled grating on a beam of light determined by Bragg's Law. X-rays and electron or neutrons are especially suitable for the study of molecular structure since their wavelengths roughly match the spacing between atoms in condensed phases, resulting in diffraction patterns that can be used to build a model of the electronic density of the studied material (Cullity, 1956; De Graef and McHenry, 2012; Hammond and Hammond, 2001; Warren, 1990). The portable XRD (pXRD) was developed for Mars research funded by NASA (Blake et al., 2012; Sarrazin et al., 2005). The main difference between the pXRD (Terra by Olympus) instrument used in this thesis and the one used in laboratory is that the sample is moving as suspension, not the parts of the instrument (Sarala and Koskinen, 2018, **Fig. 18**).

Fig. 18. Olympus TERRA portable XRD instrument.

2.6.1. Samples and sample preparation

Crystallized samples only can be measured. For the rock samples, the fraction should be powdered before analysis. For soil samples only drying is needed. The sample material should be sieved to extract its < 150 µm size fraction before placing in the sample holder. The grains oversize should be crushed, otherwise they cause a bad diffraction pattern. The minimum sample mass is in the order of a few tens of milligrams (mg).

2.6.2. Analytical conditions

Depending on the system, the measurement is made possible either by the sample motion as suspension, not the parts of the instrument or by the motion of the detector. The first case is that of the Olympus' Terra™ pXRD used in the NEXT project. The sample or detector motion choice from the manufacturer leads to contrasted analytical conditions, hence reporting needs.

i) Anode. As for any XRD system, the X-Ray tube anode may be chosen among several possibilities. That should be chosen at purchase as it cannot be changed afterwards. The most common anode is Cu even if Co ones are available for portable tools.

ii) Data collection range. The range of accessible and actually measured 2θ and the increment from one angle to the next are critical parameters for the diffractogram quality. That of the Olympus' Terra is 5 to 55˚ 2θ (10.26 to 1.94 Å), with increment of 0.25˚.

iii) Data collection time. The longer the time, the more reflections will be produced and the better signal-noise ratio. However, in the field circumstances an aim is to define a data collection time producing a pattern accurate enough. Burkett et al. (2015) has tested pXRD with data collection times of 5, 10, 20 and 40 minutes. The results indicated that even 5 minutes was enough for a qualitative analysis of all phases whereas the accuracy of the quantitative analyses concerning the minor mineral phases got significantly better the longer the data collection time was. The analysing time varies from 10 to 20 minutes in this thesis.

iv) Sample vibration chamber. The Olympus' Terra™ pXRD is equipped with a vibration chamber. It creates a convection process of the sample in front of the instrument optics leading to with multifarious orientations of the crystalline structure. This results in a superb X-ray

diffraction pattern, virtually free of the problematic preferred-orientation effects encountered when using classic preparation methods. Due to its unique powder-handling system, non-mechanical goniometers, and lack of complicated moving parts, Terra™ is extremely well suited for those applications where field portability and/or ease of use is at issue. This patented chamber decreased the sample mass to a mere 15 mg.

v) Combined XRF/XRD. Among available devices, the Olympus' Terra™ pXRD harnesses advanced dual XRD/XRF technology and renders it for earthbound applications. It combines both X-ray diffraction and X-ray fluorescence measurements. Using a specifically developed direct excitation charge coupled device (CCD) "camera", Terra is able to collect X-ray photon data for both X-ray diffraction and X-ray fluorescence simultaneously. This is the result of the integrated camera's ability to detect both photon position and photon energy at the same time. With energy resolution of ~200 eV (5.9 keV), Terra makes XRF analysis as simple as viewing the software spectrum display.

2.6.3. Data processing

Portable devices are delivered with a software for diffractogram export. Export is compatible with other software dedicated to diffractogram interpretation. With the Olympus Terra pXRD, it can be done with the XPowder software based on Reference Intensity Ratio (RIR) method and using AMCSD mineral database (American Mineralogist Crystal Structure Database). If the user wish, XPowder provides the ability to use the ICDD Powder Diffraction Files (PDF). For quantitative analysis, XPowder comes complete with reference intensity ratio (RIR) quantitative analysis methods as well as full-pattern analysis tools. Furthermore, Terra provides XRD pattern data in a variety of file formats, making XRD pattern interpretation in third-party programs easily accessible.

Terra™ operates off software embedded in the unit itself. The user accesses the operating system through a wireless connection (802.11 b/g). This remote operation method allows for a wide degree of flexibility in controlling the instrument and subsequent data handling.

2.6.4. Standards

Known mineral materials or commercial reference materials can be used as a reference to compare mineral composition. The AMCSD mineral database or equal can be used in interpretation phase of the results.

2.6.5. Applicability and limitations

XRD is most widely used for the identification of unknown crystalline materials (e.g., minerals, inorganic compounds). Determination of unknown solids is critical to studies in geology, environmental science, material science, engineering, and biology. This wide use directly arises from its extraordinary capabilities such as: low requirements in sample mass, identification of fine-grained minerals such as clays and mixed layer clays that are difficult to determine optically, measurement of sample purity. Even in its portable form, compared to handheld mineralogical techniques previously detailed, it still brings advantages:

i) Automatic identification. XRD benefits from sharp features. It also builds up on a very long history in analytical sciences. Both ease automatic identification of the sample.

ii) Quantitative analysis. Semi-quantification is easy to obtain, and full quantification can be attained. It is quite rare among techniques providing information on minerals. Some limitations are common to most mineralogical techniques and directly linked to the large number of existing minerals on Earth: homogeneous and single-phase material is best for identification of an unknown, a access to a standard reference file of inorganic compounds is compulsory and rare minerals and the ones with very small proportion of the sample do not come out clearly. Compared to the other techniques, some weaknesses are specific to XRD:

i) Non-crystalline materials. XRD is limited to crystallized solids. Very low crystallinity will provide no interpretable results, which is less critical in vibrational spectroscopies. That may render part of the sample invisible, especially for low-temperature geological contexts.

ii) Sample preparation. Sample preparation is compulsory even for qualitative studies. Samples have to be prepared as <150 μm size fractions to be introduced into the device. That is not the case with the above-mentioned techniques.

3. Summary

The rapid development of portable spectrometers has been enabled various applications in field geology. In this thesis, six spectroscopic techniques with seven commercial portable devices are employed for elemental and mineralogical analyses spanning from X-ray, UV-Vis, NIR-SWIR, mid-IR, Raman, and LIBS (**Table 3**). All the devices can be measured with solids and powders except for XRD, MIR-DRIFT and ATR modules. The grain size for XRD, especially, should be less than 150 μm. Bulk or spot analysis is available depending on the spot size of each device (**Table 3**). For example, XRF, VNIR-SWIR, and MIR-SR module have a spot size in mm, while LIBS and Raman devices have much smaller spot sizes in micron. In particular, the LIBS analyser used in this study contains the 2D raster function, thus both bulk and spot analysis can be carried out. In the case of acquisition time for obtaining one spectrum, XRF takes 2 minutes, and the other tools excluding the Raman device using red to near-infrared laser take up in seconds. The Raman device using a red to near-infrared laser automatically determines the acquisition time by the software itself. It is noted that the optimized number of accumulations should be different since the SNR of a spectrum from each device is diverse. For instance, reliable XRF data can be provided with only a single measurement that requires 2 minutes, whereas XRD for qualitative analysis demands at least 5 minutes of acquisition time (Burkett et al. 2015). Therefore, in the next chapter, a spectral database is established in consideration of these optimized analytical conditions.

Table 3. A summary of portable spectroscopic instruments used in this thesis.

Technique	Analysis	Sample condition*	Spot size	Acquisition time	Spectral range
XRF	Element	S, P	8 or 3 mm	2 min	0-60 keV
LIBS	Element	S, P	50 μm	0.1 sec	180-960 nm
VNIR-SWIR	Mineralogy	S, P	10 or 3 mm	0.1 sec	350-2500 nm
mid-IR	Mineralogy	S, P**	5 mm (SR)	30 sec	4000-400 cm^{-1}
Raman (green)	Mineralogy	S, P	~15 μm	< 3 sec	130-4000 cm^{-1}
Raman (R-NIR)	Mineralogy	S, P	~15 μm	sec-min	300-3200 cm^{-1}
XRD	Mineralogy	P	-	15 sec	5-55°

*S: solid; P: powder. **Powder only in DRIFT and ATR module

Chapter II. Spectral database creation

1. Spectral library

1.1 Summary

The spectral library in this thesis is a collection of monomineralic spectral data obtained by using the six portable instruments (i.e., elemental analyses for XRF and LIBS, and mineralogical analyses for MIR, VNIR-SWIR, Raman, and XRD). This spectral database helps rapid mineral recognition with respect to unknown materials and supports the spectral reconciliation for diverse types of spectral data. Thus, the spectral library is the beginning and the fundamental source of this dissertation. A decision tree for mineral discrimination is then built by combining the well-characterized spectral properties extracted from the library. Finally, the compositional changes in the same mineral groups such as carbonates and phyllosilicates are specifically observed by spectral comparisons from the decision tree.

This spectral library is composed of reference spectra of different mineral groups, which can be present in Volcanogenic Massive Sulphide (VMS) deposits. The spectral database has been steadily updated during the thesis. Therefore, the final number of mineral phases is 27 consisting of 52 samples in the library. The dataset provided in the spectral library contains a limited number of mineral species compared to the existing libraries, yet these mineral candidates cover almost all target minerals in the Elvira VMS deposit for the NEXT applications. It is expected that all the spectral information of a single mineral obtained from the various portable devices will be practical for understanding the comprehensive spectral characteristics of minerals by comparing data from one technique to the next one.

1.2. Sample preparation

The samples were found in public/private collections and bought from several sources. The mineral list and data acquired on it are reported in **Table 4**. Several minerals have more than one single sample. Most samples were hand specimens, a limited number consisted of powders. Three sample types (i.e., solid, powder, and pellet) are prepared based on the measurement methods of the different spectroscopic techniques. The hand specimens were cut in two halves and one half was powdered from which a subsample pressed into a 13 mm diameter pellet using a 10 tons hydraulic press.

Table 4. Sample list and details.

Group	Mineral	Name	Handheld equipment								
			MIR			RAMAN		XRF	LIBS	VNIR-SWIR	XRD (GTK)
			DRIFT	ATR	SR	532 nm	1064 nm				
silicate	albite	Ab_1	POW	POW		PE	PE	PE	PE	PE	POW
		Ab_2	POW	POW	S	PE	PE	PE	PE	PE	POW
	anorthite	An_1	POW	POW	S	PE	PE	PE	PE	PE	POW
	orthoclase	Or_1	POW	POW	S	PE	PE	PE	PE	PE	POW
	quartz	Qz_1	POW	POW	S	S	S	PE	PE	S	POW
		Qz_2	POW	POW	S	S	S	PE	PE	S	POW
	apatite	Ap_1	POW	POW	S	PE	PE	PE	PE	PE	
	kaolinite	Kln_1	POW	POW		PE	PE	PE	PE	PE	
		Kln_2	POW	POW		PE	PE	PE	PE	PE	POW
	holloysite	Hal_1	POW	POW		PE	PE	PE	PE	PE	POW
	muscovite	Ms_1	POW	POW		PE	PE	PE	PE	PE	
		Ms_2				PE	PE	PE		PE	
	lepidolite	Lpd_1	POW	POW	S	PE	PE	PE	PE	PE	
	illite	Ilt_1	POW	POW		PE	PE	PE	PE	PE	POW
	chlorite	Chl_1	POW	POW	S	PE	PE	PE	PE	PE	POW
		Chl_2				PE	PE	PE		PE	
	montmorillonite	Mnt_1	POW	POW		PE	PE	PE	PE	PE	POW
		Mnt_2	POW	POW		PE	PE	PE	PE	PE	POW
	nontronite	Ntn_1	POW	POW		PE	PE	PE	PE	PE	
		Ntn_2	POW	POW	S	PE	PE	PE	PE	PE	POW
carbonate	calcite	Cal_1	POW	POW	S	PE	PE	PE	PE	PE	POW
		Cal_2	POW	POW		PE	PE	PE	PE	PE	POW
		Cal_3	POW	POW	S	PE	PE	PE	PE	PE	POW
		Cal_4	POW	POW	S	PE	PE	PE	PE	PE	POW
		Cal_5	POW	POW	S	PE	PE	PE	PE	PE	POW
	dolomite	Dol_1	POW	POW	S	PE	PE	PE	PE	PE	POW
		Cal_6	POW	POW	S	PE	PE	PE	PE	PE	POW
		Dol_2	POW	POW	S	PE	PE	PE	PE	PE	POW
	ankerite	Ank_1	POW	POW	S	PE	PE	PE	PE	PE	POW
	siderite	Sd_1	POW	POW		PE	PE	PE	PE	PE	POW
		Sd_2	POW	POW	S	PE	PE	PE	PE	PE	POW
		Sd_3	POW	POW	S	PE	PE	PE	PE	PE	POW
	magnesite	Mgs_1	POW	POW		PE	PE	PE	PE	PE	POW
	rhodochrosite	Rds_1	POW	POW		PE	PE	PE	PE	PE	POW
		Rds_2	POW	POW	S	PE	PE	PE	PE	PE	
sulfate	barite	Brt_1	POW	POW	S	PE	PE	PE	PE	PE	POW
		Brt_2	POW	POW	S	PE	PE	PE	PE	PE	POW
	gypsum	Gp_1				PE	PE			PE	
		Gp_2				PE	PE			PE	
graphite		Gr_1				S	S			S	
sulfide	chalcopyrite	Ccp_1	POW	POW	S	PE	PE	PE	PE	PE	POW
		Ccp_2	POW	POW	S	S	S	S	S	S	
		Ccp_3	POW	POW	S	PE	PE	PE	PE	PE	
	galena	Gn_1	POW	POW	S	PE	PE	PE	PE	PE	POW
		Gn_2	POW	POW	S	PE	PE	PE	PE	PE	
	pyrite	Py_1	POW	POW	S	PE	PE	PE	PE	PE	POW
	pyrrhotite	Po_1	POW	POW	S	PE	PE	PE	PE	PE	POW
	sphalerite	Sp_1	POW	POW	S	PE	PE	PE	PE	PE	POW
		Sp_2	POW	POW		PE	PE	PE	PE	PE	POW
		Sp_3	POW	POW	S	PE	PE	PE	PE	PE	
		Sp_4	POW	POW	S	PE	PE	PE	PE	PE	
		Sp_5	POW	POW	S	PE	PE	PE	PE	PE	

POW=Powder, PE=Pellet, S=Solid

XRF, LIBS, VNIR-SWIR, and Raman were measured with pellets except for quartz that cannot be pressed as a pellet without a gluing medium. Quartz was then measured as powder held in a cup with a polypropylene film for XRF and a hand specimen for LIBS, VNIR-SWIR, and Raman techniques. MIR-ATR and MIR-DRIFT were measured on powders. Since MIR-specular reflection (SR) has to be measured with hand specimens, the samples bought as powders could not be measured with this technique. The optimised number of measurements and accumulations are applied for each spectroscopic device based on the previous chapter (**Fig. 19**).

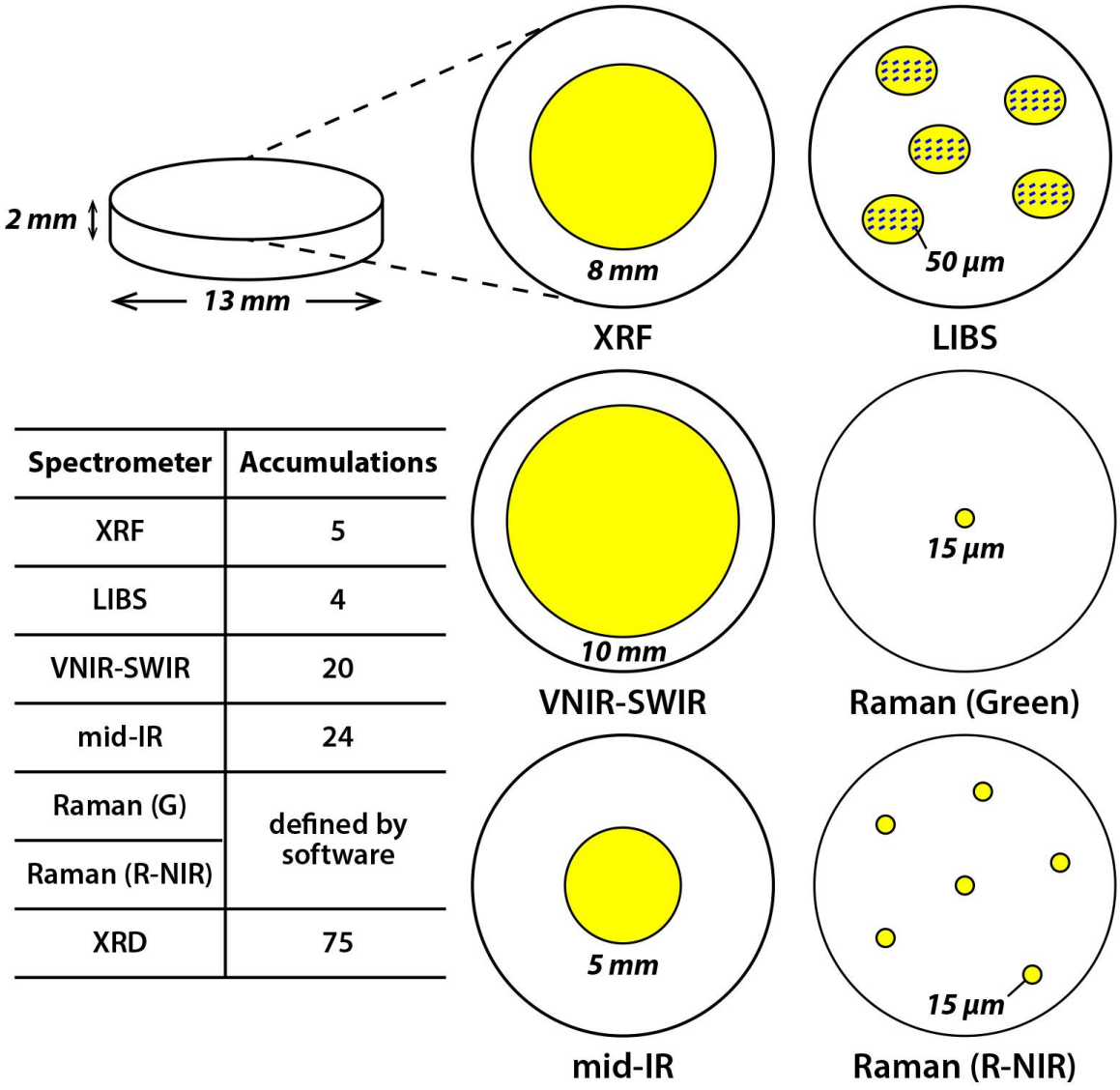

Spectrometer	Accumulations
XRF	5
LIBS	4
VNIR-SWIR	20
mid-IR	24
Raman (G)	defined by software
Raman (R-NIR)	
XRD	75

Fig. 19. Experimental protocol for spectral measurements with the portable devices used in this thesis.

Samples were named referring to Whitney and Evans (2010) and "_number" was added to the sample name to take into account that more than one mineral of the same nature can be present in the list. Some mineral species are not listed in this reference paper, they were given an abbreviation following the rules listed therein: halloysite and nontronite were abbreviated as Hal and Ntn, respectively.

1.3. Data acquisition

One XRF and one LIBS, one MIR technique with three different modules, one VNIR-SWIR, two Raman spectrometers, and one XRD were used; hence there are six techniques with nine datasets. All devices are commercial ones used without specific tuning of the experimental conditions so that any user owning the same device can benefit from the data gathered here.

1.3.1. XRF technique

XRF was measured with a Niton XL3t GOLDD+ handheld spectrometer from Thermo Fisher Scientific operating the Main, Low, High, and Light filters, each with a duration of 30 seconds in order to optimize the analysers' sensitivity for various elements (**Fig. 20**). Each filter corresponds to specific analytical conditions defined by a combination of the voltage in the X-ray tube and a thin film placed in between the X-ray tube and the sample. The film can be empty or covered by a material dedicated to producing intense specific X-rays or shield low-energy X-rays emitted by the X-ray tube. Each filter then preferentially stimulates the X-ray fluorescence of some elements and the combination of the 4 filters provides optimized detection limits from Mg to U. The "Main" filter provides optimum sensitivity for the elements manganese (Mn) through bismuth (Bi), and the "Low" filter is used for titanium (Ti) through chromium (Cr). It is noted that the main range filter can also analyse Ti, V, and Cr, but the sensitivity is not as good as when using the low filter. The "High" filter is used to optimize barium (Ba) through silver (Ag), and the "Light" filter is typically used in light element analysis with an atomic number ranging from 12 (Mg) to 17 (Cl). One spectrum is recorded for each filter, reported as raw a spectrum automatically corrected from escape peaks. The spectral data was automatically interpreted using the Mining Cu/Zn mode, which is a Fundamental Parameter method. Data are reported in ppm weight. Each sample has been measured five times on the same location (**Fig. 19**).

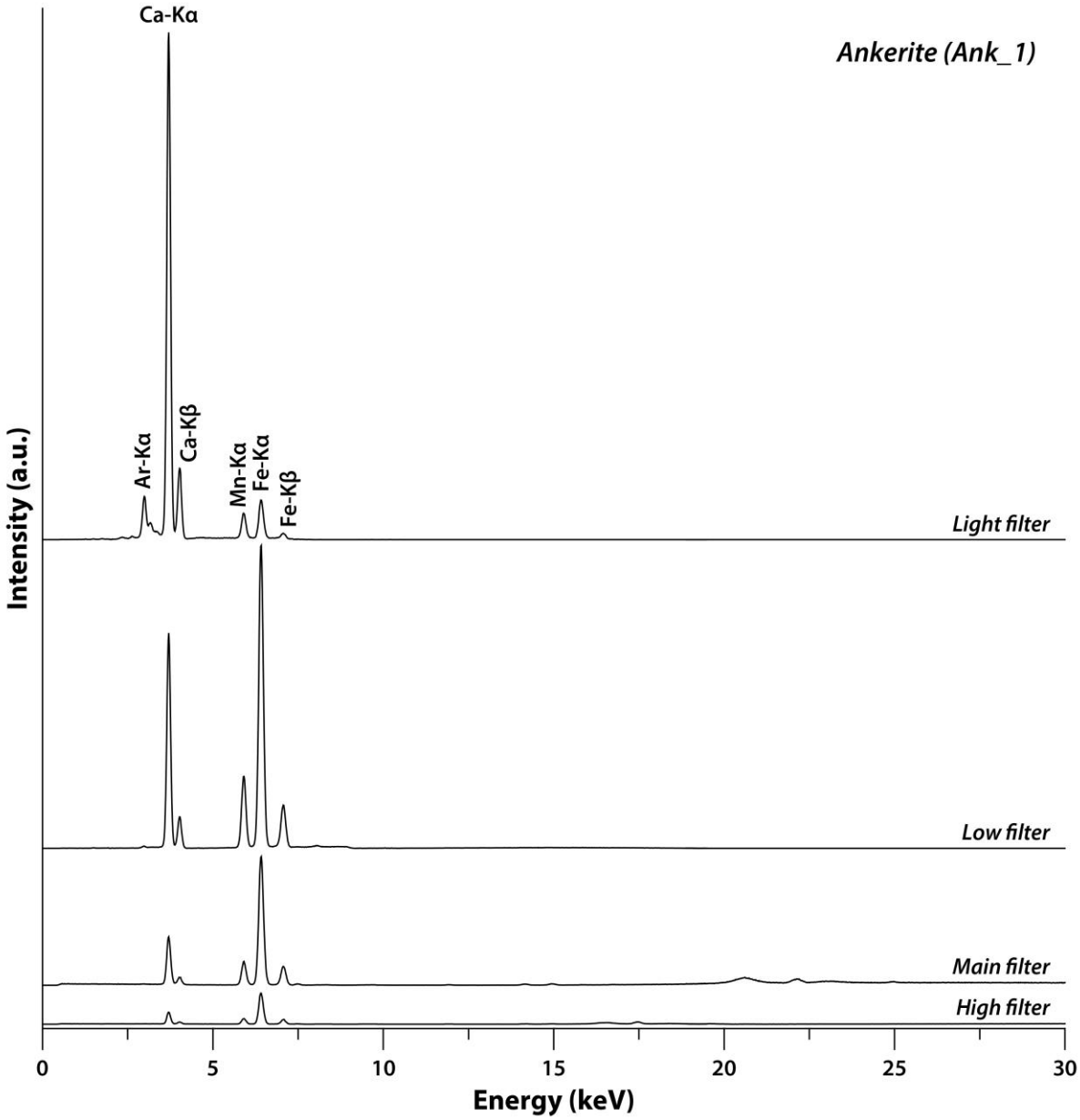

Fig. 20. XRF spectra of light, low, main, and high filter settings of the ankerite sample.

Data has to first be exported from the device to the user computer by opening the communication between the pXRF and the computer in NDT (Niton Data Transfer) software. The data appears as a table gathering device metadata, interpreted data and fields for user metadata that may have been filled by the user during analytical acquisition. Spectral data can be exported with Energy in the first column and spectra in the following columns. One to four spectra are recorded for each analysis, depending on the acquisition conditions chosen by the user.

1.3.2. LIBS technique

LIBS analysis was done using a handheld LIBS instrument, Z300 provided by SciAps ©. This device includes three diffraction gratings allowing the acquisition of the entire wavelength range, from 180 nm to 960 nm (**Fig. 21**). The portable instrument employs a 1064 nm Nd:YAG pulsed laser with a 50 µm focused beam size, operating 5-6 mJ per pulse to the sample and 10 Hz repetition rate. All the LIBS spectra were measured under a constant argon flow from an integrated and replaceable argon purge inside the instrument. The argon environment was shown to yield higher emission intensities (i.e. 10-fold increase) and minimize the effect of air on the LIBS signal (Iida, 1990). The pressure of argon gas in this study was controlled to maintain it at around 12 psi. The acquisition mode was used on 5 randomly chosen locations on each sample (**Fig. 19**). Each location was measured with a 15-points square grid on three lines. For each point of the grid, the first shot was a cleaning one and the analysis was not recorded, then 4 other laser shots provided 4 measurements. The 60 LIBS measurements done for each location were averaged in a mean LIBS spectrum used to simulate the 'bulk' composition of the sample. The elements found to be present from both geological knowledge and LIBS signal are reported with their spectral likelihood and spectral position. The Relative Standard Deviations reported in the calibration curves are those calculated on the LIBS analyses which were carried out for the 5 different locations.

The software, Profile Builder, is the interface of the SciAps HH LIBS tool to look at the spectra, to identify the element present on the plasma, to extract the data to the computer, and it can provide internal calibration as well. The software gives access to several programs for data acquisition and processing, the one used in this thesis is the GeoChem Mode. The available export options for spectra are: i) the raw LIBS spectra, is the sum of the spectra obtained in a single point of the grid pattern, ii) the calibrated spectra, is the sum of the spectra obtained in a single point of the grid pattern, calibrated in wavelength, and iii) average spectra, is the average of all the calibrated spectra obtained in one analysis.

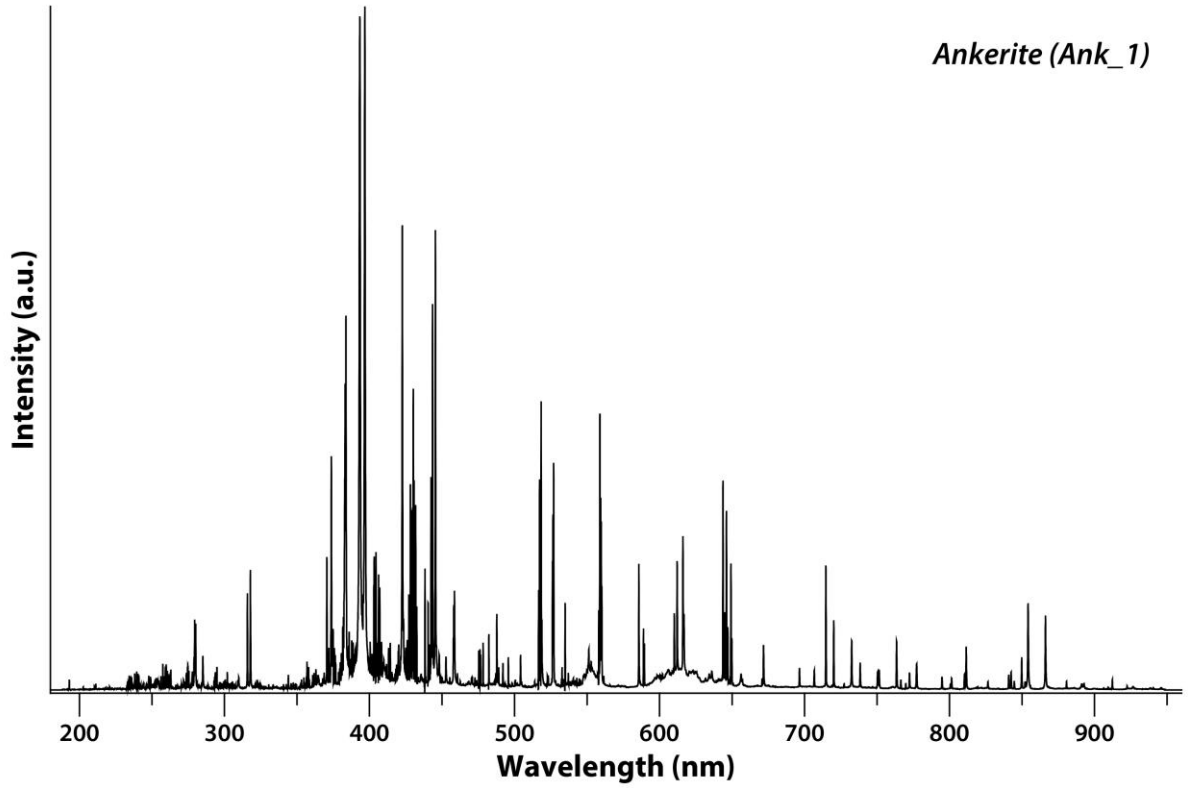

Fig. 21. Average LIBS spectrum of the ankerite sample from the spectral library.

1.3.3. MIR technique

The reflection IR spectroscopy was developed using a combination of IR spectroscopy with reflection theories, and reflectance techniques can be divided into two categories: internal reflection and external reflection (Khoshhesab, 2012, **Fig. 22**). External reflection covers two different types of reflection: specular (regular) reflection (SR) and diffuse reflection referred as diffuse reflection spectroscopy is referred as diffuse reflectance infrared Fourier transform (DRIFT) spectroscopy. Internal reflection spectroscopy is termed as attenuated total reflection (ATR) spectroscopy. In this thesis, MIR analyses using the reflectance IR spectroscopy were done using a portable infrared spectrometer ALPHA provided by Bruker. The instrument consists of two parts, first the basic module, which holds the spectrometer itself and second the sampling module, which consists in a specific "head" that allows changing the geometry of the detection. Three different sampling modules were used: DRIFT, ATR, and SR. For data transfer, data processing and file conversion, the spectrometer must be connected to a computer equipped with OPUS software (Bruker) with an Ethernet cable.

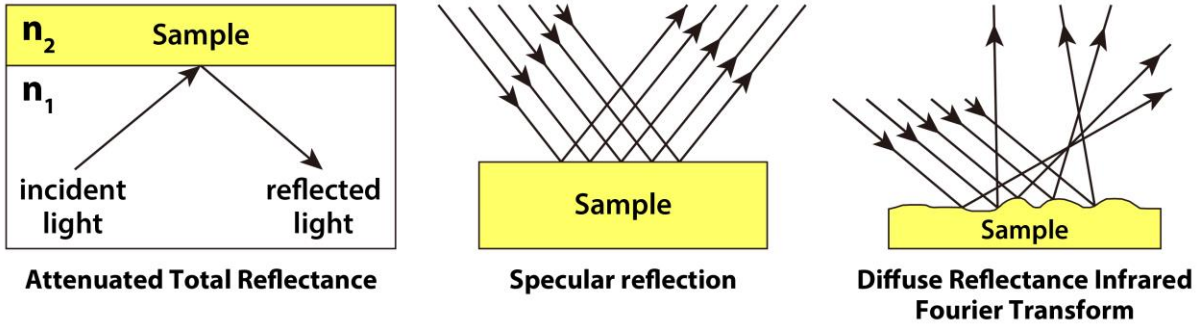

Fig. 22. Illustration of different reflection phenomenon modified from Khoshhesab (2012).

Each spectrum is acquired with 24 scans in the mid-infrared range from 4000 to 500 cm^{-1} with a spectral resolution of 2 cm^{-1} (**Fig. 23**). The ATR spectra are obtained on powders placed under a diamond crystal. For ATR crystal, diamond, zinc selenide (ZnSe), and germanium (Ge) can be used. In the MIR-ATR technique, the penetration depth of infrared radiation is greater at low wavenumbers. The SR spectra are obtained on hand specimens placed directly in front of the sample cap. The DRIFT spectra are acquired on powders which are placed in a sample cup. The MIR-DRIFT technique amplifies low-intensity bands.

Data are recorded in the OPUS file format with metadata. Spectrum acquisition, basic data visualization and management are available. The spectral data can be converted into .txt files consisting in two-column tables with infrared wavenumber in the first column (cm^{-1}) and the Transmittance (%) in the second column. The resulting spectra could be processed directly on the software with the application of conversions (AB-TR) or transformations (Kramers-Kronig Transformation). In the case of MIR-SR, the most intense bands have a characteristic shape due to the dispersion of the radiation and are called "Restsrahlen bands" (**Fig. 23**). The reflectance values at each wavelength are dependent on the absorption index (k) and the refractive index (n) of the sample. Therefore, MIR-SR spectrum can be converted in a more conventional transmission spectrum by means of the Kramers–Kronig (KK) transform (Zaffino et al., 2015). This conversion is useful in order to characterize a material, as the most common FTIR databases contain transmission spectra. However, it should be noted that other phenomena, particularly diffuse reflection, can occur, concurring to modify the shape and the position of the bands.

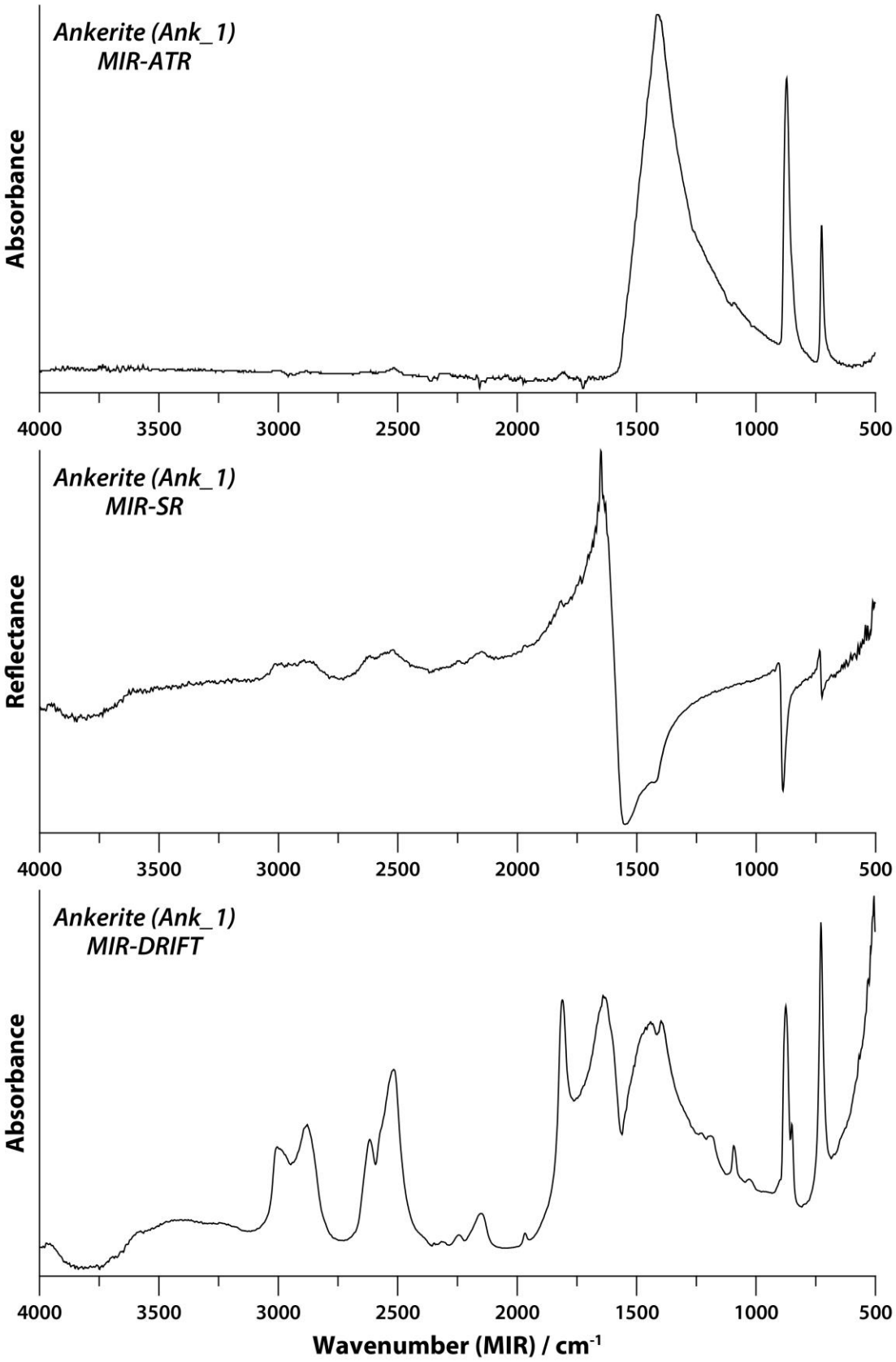

Fig. 23. MIR- ATR, SR, and DRIFT spectra of the ankerite sample from the spectral library.

1.3.4. VNIR-SWIR technique

VNIR-SWIR analysis was carried out by SR-6500 spectroradiometer (Spectral Evolution). The portable instrument covers the range of visible, near infrared and the short-wave infrared region from 350-2500 nm, and the spot size of the contact probe is 10 mm (**Fig. 19**). The device has different spectral resolutions based on the wavelength region: 1.5 nm at 700 nm, 3.0 nm at 1500 nm, and 3.8 nm at 2100 nm. Three thermoelectrically cooled photodiode arrays provide the ultimate in stable performance with a drift stability of <2%. Prior to its first usage, the instrument has to be calibrated using a specialized ceramic disk (99% whiteness in this thesis) that reflects uniformly across the spectrum. Minimum scan speed is 100 milliseconds and each spectrum for a given sample of the spectral library was produced from an average of 20 measurement to represent the overall spectral pattern (**Fig. 24**). There are no specific sample requirements other than that the analysed material should be dry, and nothing is between the sample material and the sensor. Water is active in the VNIR-SWIR region, affecting the overall spectral shape. In particular, intense absorption bands produce at around 1400 nm (OH and water) and 1900 nm (water) in the SWIR region (Pontual, 2008).

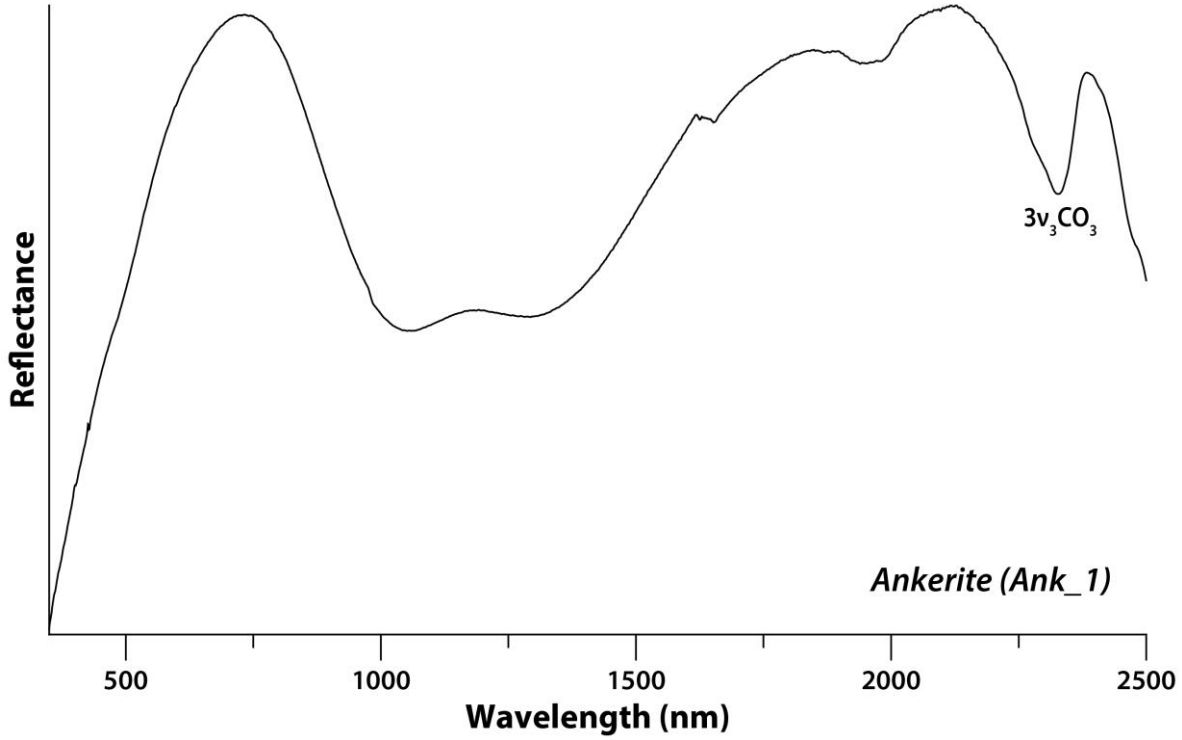

Fig. 24. VNIR-SWIR spectrum of the ankerite sample from the spectral library.

The spectral data of VNIR-SWIR are collected by DARWin software (Spectral Evolution), which is able to interface with the device and display acquired spectral scan data. The measurement parameters (i.e., averaging and integration settings and the selection of foreoptics ordered) can be set by the user or automatically adjusted. When spectra are collected, DARWin SP defaults to automatically generating a SED (Spectra Evolution Data) file for each target scan collected. The file is composed of an informational header (with particular about the scan, e.g., date, time, averaging and integration settings, system temperature, voltage, and so forth.) followed by columns of tab-separated data that can be imported to spreadsheet programs. Furthermore, DARWin SP is compatible with EZ-ID, a software dedicated to signal interpretation. EZ-ID allows to collect a scan from an unknown target and match it to a known mineral scan from various existing spectral libraries or a custom library built by users.

1.3.5. Raman technique (EnSpectr)

Raman spectra were collected using two different Raman spectrometers. The first portable Raman device, RaPort (EnSpectr), works with a 532 nm laser excitation (green) at a power of 100-150 mW. The spectra were acquired at 60% and 80% of maximum power (**Fig. 25**). The total acquisition time was set to 30 seconds, yet the number of accumulations and the duration of each individual acquisition was automatically defined (**Fig. 19**). The spectral resolution was 6 cm^{-1} in the range 130-4000 cm^{-1}, a baseline was subtracted (EnSpectr algorithm)

Data from the portable RaPort are directly obtained from the EnSpectr+ software. This manufacturer software is already installed onto the RaPort device itself (tablet) but could also be installed on the user computer. This software allows some parameter modifications such as laser power, maximum acquisition time and spectral window size. Data obtained from the analyses are exported from the device to the user computer directly from the tablet memory of the device. Data file extension is .esp, which are ASCII files holding one spectrum and its metadata. These files are readable with the manufacturer software on which spectra obtained can be shown or as text files on which 2 columns are present: a first one corresponding to Raman shift in cm^{-1} and a second one with Raman intensity in arbitrary units.

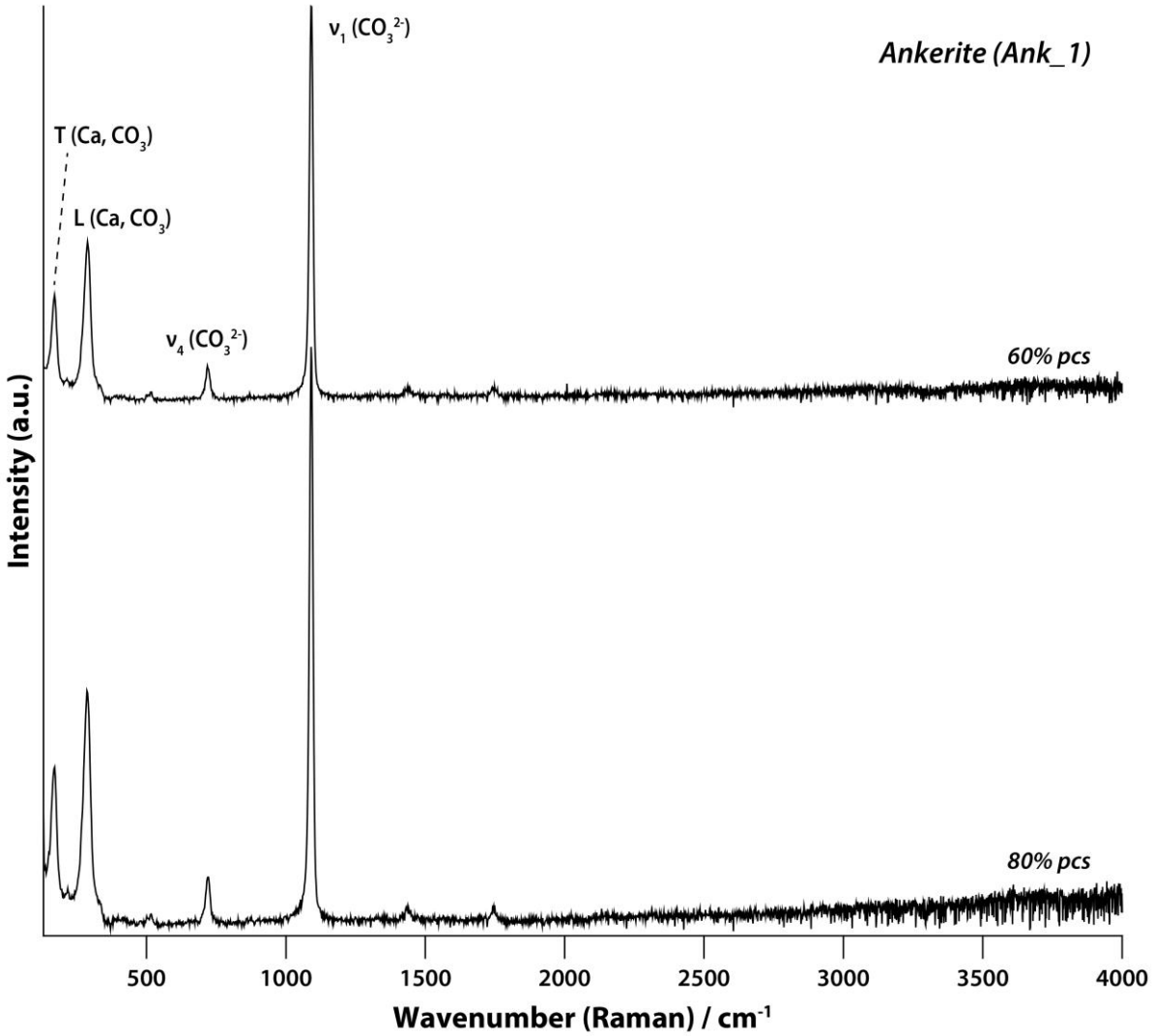

Fig. 25. Raman spectrum with a green laser of the ankerite sample from the spectral library.

1.3.6. Raman technique (Bruker)

The second portable Raman device, The BRAVO (Bruker) spectrometer, is equipped with two lasers in the 700-1100 nm range (red to near infrared) at a power lower than 100 mW (**Fig. 26**). The spectrometer is also equipped with patented fluorescence mitigation (SSE^{TM} Sequentially Shifted Excitation). The spectral resolution was 10-12 cm^{-1} in the range 300-3200 cm^{-1}. Spectrum acquisition, basic data visualization and management, and baseline subtraction are automatically controlled by OPUS software in the device through the touch screen. Since all acquisition parameters are fully automatized, in this library, six spectra were acquired on each sample with this second Raman spectrometer and averaged before interpretation (**Fig. 19**).

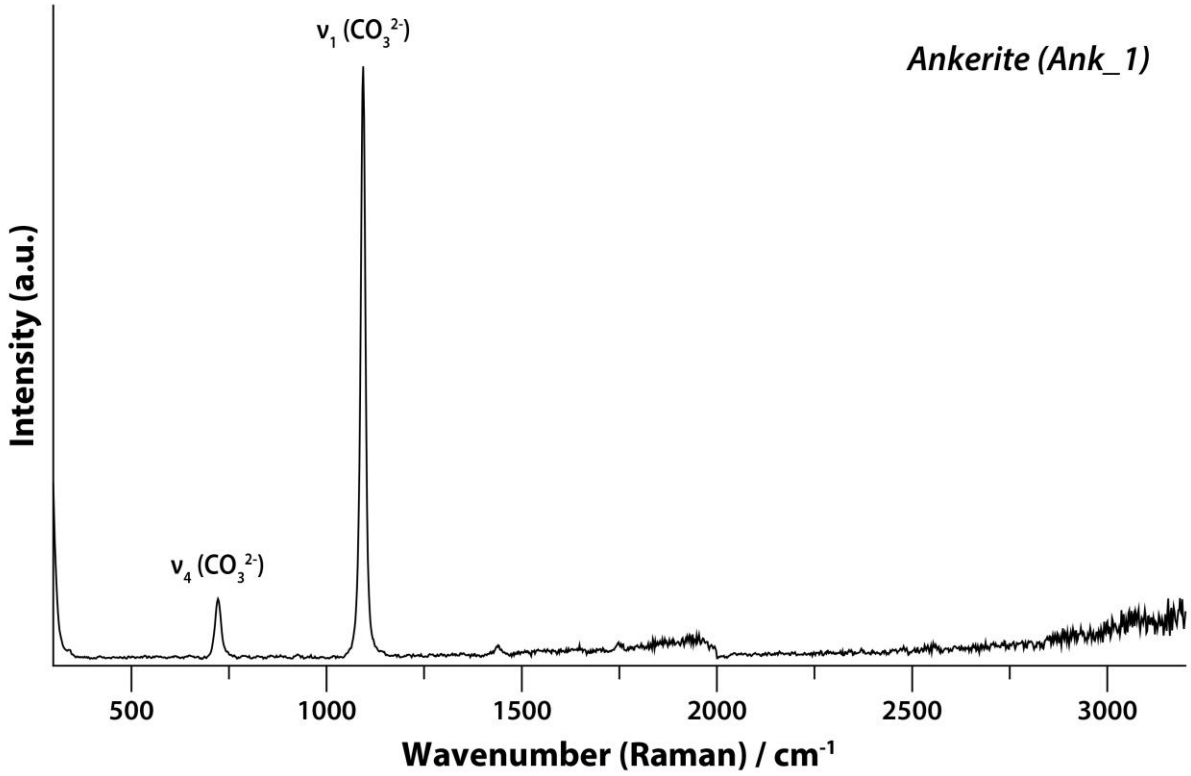

Fig. 26. Raman spectrum with a red-NIR laser of the ankerite sample from the spectral library.

Data are recorded in OPUS file format with metadata. For data transfer, data processing and file conversion, the spectrometer must be connected to a computer equipped with OPUS software. Each acquisition is repeated twice changing a little bit the laser temperature, and so the wavelength to discriminate the Raman signal from luminescence. The resulting spectra is the combination of the two spectral domains after SSE processing to remove luminescence signals.

1.3.7. XRD technique

The portable XRD device used in this library is an Olympus Terra portable XRD/XRF instrument. The powder sample is inserted into one of the two sample chambers without any specific preparation. The sample particles should be less than 150 μm and the minimum sample size is 15 mg. The data collection range of 2θ is from 5 to 55˚, with increment of 0.25˚ (**Fig. 27**). The instrument has a patented Vibrating Sample Holder (VHS) to obtain random orientation of mineral crystallites. In this type of configuration, the components are in a fixed

position: the X-ray leave the tube (cobalt target), pass through a collimator, and collide into the sample, where they are diffracted by the array of gains onto a 1024x256 pixel 2D Peltier-cooled Charge-Coupled Device (CCD) within a temperature range from -10 °C to 35 °C. The complete diffraction pattern of the sample is collected and displayed simultaneously after the first exposure (~ 20 seconds), and the data output in this library were achieved after 75 exposures.

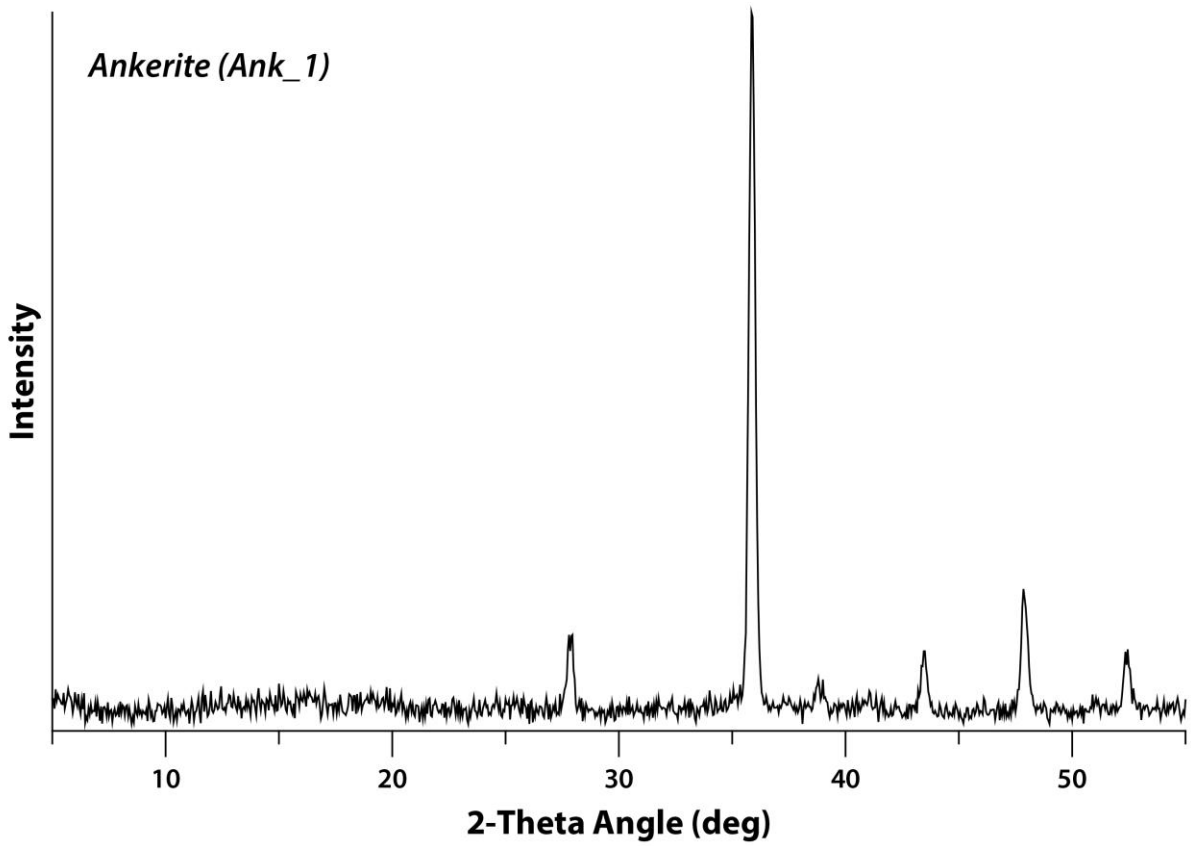

Fig. 27. XRD pattern using Cobalt-Kα radiation of the ankerite sample from the spectral library. Background subtraction operated by XPowder software.

The XPowder software provides tools for controlling background subtraction. The text file provides information such as date, integration time, exposure and parameters of piezoelectricity, geometry and energy followed by columns of tab-separated spectral data. The first column indicates the range of 2θ and the second one corresponds to intensity (counts). The data obtained with Olympus Terra pXRD was interpreted with the XPowder software based on Reference Intensity Ratio (RIR) method and using AMCSD database (American Mineralogist Crystal Structure Database) consisting of minerals only.

1.4. Access to the data

The data is freely available on the storage system of OTELo, named ORDAR (https://ordar.otelo.univ-lorraine.fr/). OTELo is the group of laboratories of the University of Lorraine working on Sciences of the Universe, Earth Sciences, and Sciences of the Environment. ORDAR provides permanent links, which will be maintained in the long term a remain accessible to users long after the end of the project.

2. Mineralogical composition database

2.1. Introduction and analytical methods

Mineral composition database aims to present accurate and precise chemical composition information so that it allows a detailed comparison of compositional changes and spectral variations within the same mineral groups. Due to the importance of chemical composition data, the quality and reliability of the information are essential for both analytical and compiled results. Chemical compositions of the mono mineral samples were determined by SX 100 (CAMECA) equipped with wavelength-dispersive spectrometers (WDS) at Service Commun de Microscopie Electronique et de Microanalyse X (SCMEM) in GeoRessources. The analyses were carried out by acceleration voltages of 15 or 20 kV, a beam current from 6 to 20 nA depending on mineral groups (**Table 5**). The counting time and the diameter of the electron beam is 15 seconds and 1 μm^2, respectively. Since some samples were provided in powder form, only 29 samples (i.e., 6 silicates, 1 phosphate, 10 carbonates, 1 sulphate, and 11 sulphides) were analysed on thin sections (**Table 6**).

Table 5. Operating conditions for EPMA analyses.

Mineral group	Acc. voltage (kV)	Beam current (nA)	Counting time (s)	Beam diameter (μm^2)
carbonate	15	6	15	1
phosphate	15	12	15	1
silicate	15	12	15	1
sulfate	15	12	15	1
sulfide	20	20	15	1

Table 6. Chemical composition (EPMA, wt%) of the minerals in the mineralogical composition database.

Group	Mineral	Name	Mineral	N*	Si		Al		Na		Ca		K		Fe		Mg		Mn		P		F		O	
					Avg.	Std.	Avg.	Std.	Avg.	Std.	Avg.	Std.	Avg.	Std.	Avg.	Std.	Avg.	Std.	Avg.	Std.	Avg.	Std.	Avg.	Std.	Avg.	Std.
silicate	albite	Ab_2-1	albite	50	30.83	0.53	11.10	0.27	7.84	0.30	1.23	0.40	0.06	0.03			0.00	0.01							48.30	0.50
	anorthite	An_1-1	bytownite	10	23.54	0.24	16.99	0.24	2.10	0.17	10.73	0.28	0.09	0.03	0.11	0.07									47.20	0.15
		An_1-2	labradorite	11	25.17	0.56	15.61	0.36	3.24	0.16	8.72	0.13	0.17	0.03	0.20	0.13									47.44	0.97
	quartz	Qz_2	quartz	20	47.33	0.22	0.00	0.01	0.01	0.01					0.02	0.03	0.00	0.00							53.97	0.24
	muscovite	Ms_1	muscovite	20	22.15	0.18	19.18	0.23	0.56	0.04	0.00	0.00	8.47	0.14	1.13	0.11	0.25	0.05	0.02	0.03			0.17	0.19	44.81	0.33
		Lpd_1	lepidolite	21	22.99	1.02	16.17	2.54	0.15	0.07	0.00	0.01	8.77	0.26	0.03	0.06	0.01	0.01	0.28	0.17			3.95	2.46	42.55	1.45
	chlorite	Chl_1	chlorite	20	13.89	0.72	10.84	0.44	0.02	0.02	0.11	0.14	0.03	0.04	11.25	0.84	13.81	1.01	0.12	0.05					37.94	0.57
phosphate	apatite	Ap_1	apatite	25							38.90	0.80			0.05	0.04			0.79	0.37	18.22	0.27	4.52	0.37	39.34	0.52

* N: Number of spot analyses by electron microprobe

Group	Mineral	Name	Mineral	N*	Ca		Fe		Mg		Mn		Co		O	
					Avg.	Std.	Avg.	Std.	Avg.	Std.	Avg.	Std.	Avg.	Std.	Avg.	Std.
carbonate	calcite	Cal_1	calcite	14	38.33	2.48	0.11	0.07	0.22	0.23	0.05	0.04	0.00	0.00	16.07	0.72
		Cal_3-1	calcite	20	40.29	0.38	0.01	0.03	0.09	0.03	0.03	0.03	0.00	0.00	16.19	0.15
		Cal_3-2	dolomite	1	23.03	0.00	0.46	0.00	14.72	0.00	0.11	0.00	0.00	0.00	19.05	0.00
		Cal_4	calcite	27	40.53	0.75	0.02	0.03	0.58	0.25	0.01	0.02	0.00	0.00	16.63	0.35
		Cal_5	calcite	25	40.01	0.67	0.13	0.19	0.19	0.13	0.17	0.13	0.18	0.15	16.26	0.21
	dolomite	Dol_1-1	dolomite	16	22.82	1.28	0.35	0.14	13.85	1.07	0.07	0.06	0.00	0.00	18.37	0.32
		Dol_1-2	calcite	1	40.42	0.00	0.05	0.00	0.05	0.00	0.03	0.00	0.00	0.00	16.20	0.00
		Cal_6	calcite	26	39.57	0.63	0.04	0.05	0.59	0.23	0.01	0.02	0.00	0.00	16.21	0.21
		Dol_2-1	dolomite	5	22.55	0.25	0.45	0.06	14.03	0.21	0.05	0.03	0.00	0.00	18.42	0.14
		Dol_2-2	calcite	19	40.19	0.68	0.05	0.05	0.45	0.29	0.04	0.04	0.00	0.00	16.37	0.25
	ankerite	Ank_1	ankerite	31	19.84	0.34	9.34	0.95	7.67	0.88	2.30	0.42	0.00	0.00	16.34	0.26
	siderite	Sd_2-1	siderite	11	0.02	0.02	38.92	1.38	3.75	0.69	3.83	0.45	0.04	0.05	14.77	0.24
		Sd_2-2	calcite	8	39.49	0.43	0.04	0.04	0.01	0.01	0.31	0.13	0.01	0.02	15.90	0.16
		Sd_3-1	siderite	13	0.04	0.04	43.55	2.58	1.91	1.01	1.92	0.91	0.00	0.00	14.33	0.23
		Sd_3-2	calcite	1	37.56	0.00	0.28	0.00	0.01	0.00	1.56	0.00	0.00	0.00	15.60	0.00

Table 6. (continued).

Group	Mineral	Name	mineral	N*	Fe		Ba		Pb		Cu		Zn		O		S	
					Avg.	Std.	Avg.	Std.	Avg.	Std.	Avg.	Std.	Avg.	Std.	Avg.	Std.	Avg.	Std.
sulfate	barite	Brt_2	barite	39			58.57	0.80							28.39	0.26	14.09	0.16
sulfide	chalcopyrite	Ccp_1	chalcopyrite	15	29.25	0.33			0.09	0.06	34.24	0.22	0.08	0.14			34.90	0.27
		Ccp_2	chalcopyrite	23	29.33	0.57			0.12	0.05	34.38	0.34	0.01	0.01			35.23	0.22
		Ccp_3	chalcopyrite	23	29.69	0.24			0.11	0.06	33.96	0.22	0.00	0.00			34.97	0.20
	galena	Gn_1	galena	15					86.89	0.37							13.66	0.09
		Gn_2	galena	25					86.82	0.26							13.80	0.16
	pyrite	Py_1	pyrite	30	46.56	0.20			0.16	0.04							53.91	0.27
	pyrrhotite	Po_1	pyrrhotite	22	58.89	1.25			0.14	0.03							38.54	0.63
		Sp_4	pyrrhotite	18	58.10	0.20			0.13	0.03							39.66	0.19
	sphalerite	Sp_1	sphalerite	19	2.50	0.33			0.09	0.05			63.30	0.63			33.27	0.20
		Sp_3	sphalerite	20	0.32	0.09			0.08	0.05			65.80	0.32			33.13	0.21
		Sp_5	sphalerite	20	0.40	0.04			0.08	0.05			66.22	0.25			33.33	0.17

* N: Number of spot analyses by electron microprobe

2.2. Comparison of elemental concentration by EPMA analysis

In order to visually identify i) the dispersion of the concentration in major elements for each mineral, and ii) compositional variations in the same mineral class, **Fig. 28** shows a quantitative comparison of the major element concentrations (Si, Al, Na, and K) in the list of silicate minerals such as albite, anorthite, quartz, muscovite, and chlorite. The vertical demi error bars indicate the standard deviation for elemental concentrations divided by the square root of the number of measurements. The albite sample has high Si and Na content (30% and 8%), but low Al and K content (11% and 0.06%). The anorthite sample was divided into two endmembers (i.e., bytownite and labradorite) of the plagioclase solid solution series by comparing Na and Ca content. The quartz sample had the highest Si content of 47% while chlorite had the lowest Si and Al content of 14% and 11%, respectively. The two muscovite samples showed similar Si and K content each other, but the lepidolite sample (Lpd_1) showed diverse variation in Al content.

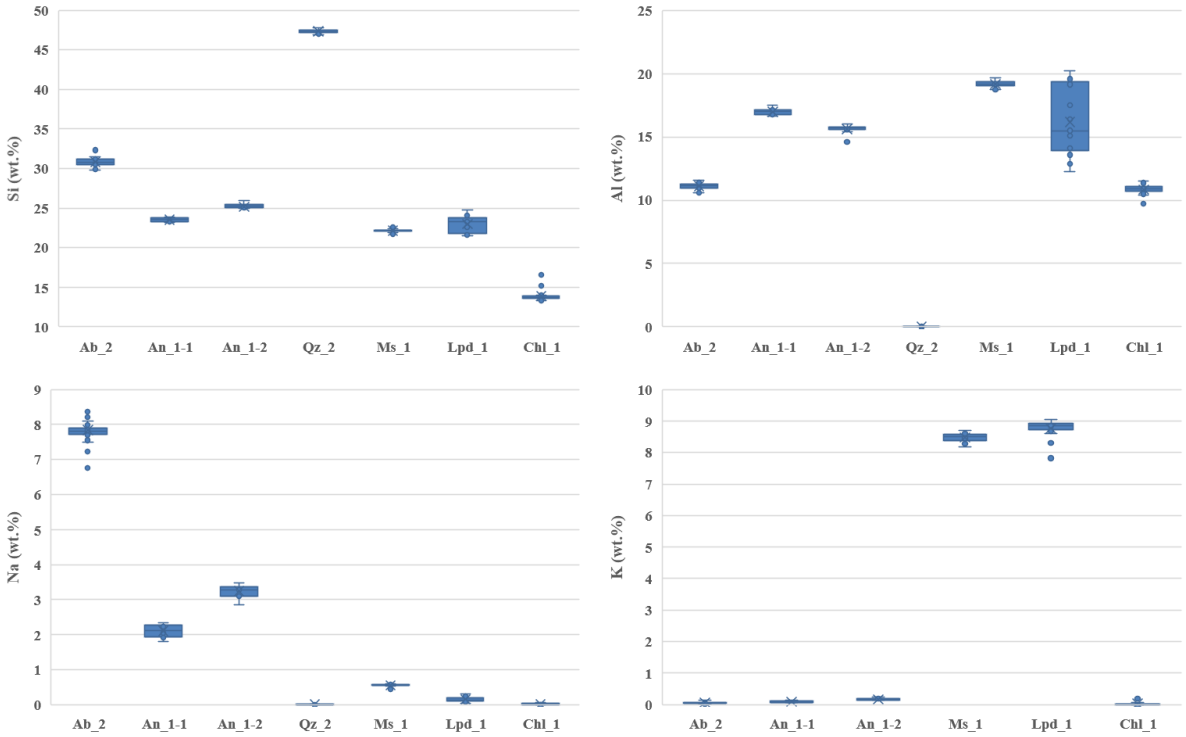

Fig. 28. Box and whisker plots showing the chemical composition for Si, Al, Na, and K.

The mineral groups corresponding to the target elements (i.e., Ca, Mg, and Mn) are silicates, phosphates, and carbonate minerals (**Fig. 29**). The anorthite samples as a calcium rich

member of the plagioclase had 8-10% Ca content, and the albite sample has 1% of Ca content. The other minerals had very low or no Ca contents. The calcite samples display obviously the highest Ca contents about 40%, which is similar to the one in the apatite sample. The presence of calcite in the different carbonate samples was determined by high Ca content. On the contrary, one calcite specimen (Cal_3-2) corresponds to dolomite (23% Ca and 15% Mg). The dolomite and ankerite specimens showed similar Ca content of 23% and 20%, respectively. However, The Mg component in both dolomite samples is about 14% analogous to the chlorite sample, and the ankerite was slightly lower than that of 8% Mg. Siderite and ankerite contained around 2-4% of Manganese, and a small amount of Mn was found in the apatite (i.e., ~1%).

Iron was examined in all the mineral groups from the mineralogical composition database (**Fig. 30**). The pyrrhotite sample showed the highest iron content, around 60%, while pyrite and siderite showed iron content at 47% and 40%, respectively. Chalcopyrite had 30% Fe content, while ankerite and chlorite showed similar iron contents of 10%. The sphalerite specimens showed a Fe range from 0.3 to 2.5%. The content of Pb in galena was found to be over 86%, and the content of Cu is about 35% in chalcopyrite. Zn has a very low content in chalcopyrite, while sphalerite displays content of about 65%.

3. Conclusion

In this chapter, the dataset provided in the spectral library contains a limited number of mineral species compared to existing libraries such as USGS and RRUFF. However, it is rare in the sense that it provides spectra and interpreted data acquired on the very same samples with several techniques. That ensures users being able to compare data from one technique to the next one. In addition to the spectral library, a new mineralogical database on the elemental composition of different mineral groups is provided. Most minerals exhibit a considerable range in chemical composition and spectral signatures of minerals produce characteristic bands in different wavenumber or wavelength regions mainly resulting in their elemental composition. Therefore, spectroscopic analysis together with the compositional variation of minerals in this mineralogical composition database allows understanding vital information about the diagnostic spectral features of each mineral before applying it to real-world samples.

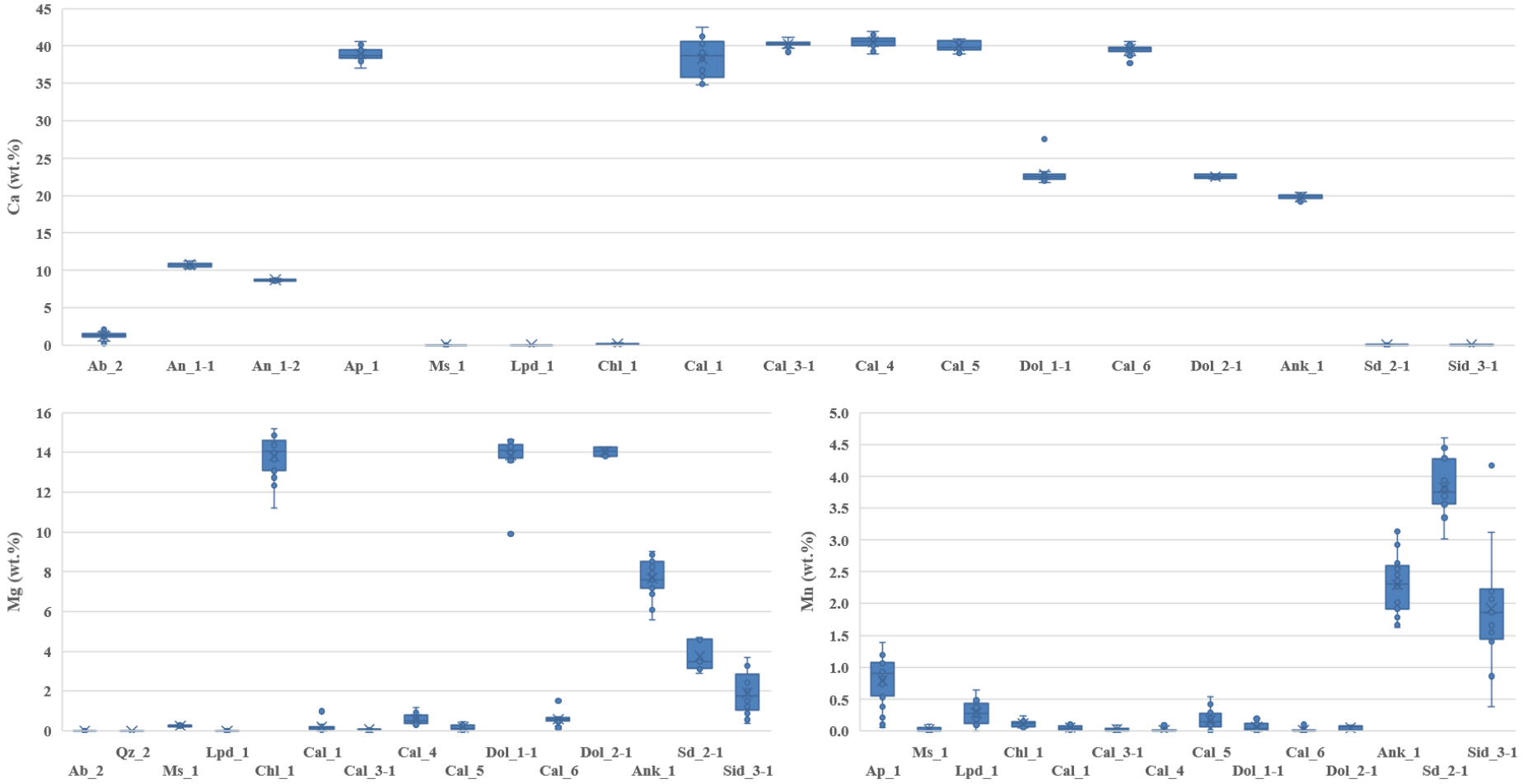

Fig. 29. Box and whisker plots showing the chemical composition for Ca, Mg, and Mn.

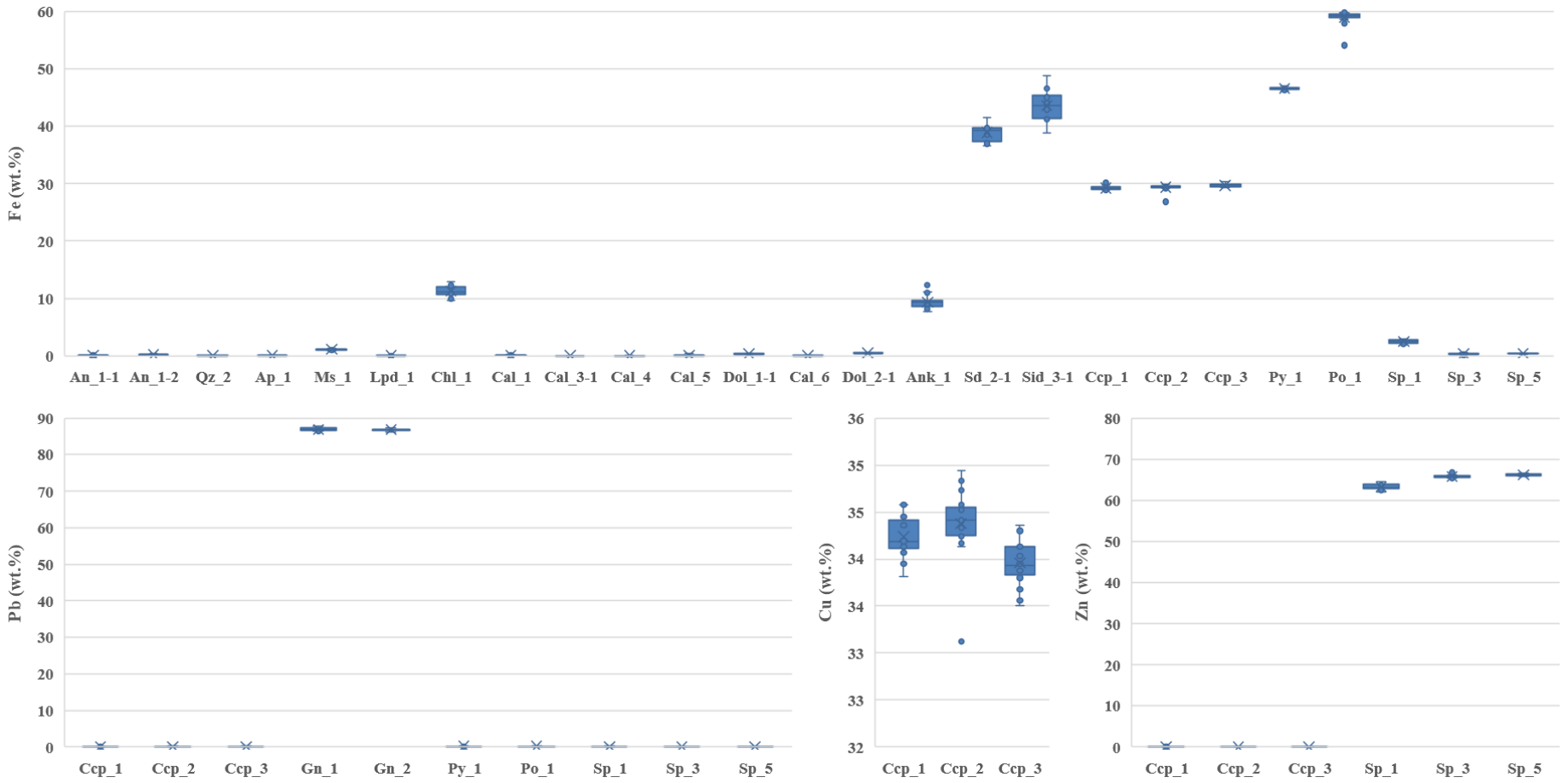

Fig. 30. Box and whisker plots showing the chemical composition for Fe, Pb, Cu, and Mn.

Chapter III. Decision tree

1. Spectral decision tree

Spectral features arising from peaks and absorptions acquired from various spectroscopies are an essential indicator of mineral identification and quantification through their positions and intensities, respectively. Recently, fast and reliable identification of minerals has become more important, resulting from technological progress of portable spectrometers for various applications on Earth. The instant information from portable spectroscopic techniques in the field helps geologists or people working in mining to make fast decision-making supports such as the future direction of exploration on the location by providing quick sample screening and discriminating minerals in samples with rapid control of concentrate quality.

Mineral spectral data are scattered and stored in different spectral libraries worldwide. The spectral characteristic of known minerals (i.e., standards) in the spectral libraries helps mineral identification for various applications by comparing with the spectral data of an unknown mineral (i.e., targets). However, the spectral data may not be compatible with each other due to different spectral resolutions, mineral categories, chemical composition, and measurement parameters for each device, even with the same mineralogical techniques. In addition, some existing libraries consist of a few thousand reference spectra with a broad range of materials, yet the number of techniques is limited. Therefore, the incompatibility and restricted techniques can hinder spectral applications in field investigation, mineral identification, landcover identification, and geological mapping.

Band information regarding individual minerals has been well established in diverse spectroscopic techniques. However, no comprehensive study has presented diagnostic bands for distinguishing minerals in various or the same mineral groups. Therefore, a decision tree provides the proper order for the presence, absence, and ranking of minerals by combining the diverse spectroscopic data. It consequently classifies band areas based on the mineral groups and determines the representative band areas of minerals. Because each device has a different beam size, spectral comparisons from different techniques for exactly matching areas can be difficult. Therefore, each spectrum was compared for the nearest position as close as possible. According to the objective of this study, which focuses on obtaining precise and accurate

spectral information on minerals first, spectral measurement was carried out on the flat surface of pelletized samples composed of a single (i.e., pure) mineral in order to unify sample conditions and represent homogeneity of the samples.

1.1. Non-destructive analysis

Minerals have been classified based on their chemical composition with their dominant anion or anionic groups. Each mineral group is reflected as specific bands using different techniques and functions as fingerprints for specific minerals. Non-destructive spectroscopic methods are widely recognized as valuable tools in mineral analyses due to the several advantages: rapid, less or no sample preparation, cost-effective, repeatability, capability for bulk measurements, and their ability to provide multi-constituent analysis of virtually any matrix from a single spectrum. In this study, three non-destructive spectroscopic techniques are used for the decision tree: Raman, MIR-SR, and VNIR-SWIR. In order to establish the decision tree, the reference spectra acquired from the mineralogical techniques from the spectral library in **Chapter II** first have comprehensively been reviewed. The following six classes can be identified in Raman: (1) sulphides, (2) silicates, (3) phosphates, (4) sulphates, (5) carbonates, and (6) graphite (**Fig. 31**). IR-SR can distinguish all the classes except for sulphides and some phyllosilicates. VNIR-SWIR effectively distinguishes OH- or H_2O-bearing sulphates, phyllosilicates and carbonates. An excellent example of the decision tree is the carbonate group. Carbonate minerals of the calcite structure referred to the D_{3d} group have four Raman active modes in the range 135-1200 cm^{-1}, and two internal vibration modes of CO_3^{2-} are found to be active in the infrared spectrum (**Table 7**).

Table 7. Band position (cm^{-1}) of Raman and infrared (SR mode) spectrum of calcite.

Raman	IR-SR	Assignment
154	-	T (Ca,CO_3)
279	-	L (Ca,CO_3)
710	-	ν_4 : Symmetric CO_3 bending
-	885	ν_2 : Asymmetric CO_3 bending
1083	-	ν_1 : Symmetric CO_3 stretching
-	1418	ν_3 : Asymmetric CO_3 stretching

*T, translational lattice mode; L, librational lattice mode

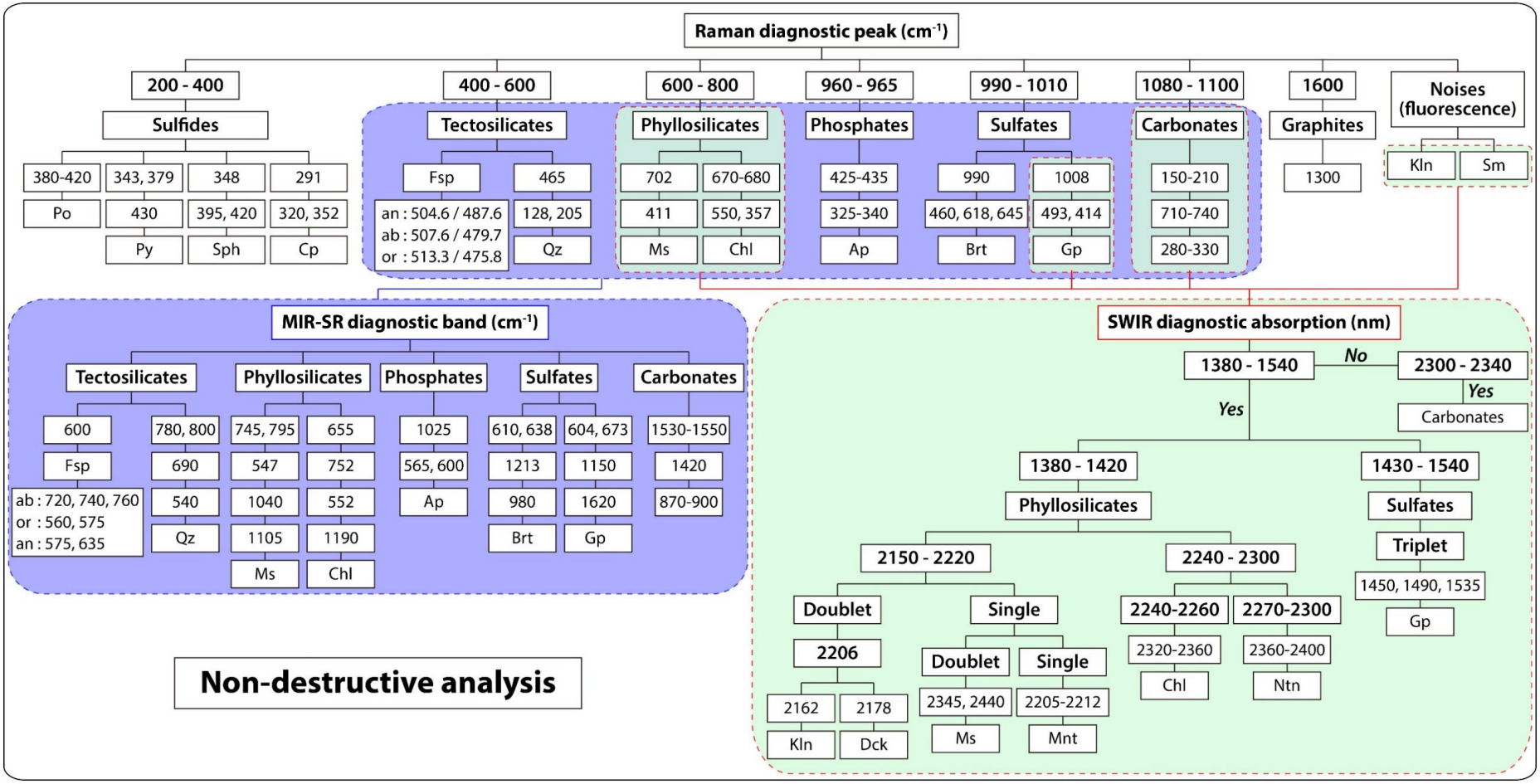

Fig. 31. Decision tree of non-destructive analysis

The symmetric stretching mode ν1 is the most intensive band in the Raman spectrum; thus, the region of the ν_1 mode (1080-1100 cm^{-1}) became the first diagnostic peak region in the decision tree. Although this region effectively distinguishes carbonate minerals among other mineral groups, it is difficult to identify their composition due to narrow intervals with a significant level of dispersion (Kim et al., 2021). Carbonate minerals are constituted by combining one CO_3^{-2} ion and various monovalent or divalent cations, such as Ca, Mg, Fe, Mn, and so forth. According to Kim et al. (2021), the T mode is the most diagnostic region for carbonate discrimination. For some Raman devices equipped with a red or near-infrared laser for excitation, the spectral range starts at 300 cm^{-1} and thus does not cover the T and L modes. In this case, the symmetric bending mode ν_4 can be the second option to identify carbonate composition (**Fig. 31** and **Fig. 32**A).

The asymmetric stretching ν_3 mode at 1418 cm^{-1} shows a maximum of reflectance in the infrared spectrum, following the so-called reststrahlen effect due to the strong absorption coefficient (**Fig. 32**B). The calcite reststrahlen band shows an extensive splitting of the transverse and longitudinal component of the vibration ($\Delta_{LO\text{-}TO}$ = 100 cm^{-1}) (Ricci et al., 2006). Even though the ν_3 mode is the most profound absorption in carbonate minerals, the absorption is not narrow nor sharp. Furthermore, the spectral shape and absorption can be affected by sample conditions such as roughness and grain size (Ricci et al., 2006). Therefore, as the method of the Raman part in the decision tree, the region of the ν_3 mode was used to determine the presence of carbonate, and the asymmetric bending ν_2 mode determined the carbonate composition.

Carbonate minerals in the SWIR region has several diagnostic absorption features resulting from combinations and overtones of the CO_3 fundamental vibrations (**Fig. 32**C). Since the first overtones of the OH stretches (Al_2-O-H) occur in the 1400 nm region (Laukamp, 2011), carbonate minerals are not active in this region as described in the decision tree. The main diagnostic absorption feature is located between 2300 nm and 2340 nm, showing a characteristic left-hand asymmetry due to $3\nu_3CO_3$ (Gaffey, 1985). With an increasing amount of Mg and Fe, the $3\nu_3CO_3$ shifts to shorter wavelengths.

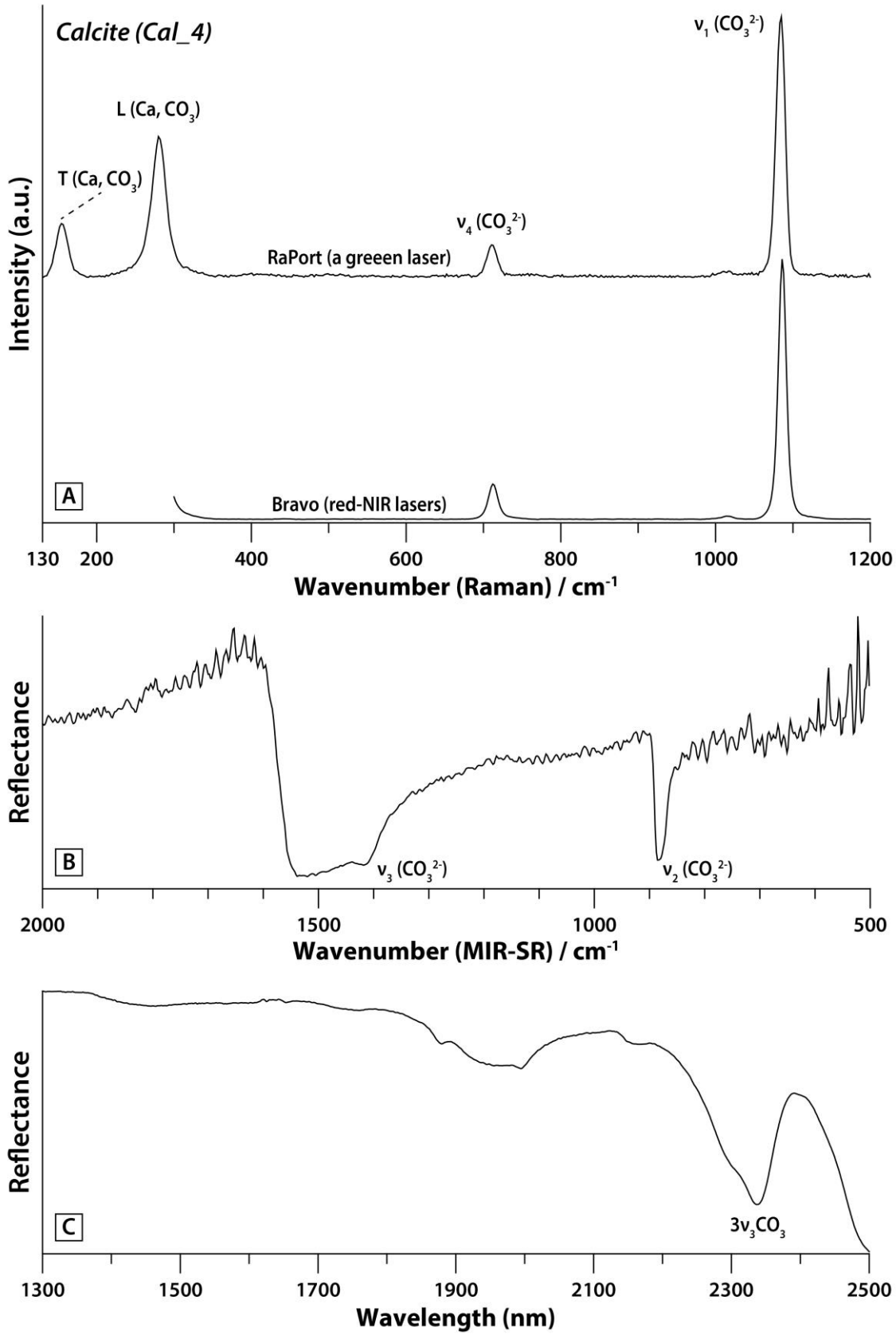

Fig. 32. Calcite reference spectra. A) Raman spectra; B) MIR-SR spectrum; C) SWIR spectrum.

1.2. Destructive analysis

This part aims to provide secondary spectral information using destructive analysis between two portable devices. The decision tree of destructive analysis such as XRD and MIR-ATR (**Fig. 33**) begins with the assumption that a sample can be cut/grinded or powdered on site. In order to obtain the XRD pattern, the sample particles should be less than 150 μm, and the minimum sample size is 15 mg. If carbonate minerals, as an example in the non-destructive analysis part, are applied in the destructive analysis part, the main region of the diagnostic peak is 34-39˚ 2θ (3.06 to 2.68 Å) in XRD patterns (CoK_{α}) (**Fig. 34**A). The sharp peak in this range is the highest in the pattern. The position of each carbonate mineral reflects its composition; for example, calcite positioned at 34.3˚ (3.03 Å) and magnesite positioned at 38.1˚ (2.74 Å).

For MIR-ATR, a powder sample of 5-10 milligrams (mg) are placed onto a diamond crystal and pressed with an anvil. MIR-DRIFT is able to measure samples directly in bulk form of neat powders with very little preparation. However, spectra can be affected by crystal disorder or crystal symmetry, causing changes to the number of observed peaks and to peak width and intensity (Madejová, 2003). Therefore, the samples are generally analysed as dispersions in IR transparent matrices such as potassium bromide (KBr) and potassium chloride (KCl) to improve the quality of the spectrum. For this reason, MIR-DRIFT method is excluded in this decision tree due to hardly being feasible in the field conditions. Four internal vibration modes of CO_3^{2-} are active in the IR-ATR spectrum measured from the carbonate minerals (**Fig. 34**B). The ν_3 band gives rise to a strong and extensive peak range in the infrared spectrum, but the largest dispersion, without a clear correlation between the band position and chemical composition. However, the narrow and sharp ν_4 band shows two trend lines (i.e., Ca-Mg and Fe-Mg) having a strong correlation, respectively (Kim et al., 2021). Therefore, in the decision tree for IR-ATR, the ν_3 band is used first to determine the presence of carbonates. Then the ν_4 band is applied to determine the chemical composition of carbonate minerals.

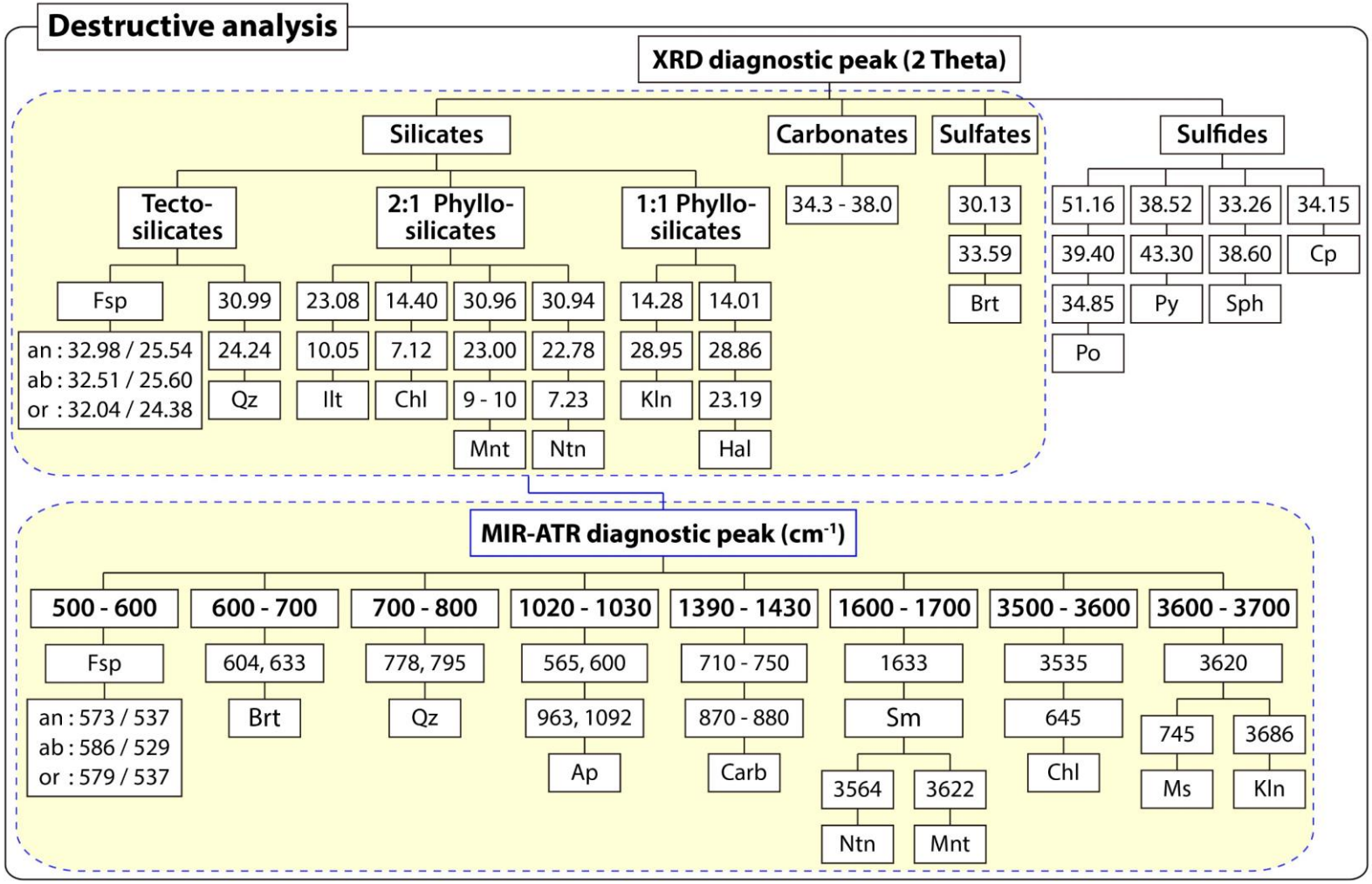

Fig. 33. Decision tree of destructive analysis

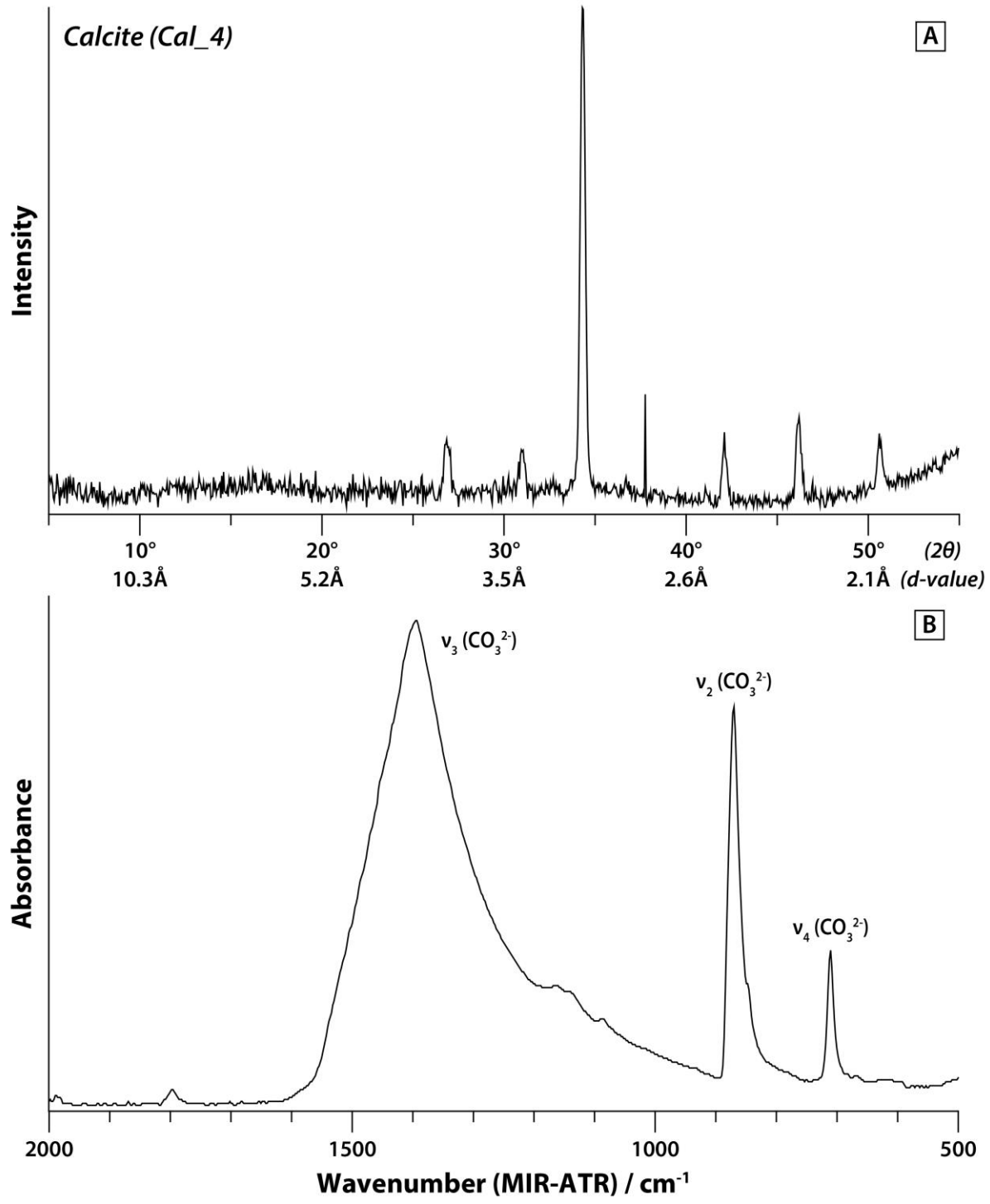

Fig. 34. Calcite reference spectra. A, XRD pattern; B, MIR-ATR spectrum.

2. Spectral quantification for light elements using handheld LIBS

2.1. Introduction

Light elements are generally referred to as elements with atomic number (Z) less than 11. There is no official cut-off in terms of the light elements. One consideration is that up until about 1990, conventional energy dispersive spectroscopy (EDS) detectors were used entrance windows made of beryllium, and this window confines to the identification of elements of atomic number Z = 11 (sodium) or larger (Fultz and Howe, 2012; Thomas, 1985). However, in portable spectroscopy, Sodium (Na) and Magnesium (Mg) are also considered light elements (Lemière and Harmon, 2021). The European Raw Materials Initiative established a list of critical non-energy raw materials (CRMs) combining high economic importance to the EU with a high risk of supply disruptions (Commission, 2020). Thirty raw materials or groups are identified as critical in 2020, and beryllium (Be), Borates, Fluorspar, Lithium (Li), and Magnesium (Mg) were listed as members of light elements.

Handheld XRF analysers cannot measure elements of low atomic numbers, hence light element identification is notoriously challenging in XRF. The portable devices are not currently able to reliably quantify Mg or detect Na due to the severe drop in fluorescence yield with decreasing atomic number and the absorption of fluorescent X-rays by air (Hall et al., 2011; Horta et al., 2015; Jenkins, 2008; Ravansari et al., 2020). Handheld LIBS, however, is the only technique available for the direct measurement of light elements in the field. In principle, LIBS can detect any element of the periodic table but is particularly suited for analysis of light elements with low ionization potentials that X-ray cannot, such as Be, B, C, F, Li, and Na (Lemière and Harmon, 2021). Especially, quantitative estimation of F content using molecular bands of CaF and Li content in materials using handheld LIBS demonstrated the capacity of this technique to establish the univariate calibrations of each element (Fabre et al., 2021; Foucaud et al., 2019).

Na and Mg are some of the most abundant elements in the earth's crust, and many minerals contain these elements. Significantly, these elements are essential to identify a mineral belonging to a solid solution. For example, K-Na exchange equilibria between muscovite-paragonite solid solution, a plagioclase feldspar solid solution series, Ca-Mg-Fe-Mn substitution in the crystal structure of carbonate minerals, and Fe-Mg substitution in

trioctahedral chlorites and biotites. As these compositional variations can be distinct indicators to locate ores in the field, it is crucial to identify and quantify these elements in the field. However, there has been no case of univariate calibration by comparing the content of Na and Mg obtained from various mineral groups. For LIBS quantitative analysis, this chapter deals with selecting the best emission lines for Na and Mg and establishing linear univariate curves based on element content.

2.2. Materials and experimental method

2.2.1. Samples

The pure samples used in this study were obtained from the spectral library in **Chapter II**. Some minerals, including diverse contents of the target elements (i.e., Na and Mg), were selected (**Table 8**). Three different chemical analyses were carried out to verify chemical composition. Seven Na-bearing minerals such as feldspars and phyllosilicates were selected, and a set of eleven Mg-bearing minerals consisting of phyllosilicates and carbonates were used in this LIBS study. LIBS analysis was carried out on 13 mm diameter pellets made with a 10-ton hydraulic press. The same sample condition (i.e., palletisation) was used for all samples to minimize the potential matrix effect that occurs during plasma formation and its emission.

2.2.2. Experimental setup

All LIBS spectra were acquired by the Handheld Z300 LIBS analyser (Sci-Aps ©, Woburn, MA). Z300 LIBS instrument covers the spectral range from 190 to 950 nm, allowing for the detection of Na and Mg elements. The portable instrument utilizes a 1064 nm Nd:YAG pulsed laser with a 50 μm focused beam size, operating 5-6 mJ per pulse to the sample and 10 Hz repetition rate. The pressure of argon gas in the device was maintained at around 12 psi.

Five random locations were measured for each pellet. Each location was measured with a 15-point square grid on three lines, and the step size between the ablated craters was set at 60 μm to avoid the effects by overlapping between craters. Each point of the grid consists of 4 successive single shots after one first cleaning shot, thus the total 60 LIBS measurements collected for each location were averaged into one LIBS spectrum per sample to reflect the ‘bulk’ composition of the sample.

Table 8. Elemental concentration of Na and Mg in wt.% obtained from chemical analyses.

Samples for sodium (Na) quantification					
Mineral	**Sample**	**Analysis***	**N****	**Na (wt.%)**	
				Avg	**Std**
albite	Ab_2	EPMA	50	7.84	0.30
anorthite	An_1	EPMA	21	2.70	0.59
muscovite	Ms_1	EPMA	20	0.56	0.04
muscovite	Ms_2	ICP-OES	1	0.60	0.00
lepidolite	Lpd_1	EPMA	21	0.15	0.07
chlorite	Chl_1	EPMA	20	0.02	0.02
chlorite	Chl_2	ICP-OES	1	0.04	0.00

Samples for magnesium (Mg) quantification					
Mineral	**Sample**	**Analysis***	**N****	**Mg (wt.%)**	
				Avg	**Std**
muscovite	Ms_1	EPMA	20	0.25	0.05
muscovite	Ms_2	ICP-OES	1	0.03	0.00
chlorite	Chl_1	EPMA	20	13.81	1.01
chlorite	Chl_2	ICP-OES	1	18.63	0.00
calcite	Cal_1	EPMA	14	0.22	0.23
calcite	Cal_4	EPMA	27	0.58	0.25
ankerite	Ank_1	EPMA	31	7.67	0.88
dolomite	Dol_1	EPMA	17	13.03	3.41
magnesite	Mgs_1	AAS	1	27.18	0.00
siderite	Sd_2	EPMA	19	2.17	1.92
siderite	Sd_3	EPMA	14	1.78	1.09

* **EPMA** data analyzed by SX100 at SCMEM (GeoRessources); **ICP-OES** data from SARM (CRPG); **AAS** data analyzed by Perkin ELMER A800 at STEVAL (GeoRessources)
** Number of spot analysis

2.3. Analytical methods

2.3.1. Methodology

Fig. 35 outlines univariate calibration methods for the quantification of Na and Mg elements. The univariate calibration has been widely used as the most straightforward approach to correlate emission intensity or peak area and analyte content (Mermet, 2010). LIBS suffers from considerable background noise, and heavy baseline drift since many factors affect the predictions of quantitative analysis, such as the environment change, experimental parameters fluctuation, material physical and chemical characteristics, and the laser energy variation (Yi et al., 2017). These factors make the analysis of the spectra unreliable and inaccurate without applying some pre-processing steps such as normalization and baseline correction before the univariate analysis (Guezenoc et al., 2019; Haddad et al., 2014). Therefore, data pre-processing is crucial in the case of quantitative analysis as it is more difficult to identify the concentration of an element than to determine if it is present or not inside a sample (**Fig. 35**). Both normalization and baseline correction is processed by Spectragryph v1.2.15 (Menges, 2020).

In order to get a first understanding of the relationship between the physical parameters, univariate analysis was carried out using the peak area on the one hand, and the concentration of the analyte on the other hand. In LIBS, the signal usually corresponds to the intensity or the peak area of the most relevant line (Sarkar et al., 2012). Thus, the selection of suitable Na and Mg analytical emission lines becomes a significant preliminary study in the design of the univariate analysis (**Fig. 35**).

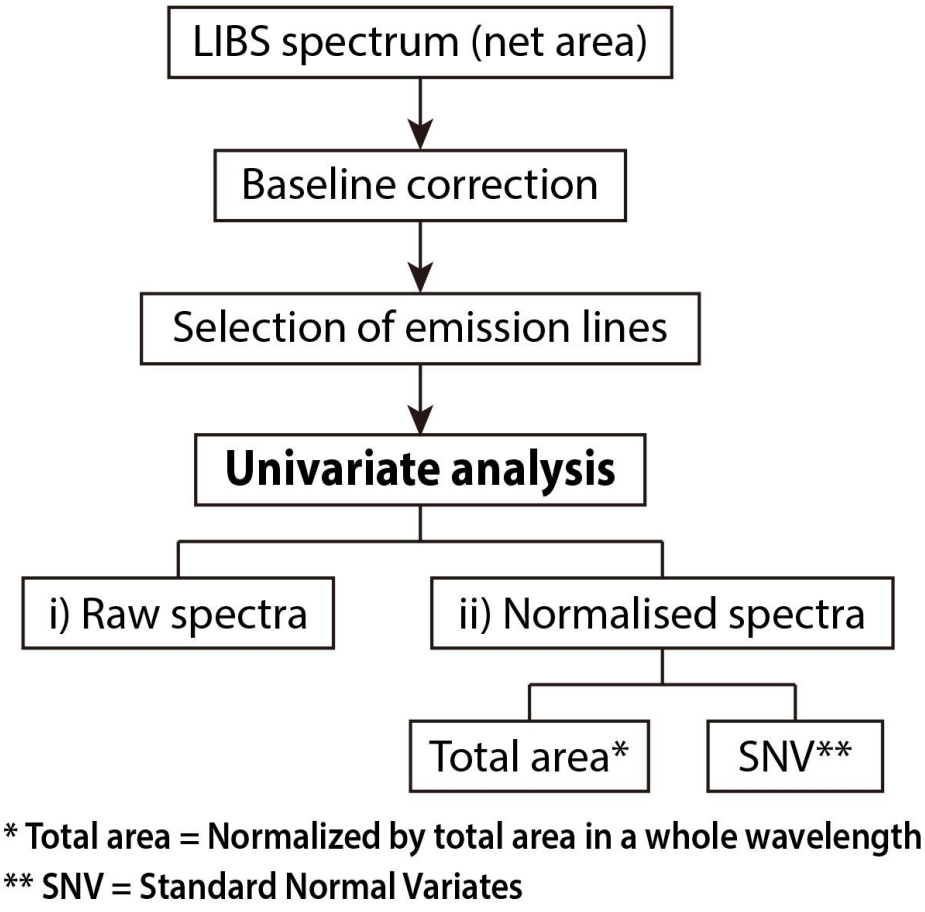

Fig. 35. Schematic diagrams of the procedure for univariate calibration.

LIBS spectra are commonly normalized to take into account signal fluctuations and thus obtain enhanced analytical performance. However, this does not indicate that normalized data always provide better analytical performance than uncorrected ones (Guezenoc et al., 2019). In univariate calibration, therefore, the peak area from both normalized and uncorrected data are systematically compared with the elemental concentration acquired from chemical analyses

to select the best analytical performance (**Fig. 35**). For each model, the baseline-subtracted signal was plotted on the vertical axis as a function of the concentration of the analyte on the horizontal axis in three cases: i) without normalization; ii) after normalization to the total area of the spectrum; iii) after normalization by SNV. In the case of normalization to the total area, for each LIBS spectrum, the peak intensity value of the emission line related to the analyte is divided by the value of area of the spectrum over the whole spectral range. SNV calculation is processed on each spectrum individually by centring the spectrum on the mean value and then dividing the corrected spectrum by the standard deviation of the original spectrum (Eqs. (2), Guezenoc et al., 2019).

$$\mathbf{I_{SNV}\ (\lambda)} = \frac{I_{Raw} - I_{Mean}}{\sigma} \tag{2}$$

To work towards understanding the relationship between the elemental concentrations and between the peak area, the determination coefficient (R^2) which is a simple and common univariate statistical model was given by:

$$\mathbf{R^2} = \mathbf{1} - \frac{\sum_{i=1}^{N}(\hat{y}_i - y_i)^2}{\sum_{i=1}^{N}(\hat{y}_i - \bar{y}_i)^2} \tag{3}$$

where $\hat{y}_i$ represents the reference values of concentration, y_i the predicted ones, and $\bar{y}$ the average value of $\hat{y}_i$ over N samples in the dataset. This regression formulation only takes into account observational errors in the dependent variable and could therefore be effective for the calibration dataset and for cross-validation. However, since the R^2 is definitely not sufficient to assess the predictive ability of a model, another model assessment was necessary to support the estimation of accuracy for a quantitative method. The root mean square error (RMSE) and mean absolute error (MAE) are the most widely used measures of forecast accuracy, but they are all scale-dependent measures because their own scale depends on that of the data. Therefore, these models are insufficient for this study to compare the integrated area from either normalized or uncorrected LIBS spectrum, each of which has a different scale.

Mean absolute percentage error (MAPE) is commonly used as a non-scale dependent measure but has the significant disadvantage of producing infinite or undefined values for zero or close-to-zero actual values, which correspond to the peak area. To address this issue linked to MAPE, the mean arctangent absolute percentage error (MAAPE) proposed by Kim and Kim

in 2016 was used in this study as an alternative statistical function of forecast accuracy, which is defined in Eqs. (4),

$$\mathbf{MAAPE} = \frac{1}{N}\sum_{1}^{N}(\boldsymbol{AAPE_t}) \quad (4)$$

where N is the number of samples

$AAPE_t = \arctan\left(\left|\frac{A_t - F_t}{A_t}\right|\right)$.

where At and Ft represent the actual and forecast values at the sample t, respectively. Ideally, the R2 value should be equal to 1, while the MAAPE value is equal to 0.

2.3.2. Emission line selection

The raw LIBS spectra, which is the sum of the spectra obtained in a single point of the grid pattern, are acquired from the integral software of Z300. It should be prioritized for quantitative analysis to select each key atomic line (i.e., Na and Mg) exhibiting linear correspondence to the peak area and the elemental concentration. The criteria for the selection of the emission lines are as follow: under-saturated and minimum self-absorption; good signal to noise ratio (SNR); avoiding spectral interference; intensity variation with the elemental concentration (Haddad et al., 2014). These criteria allowed most candidates to be readily excluded. The candidate lines commonly used in previous studies with respect to Na and Mg are listed in **Table 9**. This method requires assigning each peak of the LIBS spectra to the corresponding element in agreement with the NIST or AtomTrace databases.

In the case of Na, representative emission lines are divided into three groups: one peak around 330 nm and two sets of doublet near 589 nm and 819 nm, respectively. Because the emission line at 330 nm is not intense enough to compare the peak area, univariate regression using only two regions of the doublet is carried out by comparing the changes in sodium concentration (**Fig. 36**). Univariate calibrations after SNV normalization show that the doublet near 589 nm is saturated assumed by self-absorption despite the most intense and prominent emission line (**Fig. 37**). However, the region near 819 nm displays a near-linear correlation coefficient (R^2) of 0.97 with compositional variation without spectral interference. Therefore, this region is selected as the representative emission line in terms of sodium (Na).

Table 9. Candidate emission lines for Na and Mg used in previous studies.

Emission line	Wavelength (nm)	Reference
Na I	330.24	[1]
Na I	589.00	[2], [3], [4], [5], [6]
Na I	589.59	[1], [2], [4]
Na I	818.33	[6], [7]
Na I	819.48	[6], [7]
Mg I	277.67	[8]
Mg II	279.55	[1], [2], [5], [6], [9]
Mg II	279.80	[1], [4]
Mg II	280.27	[2], [4]
Mg I	285.21	[2], [3], [4]
Mg I	383.33	[1]
Mg I	516.73	[4]
Mg I	517.27	[4], [5]
Mg I	518.36	[4], [10]

[1] Harmon et al. 2019; [2] Díaz Pace et al. 2011; [3] Fontana et al. 2021; [4] Lasheras et al. 2020; [5] McMillan et al. 2007; [6] Singh et al. 2017; [7] Li et al. 2018; [8] de Carvalho et al.; [9] Hausmann et al. 2017; [10] Lanza et al. 2010.

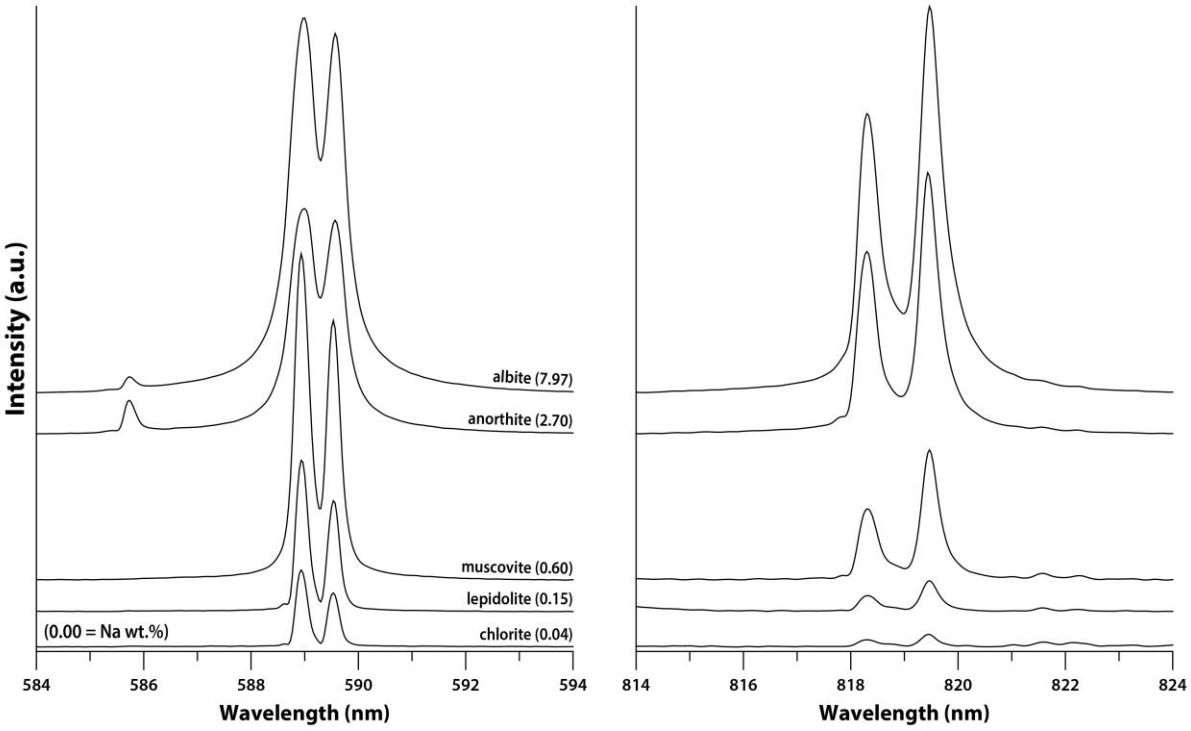

Fig. 36. Two regions of interest for Na from the SNV corrected LIBS spectra from different silicate minerals containing different Na concentrations.

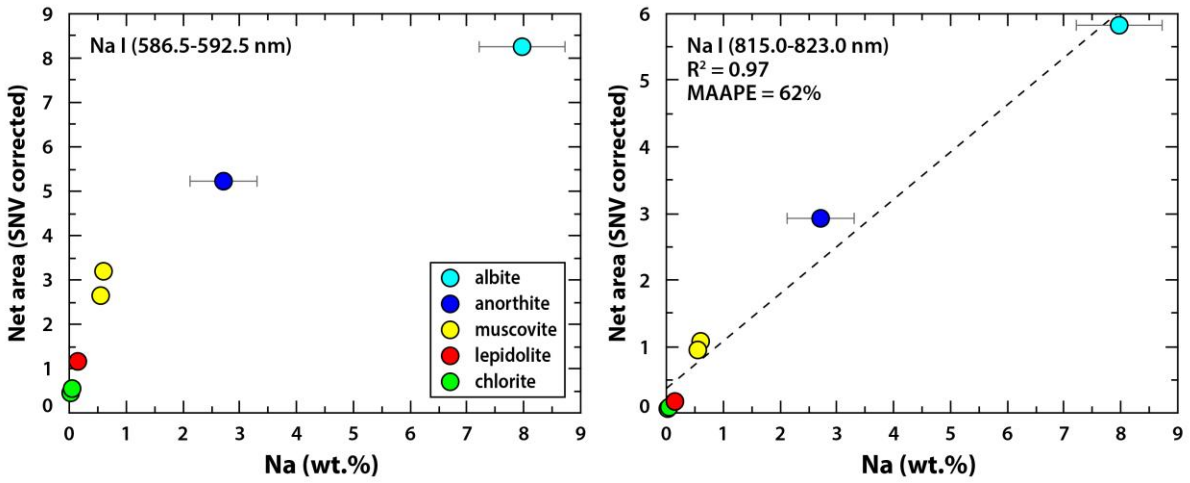

Fig. 37. Scatter plots from LIBS SNV corrected spectra for peak areas of the 589 nm and 819 nm doublets vs. Na concentration.

Regarding Mg, all nine emission-line candidates in previous studies correspond at least one reason in the criteria of the line selection above, so they are excluded from the subsequent study. For example, the magnesite sample in **Fig. 38** shows a dip at the peak of the Mg emission line at 285.21 nm. This dip, known as "self-reversal", is produced by the concomitance of a temperature gradient and an electron density gradient in the plasma (Rezaei et al., 2020). The self-reversal can give rise to a doubt of two lines and interfere with LIBS quantitative analysis. Furthermore, this region has spectral interference with the atomic emission line of Fe I 285.18 nm. In this reason, the siderite sample has the most intense peak in spite of low Mg content (2.17 wt.%) (**Fig. 38**). In this study, therefore, three newly confirmed lines (293, 310 and 810 nm) are compared to the elemental concentration for univariate analysis.

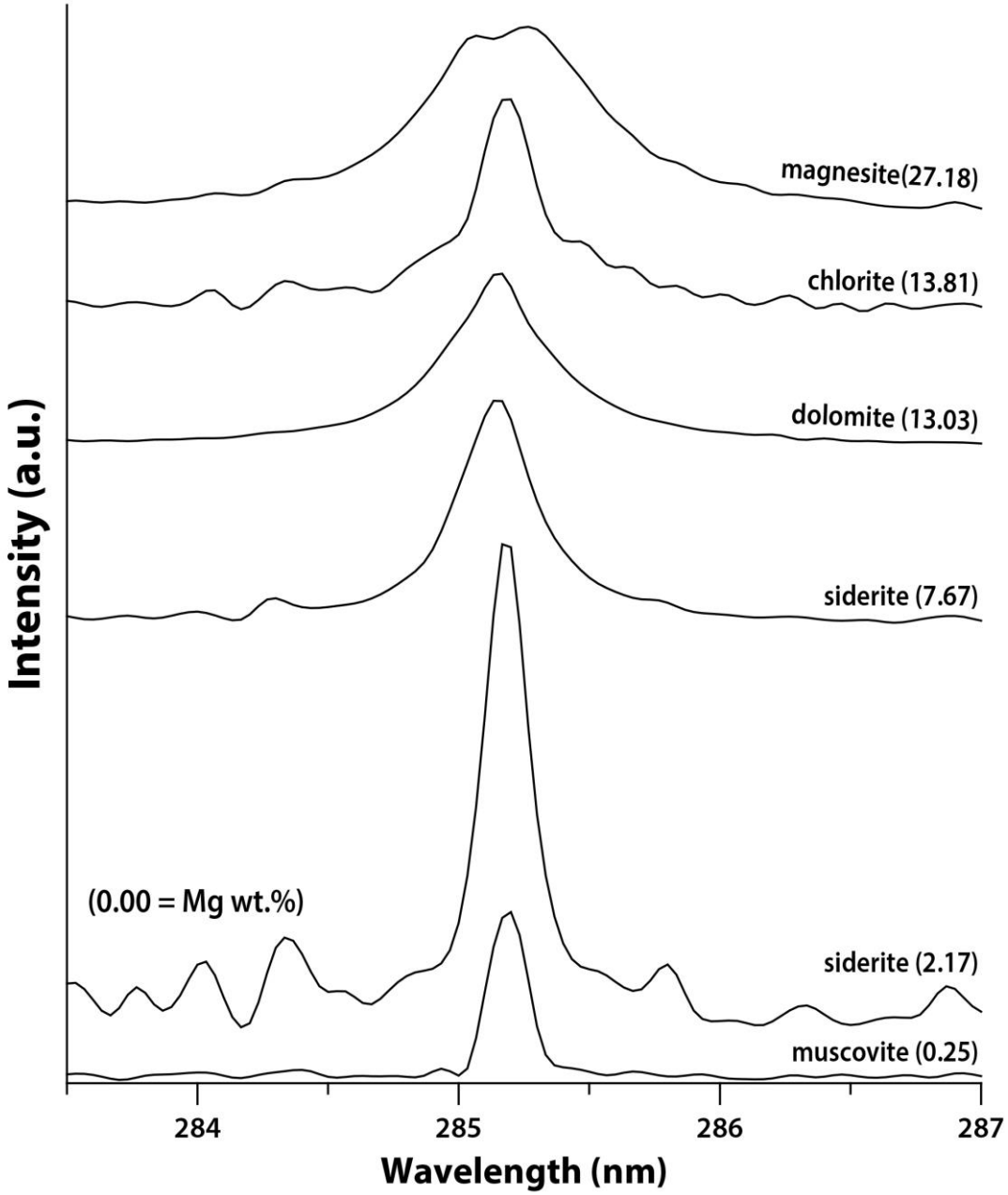

Fig. 38. SNV corrected LIBS spectra of the emission line at 285 nm from carbonate and silicate minerals.

2.4. Results of univariate analysis

2.4.1. Sodium (Na)

Fig. 39 shows the average peak area of the Na emission line in the region of 819 nm obtained by using the handheld LIBS analyser versus Na concentration verified by chemical analyses such as EPMA and ICP-OES. The vertical error bars correspond to the Relative

Standard Deviation (RSD) of the peak information calculated over 5 locations containing each of the 15 analysed zones. The horizontal error bars represent the error range of the different concentrations obtained from EPMA. A linear fit was performed in order to obtain a calibration curve model. The calibration models built from three different emission lines; i) uncorrected (i.e., the baseline subtracted) peak area value, ii) normalization by the total area of the spectrum, c) normalization by SNV. As a result, all the linear calibration curves in Na show high R^2 values higher than 0.97 regarding all the variables, either normalized or uncorrected data. This result is satisfactory given the different compositions of samples.

In addition to the linear regression coefficient, the quality of the calibration curve is gauged from the MAAPE of the predicted Na contents. Each calibration curve of Na displays a linear correlation between LIBS data and Na concentration with a high R^2 value (0.97) in all the variables with similar MAAPE (~60%) (**Fig. 39**).

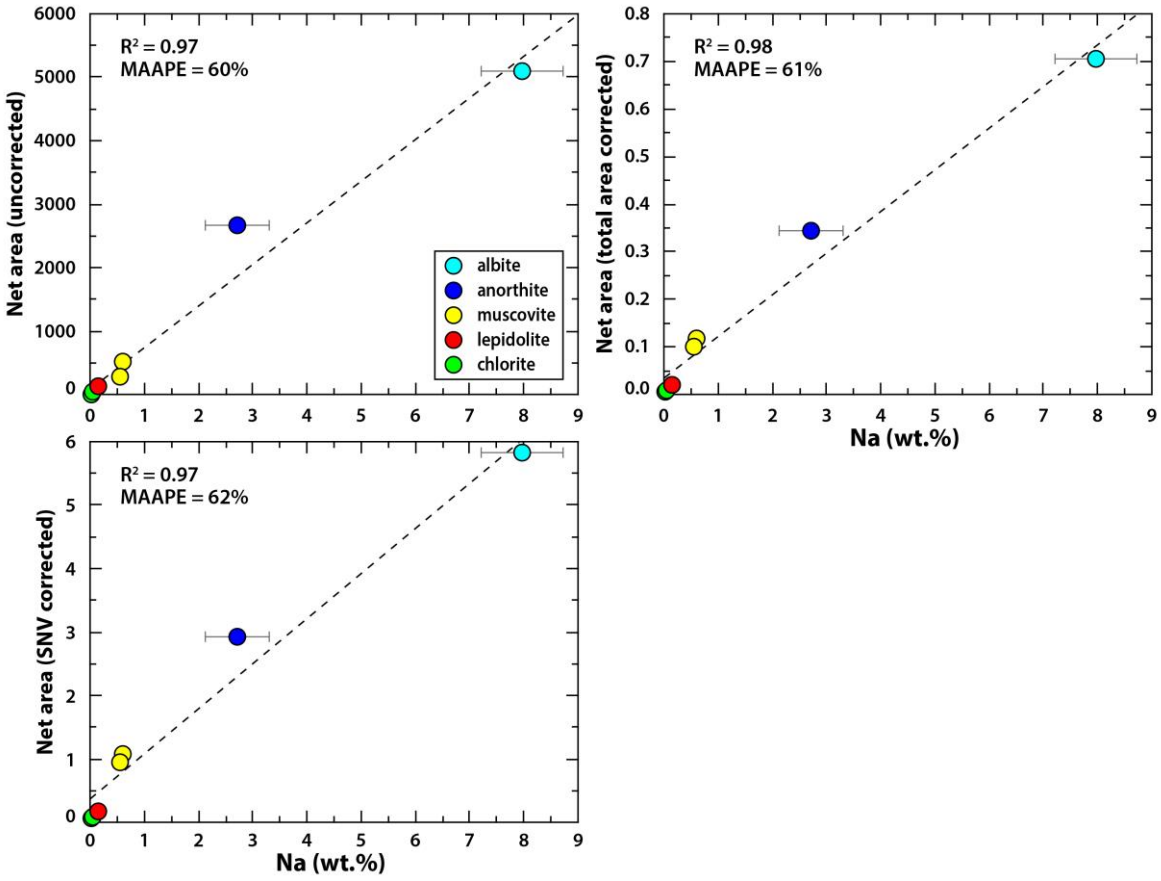

Fig. 39. Calibration curves between emission lines from the three extraction methods and the Na concentration.

2.4.2. Magnesium (Mg)

The univariate calibration model for Mg was built from a set of 11 samples consisting of phyllosilicates and carbonate minerals. **Fig. 40** shows the diagnostic Mg emission lines appearing in the form of a single peak at Mg (II) 292.86 nm, Mg (I) 309.69 nm, and Mg (I) 880.68 nm, different from the Na emission lines in the form of doublet, in the LIBS emission spectrum concerning different Mg concentrations of minerals. Both peaks at 292.86 and 309.69 nm show the potential for spectral interference due to the peaks of other elements nearby them, while the other peak at 880.68 nm shows only a single peak without the presence of another peak around it.

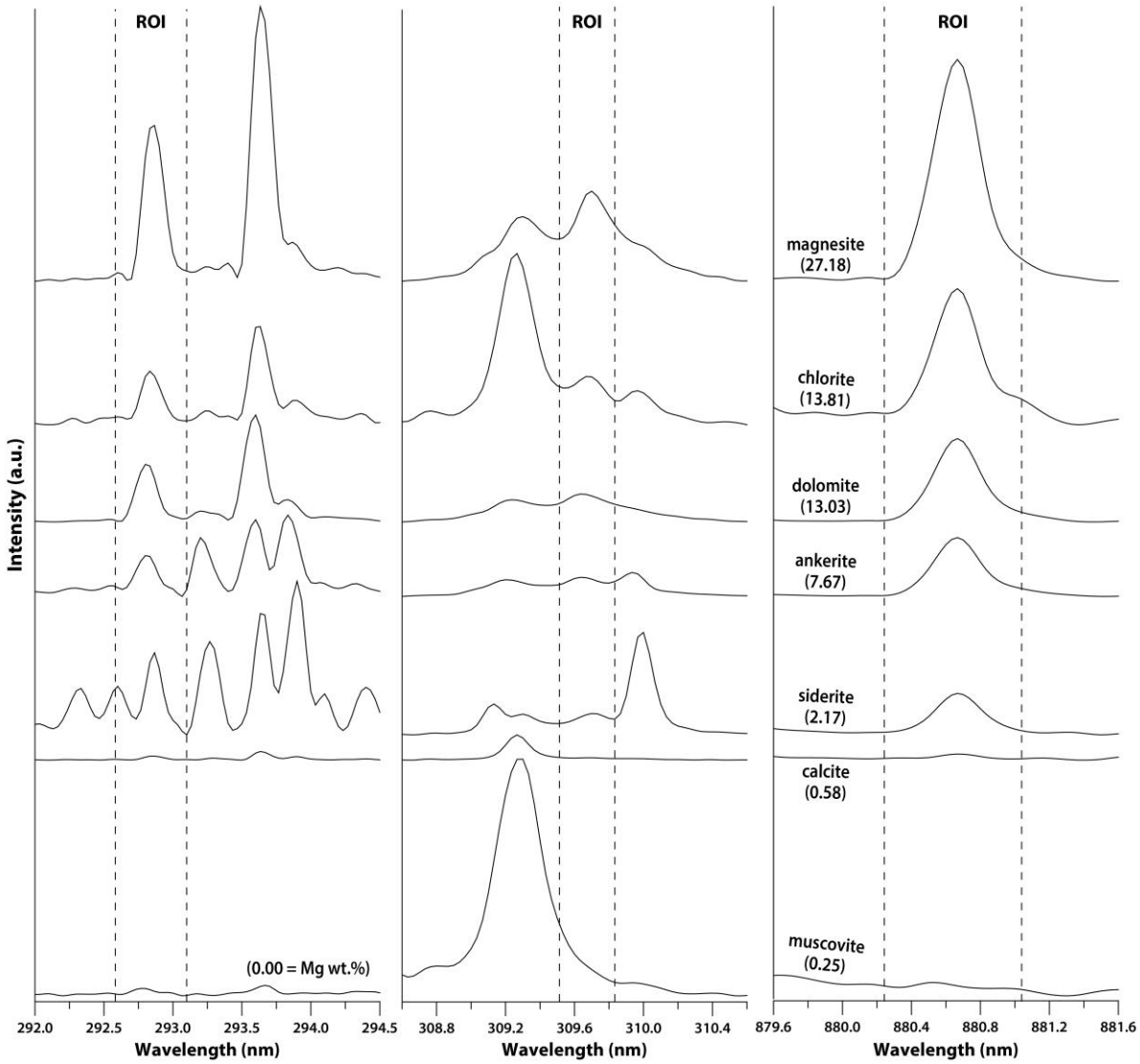

Fig. 40. Three regions of interest for Mg in the LIBS emission spectra after SNV normalization.

Fig. 41 shows that all the R^2 values, regardless of the emission lines, are generally higher after normalization in agreement with the a priori expectation. It is noted that considering a range of calibration from 0 to 27 wt.% of Mg concentration, six of the total eleven samples for the calibration set correspond to concentration values lower than 2.5 wt.%. Furthermore, there is no correlation between the LIBS signal and the concentration values for these samples, whatever the normalization process. In such conditions, the increase of the R^2 from the uncorrected data to the normalized data should be considered with caution since the regression models over the full concentration range are, in this cause, not robust. Indeed, none of the samples from the calibration set is between 2.5 and 8 wt.% and between 18 and 27 wt.%. In such conditions, the coefficient of determination value is highly sensitive to extreme samples, considered as outliers (Taylor, 2018).

In the region of 292.86 nm, the correlation coefficient has the lowest value of 0.68 from the uncorrected data, and the correlation coefficients are 0.86 and 0.82 when the spectral data are normalized by total area and SNV, respectively (**Fig. 41**). Similar MAAPE values exhibit between 65% and 69% among the three LIBS parameters. The regressions in this region show that the quality and correlation of peak area to Mg concentration within natural samples is poor compared to the other emission lines present afterwards.

Each calibration curve from the region at 309.69 nm displays diverse R^2 values, exhibiting the lower value (0.79) in the uncorrected data than the highest value (0.83) in both normalized data (**Fig. 41**). MAAPE values vary diversely that the values from the uncorrected and normalized by total area have 61% and 64%, while the SNV data has a better MAAPE value (54%). The calibration obtained from this region is not sufficient for Mg quantification due to overlapping among emission lines of different elements. Thus, the Mg peak from the magnesite and dolomite sample has a doublet in contrast to chlorite, ankerite, and siderite with a triplet (**Fig. 40**). Furthermore, the muscovite sample shows an intense titanium (Ti II) emission line at 308.80 nm overlapped with the Mg emission line.

The univariate calibration curves from the region at 880.68 nm show the highest R^2 value over 0.95 from both normalized data with different MAAPE (i.e., 64% for the normalized by total area, and 54% for SNV) compared to the other emission lines above (**Fig. 41**). Thus, the univariate model used peak integration using SNV normalized data from this region shows the

best result obtained by comprehensively analysing both cross-validation (R^2) and prediction accuracy (MAPPE) value for Mg quantification.

2.5. Conclusion

LIBS spectrum is typically normalized to take into account signal fluctuations and thus obtain enhanced analytical performance. Nevertheless, since normalization in LIBS may not always provide the best analytical performance in some cases, this study comprehensively investigated the optimal emission lines with different spectral types for the quantification of sodium (Na) and magnesium (Mg). After baseline correction, three different LIBS spectra were used in this study: i) non-normalized, ii) normalized by total area, and iii) SNV normalization. It is emphasized that high cross-validation (R^2) values with similar MAAPE values appear in both uncorrected and normalized LIBS data in the region of the Na doublet near 819 nm. However, for magnesium emission lines, the univariate models from both normalized data are better correlated with elemental concentration than the uncorrected data. Among three regions of the Mg emission lines, the best R^2 value showed in the 880 nm region corresponding to the visible region, especially the best prediction accuracy (MAAPE) value appears in the LIBS data after SNV normalization. These results indicate that spectral normalization after baseline correction is preferred for more accurate quantification of sodium and magnesium by minimizing the potential matrix effect of each sample. Furthermore, these calibration curves can be applied to various mineral classes such as silicates and carbonates. The result of the univariate analyses in this study suggests the potential of quantifying lithium and magnesium in the material and comparing elemental concentration among minerals classified through the decision tree. Particularly, these calibrations can provide critical evidence for decision making in the field by identifying the compositional changes in the same mineral classes such as plagioclases, phyllosilicates, and carbonates which can be geologically important indicators.

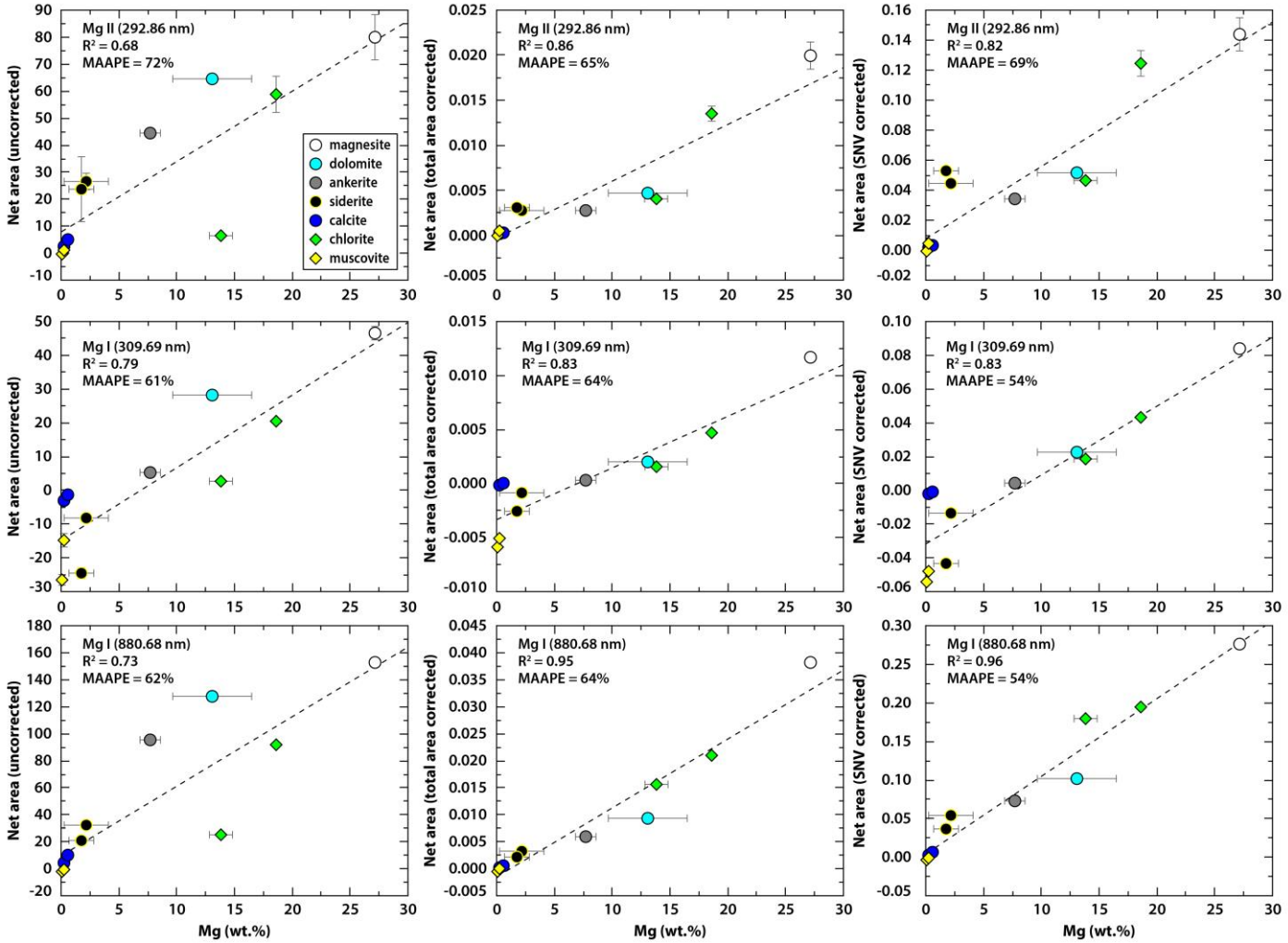

Fig. 41. Calibration curves between emission lines from the three extraction methods and the Mg concentration

Chapter IV. Carbonate mineral identification and quantification

Carbonate minerals are formed by the combination of a $(CO_3)^{2-}$ ion with various monovalent or divalent cations. There are approximately 60 known carbonates minerals and the commonest rock-forming carbonate minerals within the trigonal crystal system are calcite ($CaCO_3$), magnesite ($MgCO_3$), siderite ($FeCO_3$), rhodochrosite ($MnCO_3$), dolomite ($CaMg[CO_3]_2$), and ankerite ($Ca[Fe,Mg,Mn][CO_3]_2$) (Deer et al., 2013). Carbonate rocks act as reservoirs in sedimentary rocks and can also be host rocks related to numerous metalliferous ore deposits in magmatic, hydrothermal, or sedimentary contexts (Ridley, 2013). As carbonates are one of the minerals which can be prone to be altered according to geological activities, understanding the compositional changes in carbonate minerals is important as is the spatial distribution of alteration zones in detail surveys (Pirajno, 2009). Therefore, mineral discrimination and quantitative analysis of carbonate minerals act as important indicators in mineral resource exploration. In particular, the composition of carbonates, which are widely distributed in near-surface environments as a host rock related to numerous metalliferous ore deposits, are easily changed by thermal sources due to strong solubility in high-temperature hydrothermal fluids, and also much faster dissolvability than silicate minerals at similar temperatures (Ridley, 2013). Thus, this mineralogical characteristic can be used as a pathfinder to locate hidden ores. However, in the field, numerous carbonates may display similar characteristics in colour, grain size, and texture, and a series of changes in composition also make it complicated to discriminate between them with the naked eye.

A geological model of the Elvira Volcanogenic Massive Sulphide (VMS) deposit in the South-Eastern Iberian Pyrite Belt (IPB) is currently being developed by the Consejo Superior de Investigaciones Cientificas (CSIC) and the Minas de Aguas Teñidas SAU (MATSA) mining company in the NEXT (New Exploration Technologies) project (G.A. No. 776804), funded by the European Union's Horizon 2020 research and innovation programme. The hydrothermal carbonates associated with the ores in Sotiel-Migollas, which is the eastward continuation of the Elvira deposit, show a systematic variability according to depth with a predominance of dolomite in the deepest part under the ore, which is gradually replaced by ferroan dolomite in the intermediate zone to ankerite and even siderite in the shallowest part (Gisbert et al., 2019; Velasco-Acebes et al., 2019). Therefore, quick identification of carbonates in the field can be

effectively used as a discriminant parameter as an inexpensive and fast guide to determine the implication for ore mineralization in hidden ore explorations.

This study focuses on spectral identification and quantification of carbonate minerals, one of the indicative minerals in the Elvira deposit, using Raman, MIR, and handheld LIBS as well as other portable spectroscopic techniques such as XRF, VNIR-SWIR, and XRD. This means that access to the carbonate composition in the field is of great interest for geologists wishing to better deal with a potential mineral deposit. Recent developments of lightweight portable spectroscopic tools have provided useful information for non-experts or in situations where geological interpretation is difficult, e.g., obscure alteration zones or rocks including opaque minerals in the field.

1. Identification and composition of carbonate minerals of the calcite structure by Raman and infrared spectroscopies using portable devices

This part shows the identification and composition determination of carbonate minerals in the calcite group using their spectral properties in the Raman and infrared spectra. The systematic study comparing the band positions with elemental ratios focuses on selecting the most suitable spectral region and ratio for carbonate discrimination, suggesting the possibility of portable Raman and IR spectroscopy in the field. This part was published in Spectrochimica Acta Part A: Molecular and Biomolecular Spectroscopy in 2021. Therefore, it is noted that some parts of the introduction and methods can be repeated with the previous paragraphs.

Spectrochimica Acta Part A: Molecular and Biomolecular Spectroscopy 261 (2021) 119980

Contents lists available at ScienceDirect

Spectrochimica Acta Part A: Molecular and Biomolecular Spectroscopy

journal homepage: www.elsevier.com/locate/saa

Identification and composition of carbonate minerals of the calcite structure by Raman and infrared spectroscopies using portable devices

Yonghwi Kim *, Marie-Camille Caumon, Odile Barres, Amadou Sall, Jean Cauzid

GeoRessources Laboratory –Université de Lorraine, Faculté des Sciences et Technologies, BP 70239, F-54506 Vandœuvre-lès-Nancy, France

HIGHLIGHTS

- Characterization of carbonate minerals by using portable Raman and IR instruments.
- Identification and composition determination of Ca-Mg-Fe-Mn carbonate minerals.
- Elemental variation in carbonates using band shifts in Raman and infrared spectra.

GRAPHICAL ABSTRACT

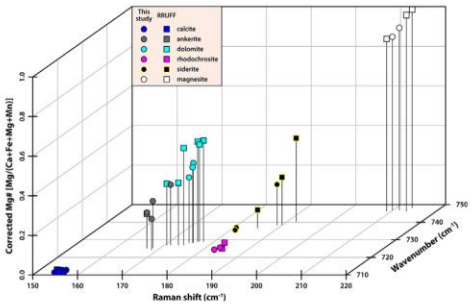

ARTICLE INFO

Article history:
Received 9 February 2021
Received in revised form 20 April 2021
Accepted 17 May 2021
Available online 26 May 2021

Keywords:
Qualitative analysis
Carbonate minerals
Raman spectroscopy
Infrared spectroscopy
Portable spectrometers

ABSTRACT

A portable Raman device with a 532 nm excitation laser and a portable infrared spectrometer with ATR (Attenuated Total Reflection) mode were used to analyse the spectral features associated with the identification and compositional variation of Ca-Mg-Fe-Mn natural carbonate minerals with a calcite structure (calcite, ankerite, dolomite, siderite, rhodochrosite, and magnesite). A systematic study of the variations of the peak positions with various compositional ratios was carried out. Most of the band positions were shifted to lower wavenumbers with increasing ionic radius or atomic mass of the divalent cations but the band of the translational lattice (T) mode in Raman and the symmetric bending (ν_4) band in the mid-infrared were the most sensitive. Therefore, the elemental variation of the Ca-Mg-Fe-Mn ratio in this carbonate series can be estimated from Raman and infrared band positions from spectra acquired with portable spectrometers.

1. Introduction

Carbonate rocks act as reservoirs in sedimentary rocks and can also be host rocks related to numerous metalliferous ore deposits in magmatic, hydrothermal, or sedimentary contexts [32]. As carbonates are one of the minerals which can be prone to be altered according to geological activities, understanding the compositional changes in carbonate minerals is important as is the spatial distribution of alteration zones in detail surveys [29]. For example, a geological model of the Elvira Volcanogenic Massive Sulfide (VMS) deposit in the south-eastern Iberian Pyrite Belt (IPB) is currently being developed in the framework of the NEXT (New Exploration Technologies) project (G.A. No. 776804) funded by the European Union's Horizon 2020 research and innovation programme. The hydrothermal carbonates associated with the ores in Sotiel-Migollas, which is the eastward continuation of the Elvira deposit, show a systematic variability according to depth with a predominance of dolomite in the deepest part under the ore, which is gradually replaced by ferroan dolomite in the intermediate zone

* Corresponding author.
E-mail address: yonghwi.kim@univ-lorraine.fr (Y. Kim).

https://doi.org/10.1016/j.saa.2021.119980
1386-1425/

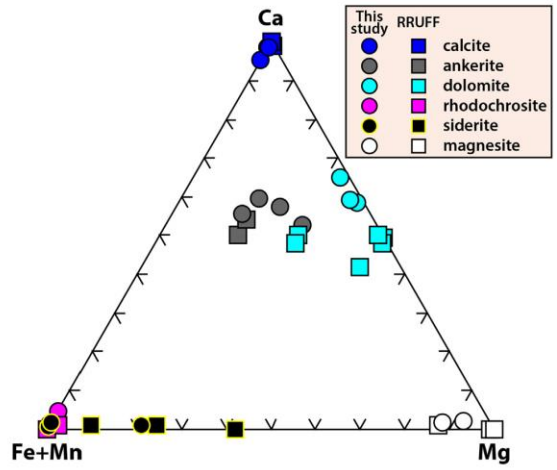

Fig. 1. Chemical composition of monomineralic carbonate samples plotted in the Ca-Mg-Fe + Mn ternary diagram.

to ankerite and even siderite in the shallowest part [13,36]. Therefore, quick identification of carbonates in the field can be effectively used as a discriminant parameter as an inexpensive and fast guide to determine the implication for ore mineralization in hidden ore explorations.

XRD (X-ray Diffraction), VNIR-SWIR (Visible, Near-InfraRed and ShortWave-InfraRed), Raman and FTIR (Fourier-Transform Infra-Red) spectroscopies have commonly been used for the mineralogical determination of carbonate minerals [6,12,19,34]. However, some of these techniques present several limitations. XRD analysis is often time-consuming and requires extensive sample preparation. Therefore, analysis needs lengthy experimental and evaluation time despite being one of the most common and reliable techniques for mineralogical characterization. In VNIR-SWIR spectroscopy, the carbonate minerals have a main band located between 2300 and 2400 nm. However, qualitative analysis is difficult due to overlapping with the absorption bands of the hydroxyl-bearing minerals in this region [30]. Furthermore, the carbonate bands can be disturbed by water, which has a strong signal in the SWIR region near 1900 nm. Raman and FTIR spectroscopies, however, are useful techniques for carbonate identification. These are non-destructive methods that require little or no sample preparation. Moreover, all the bands related to carbonates in the mid-infrared region have characteristic positions which make it easy to differentiate from other minerals [3,38]. Raman and FTIR analyses of carbonates have long been used in mineralogical and geochemical research but newly developed portable devices are reliable, fast, and economic tools that allow new applications [18,33]. Furthermore, Raman and IR spectroscopies for archaeometral and mineralogical applications associated with cultural heritage materials provide more important practical information on both the proper conservation but reconstruction of damaged ancient objects and paintings that have lost their original appearance [2,20]. Remote-sensing Raman and IR techniques that can be measured at a long distance have been installed in the SuperCam instrument on the Mars 2020 Rover, Perseverance, to attempt to recognize carbonates, silicates, sulfates, and, phosphates [39]. This shows that carbonate discrimination using Raman and IR spectroscopies has continued to expand the field of its research applications in diverse ways.

Carbonate minerals are constituted by the combination of one $(CO_3)^{2-}$ ion and various monovalent or divalent cations. Rhombohedral carbonates such as calcite, magnesite, siderite, and rhodochrosite crystallize in the R-3c group [14]). Dolomite and ankerite minerals are structurally similar to the rhombohedral carbonates (R-3 group) but with different site symmetry due to substitutions by divalent atoms such as Ca, Mg, Fe, and Mn in the crystal structure. Despite this site symmetry difference, the molecular symmetry as observed by Raman and infrared spectroscopy is not affected [1]. The minerals in these carbonate groups have six active modes; four internal vibrations within the $(CO_3)^{2-}$ unit and two external vibrations of the crystal lattice which involve translational and rotational oscillations of a carbonate group [16,23]. Previous Raman studies have demonstrated this tech-

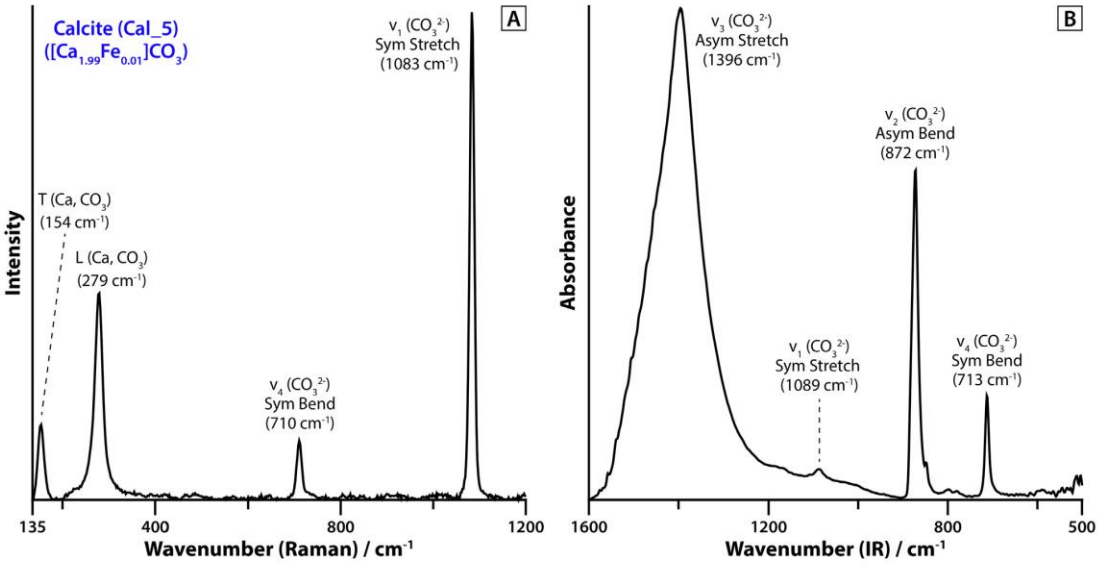

Fig. 2. A) Raman spectrum and B) infrared spectrum (ATR mode) of calcite.

nique's capacity to characterize carbonates but only for a few groups of solid solutions using laboratory devices [3,5,9,28,33,34]. First carbonate identification using calcite under field conditions by portable Raman instruments was reviewed by Jehlička et al. [22]. Previous portable Raman studies showed latent possibilities by determining Raman peaks in various carbonate groups, but these handheld spectrometers used in the studies were equipped with red to near-infrared diode lasers excitation only, not considering a green laser excitation [21,37]. For this reason, decreased sensitivity and limited spectral range can result from near-infrared excitation despite fluorescence suppression. Furthermore, no comprehensive comparison among all rhombohedral carbonates has been carried out by a portable Raman instrument.

Some carbonate minerals have also been investigated by infrared spectroscopy [1,4,8,19,27,38]. However, the studies were limited to a few minerals, and only took measurements with a transmission technique using pellets prepared with potassium bromide (KBr). This is hardly feasible in field conditions due to the hygroscopy of KBr. Spectral comparisons using both Raman and infrared spectroscopies were carried out by Gunasekaran et al. [15], but calcite and dolomite were the only minerals studied and these were analysed with a laboratory device. To date, no study has reported using a combination of a portable Raman and a portable IR instrument for the identification and characterisation of the carbonate minerals in the calcite structure.

This study aimed to obtain an optimized methodology to discriminate between different carbonates during field analyses by using Raman and IR spectroscopies. For this study, a set of monomineralic carbonate minerals in the Ca-Mg-Fe-Mn system were measured by portable Raman and IR spectrometers. The band shifts were associated with mineralogical and compositional changes to determine the most reliable parameters and methodology.

2. Materials and methods

2.1. Materials

2.1.1. Samples

Two sets of samples were used in this study. The first set consisting of 20 carbonate samples was analysed using atomic absorption spectroscopy (A800; Perkin Elmer, Norwalk, CT) to determine their elemental composition in Si, Mg, Ca, Mn and Fe. The elemental data were then used to calibrate the pXRF values. Among these samples, 7 were taken out of the subsequent study for at least one

Table 1
Position of the bands (cm^{-1}) in the Raman and infrared spectra and Mg# calculated from the corrected pXRF data.

Sample	Group	Raman				Infrared			Mg#**
		E_g (T)	E_g (L)	E_g (ν_4)	A_{1g} (ν_1)	ν_4	ν_2	ν_3	
Cal_1	calcite	154	280	711	1084	712	872	1395	0.00
Cal_2	calcite	154	280	710	1085	712	871	1396	0.00
R040070*	calcite	154	281	712	1086	712	872	1394	0.01
Cal_3	calcite	154	280	711	1084	713	872	1395	0.00
Cal_4	calcite	154	280	710	1085	712	871	1394	0.00
R050009*	calcite	155	280	712	1086	712	872	1396	0.00
R050048*	calcite	155	280	712	1086	712	872	1394	0.00
R040170*	calcite	155	279	711	1086	712	872	1398	0.01
R050307*	calcite	155	281	712	1086	712	872	1394	0.00
Cal_5	calcite	155	281	711	1086	713	872	1396	0.00
R050127*	calcite	156	282	713	1087	712	872	1394	0.00
R050130*	calcite	156	282	713	1087	712	872	1394	0.00
Cal_6	calcite	156	281	710	1085	713	872	1396	0.00
Ank_1	ankerite	167	285	718	1091	726	873	1416	0.18
R050181*	ankerite	167	281	721	1092	725	870	1408	0.18
R050197*	ankerite	168	283	721	1092	–	–	–	0.18
Ank_2	ankerite	168	289	719	1090	726	873	1405	0.23
Ank_3	ankerite	169	287	721	1091	724	871	1412	0.16
Ank_4	ankerite	171	291	721	1092	727	874	1419	0.30
R050129*	dolomite	171	289	721	1094	727	876	1410	0.31
R050272*	dolomite	173	294	722	1095	727	874	1412	0.32
R050370*	dolomite	174	296	723	1096	727	874	1408	0.49
Dol_1	dolomite	175	300	722	1096	728	877	1418	0.33
Dol_2	dolomite	176	298	721	1095	728	877	1418	0.38
Dol_3	dolomite	176	298	724	1096	729	877	1419	0.40
R040030*	dolomite	176	300	724	1099	729	877	1425	0.51
R050357*	dolomite	177	300	724	1099	729	877	1419	0.49
R050241*	dolomite	178	301	725	1099	729	881	1435	0.51
Sd_1	siderite	181	280	726	1082	737	862	1403	0.00
Sd_2	siderite	181	283	729	1083	736	862	1403	0.00
R050349*	siderite	185	286	729	1086	737	862	1400	0.09
Sd_3	siderite	189	293	730	1085	738	865	1405	0.21
R040034*	siderite	190	294	730	1088	739	866	1406	0.24
R050262*	siderite	192	296	731	1089	741	866	1410	0.42
Rds_1	rhodochrosite	183	287	717	1083	724	861	1394	0.00
Rds_2	rhodochrosite	183	290	716	1083	726	860	1397	0.00
R050019*	rhodochrosite	184	288	718	1085	725	860	1392	0.00
R040133*	rhodochrosite	184	289	718	1085	726	860	1398	0.02
R050676*	magnesite	209	324	737	1093	746	877	1427	0.87
Mgs_1	magnesite	210	325	734	1092	747	879	1426	0.88
Mgs_2	magnesite	211	325	735	1093	747	880	1430	0.92
R040114*	magnesite	213	330	738	1094	746	881	1433	0.99
R050443*	magnesite	213	331	738	1094	748	879	1431	1.00

* reference data from RRUFF[25].
** Mg# (Mg/[Ca + Mg + Fe + Mn]) calculated from corrected pXRF data.

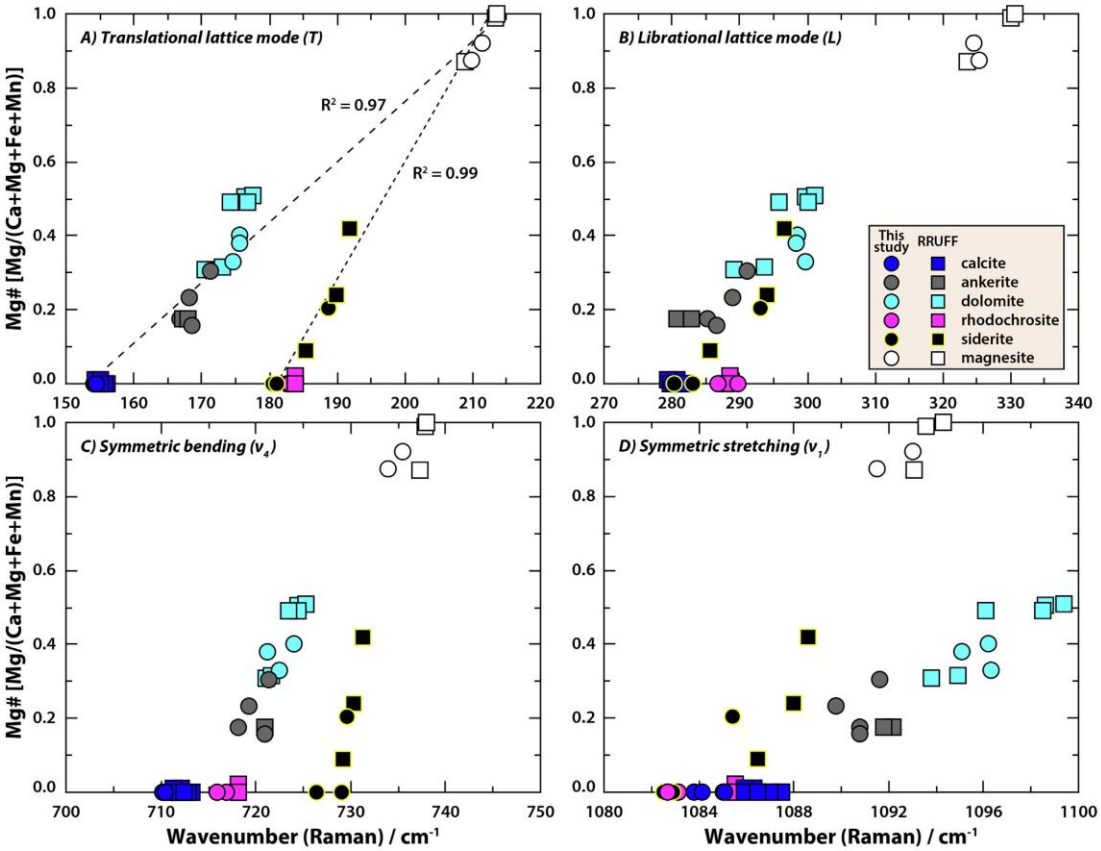

Fig. 3. Correlation between the different peak regions in the Raman spectrum and Mg#. Calibration curves among calcite, ankerite, dolomite, and magnesite (R^2 = 0.97), and between siderite and magnesite (R^2 = 0.99).

of the following reasons: a mixture of several carbonate minerals; out of the expected Raman region for the main carbonate peak; fluorescence during Raman acquisition, and presence of aragonite. The remaining 13 samples were added to 7 extra samples of unchecked elemental composition providing an interpretable Raman signal. In the end, 20 crystals were used, distributed amongst 6 phases covering the most common natural carbonate minerals: calcite ($CaCO_3$), magnesite ($MgCO_3$), siderite ($FeCO_3$), rhodochrosite ($MnCO_3$), dolomite ($CaMg[CO_3]_2$), and ankerite ($Ca[Fe,Mg,Mn][CO_3]_2$).

2.1.2. Sample preparation

The samples were prepared as powders and pellets. ATR spectra were measured on the powders while Raman and portable X-Ray Fluorescence (pXRF) spectra were measured on 13 mm diameter and 2 mm thick pellets prepared by using a 10 tons hydraulic press. Furthermore, raw data files of Raman spectra and infrared spectra in ATR mode which are chemically determined and come from the RRUFF database were added to extend the dataset in this study and compare them with the results from our samples [25].

2.2. Methods

2.2.1. Portable X-ray fluorescence spectroscopy

XRF data were measured with a Thermo Fisher Scientific Niton XL3t GOLDD + handheld spectrometer. The instrument used an Ag-anode X-ray tube with a voltage of 50 kV and was equipped with a silicon drift detector (SDD). The X-ray beam covered a circular area of 8 mm in diameter on the sample. It operated the Main, Low, High, and Light filters with a duration of 30 s for each filter. Each sample was measured 5 times at the same point to obtain statistically reliable data. The spectral data was automatically interpreted using the Mining Cu/Zn mode, which is particularly suitable for measuring lighter elements such as Mg, Al, Si, P, and S. The samples from the RRUFF database were analysed by UA's modified CAMECA SX50 electron microprobe [25]. The elemental concentrations measured by the pXRF device were corrected by drawing calibration curves built by plotting pXRF values against the corresponding values determined by atomic absorption spectroscopy (A800; Perkin Elmer, Norwalk, CT). The cation composition of carbonate standards was plotted in the Mg-Ca-Fe-Mn ternary diagram (Fig. 1). To compare the band positions from Raman and ATR-FTIR spectroscopy with chemical composition, the modified Mg ratio [Mg# = Mg/(Ca + Fe + Mg + Mn)] was used to represent the cation composition in our target minerals.

2.2.2. Portable Raman spectroscopy

Raman spectra were collected using a RaPort portable spectrometer (Enhanced Spectrometry, Inc., San José, CA, United States). This handheld device (weight c. 2 kg) was equipped with a green Nd:YAG laser (532 nm) for excitation with a maximum output power of 30 mW. The minimum spot size was around 15 μm. The spectral range was 130–4000 cm^{-1} at a spectral resolution of 6 cm^{-1}. A baseline was automatically subtracted by EnSpectr soft-

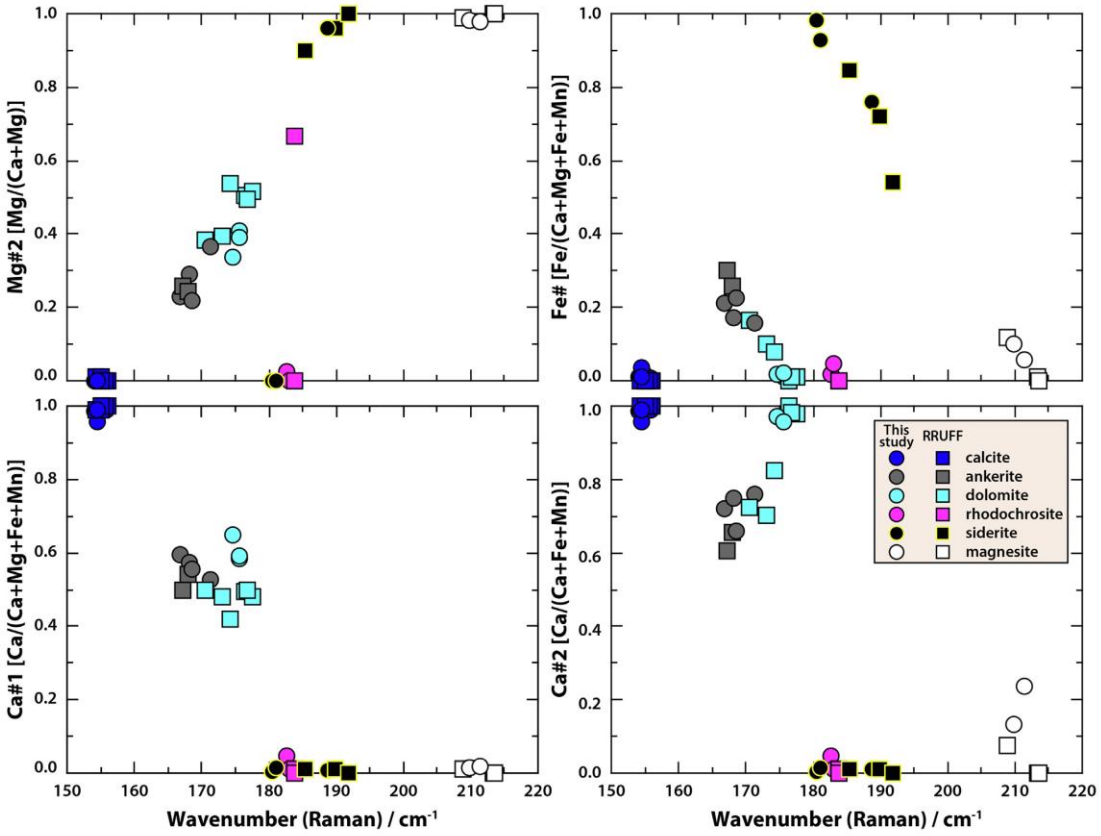

Fig. 4. Correlation between the peak positions in the T mode and the different compositional ratios.

ware. While the total acquisition time was set to 30 s, the number of accumulations and the duration of each individual acquisition were automatically defined. The selection of the peak position was determined by the wavenumber at maximum intensity after two correction steps: i) a baseline correction of the raw spectra by EnSpectr software followed by ii) an automated background removal which was installed in the Crystal Sleuth software [24].

2.2.3. Portable IR spectroscopy

IR analyses in ATR (Attenuated Total Reflection) mode were performed using a portable infrared spectrometer ALPHA (Bruker, Optik GmbH, Ettlingen, Germany). The instrument consisted of a base module with an exchangeable sampling module. The module used for this study was the Platinum ATR module. The IR spectra were obtained on powders placed on a diamond crystal and pressed with an anvil. In this technique, the penetration depth of the infrared radiation is greater at low wavenumbers. The spectra were acquired from 4000 to 500 cm^{-1}, and 24 scans were averaged with a spectral resolution of 2 cm^{-1}.

3. Result

3.1. Raman characterization of carbonate minerals

Calcite structure referred to the D_{3d} group has six Raman active modes in a Raman spectrum [34]. The four prominent peaks in the range 135–1200 cm^{-1} were selected for this study because they are narrow, sharp, and intense. In the Raman spectrum of calcite, for example, the positions of the peak related to translational (T) and librational (L) lattice mode from the external vibration of the CO_3 group are at 154 and 279 cm^{-1} (Fig. 2A). The Raman peaks at 710 and 1083 cm^{-1} are assigned respectively to the out-of-plane bending (ν_4) and stretching (ν_1) internal vibration modes. The $\nu 1$ mode is the most intense, while the ν_4 mode is weaker. The shifts of the peak positions for the different carbonate minerals with diverse mineral chemistries are reported in Table 1. The two peaks of the external modes (T and L) arise from 154 to 214 cm^{-1}, and 279 to 331 cm^{-1}, respectively. The two peaks of the internal modes vary from 710 to 738 cm^{-1} (ν_4) and 1082 to 1100 cm^{-1} (ν_1).

Fig. 3 shows the Raman peak positions plotted against Mg# in order to determine the spectral region which is the most sensitive to compositional variations. Two factors should be considered: the range and the distribution of the peak positions within each group, and the unique characteristic of the relation between peak characteristics and mineral chemistry. The Mg# plotted against the Raman peak positions of the T mode displayed two distinct trend lines from calcite to magnesite on one hand and from siderite to magnesite on the other hand. This mode also shows the largest range of the peak positions (60 cm^{-1}) (Fig. 3A). Furthermore, the distribution of the peak positions for each mineral phase has a small dispersion in the T mode which led to the phases being separated from each other.

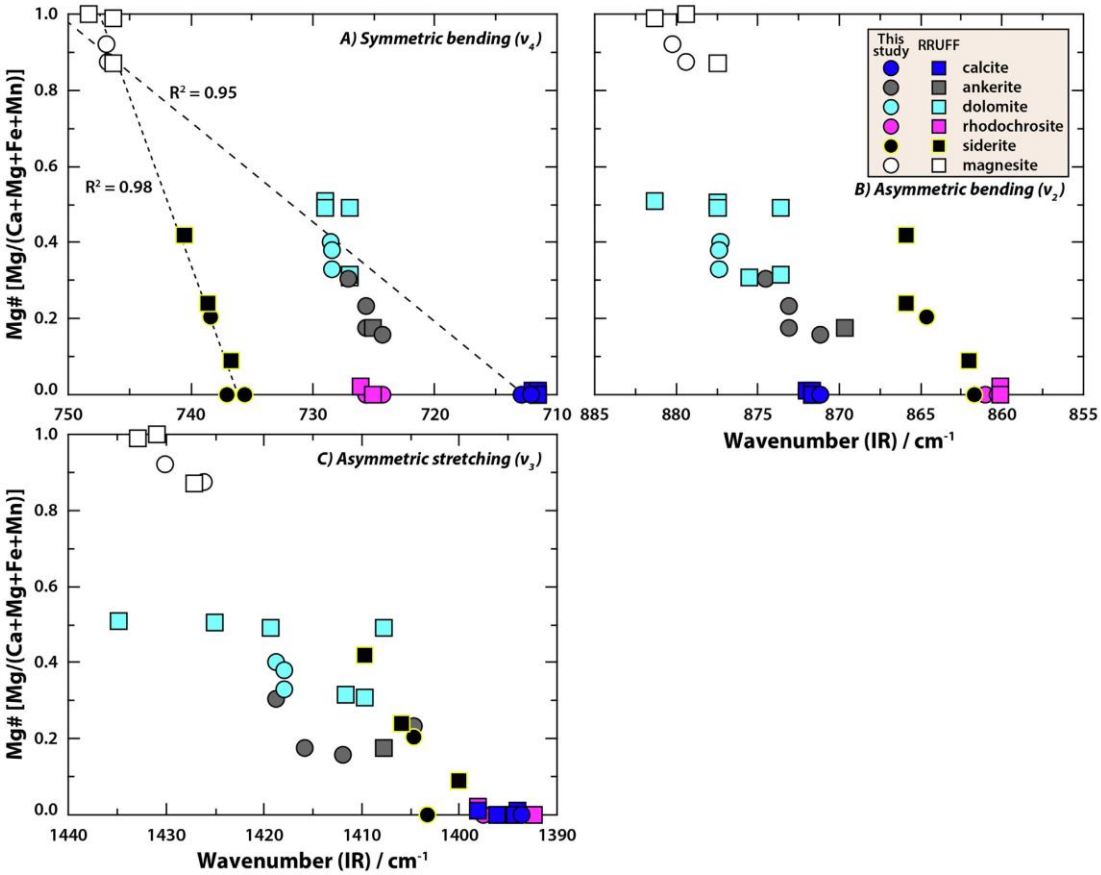

Fig. 5. Correlation between the different bands of the infrared spectrum and Mg#. Calibration curves among calcite, ankerite, dolomite, and magnesite (R^2 = 0.95), and between siderite and magnesite (R^2 = 0.98).

The L mode has a narrower peak interval (51 cm^{-1}) with a wider range of peak dispersion than the T mode, whereas the peak shift was well-reflected in Mg# regardless of mineral phases, showing a single linear trend (Fig. 3B). The ν_4 mode (Fig. 3C) exhibits two trends of peak positions like the T mode, but over a much narrower interval (28 cm^{-1}). Although two trend lines (i.e., calcite-ankerite-dolomite and rhodochrosite-siderite-magnesite) are identified in the ν_1 mode, these trends show a large level of dispersion (Fig. 3D). Thus, the T mode is the best region for carbonate discrimination. Two trend lines can be highlighted with a regression coefficient (R^2) greater than 0.97 (Fig. 3A). The L mode can be used for determining Mg# in carbonate minerals within the regions.

The other compositional combinations were plotted against the Raman peak position of the T mode: another Mg# (Mg#2 = Mg/[Ca + Mg]), Fe# (Fe# = Fe/[Ca + Mg + Fe + Mn]) and two Ca# (Ca#1 = Ca/[Ca + Fe + Mg + Mn], and Ca#2 = Ca/[Ca + Fe + Mn]) were plotted against the Raman wavenumbers of the T mode (Fig. 4). Mg#2 shows a positive trend with the peak positions except for rhodochrosite, and Fe# has two correlations between ankerite and dolomite, and between siderite and magnesite (Fig. 4). No clear trends are observed with Ca#. These results confirm that Mg# against the Raman peak position of the T mode is the best parameter to discriminate and characterize the carbonate minerals with this Raman portable spectrometer.

3.2. IR characterization of carbonate minerals

Four internal vibration modes of CO_3^{2-} at 1396 cm^{-1} (asymmetric stretching, ν_3), 1089 cm^{-1} (symmetric stretching, ν_1), 872 cm^{-1} (asymmetric bending, ν_2) and 713 cm^{-1} (symmetric bending, ν_4) are found to be active in the infrared spectrum measured from the calcite reference (Fig. 2B). The two bending bands ν_2 and ν_4 are narrow and sharp. The ν_3 band gives rise to a strong and very broad feature in the infrared spectrum, whereas the Raman spectrum displays a very weak peak in that region [38]. In contrast, the intensity of the ν_1 band is very weak, while the peak is very strong in the Raman spectrum. Therefore, the ν_1 band was not considered for the IR part of this study.

The ν_4 and ν_2 bands are observed respectively from 711 to 749 cm^{-1} and from 860 to 882 cm^{-1}, and the ν_3 band arises from 1392 to 1435 cm^{-1} (Table 1). The position of the bands in the ν_4, ν_2, and the ν_3 modes moves generally towards high wavenumbers as Mg# increases, except for rhodochrosite. Fig. 5 shows the infrared band positions for the three modes plotted against Mg#. In a similar fashion to the T mode in the Raman spectra, two trend lines in four regions are observed within the ν_4 mode. The Ca-Mg and Fe-Mg trend lines have a strong correlation between the band position and the chemical composition of carbonates, showing high R^2 values of 0.95 and 0.98, respectively. In the ν_4 mode, the

distribution of the band position can be well distinguished for each phase with a low level of dispersion except for the overlap of ankerite-dolomite series and rhodochrosite (Fig. 5A). The ν_2 mode exhibits a narrower range (21 cm^{-1}) than the $\nu 4$ mode and also a with a broader dispersion. The band shift displays two correlations with Mg# from calcite to magnesite and from rhodochrosite to magnesite. Rhodochrosite can be easily identified by the lowest wavenumbers in this spectral range (Fig. 5B). The ν_3 mode displays the broader peak range (42 cm^{-1}) and the largest dispersion for the positions of the bands for each group, without a clear correlation between the position of the band and Mg# (Fig. 5C). The ν_4 spectral range is therefore the best region for carbonate discrimination allied with using the ν_2 mode for rhodochrosite.

Fig. 6 displays the position of the ν_4 bands plotted against Ca#1, Ca#2, Mg#2, and Fe#. Mg#2 shows a positive correlation with the band positions except for rhodochrosite and siderite. Fe# displays a linear trend between siderite and magnesite, but dolomite, ankerite, and rhodochrosite are close to each other between 730 and 724 cm^{-1}. The band shift in the ankerite-dolomite samples has an unclear trend with Ca#1 in comparison with Mg#. Ca#2 displays a linear correlation between ankerite and dolomite, whereas magnesite does not correlate with the peak position. Thus, Mg# is the best-correlated ratio with band shift in the ν_4 mode.

3.3. Combination of chemical composition and spectral characteristics

Fig. 7 shows the ATR band positions of the ν_4 mode plotted against the Raman shift of the T mode. The combination of these two spectral data shows that there are well-defined clusters for the calcite and magnesite phases separately from other phases. Rhodochrosite plots together with siderite in Raman data but with ankerite and dolomite in ATR, making both siderite and rhodochrosite recognizable. Ankerite and dolomite are the most difficult to distinguish, with a non-sharp transition from ankerite below

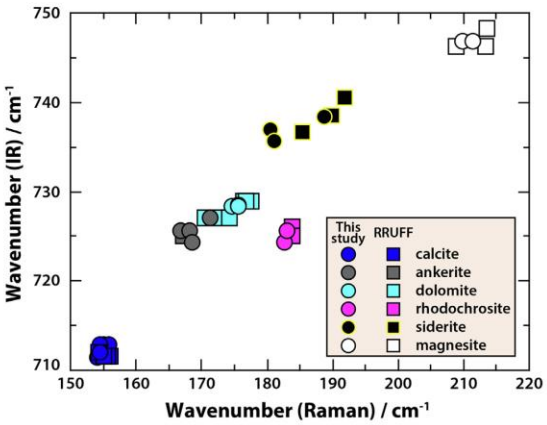

Fig. 7. Correlation between the positions of Raman peak and the positions of infrared band.

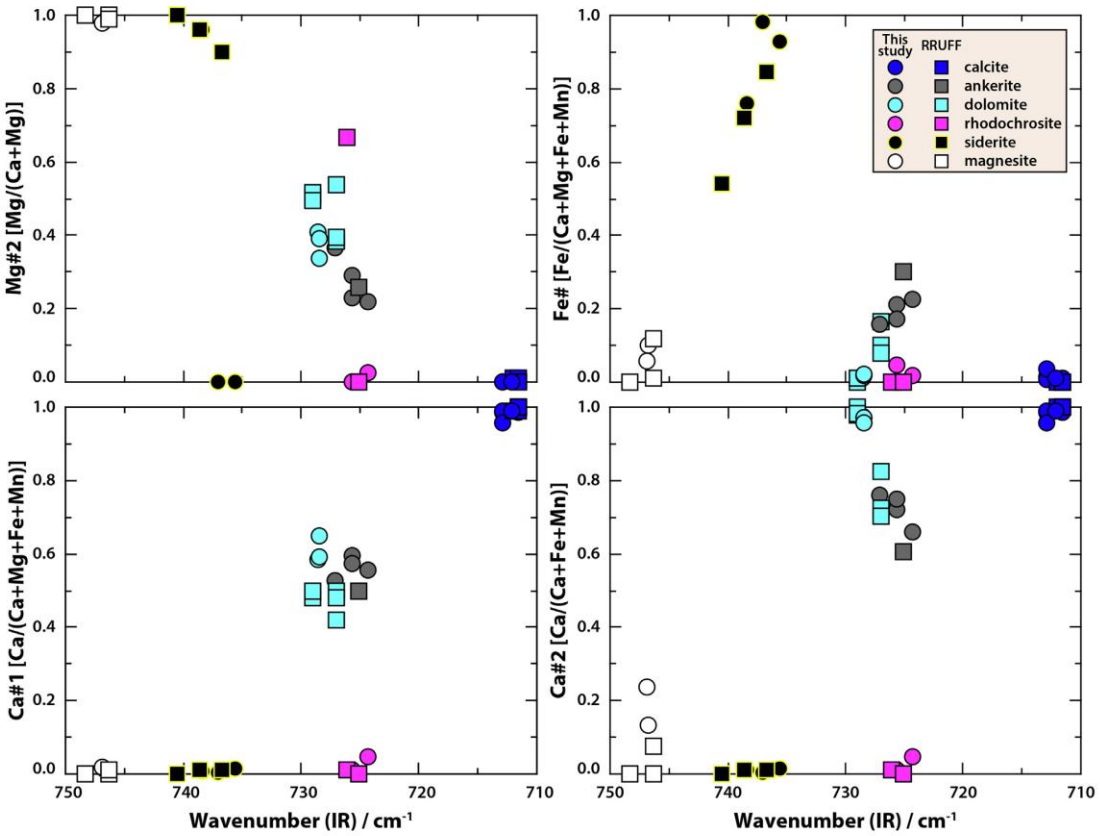

Fig. 6. Correlation between the positions of the band in the ν_4 mode and the different compositional ratios.

171 and 727 cm^{-1} to dolomite above 170 and 727 cm^{-1} from the Raman and infrared spectra, respectively. We thus confirm that the combination of Raman and infrared spectroscopies enables discrimination between all the carbonates, with some remaining overlap between Mn-Fe rich dolomites and Ca-Mg rich ankerites.

Fig. 8 shows the band positions from the Raman and infrared spectra and chemical composition (pXRF) in a 3D plot, making the identification of carbonates even easier by adding pXRF. The calcite samples (0.00–0.01 Mg#) are very well distinguished due to a very low Mg# and very low band positions in both Raman and infrared spectra (153–159 cm^{-1} and 712–713 cm^{-1}, respectively). The magnesite samples, the most Mg-rich carbonate (0.79–1.00 Mg#), exhibit the highest wavenumbers from 209 to 213 cm^{-1} in the Raman spectra and from 746 to 748 cm^{-1} in the infrared spectra. The Mg# of ankerite samples (0.11–0.18) corresponds to a spectral range of 165–171 cm^{-1} and 725–726 cm^{-1} in the Raman and infrared spectra, respectively. The dolomite samples have a strong band from 170 to 178 cm^{-1} in the Raman spectra and 727–729 cm^{-1} in the infrared spectra with 0.18–0.51 Mg#. The band of siderite samples is between 181 and 192 cm^{-1} in the Raman spectra and between 736 and 741 cm^{-1} within the infrared spectra with 0.00–0.42 Mg# and the rhodochrosite samples (0.00–0.04 Mg#) are identified with a band position at 183–184 cm^{-1} in the Raman spectra and 725–726 cm^{-1} in the infrared spectra.

4. Discussion

4.1. Divalent cation in the carbonate minerals

For the same carbonate structure, changes in the atomic constitution induce variations of chemical bond strengths and atomic masses, which have consequences on the vibration frequencies and thus on spectral band positions [5]. As Mg# increased, the band position in the Raman spectrum shifted from 150 to 215 cm^{-1} and from 710 to 750 cm^{-1} in the infrared spectrum (Fig. 8). We noticed that the band positions are shifted to lower wavenumbers with respect to cation radius and atomic mass in both Raman and infrared spectra. Fisler et al. [10] revealed a positive correlation between the ionic radius of the divalent cation, i.e., Ca, Mg, Mn, Fe, Cd, Zn, Co, and Ni, and the calculated lattice energies in carbonate minerals. We, therefore, added an otavite ($CdCO_3$), smithsonite ($ZnCO_3$), and spherocobaltite ($CoCO_3$) sample from the RRUFF database to our data set to highlight the trend between peak position and ionic radius (Fig. 9A). Ionic radius and atomic mass were represented as mean values weighted by the cation composition ratio (i.e., Ca, Mg, Fe, and Mn). The peak positions of siderite and rhodochrosite in this study overlap in the Raman spectrum between 180 cm^{-1} and 185 cm^{-1}. This overlapping region associated with the lattice mode can be explained by the similar effective atomic mass of iron (55.85 AMU) and manganese (54.94 AMU), respectively (Fig. 9B). Infrared spectra also show a correlation between the band position in the ν_4 region and ionic radius (Fig. 10A). This is consistent with the finding showing that a decrease in the ionic radius induces an increase of the wavenumber [17]. Furthermore, the positions of the bands are slightly shifted as the masses of the divalent cations decrease from calcium to magnesium (Fig. 10B). Siderite and rhodochrosite have different band regions in the infrared spectrum but overlap in the Raman spectrum. This can be explained by the use of different vibration modes in the two techniques.

4.2. Mg:Fe ratio in ankerite-dolomite relationship

Mineral identification in a solid ankerite-dolomite solution is always a difficult and complicated challenge due to a continuous variation in terms of chemical composition with Mg, Fe, and Mn. The term dolomite is restricted to the ratio Mg:Fe > 4, while ankerite is defined by the ratio Mg:Fe $\leq$ 4:1 [7]. Our ankerite samples, including the RRUFF database, have Mg:Fe lower than 4.5 and the dolomite samples have Mg:Fe ratio between 4.3 and 117.3 (Fig. 11). The ankerite and dolomite samples show that an increase in Mg:Fe ratio appears to be associated with a shift of the Raman

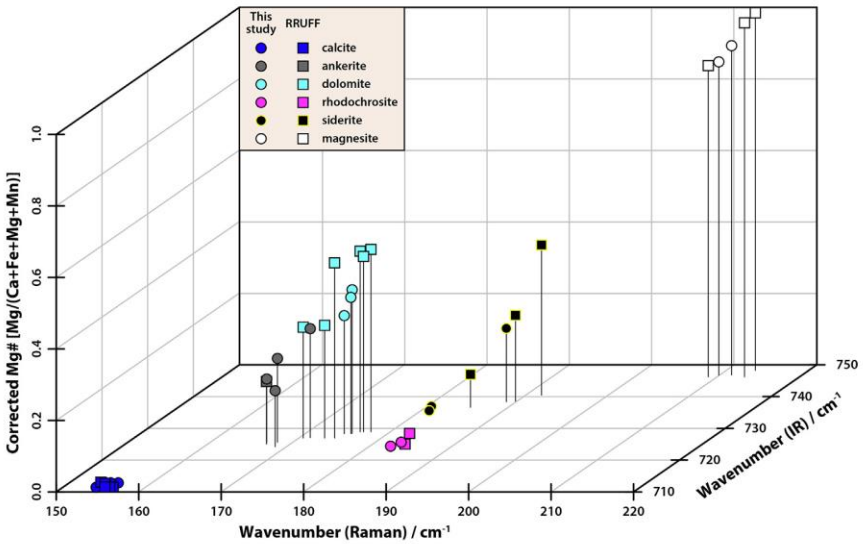

Fig. 8. 3D plot among the band positions in Raman and infrared spectra with Mg#.

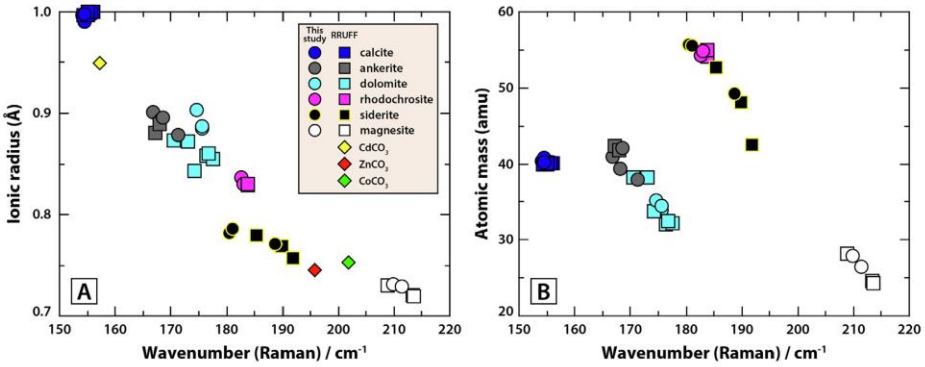

Fig. 9. Comparison between the ionic radius and atomic mass in the carbonate standards against Raman peak positions.

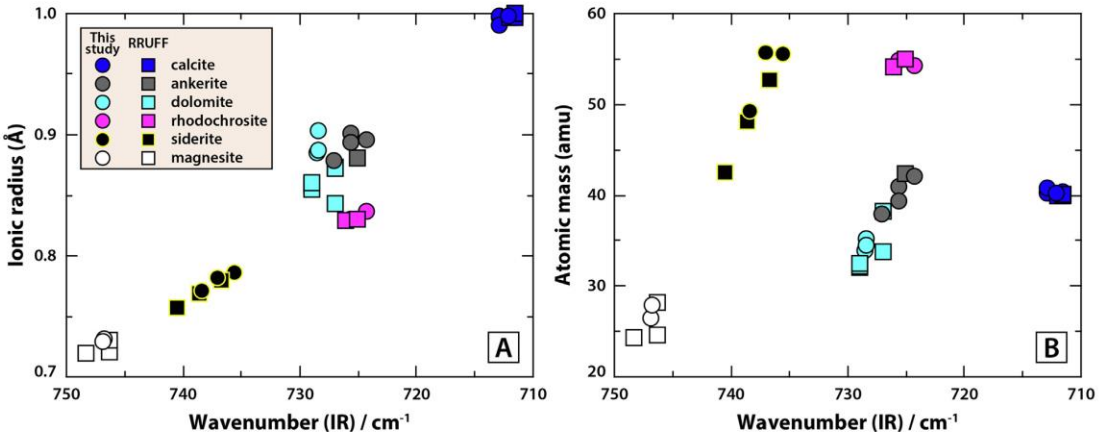

Fig. 10. Comparison between the ionic radius and atomic mass in the carbonate standards against infrared band positions.

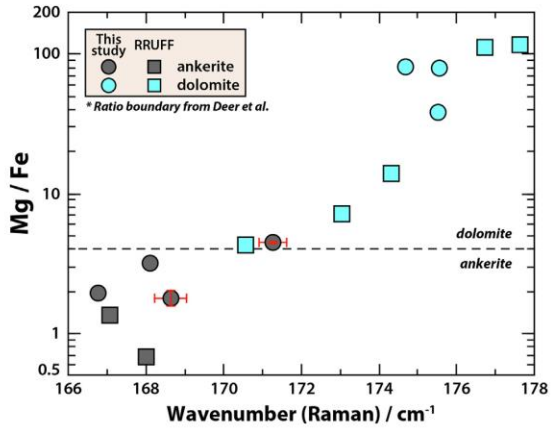

Fig. 11. Variation diagram showing Mg/Fe ratio against the Raman peak position in the ankerite and dolomite samples.

peak position to higher wavenumbers. The vertical demi error bars of two ankerite samples correspond to the uncertainty on the mean value of the atomic % for the magnesium and iron (Fig. 11). The propagation of uncertainty for the Mg:Fe ratio is defined in Eqs. (1),

$$\delta\frac{\frac{Mg}{Fe}}{\frac{Mg}{Fe}} = \sqrt{\left(\frac{\delta Mg}{Mg}\right)^2 + \left(\frac{\delta Fe}{Fe}\right)^2} \quad (1)$$

$\delta Mg = \frac{\sigma Mg}{\sqrt{N}}$ and $\delta Fe = \frac{\sigma Fe}{\sqrt{N}}$

where Mg and Fe are the values of the atomic percentage calculated from the weighted percentage provided by pXRF, and δMg and δFe the standard deviations of magnesium and iron atomic values divided by the square root of the number of measurements (5 times at the same point on each sample). The horizontal demi error bars indicate the standard deviation of peak position divided by the square root of the number of measurements (5 random locations on each sample). Most of the ankerite samples have a position at 166–169 cm^{-1} with Mg:Fe < 4 except for one sample at 171.3 cm^{-1} with Mg:Fe = 4.5 (Fig. 11). The dolomite sample with the lowest Mg:Fe shows a similar position to that

of the highest Mg:Fe ankerite at Mg:Fe = 4.3 and 170.5 cm^{-1}. Therefore, 170 – 172 cm^{-1} in the Raman spectrum can be interpreted as the value corresponding to the border or transition region between ankerite and dolomite.

4.3. Applicability of portable devices in the field

This study was carried out on the flat surface of pelletized samples composed of a single (i.e., monomineralic) mineral in order to unify sample conditions and represent the homogeneity of the samples. However, mixed samples, including various particle sizes and diverse mineral groups, are more common in the field. Raman analysis can be performed without sample preparation. Solid samples have generally lower absolute intensity than pressed pellets and the signal-to-noise ratio can be affected by the surface condition. However, these factors are not critical for position determination (Fig. 12). Furthermore, Raman analysis also suffers from fluorescence effects, precluding the identification of some carbonates. That effect was often encountered in this study and lead to the exclusion of 2 samples from the study, siderite, and magnesite, respectively. ATR requires the extraction of a small piece of the sample. It is however much simpler to apply than XRD as no crushing and sieving of the <100 μm are required. Both techniques can be applied to the same grains as the Raman beam is smaller than the grain to be analysed by ATR. Adding pXRF on the field would facilitate mineral recognition but the large beam size (8 mm) makes it difficult to apply to heterogeneous samples. Assuming that only two techniques are to be applied, the combination of i) Raman and pXRF or ii) Raman and IR analysis is the most appropriate to identify carbonate minerals. i) The Raman and pXRF combination can be applied directly to a rock or core sample and is capable of providing elemental and mineralogical information simultaneously. ii) Raman and IR analyses are effective in identifying minerals in mixed samples made up of the same carbonate group and also various mineral groups such as silicates and sulfates. Furthermore, Raman analysis would be the most effective to distinguish carbonate minerals if only one method in the three techniques was required on a limited basis. Unlike pXRF with the large beam size and IR analysis that cannot distinguish ankerite and dolomite relationship, Raman spectroscopy is able to discriminate between the other carbonate phases except for siderite and rhodochrosite, which are readily identified with the naked eye.

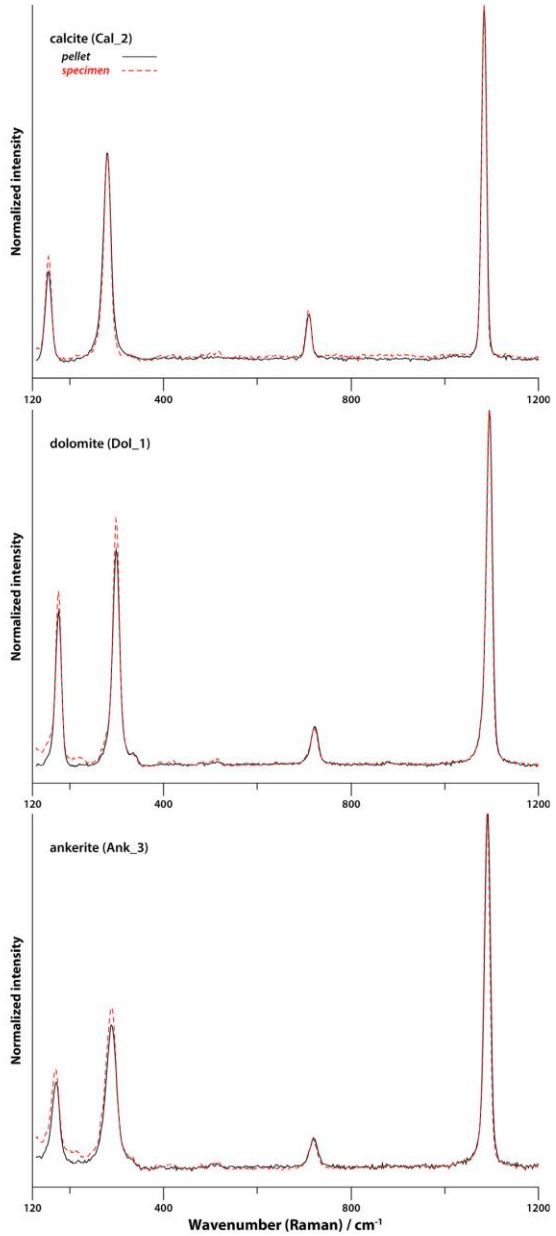

Fig. 12. Changes of Raman spectra from the surface condition on carbonate minerals.

4.4. Principal Component analysis (PCA)

To investigate the chemometric capability of the discrimination of carbonate minerals, a Principal Component Analysis (PCA) which reduces the number of variables of the input spectra was applied (Fig. 13). PCA analysis was carried out by FactoMinR (Factor Analysis and Data Mining with R) package in R platform [26,31,35]. The spectral data for PCA consisted of the position of each band for Raman and infrared spectra, and the concentration of the four cations measured by pXRF. The two principal components (i.e.,

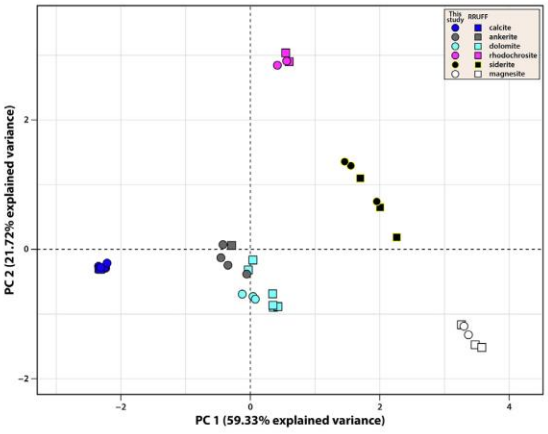

Fig. 13. PCA scores bi-plot using each band position from Raman and infrared spectra, and corrected concentration data of the four cations (Ca, Mg, Fe, and Mn) from pXRF.

Table 2
Coefficients of determination between primary variables and principal components.

	Raman	IR	Ca	Mg	Fe	Mn
	Position (cm^{-1})		Concentration (wt.%)			
PC1	0.96	0.98	0.86	0.57	0.17	0.01
PC2	0.00	0.01	0.13	0.34	0.10	0.72
PC3	0.03	0.00	0.00	0.08	0.73	0.26
PC4	0.01	0.00	0.00	0.00	0.00	0.00

PC1 and PC2) account for 81% of the variance, with 59.3% and 21.7%, respectively (Fig. 13). The PC 1/PC 2 score plot indicates a clear separation of the pure carbonate clusters from each other, except for the ankerite and dolomite that are close to each other and close to the origin in the PC 1/PC 2 field, meaning that neither of these variables is critical in distinguishing them. However, they remain separated by positive PC1 values for dolomite and negative PC1 values for ankerite. These analogous plots can be interpreted as a result of a similar composition that results in similar band positions between the ankerite-dolomite series. The siderite samples show a linear distribution on the score plot due to the variation in composition within the siderite group as described above. Table 2 shows that Raman, IR, and Ca are strongly correlated to PC1 (coefficient close to 1). Mn and Fe are highly correlated in PC2 and PC3 with both showing coefficients above 0.70. Thus, the PCA plot provides a well-classified graphical representation for the carbonate endmembers based on the combination of the three different spectral datasets.

5. Conclusions

This study aimed to compare chemical compositions with spectral properties using 20 samples of six natural carbonate minerals (calcite, ankerite, dolomite, siderite, rhodochrosite, and magnesite) in order to effectively identify the minerals from spectral differences. We clearly demonstrated a strong correlation between Mg# acquired from a portable XRF device and the band positions from both a portable Raman and a portable infrared spectrometer with an ATR module. The compositional variation is highly correlated to the spectral regions with respect to translational (T) lattice mode in the Raman spectra and symmetric bending vibration (ν_4) in the infrared spectra. Two different trends for the calcite-ankerite-dolomite-magnesite group and the siderite-magnesite group were identified by combining the chemical composition and the wavenumbers from Raman and IR spectra. Our detailed mineralogical and spectral study suggests that spectral analysis using portable tools is effectively applicable to the determination of carbonate minerals in the field. Most processing and plots in this study, including the PCA, can be automatized to accurately identify unknown samples against references using handheld devices. Another alternative to pXRF would be handheld Laser-induced breakdown spectroscopy (HH LIBS). While pXRF has limitations in measuring low-Mg carbonates, HH LIBS is able to analyse the elements that are lighter than Mg such as lithium, beryllium, and fluorine with a small laser spot size (100 μm) [11]. Finally, the continual shifts in Raman and ATR linked to the variation of the Ca-Mg-Fe-Mn ratio in the carbonate minerals suggest that a semi-quantitative analysis of carbonates by Raman or ATR is most probably feasible.

Declaration of Competing Interest

The authors declare that they have no known competing financial interests or personal relationships that could have appeared to influence the work reported in this paper.

Acknowledgment

This research is part of the NEXT project, supported by funding from the European Union's Horizon 2020 research and innovation programme under Grant Agreement No. 776804 – H2020-SC5-2017. We thank all the anonymous reviewers for their critical reviews and comments.

References

[1] H.H. Adler, P.F. Kerr, Infrared spectra, symmentry and structure relations of some carbonate minerals, Am. Mineral. 48 (1963) 839–853.
[2] D. Bersani, P.P. Lottici, Raman spectroscopy of minerals and mineral pigments in archaeometry, J. Raman Spectrosc. 47 (2016) 499–530, https://doi.org/10.1002/jrs.4914.
[3] W.D. Bischoff, S.K. Sharma, F.T. MacKenzie, Carbonate ion disorder in synthetic and biogenic magnesian calcites: a Raman spectral study, Am. Mineral. 70 (1985) 581–589.
[4] M.E. Böttcher, P.-L. Gehlken, E. Usdowski, Infrared spectroscopic investigations of the calcite-rhodochrosite and parts of the calcite-magnesite mineral series, Contr. Mineral. Petrol. 109 (1992) 304–306, https://doi.org/10.1007/BF00283320.
[5] E. Boulard, F. Guyot, G. Fiquet, The influence on Fe content on Raman spectra and unit cell parameters of magnesite–siderite solid solutions, Phys. Chem. Minerals 39 (2012) 239–246, https://doi.org/10.1007/s00269-011-0479-3.
[6] K.E. Chave, A solid solution between calcite and dolomite, J. Geol. 60 (1952) 190–192, https://doi.org/10.1086/625949.
[7] W.A. Deer, FRS, R.A. Howie, J. Zussman, An Introduction to the Rock-Forming Minerals, Mineralogical Society of Great Britain and Ireland, 2013. https://doi.org/10.1180/DHZ.
[8] J.V. Dubrawski, A.L. Channon, S.S.J. Warne, Examination of the siderite-magnesite mineral series by Fourier transform infrared spectroscopy, Am. Mineral. 74 (1989) 187–190.
[9] W.J.B. Dufresne, C.J. Rufledt, C.P. Marshall, Raman spectroscopy of the eight natural carbonate minerals of calcite structure, J. Raman Spectrosc. 49 (2018) 1999–2007, https://doi.org/10.1002/jrs.5481.
[10] D.K. Fisler, J.D. Gale, R.T. Cygan, A shell model for the simulation of rhombohedral carbonate minerals and their point defects, Am. Mineral. 85 (2000) 217–224, https://doi.org/10.2138/am-2000-0121.
[11] Y. Foucaud, C. Fabre, B. Demeusy, I.V. Filippova, L.O. Filippov, Optimisation of fast quantification of fluorine content using handheld laser induced breakdown spectroscopy, Spectrochim. Acta, Part B 158 (2019), https://doi.org/10.1016/j.sab.2019.05.017 105628.
[12] S.J. Gaffey, Reflectance spectroscopy in the visible and near-infrared (0.35–2.55 μm): applications in carbonate petrology, Geology 13 (1985) 270–273, https://doi.org/10.1130/0091-7613(1985)13<270:RSITVA>2.0.CO;2.
[13] G. Gisbert, E. Losantos, J.M. Pons, J.C. Videira, F. Tornos, Elvira: a new shale-hosted VMS deposit in the Iberian Pyrite Belt, 2019.
[14] D.L. Graf, Crystallographic tables for the rhombohedral carbonates, Am. Mineral. 46 (1961) 1283–1316.
[15] S. Gunasekaran, G. Anbalagan, S. Pandi, Raman and infrared spectra of carbonates of calcite structure, J. Raman Spectrosc. 37 (2006) 892–899, https://doi.org/10.1002/jrs.1518.
[16] R.S. Halford, Motions of molecules in condensed systems: I. Selection rules, relative intensities, and orientation effects for Raman and infra-red spectra, J. Chem. Phys. 14 (1946) 8–15, https://doi.org/10.1063/1.1724065.
[17] H.A. Hans, F.K. Paul, Infrared ansorption frequency trends for anhydrous normal carbonates, Am. Mineral. 48 (1963) 124–137.
[18] D.G. Henry, J.S. Watson, C.M. John, Assessing and calibrating the ATR-FTIR approach as a carbonate rock characterization tool, Sed. Geol. 347 (2017) 36–52, https://doi.org/10.1016/j.sedgeo.2016.07.003.
[19] C.K. Huang, P.F. Kerr, Infrared study of the carbonate minerals, Am. Mineral. 45 (1960) 311–324.
[20] F. Izzo, C. Germinario, C. Grifa, A. Langella, M. Mercurio, External reflectance FTIR dataset (4000–400 cm−1) for the identification of relevant mineralogical phases forming Cultural Heritage materials, Infrared Phys. Technol. 106 (2020), https://doi.org/10.1016/j.infrared.2020.103266 103266.
[21] J. Jehlička, A. Culka, F. Košek, Obtaining Raman spectra of minerals and carbonaceous matter using a portable sequentially shifted excitation Raman

spectrometer – a few examples, J. Raman Spectrosc. 48 (2017) 1583–1589, https://doi.org/10.1002/jrs.5105.
[22] J. Jehlička, P. Vítek, H.G.M. Edwards, M. Heagraves, T. Čapoun, Application of portable Raman instruments for fast and non-destructive detection of minerals on outcrops, Spectrochimica Acta Part A: Mol. Biomol. Spectrosc., Raman Spectrosc. Appl. Earth Sci. - Sensu Latu 73 (2009) 410–419, https://doi.org/10.1016/j.saa.2008.09.004.
[23] D. Krishnamurti, The Raman spectrum of calcite and its interpretation, Proc. Indian Acad. Sci. 46 (1957) 183–202, https://doi.org/10.1007/BF03045968.
[24] T. Laetsch, R. Downs, Software for identification and refinement of cell parameters from powder diffraction data of minerals using the RUFF Project and american mineralogist crystal structure databases, Abstracts from the 19th General Meeting of the International Mineralogical Association 23–28, 2006.
[25] B. Lafuente, R.T. Downs, H. Yang, N. Stone, The power of databases: the RRUFF project, in: T. Armbruster, R.M. Danisi (Eds.), Highlights in mineralogical crystallography, W. De Gruyter, Berlin, Germany 1, 2015, p. 30.
[26] S. Lê, J. Josse, F. Husson, FactoMineR: an R package for multivariate analysis, J. Stat. Softw. 25 (2008) 1–18. https://doi.org/10.18637/jss.v025.i01.
[27] P. Makreski, G. Jovanovski, MINERALS FROM MACEDONIA 9, 2003.
[28] J. Perrin, D. Vielzeuf, D. Laporte, A. Ricolleau, G.R. Rossman, N. Floquet, Raman characterization of synthetic magnesian calcites, Am. Mineral. 101 (2016) 2525–2538, https://doi.org/10.2138/am-2016-5714.
[29] F. Pirajno, Metalliferous sediments and sedimentary rock-hosted stratiform and/or stratabound hydrothermal mineral systems, in: F. Pirajno (Ed.), Hydrothermal Processes and Mineral Systems, Springer, Netherlands, Dordrecht, 2009, pp. 727–883, https://doi.org/10.1007/978-1-4020-8613-7_8.
[30] S. Pontual, GMEX spectral analysis guides for mineral exploration, 2008.
[31] Rf. R Core Team, R: A language and environment for statistical computing. R foundation for statistical computing Vienna, Austria, 2013.
[32] J.R. Ridley, Ore Deposit Geology, 2013. https://doi.org/10.1017/CBO9781139135528.
[33] N. Rividi, M. van Zuilen, P. Philippot, B. Menez, G. Godard, E. Poidatz, Calibration of carbonate composition using micro-Raman analysis: application to planetary surface exploration, Astrobiology 10 (2010) 293–309.
[34] H.N. Rutt, J.H. Nicola, Raman spectra of carbonates of calcite structure, J. Phys. C: Solid State Phys. 7 (1974) 4522–4528, https://doi.org/10.1088/0022-3719/7/24/015.
[35] Rs. Team, RStudio: integrated development for R. RStudio, Inc., Boston, MA, 2015, URL http://www.rstudio.com 42, 14.
[36] J. Velasco-Acebes, F. Tornos, A.T. Kidane, M. Wiedenbeck, F. Velasco, A. Delgado, Isotope geochemistry tracks the maturation of submarine massive sulfide mounds (Iberian Pyrite Belt), Miner. Deposita 54 (2019) 913–934, https://doi.org/10.1007/s00126-018-0853-x.
[37] P. Vítek, J. Jehlicka, H.G.M. Edwards, Practical considerations for the field application of miniaturized portable Raman instrumentation for the identification of minerals, Appl. Spectrosc. 67 (2013) 767–778, https://doi.org/10.1366/12-06774.
[38] W.B. White, 1974. The Carbonate Minerals, in: V.C. Farmer (Ed.), The Infrared Spectra of Minerals. Mineralogical Society of Great Britain and Ireland, London, pp. 227–284. https://doi.org/10.1180/mono-4.12.
[39] R.C. Wiens, S. Maurice, S.H. Robinson, A.E. Nelson, P. Cais, P. Bernardi, R.T. Newell, S. Clegg, S.K. Sharma, S. Storms, J. Deming, D. Beckman, A.M. Ollila, O. Gasnault, R.B. Anderson, Y. André, S. Michael Angel, G. Arana, E. Auden, P. Beck, J. Becker, K. Benzerara, S. Bernard, O. Beyssac, L. Borges, B. Bousquet, K. Boyd, M. Caffrey, J. Carlson, K. Castro, J. Celis, B. Chide, K. Clark, E. Cloutis, E.C. Cordoba, A. Cousin, M. Dale, L. Deflores, D. Delapp, M. Deleuze, M. Dirmyer, C. Donny, G. Dromart, M. George Duran, M. Egan, J. Ervin, C. Fabre, A. Fau, W. Fischer, O. Forni, T. Fouchet, R. Fresquez, J. Frydenvang, D. Gasway, I. Gontijo, J. Grotzinger, X. Jacob, S. Jacquinod, J.R. Johnson, R.A. Klisiewicz, J. Lake, N. Lanza, J. Laserna, J. Lasue, S. Le Mouélic, C. Legett, R. Leveille, E. Lewin, G. Lopez-Reyes, R. Lorenz, E. Lorigny, S.P. Love, B. Lucero, J.M. Madariaga, M. Madsen, S. Madsen, N. Mangold, J.A. Manrique, J.P. Martinez, J. Martinez-Frias, K.P. McCabe, T.H. McConnochie, J.M. McGlown, S.M. McLennan, N. Melikechi, P.-Y. Meslin, J.M. Michel, D. Mimoun, A. Misra, G. Montagnac, F. Montmessin, V. Mousset, N. Murdoch, H. Newsom, L.A. Ott, Z.R. Ousnamer, L. Pares, Y. Parot, R. Pawluczyk, C. Glen Peterson, P. Pilleri, P. Pinet, G. Pont, F. Poulet, C. Provost, B. Quertier, H. Quinn, W. Rapin, J.-M. Reess, A.H. Regan, A.L. Reyes-Newell, P.J. Romano, C. Royer, F. Rull, B. Sandoval, J.H. Sarrao, V. Sautter, M.J. Schoppers, S. Schröder, D. Seitz, T. Shepherd, P. Sobron, B. Dubois, V. Sridhar, M.J. Toplis, I. Torre-Fdez, I.A. Trettel, M. Underwood, A. Valdez, J. Valdez, D. Venhaus, P. Willis, The SuperCam instrument suite on the NASA Mars 2020 rover: body unit and combined system tests, Space Sci. Rev. 217 (2020) 4, https://doi.org/10.1007/s11214-020-00777-5.

2. Access to quantitative analysis of carbonates using a portable LIBS instrument: First applications to single minerals and mineral mixtures

The manuscript of this part was published in Spectrochimica Acta Part B: Atomic Spectroscopy in 2022. Therefore, it is noted that some parts of the introduction and methods can be repeated with the previous paragraphs.

Spectrochimica Acta Part B: Atomic Spectroscopy 191 (2022) 106397

Contents lists available at ScienceDirect

Spectrochimica Acta Part B: Atomic Spectroscopy

journal homepage: www.elsevier.com/locate/sab

Access to quantitative analysis of carbonates using a portable LIBS instrument: First applications to single minerals and mineral mixtures

Yonghwi Kim *, Cécile Fabre, Jean Cauzid

GeoRessources Laboratory –Université de Lorraine, Faculté des Sciences et Technologies, BP 70239, F-54506 Vandœuvre-lès-Nancy, France

ARTICLE INFO

Keywords:
Handheld LIBS
Carbonate minerals
Univariate calibration curve
Quantitative analysis
Principal component analysis

ABSTRACT

Natural carbonate standards of calcite structure were analysed using a handheld Laser-Induced Breakdown Spectroscopy (LIBS) device to investigate the spectral applicability for quantitative analysis in the Ca-Mg-Fe-Mn carbonate system. To obtain an initial understanding of the relationship between the elemental concentrations and LIBS signals, the determination coefficient (R^2), root mean square error (RMSE) and mean arctangent absolute percentage error (MAAPE) for cross-validation and forecast accuracy were used, respectively. To relate the changes in spectral characteristics to the mineral content of carbonate mixtures, different spectral ratios were compared with mixture ratios between the two carbonate minerals. We found that spectral information from LIBS emission lines showed high correlations to their elemental concentration (Ca, Mg, Fe, and Mn), and their spectral ratios in carbonate mixtures showed a linear correlation with mineral content. Principal component analysis (PCA) was investigated the chemometric capability of the discrimination for carbonate minerals. This study demonstrates that handheld LIBS can be effectively applied in the field for the discrimination and identification of carbonate endmembers and their quantification for the case of mixtures.

1. Introduction

Carbonates are widespread on Earth and involved in a variety of geologic processes, most notably as sedimentary deposits but also as secondary weathering products, hydrothermal deposits, and as the result of metamorphism. Carbonate minerals are formed by the combination of a $(CO_3)^{2-}$ ion with various monovalent or divalent cations. There are approximately 60 known carbonates minerals and the commonest rock-forming carbonate minerals within the trigonal crystal system are calcite ($CaCO_3$), magnesite ($MgCO_3$), siderite ($FeCO_3$), rhodochrosite ($MnCO_3$), dolomite ($CaMg[CO_3]_2$), and ankerite ($Ca[Fe, Mg,Mn][CO_3]_2$) [4]. Mineral discrimination and quantitative analysis of carbonate minerals act as important indicators in mineral resource exploration. In particular, the composition of carbonates, which are widely distributed in near-surface environments as a host rock related to numerous metalliferous ore deposits, are easily changed by thermal sources due to strong solubility in high-temperature hydrothermal fluids, and also much faster dissolvability than silicate minerals at similar temperatures [29]. Thus, this mineralogical characteristic can be used as a pathfinder to locate hidden ores. However, in the field, numerous carbonates may display similar characteristics in colour, grain size, and texture, and a series of changes in composition also make it complicated to discriminate between them with the naked eye.

A geological model of the Elvira Volcanogenic Massive Sulfide (VMS) deposit in the South-Eastern Iberian Pyrite Belt (IPB) is currently being developed by the Consejo Superior de Investigaciones Científicas (CSIC) and the Minas de Aguas Teñidas SAU (MATSA) mining company in the NEXT (New Exploration Technologies) project (G.A. No. 776804), funded by the European Union's Horizon 2020 research and innovation programme. This project aims to develop new geo-models and novel sensitive exploration technologies, and one of the tasks involved focuses on obtaining rapid, reliable, and efficient data in the field within this frame. Although the specific characteristics of the stratigraphic sequence and the style of mineralization associated with the Elvira deposit have not been yet studied in detail, the vectors to the ores can be based on the mineralogical and geochemical variation from the Sotiel-Migollas massive sulfide cluster due to the westward continuation of the Elvira deposit [9]. Alteration characteristics in the Sotiel-Migollas area show that the least hydrothermally altered shale mainly consists of a foliated groundmass of fine-grained illite ± muscovite, sparse pyrite, disperse grains of anhedral quartz, carbonates, ilmenite (altered to rutile), and zircon [37]. In areas affected by hydrothermal alteration,

* Corresponding author.
E-mail address: yonghwi.kim@univ-lorraine.fr (Y. Kim).

https://doi.org/10.1016/j.sab.2022.106397
Received 4 June 2021; Received in revised form 7 March 2022; Accepted 8 March 2022
Available online 13 March 2022
0584-8547/

chloritic alteration is closely associated with zones of brecciation or veinlets of carbonates and sulfides ± quartz [9]. Furthermore, the hydrothermal carbonates associated with the ores in Sotiel-Migollas show a systematic variability according to depth with a predominance of dolomite in the deepest part under the ore, which is gradually replaced by ferroan dolomite in the intermediate zone to ankerite and even siderite in the shallowest part [37]. This study is included in the NEXT project, which is focused on indicative minerals such as carbonates and chlorites present in the Elvira deposit for mineral identification and the compositional variations in the same mineral group using handheld LIBS as well as other portable spectroscopic techniques such as XRF, Raman, medium infrared and visible-near infrared to short-wavelength infrared spectroscopy. This means that access to the carbonate composition in the field is of great interest for geologists wishing to better deal with a potential mineral deposit. Recent developments of light portable spectroscopic tools have provided useful information for non-experts or in situations where geological interpretation is difficult, e.g., obscure alteration zones or rocks including opaque minerals in the field.

Laser-Induced Breakdown Spectroscopy (LIBS) has been already widely used for qualitative and quantitative analysis in mineralogical and geochemical research by observing the position and intensity of specific each elemental emission line in the spectra. LIBS can be quantified by the intensity of plasma emission lines at specific wavelengths proportional to the elemental abundance as the Boltzmann equation also describes [27]. The most common approach to LIBS quantitative analysis relies on establishing a univariate calibration curve generated after LIBS measurements on standards with certified composition. The calibration curves of characteristic elements for carbonate references have already been investigated by applying the peak intensity of each elemental emission line, but the target minerals were only calcium carbonate endmembers analysed by a laboratory device [22]. As qualitative analysis for carbonates, the laboratory LIBS set-up has demonstrated its potential to characterize carbonates by calculating the correlation coefficient of the emission intensity for each pair of LIBS spectra [14,24]. The correlation coefficient using similarity is effective when applied to diverse mineral groups as a simple univariate analysis between two LIBS spectra, but the same mineral family or minerals having similar composition are difficult to discriminate. Furthermore, carbonates have been identified on the surface in extra-terrestrial environments and therefore the importance of real-time analysis in the field has been increasing in situations where numerous samples cannot be brought to the laboratory for further bulk analyses [2,3,6,31,33]. Lanza et al. [21] reported that different carbonates could be distinguished from igneous materials, and each other, thanks to multivariate techniques on LIBS spectra using the replicate of the ChemCam instrument onboard the Curiosity rover under simulated Martian conditions.

Handheld LIBS devices are able to perform real-time determination in the field with limited sample pre-treatment. They also enable accurate and faster analyses than other conventional techniques usually present in the laboratory such as Electronic Micro Probe Analysis or Laser Ablation – Inductively Coupled Plasma Mass Spectrometry. A portable LIBS device can help geologists to make decisions in the field by providing quick sample screening and discriminating between rocks or minerals with rapid control of concentrate quality [7,8]. This developed technique, therefore, makes it possible to reduce analysis delay and cost, and save energy and manpower. Harmon et al. studied the identification and classification between different mineral groups and within the same carbonate group through multivariate analyses using the LIBS spectra obtained by a handheld instrument [12]. To date, no studies have reported elemental quantification using a handheld LIBS analyser on univariate calibration methods for the common carbonate minerals in the calcite structure.

The aim of this study was therefore to develop an optimized methodology using a handheld LIBS analyser to quantify elemental information among the different carbonates in the field. For this study, the area of cation emission lines was compared with the abundance of a single element obtained from a set of carbonate-mineral standards in the Ca-Mg-Fe-Mn system. Furthermore, emission-line ratios were investigated with respect to the synthetic mixtures of two carbonate minerals. Different ratios of spectral lines associated with compositional and quantitative changes were compared in order to determine the most diagnostic parameters and methodology in the field.

Table 1
Elemental concentrations for carbonate mineral references used in this study.

sample	mineral	corrected mass (wt%)			
		Ca	Mg	Fe	Mn
Cal_1	calcite	38.67	0.00	0.39	0.05
Cal_2	calcite	37.69	0.00	0.51	0.05
Cal_3	calcite	35.37	0.00	0.57	0.06
Cal_4	calcite	37.77	0.00	0.41	0.05
Cal_5	calcite	39.12	0.00	0.35	0.04
Dol_1	dolomite	22.25	11.30	0.58	0.11
Dol_2	dolomite	21.54	13.85	0.87	0.10
Ank_1	ankerite	21.57	6.09	8.85	2.34
Mgs_1	magnesite	0.48	25.77	2.96	0.20
Sid_1	siderite	0.21	1.43	43.49	2.57
Sid_2	siderite	0.18	0.00	45.43	2.34
Rhd_1	rhodochrosite	2.26	0.06	0.90	45.20
Rhd_2	rhodochrosite	1.47	0.00	1.40	46.94

2. Materials and methods

2.1. Sample preparation

The standards used in this study consisted of 6 natural carbonate minerals with 13 reference samples, including calcite ($CaCO_3$), magnesite ($MgCO_3$), siderite ($FeCO_3$), rhodochrosite ($MnCO_3$), dolomite ($CaMg[CO_3]_2$), and ankerite ($Ca[Fe,Mg,Mn][CO_3]_2$) (Table 1). In this study, the samples were prepared from carbonate powders with grain sizes less than 50 μm were pressed. Portable X-Ray Fluorescence (pXRF) and handheld LIBS spectra were obtained from pellets of a 13 mm diameter and 2 mm in thickness which were prepared using a 10-ton hydraulic press.

Synthetic mixtures of calcite, ankerite, and dolomite were used to assess the quantitative relationship between their spectral characteristics and mineralogical compositions. The mixture sets of two reference samples such as calcite-ankerite, calcite-dolomite, and ankerite-dolomite were prepared in different proportions, weighing 25:75, 50:50, and 75:25. Since calcite (2.72), ankerite (2.93), and dolomite (2.86) had similar densities, the pressed pellets of the mixtures were prepared by applying a mass ratio in two-component experiments [4].

2.2. Experimental setup

2.2.1. Portable X-ray fluorescence spectroscopy

As the ultimate objective of this study is effective carbonate identification and quantification in the field, all the elementary analyses were undertaken using LIBS and XRF portable devices. Portable XRF data were performed with a Thermo Fisher Scientific Niton XL3t GOLDD+ handheld spectrometer. The instrument uses an Ag-anode X-ray tube with a voltage of 50 kV and is equipped with a silicon drift detector (SDD). It operates the Main, Low, High, and Light filters with a duration of 30 s for each filter. The spectral data was automatically interpreted by the Mining Cu/Zn mode, which is effective for the measurement of lighter elements such as Mg, Al, Si, P, and S. In order to obtain a statistically reliable result, the elemental concentrations of each sample were averaged from 5 measurements at the same point with an 8 mm diameter for an analytical window. The elemental concentrations obtained from pXRF for Ca, Mg, Fe, and Mn were calibrated with atomic absorption spectroscopy (A800; Perkin Elmer, Norwalk, CT) (Table 1).

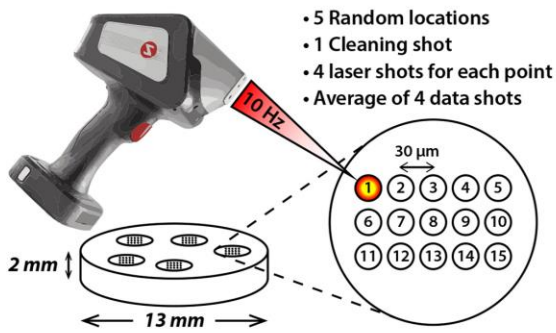

Fig. 1. Experimental protocol on pellets with the handheld LIBS pixel mode.

2.2.2. Handheld laser induced-breakdown spectroscopy

The Handheld Z-300 LIBS analyser (Sci-Aps ©, Woburn, MA) is equipped with multiple CCD-based spectrometers covering the acquisition of the entire spectral range, from 180 nm to 960 nm. The portable instrument employs a 1064 nm Nd:YAG pulsed laser with a 50 µm focused beam size, operating 5–6 mJ per pulse to the sample and 10 Hz repetition rate. All the LIBS spectra were measured under a constant argon flow from an integrated and replaceable argon purge inside the instrument. The argon environment was shown to yield higher emission intensities (i.e., 10-fold increase) and minimize the effect of air on the LIBS signal [16]. The pressure of argon gas in this study was controlled to maintain it at around 12 psi.

For each pellet, the Element Pro mode was used on 5 randomly chosen locations (Fig. 1). Each location was measured with a 15-point square grid on three lines, and the step size between the ablated craters was set at 60 µm to avoid the effects by overlapping between craters. Each point of the grid consists of 4 successive single shots after one first cleaning shot, thus the total 60 LIBS measurements collected for each location were averaged into one LIBS spectrum per sample in order to reflect the 'bulk' composition of the sample. The Relative Standard Deviations reported in the calibration curves are those calculated on the LIBS analyses carried out for the 5 different locations.

2.3. Standard normal variate (SNV) transformation

LIBS spectra are often normalized in order to take into account signal fluctuations and thus obtain enhanced analytical performance. Standard Normal Variate (SNV) transformation, which is one of the pre-processing methods commonly applied in Near-Infrared spectroscopy or Raman spectroscopy, allows the quality in LIBS to be increased by reducing the signal fluctuations observed in the LIBS data [1,15,30,32]. This transformation could replace normalization with a spectral line and could also be used to eliminate the fluctuations of experimental conditions (external factors) such as temperature, pressure, and pulse energy. SNV calculation is processed on each spectrum individually by centering the spectrum on the mean value and then dividing the corrected spectrum by the standard deviation of the original spectrum (Eqs. (1)):

$$I_{SNV}(\lambda) = \frac{I_{Raw} - I_{Mean}}{\sigma} \quad (1)$$

where I_{SNV} represents the normalized intensity calculated for a given wavelength λ of the LIBS spectrum; I_{Raw} is the raw intensity for a given wavelength of the LIBS spectrum; I_{Mean} is the intensity of the baseline corresponding at the given wavelength; σ, the standard deviation of the original spectrum. A few studies have been made of SNV on LIBS spectra and these demonstrated good correlations between the SNV-corrected LIBS data and elemental concentration values in the context of quantitative analysis [17,34,35]. For this reason, we compared the initial and SNV-corrected LIBS data of the carbonate standards and mixtures used in this study in order to examine the different R^2, RMSE, and MAAPE values.

2.4. Intensity and integrated area

To verify the spectral emission for different carbonates and the carbonate mixtures quantitatively, we implemented three different methods using intensity and integrated area from the LIBS spectra as detailed hereafter and summarized in Fig. 2. The first method consists of simply extracting the maximum pixel intensity of a selected emission line. The other two methods are based on the calculation of the peak area and involve either the total area with a straight baseline at zero or the net area method, which sets the start and stop points at the valley between the peaks. Both total and net area were calculated by Spectragryph v1.2.13 after exporting the spectra from the handheld device

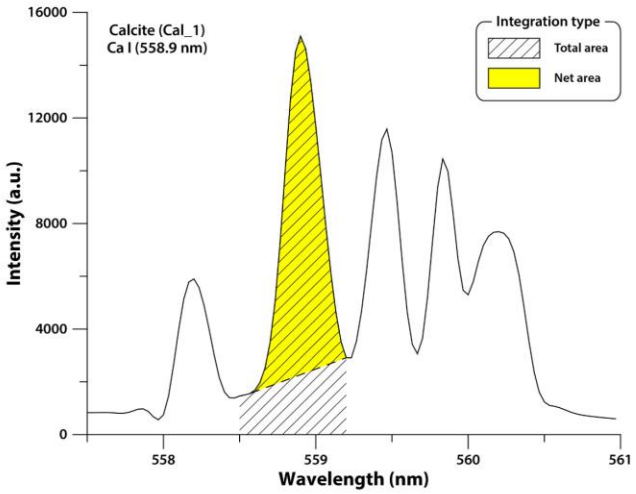

Fig. 2. Three methods for data extraction from LIBS spectrum.

Table 2
Candidate emission lines for each element used in this study.

Emission line	Wavelength (nm)	Reference
Ca II	318.0	
Ca I	393.4	[24]
Ca I	422.7	[21]
Ca I	445.5	
Ca I	558.9	
Mg II	279.6	[24]
Mg I	285.2	[5]
Mg I	309.7	
Mg I	518.4	[21]
Fe I	404.6	[21]
Fe I	495.8	[24]
Mn I	478.3	
Mn I	482.4	[24]

[25]. The three methods of data extraction presented in Fig. 2 were applied to the spectral emission lines of calcium, magnesium, iron, and manganese, respectively.

2.5. Emission line selection

The raw LIBS spectra, which is the sum of the spectra obtained in a single point of the grid pattern, are acquired from the integral software of Z300. It should be prioritized for quantitative analysis to select each key atomic line (i.e., Ca, Mg, Fe, and Mn) exhibiting linear correspondence to the peak area and the elemental concentration. The following criteria for the selection of the emission line were chosen: undersaturated and minimum self-absorption; good signal to noise ratio (SNR); avoiding spectral interference; intensity variation with the elemental concentration [11]. These criteria excluded many candidate

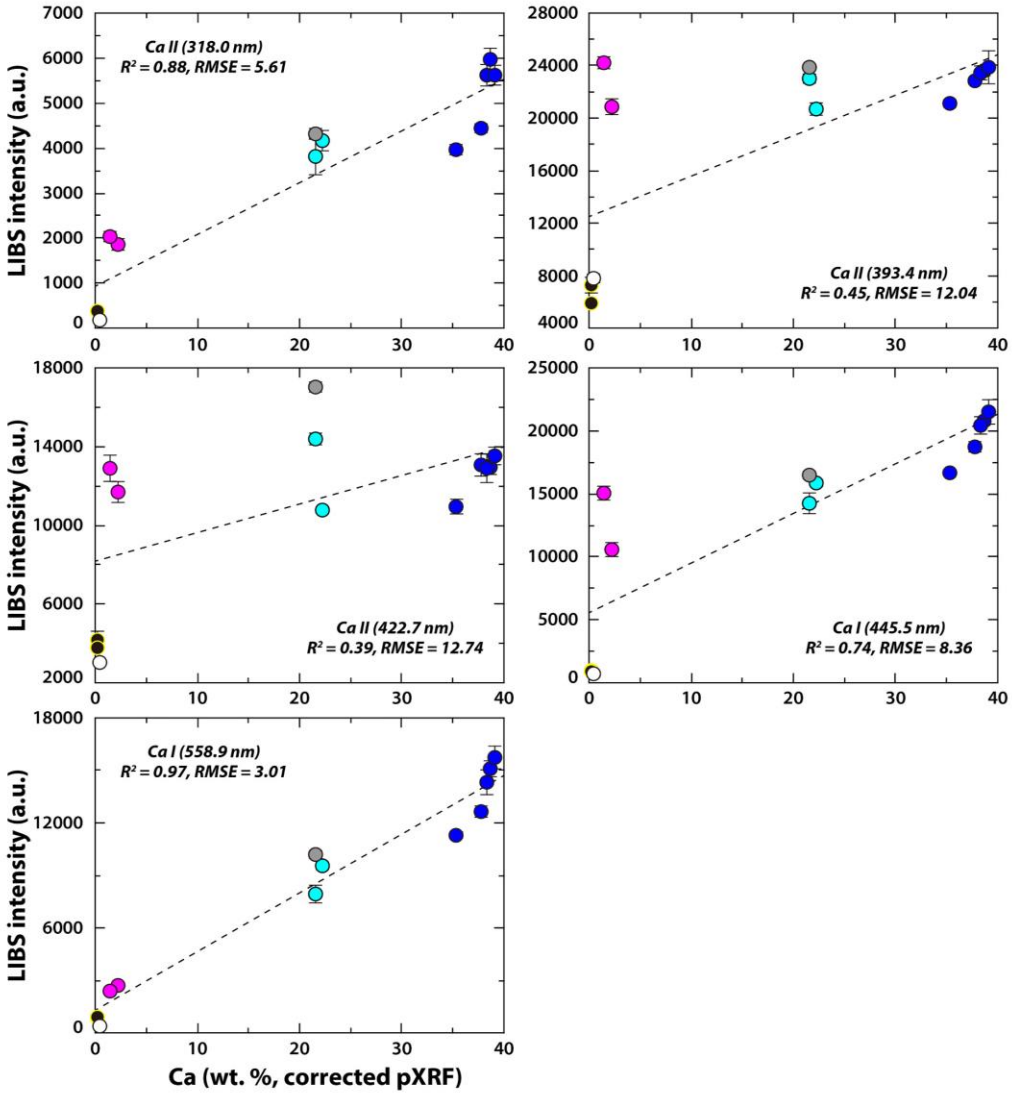

Fig. 3. Scatter plots of LIBS maximum pixel intensity of different calcium emission lines vs. calcium concentration from pXRF.

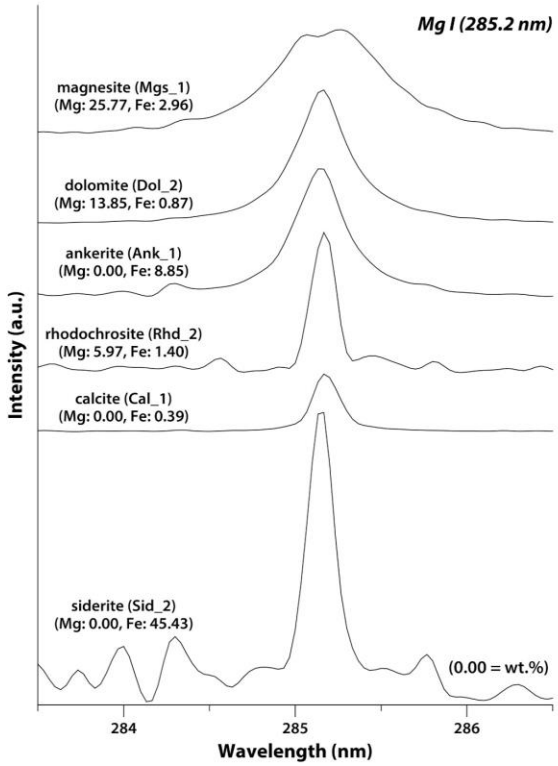

Fig. 4. SNV corrected LIBS spectra of the emission line at 285 nm from carbonate and silicate minerals.

lines which have been commonly used in previous studies. The candidate lines commonly used in previous studies with respect to Ca, Mg, Fe, and Mn are listed in Table 2. This method requires assigning each peak of the LIBS spectra to the corresponding element in agreement with the NIST or AtomTrace databases.

In the case of Ca, two emission-line candidates of calcium for carbonates in previous studies and three newly confirmed lines in this study were compared to the changes in calcium concentration [21,24]. Univariate calibration curves for concentration measurement are established by comparing the LIBS signals, such as peak intensity or area, on the vertical axis with concentration values of the analyte on the horizontal axis. Nonlinear calibration curves are inappropriate for concentration estimation because signal changes according to the increase in elemental concentration are constant at higher concentrations. This nonlinear behaviour, which is not proportional to the concentration, can be explained by self-absorption or saturation effects [11]. As a result, all the Ca emission lines except 558.9 nm were thus not selected (Fig. 3).

Regarding Mg, all three emission-line candidates in previous studies correspond at least one reason in the criteria of the line selection above, so they are excluded from the subsequent study (Table 2, [5,21,24]). For example, the magnesite sample in Fig. 4 shows a dip at the peak of the Mg emission line at 285.2 nm. This dip, known as "self-reversal", is produced by the concomitance of a temperature gradient and an electron density gradient in the plasma [28]. The self-reversal can give rise to a doubt of two lines and interfere with LIBS quantitative analysis. Furthermore, this region has spectral interference with the atomic emission line of Fe I 285.2 nm, thus the siderite sample has the most intense peak in spite of low Mg content (2.17 wt%) (Fig. 4). For this reason, the concentration and mixing ratio were compared in consideration of both the intensity and the total/net area as the spectral parameters. In this study, the relatively weak Mg 309.7 nm was preferred to other strong Mg emission lines since it has a linear correlation with compositional variation and is located in a region with less interference from other lines.

The representative emission line for Fe was selected at 495.8 nm since the other Fe emission line at 404.6 nm interferes with the manganese emission line at 404.9 nm. Both manganese emission-line candidates are saturated, but one peak at 478.3 nm displays a higher linear correlation coefficient (R^2) of 0.98 with stronger intensity than the other peak. In conclusion, the representative emission lines for Ca I (558.9 nm), Mg I (309.7 nm), Fe I (495.8 nm), and Mn I (478.3 nm) were selected for this carbonate investigation (Fig. 5).

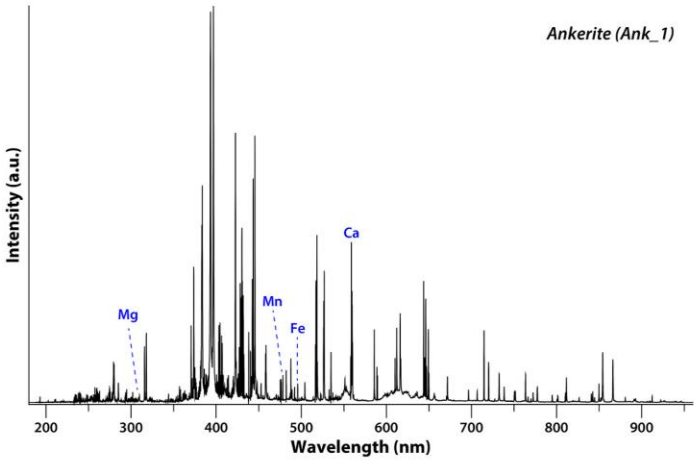

Fig. 5. Average LIBS spectrum of the ankerite sample from the spectral database.

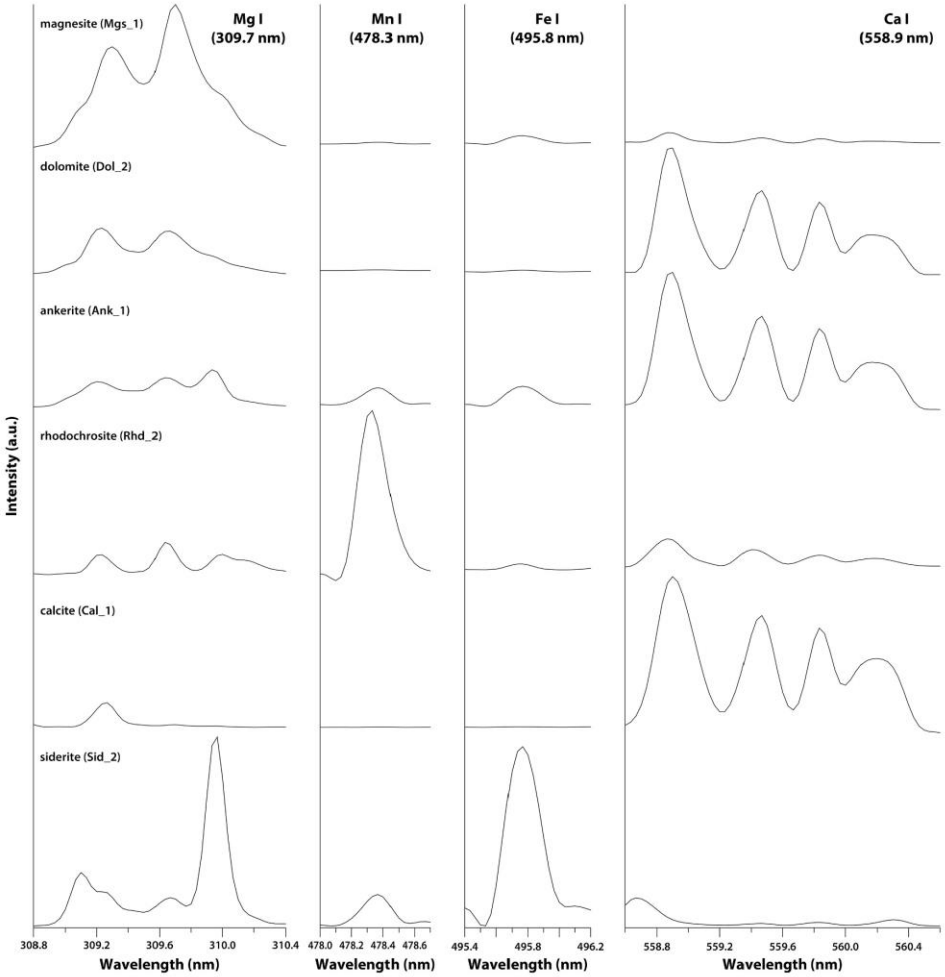

Fig. 6. Four elements of interest in the initial LIBS emission spectrum for each natural carbonate standard.

3. Results

3.1. Quantification of major element contents

3.1.1. Error calculation

To work towards understanding the relationship between the elemental concentrations and between the peak intensity or area, the determination coefficient (R^2), which is a simple and common univariate statistical model, was given by:

$$R^2 = 1 - \frac{\sum_{i=1}^{N}(\hat{y}_i - y_i)^2}{\sum_{i=1}^{N}(\hat{y}_i - \bar{y}_i)^2} \quad (1)$$

where $\hat{y}_i$ represents the reference values of concentration, y_i the predicted ones, and $\bar{y}$ the average value of $\hat{y}_i$ over N samples in the dataset. This regression formulation only takes into account observational errors in the dependent variable and could therefore be effective for the calibration dataset and for cross-validation. However, since the R^2 is definitely not sufficient to assess the predictive ability of a model, other model assessments were necessary to support the estimation of accuracy for a quantitative method.

Root mean square error (RMSE) is one of the most frequently standard methods using a quadratic scoring rule to measure the error of a model in predicting quantitative data. The RMSE, which is directly interpretable in terms of measurement units, is defined for parameter an estimate as:

$$\mathrm{RMSE} = \sqrt{\frac{1}{N}\sum_{i=1}^{N}(\hat{y}_i - y_i)^2} \quad (2)$$

Although RMSE is considered an excellent general-purpose error metric for numerical predictions, RMSE only compares prediction errors of different models or model configurations for a particular variable and not between variables, as it is scale-dependent. In order to evaluate the validation curve, mean absolute percentage error (MAPE) is commonly used as a non-scale dependent measure. However, this metrics has the significant disadvantage of producing infinite or undefined values for zero or close-to-zero actual values. To address this issue linked to MAPE, the mean arctangent absolute percentage error (MAAPE) proposed by Kim and Kim [19] was used in this study as an alternative statistical function of forecast accuracy, which is defined in Eq. (3),

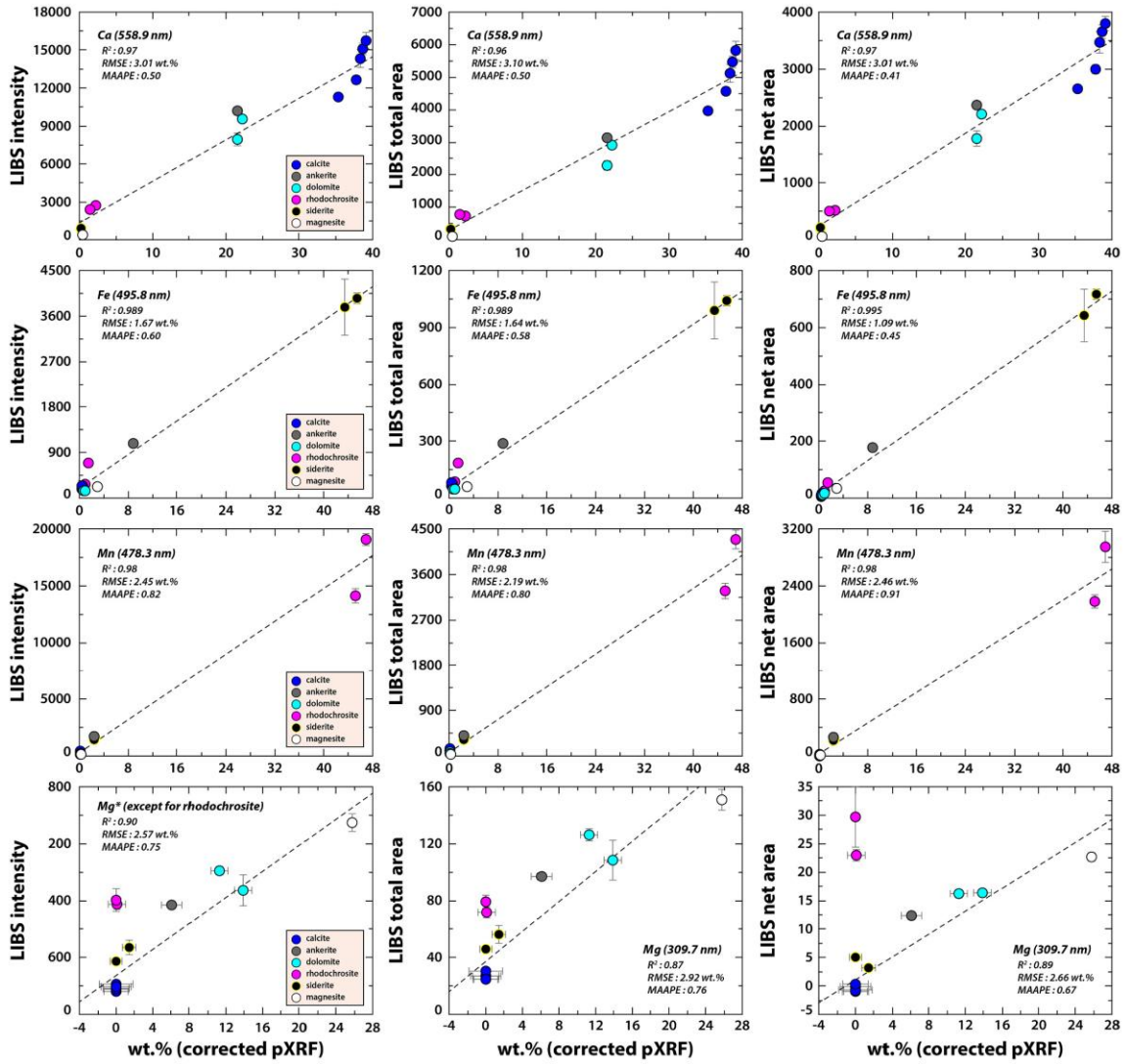

Fig. 7. Calibration curves between emission lines from the three extraction methods and the elemental concentration.

$$\mathrm{MAAPE} = \frac{1}{N}\sum_{1}^{N}(AAPE_t) \tag{3}$$

where N is the number of samples

$$\mathrm{AAPE_t} = arctan\left(\left|\frac{A_t - F_t}{A_t}\right|\right).$$

where A_t and F_t represent the actual and forecast values at the sample t, respectively. Ideally, the R^2 value should be equal to 1, while the RMSE and MAAPE values are equal to 0.

In order to avoid possible overfitting, which may occur if data are adjusted very well to the training data but exhibit a low predictive capacity, they were validated by the leave-one-out cross-validation (LOOCV) method by which one sample is taken out from the training set and used later for testing. In this method as an external validation, a concentration can be predicted for the external sample and compared with the reference value. The process was repeated by leaving each sample out of the training so that all samples could be validated by the model trained with the remaining N-1 samples.

3.1.2. Results for calibration curves

Fig. 6 shows four elements of interest in the LIBS emission spectrum with respect to each representative carbonate mineral. For each region in a spectrum, the spectral parameters such as intensity and total/net area were analysed without either normalization or baseline correction. The univariate calibration curves were developed by analysing the intensity and integrated area of each atomic emission line against elemental abundance (Fig. 7). The vertical error bars correspond to the Relative Standard Deviation (RSD) of the peak information calculated over 5 locations containing each of the 15 analysed zones. The

Table 3
Comparison of evaluation between the models and LOOCV results.

element	LIBS Parameter	Univariate calibration curve			LOOCV		
		R^2	RMSE (wt%)	MAAPE	R^2	RMSE (wt%)	MAAPE
Ca	intensity	0.97	3.01	0.50	0.97	3.43	0.53
	total area	0.96	3.10	0.50	0.96	3.65	0.54
	net area	0.97	3.01	0.41	0.97	3.46	0.46
Fe	intensity	0.989	1.67	0.60	0.993	1.79	0.62
	total area	0.989	1.64	0.58	0.988	1.82	0.61
	net area	0.995	1.09	0.45	0.995	1.49	0.49
Mn	intensity	0.98	2.45	0.82	0.99	4.91	0.93
	total area	0.98	2.19	0.80	0.98	4.38	0.84
	net area	0.98	2.46	0.91	0.98	4.87	0.96
Mg*	intensity	0.90	2.57	0.75	0.90	3.69	0.79
	total area	0.87	2.92	0.76	0.87	4.24	0.80
	net area	0.89	2.66	0.67	0.90	3.85	0.70

* Except for rhodochrosite

horizontal error bars represent the error range of the different concentrations obtained using the portable XRF, with a maximum of 0.3, 1.8, 0.5, and 0.4 wt%, for Ca, Mg, Fe, and Mn, respectively.

Each calibration curve of Ca displays a linear correlation between LIBS data and Ca concentration with higher R^2 values than 0.96 in all the variables with different RMSE (i.e., 3.01 wt% for intensity and net area, and 3.10 wt% for total area) (Fig. 7). MAAPE shows that net area (0.41) is the best parameter for Ca quantification than the other parameters (0.50). All the calibration curves in Fe showed very high R^2 values over 0.99, but the net area displayed the best RMSE and MAAPE values, 1.09 wt% and 0.45, respectively. Mn shows very high R^2 values higher than 0.98 with similar RMSE in the variables (Fig. 7). However, MAAPE values vary diversely, exhibiting the lowest value (0.80) in the total area method, and the highest value (0.91) in the net area method. In the case of magnesium, the calibration curve was created by excluding rhodochrosite due to spectral interference with manganese emission lines in

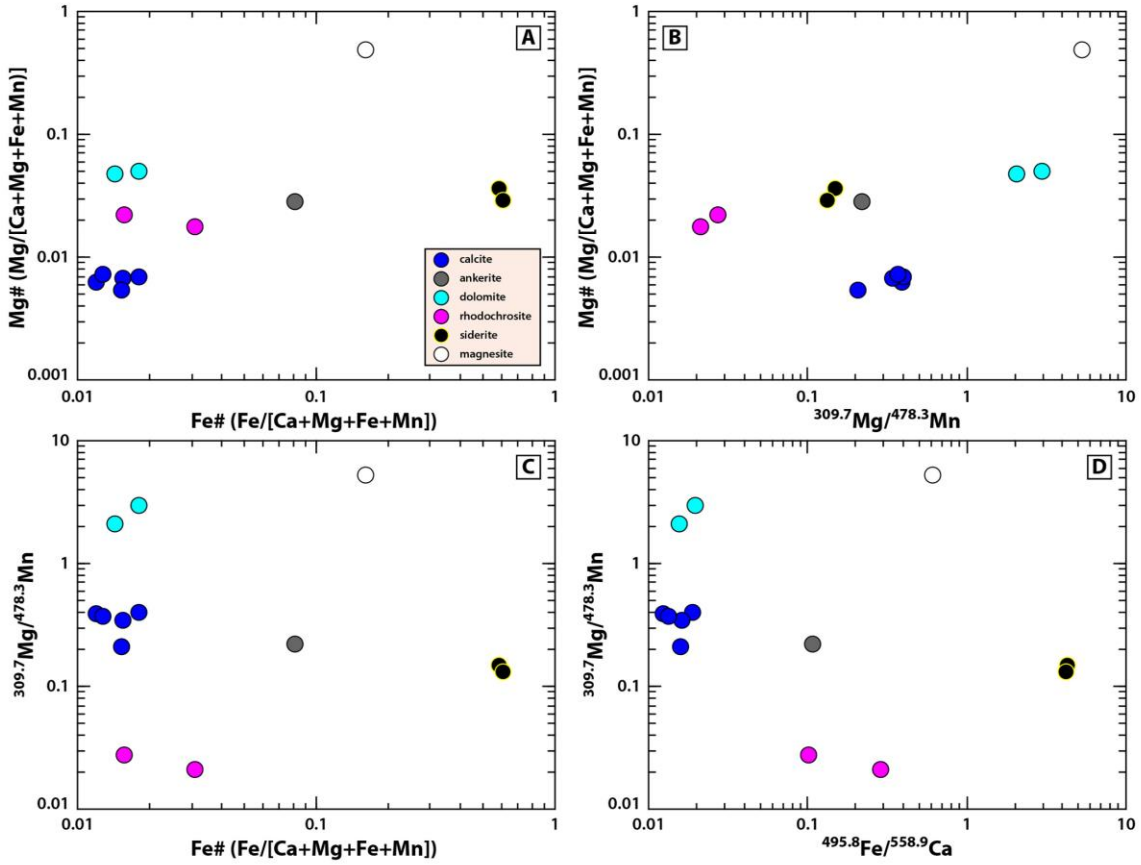

Fig. 8. The spectral intensity ratios using the emission lines of the four cations from LIBS spectra.

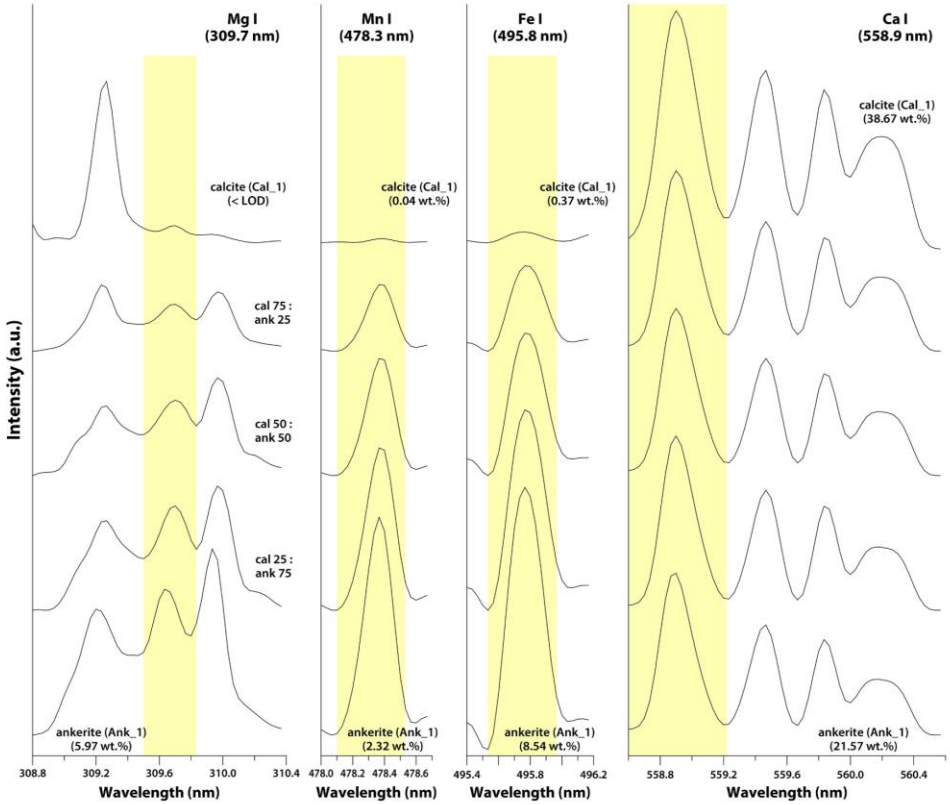

Fig. 9. LIBS spectra of the four emission lines within the calcite-ankerite mixtures.

LIBS. Similar R^2 values were shown based on the three LIBS parameters, with the highest value at 0.90 for the intensity method, and the lowest value at 0.87 for the total area method. Although the intensity parameter shows the best fit for Mg based on R^2 and RMSE, the MAAPE value from the net area method displayed the lowest value (0.67) as compared to the intensity method (0.75). Comprehensive analysis among determination coefficient (R^2), RMSE values of each calibration curve, and prediction accuracy (MAAPE), led us to conclude that the use of peak intensity or integration using the net area method is the best approach to obtain satisfactory univariate models for each element, whereas Ca, Mg, Fe, and Mn can be directly quantified using the LIBS analyses.

Leave-one-out cross-validation (LOOCV) method was performed to avoid possible overfitting due to a small number of samples in the training set. The calculation of the predicted value for the elemental concentration was repeated by removing each sample out of the total 13 carbonate samples in each spectral parameter. Therefore, all the samples could be validated by the model trained with the remaining 12 samples. Comparison of evaluation between the models and LOOCV results is summarized in Table 3.

The calibration curves for Ca have the same R^2 and similar RMSE of the LOOCV in the intensity and net area. R^2 from LOOCV of the total area is lower than that of the calibration curve by showing similar RMSE values. The MAAPE values of the Ca calibration curves were lower than those of LOOCV at all LIBS parameters. We found that all the parameters in Fe have very high R^2 values with low RMSE and MAAPE for both the calibration curves and the LOOCV. For manganese and magnesium, the R^2 and MAAPE values are similar between the calibration curves and the LOOCV. However, RMSE values in the LOOCV have higher than those of the calibration curves. These results proved that the LIBS parameters for each element, especially the intensity or net area, are linearly correlated with the elemental concentrations.

3.1.3. Ratios of emission lines for carbonate discrimination

Correlations between specific LIBS emission-line ratios using maximum intensity were established to investigate the applicability of carbonate discrimination using a handheld LIBS analyser in the field. Fe# (Fe# = Fe/[Ca + Mg + Fe + Mn]), Mg# (Mg# = Mg/[Ca + Mg + Fe + Mn]), Mg/Mn, and Fe/Ca were plotted against each other (Fig. 8). Fe#-Mg# was found to show separation among ankerite, magnesite, and siderite, but calcite, rhodochrosite, and dolomite were close, making it difficult to discriminate between them (Fig. 8A). Fe/Ca-Mg# is difficult to apply for ankerite and siderite because they are adjacent to each other (Fig. 8B). However, Fe#-Mg/Mn and Fe/Ca-Mg/Mn were found to exhibit clear separation of the single carbonate clusters from each other. Therefore, these two ratios seem to be the most suitable variables for efficiently distinguishing carbonate minerals of the calcite structure (Fig. 8C and D). Since carbonate minerals are defined as solid solution which has a continuous compositional variation in a single crystalline phase [4], we did not make boundaries separating the carbonate groups in Fig. 8.

3.2. Synthetic carbonate mixtures

The emission LIBS spectra dramatically change according to the

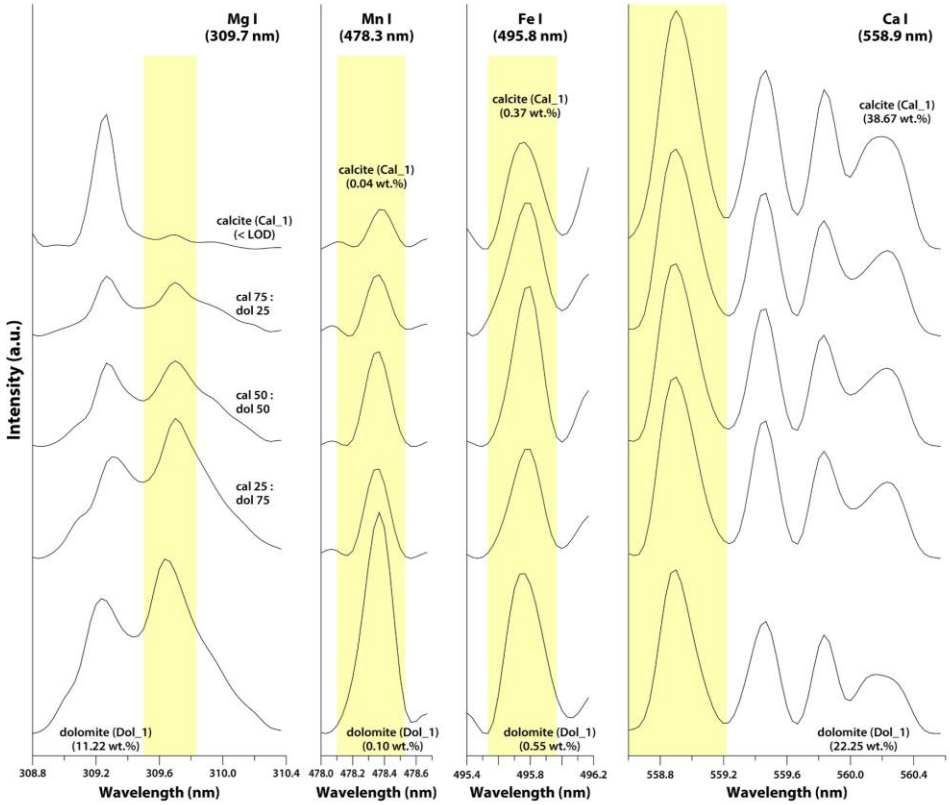

Fig. 10. LIBS spectra of the four emission lines within the calcite-dolomite mixtures.

difference in the mineral content of calcite-ankerite, calcite-dolomite, and ankerite-dolomite, which can be found in various geological environments. As the content of calcite increased in the calcite-ankerite mixtures, the emission intensity of Mg, Mn, and Fe, excluding Ca, was also found to increase without any change to its wavelength position (Fig. 9). These characteristics were similarly found in the calcite-dolomite mixtures, but the Mg peak in the 308.8–310.4 nm region has a doublet (Fig. 10) in contrast to ankerite with a triplet (Fig. 9). In order to correlate the changes in spectral characteristics with the mineral content of carbonate mixtures, we compared the ratio using the intensity and area obtained from the LIBS spectrum with the mixture ratios (i.e., 25:75, 50:50, and 75:25) between the two carbonate minerals. Each mixture was compared with Mg/Ca and Fe/Ca ratios using the emission lines of calcium, magnesium, and iron. The calcite-ankerite mixture displayed a good level of correlation in both Mg/Ca and Fe/Ca ratios, and especially the intensity and the total area method displayed good R^2, RMSE, and MAAPE values (Fig. 11, Table 4). In the calcite-dolomite mixture, only Mg/Ca ratio showed a linear tendency due to low Fe content in both calcite and dolomite endmembers. In this case, the intensity method has the highest R^2 (0.995) with the best RMSE and MAAPE values of 2.59 wt% and 0.24, respectively (Fig. 11).

The two-component experiment was carried out on a mixture of ankerite ($Ca[Fe,Mg,Mn][CO_3]_2$) and dolomite ($CaMg[CO_3]_2$) to investigate the gradual changes of a solid ankerite-dolomite solution with similar chemical composition and continuously compositional changes (Fig. 12). The calibration obtained with the Mg/Ca ratio is not sufficient for carbonate discrimination because the Mg and the Ca contents do not differ significantly enough in the two reference minerals (Fig. 13). In fact, only Fe and Mn can be used to discriminate a potential mixture of these two end members. Thus, a significant result was obtained from the Fe/Ca ratio, and the intensity and the total area methods gave R^2 values higher than 0.990 with lower RMSE of 3.58 and 3.15 wt%, respectively. Furthermore, MAAPE values in Fe/Ca ratio indicates that the intensity and the total area method are good indicators for carbonate quantification of ankerite-dolomite mixtures (Fig. 13, Table 4). These results confirmed that we could use the LIBS technique to investigate the potential content differences in unknown carbonate mixtures.

3.3. Principal component analysis (PCA)

Principal component analysis (PCA) is one of the most widely used chemometric procedures for multivariate data systems. It reduces the dimensions of the input data to reveal the simple underlying structure that provides an adequate visual representation of that data. PCA of the LIBS spectra was carried out using FactoMineR (Factor Analysis and Data Mining with R) package in the R platform [23,26,36]. To systematically investigate the chemometric capability for carbonate discrimination, four different datasets were used: i) all the signals from the entire LIBS spectra, ii) the total area calculated from the region of interest of LIBS spectra for the four selected emission lines used in this study, iii) the net area of each selected emission line, and iv) LIBS total area and the concentration of the four cations obtained from pXRF (Fig. 14). Based on our results above, we further carried out PCA by adding the binary carbonate mixtures among calcite, ankerite, and dolomite with

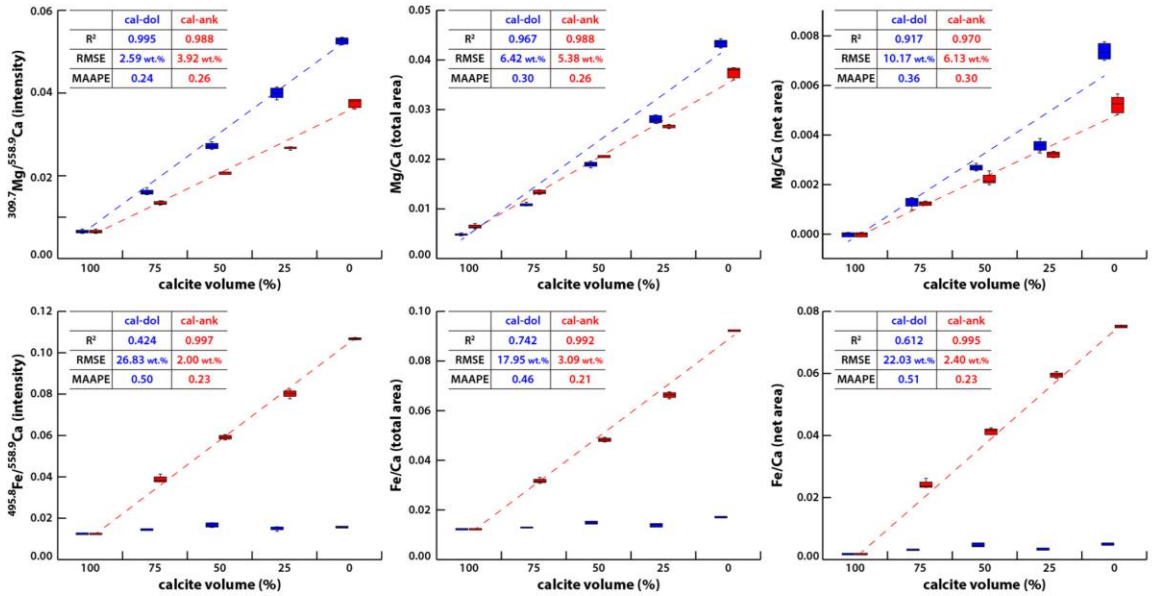

Fig. 11. Boxplot of the Mg/Ca and Fe/Ca spectral ratio obtained by LIBS analysis on the calcite-dolomite (blue) and calcite-dolomite (red) mixtures. (For interpretation of the references to colour in this figure legend, the reader is referred to the web version of this article.)

Table 4
The RMSE and MAAPE values for calibration and forecast accuracy among different carbonate mixtures by using Mg/Ca and Fe/Ca spectral ratios from the different methods.

Mixtures	Ratio	Intensity			Total area			Net area		
		R^2	RMSE (wt%)	MAAPE	R^2	RMSE (wt%)	MAAPE	R^2	RMSE (wt%)	MAAPE
calcite-ankerite	Mg/Ca	0.988	3.92	0.26	0.988	5.38	0.26	0.970	6.13	0.30
	Fe/Ca	0.997	2.00	0.23	0.992	3.09	0.21	0.995	2.40	0.23
calcite-dolomite	Mg/Ca	0.995	2.59	0.24	0.967	6.42	0.30	0.917	10.17	0.36
	Fe/Ca	0.424	26.83	0.50	0.742	17.95	0.46	0.612	22.03	0.51
ankerite-dolomite	Mg/Ca	0.796	15.96	0.42	0.796	18.95	0.42	0.572	23.13	0.50
	Fe/Ca	0.990	3.58	0.26	0.992	3.15	0.25	0.968	6.37	0.30

the LIBS dataset i), ii), and iii). All the datasets were applied baseline correction and normalization to the total area of the spectrum processed by Spectragryph v1.2.15 [25].

The entire spectrum corresponds to the LIBS broadband spectra, which consists of all the intensities in the whole wavelength region of the detector from 180 to 960 nm. The data for the entire spectrum projected on the PC1 vs. PC2 plane account for 72.58% of the variance. The PCA plot shows that rhodochrosite, siderite, and magnesite are well classified and scattered on the PCA plot, while calcite, dolomite, and ankerite are clustered closely together (Fig. 14A). In the ankerite-dolomite solid solution, one dolomite sample (Fe#: 0.024) is plotted between another dolomite sample (Fe#: 0.017) and the ankerite sample (Fe#: 0.23) instead of being separated from each carbonate group (Fig. 14A). This result shows that the dataset consisting of all the LIBS signals from the entire region is the simplest to apply to PCA compared to the other datasets since it is directly applicable after exporting and correcting the LIBS data. However, we also confirmed that this dataset required much time consumption according to many variables (i.e., 8262 variables) and difficulty in distinguishing among calcite, dolomite, and ankerite from the PCA plot. The PCA plot consisting of the total area calculated from the region of interest of four emission lines shows the best classification for carbonate discrimination, exhibiting 74.81% for the sum of the PC1 and PC2 (Fig. 14B). Each mineral phase is clustered each other, and the dolomite samples are well separated away from the ankerite ones. Furthermore, the dolomite and ankerite are located on the trendline between calcite and magnesite, and between calcite and siderite, respectively (Fig. 14B). The sum of the PC1 and PC2 for the other datasets were 77.04% and 72.96%, respectively (Fig. 14C and D). The PCA plot using the net area shows well scattered among the carbonates, but magnesite and rhodochrosite are gathered from each other (Fig. 14C). The last plot consisting of the LIBS total area and four elemental concentrations from pXRF (Fig. 14D) has a similar distribution with the one using the total area only (Fig.14B). Therefore, this result shows that LIBS data using the total area is able to provide effective carbonate classification.

The coefficients of determination for ii) the total area and iii) the net area between the primary variables and the principal components are shown in Table 5. Calculated coefficients of determination from both parameters show that Ca variable has the highest more than 0.98 in the first principal component. Due to the necessity to explain the variance of all the variables, the three principal components are used to cover the satisfactory level of variance representation of all the variables more than 0.99. For Mg and Mn variables from the total area, the second principal components explain more than 0.52 of the variances. Fe variable from the total area is explained that 0.55 falls on the third principal component. From the net area, the second principal component explains

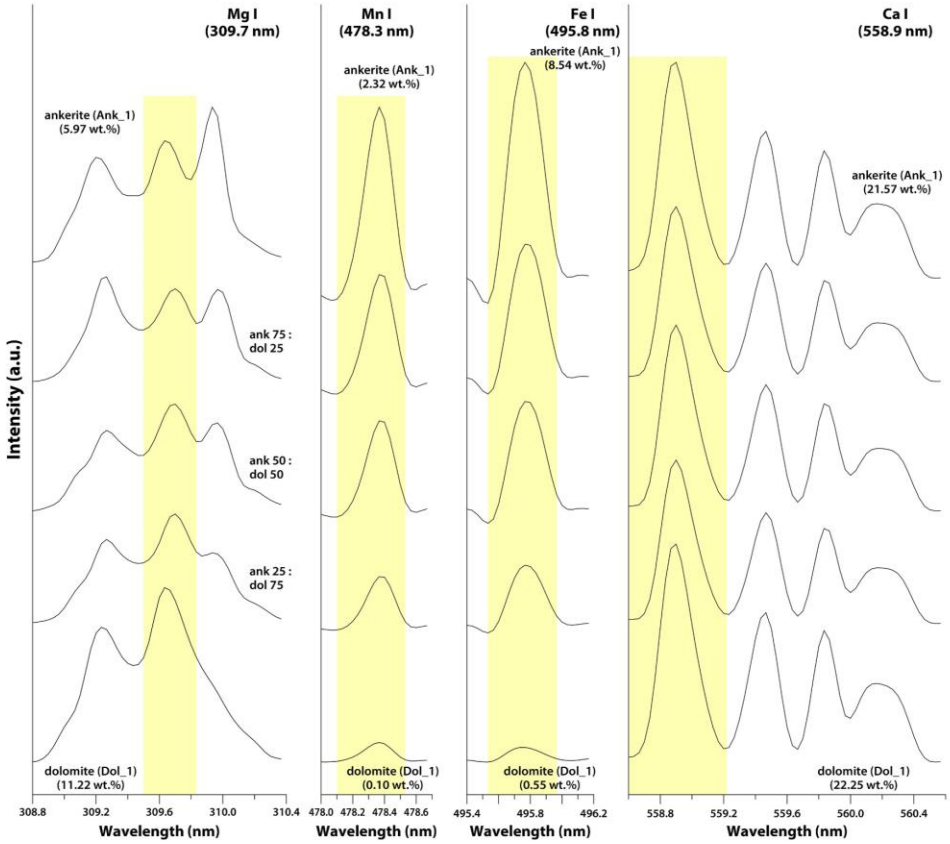

Fig. 12. LIBS spectra of the four emission lines within the ankerite-dolomite mixtures.

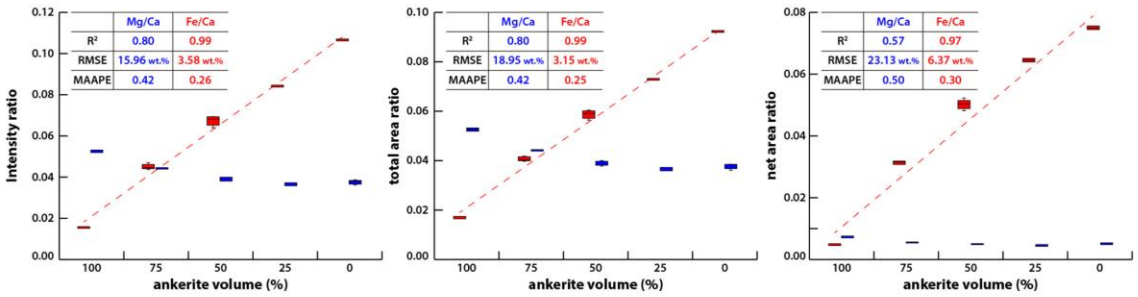

Fig. 13. Boxplot of the Mg/Ca (blue) and Fe/Ca (red) spectral ratio obtained by LIBS analysis of the ankerite-dolomite mixture. (For interpretation of the references to colour in this figure legend, the reader is referred to the web version of this article.)

0.71 of the variance of Fe variable, and more than 0.94 of the variance Mg and Mn variables in the third principal component.

To further examine carbonate classification, the three mixture samples (i.e., calcite-dolomite, calcite-ankerite, and ankerite-dolomite) used in this study were added in PCA. The two PCs account for 69.49% of the total variance among the entire spectra (Fig. 15A). The plot of the monomineralic carbonates was similar to the PCA plot shown in Fig. 14A. The clusters of the mixtures are located between the endmembers, but the points for the calcite-dolomite mixtures do not show a linear correlation (Fig. 15A). On the other hand, the region of interest from the LIBS total area, which explains the total variances of the two PCs as 75.95%, is not only well separated among the single carbonates but also all the binary mixtures show linear distribution on the score plot between the endmembers used in mixing (Fig. 15B). In the case of the net area, all the mixtures are located together with the single carbonates, accounting for 77.94% of the variance. However, the mixture plots do not show any linear correlation for the corresponding endmembers (Fig. 15C). Furthermore, this PCA plot does not distinguish between

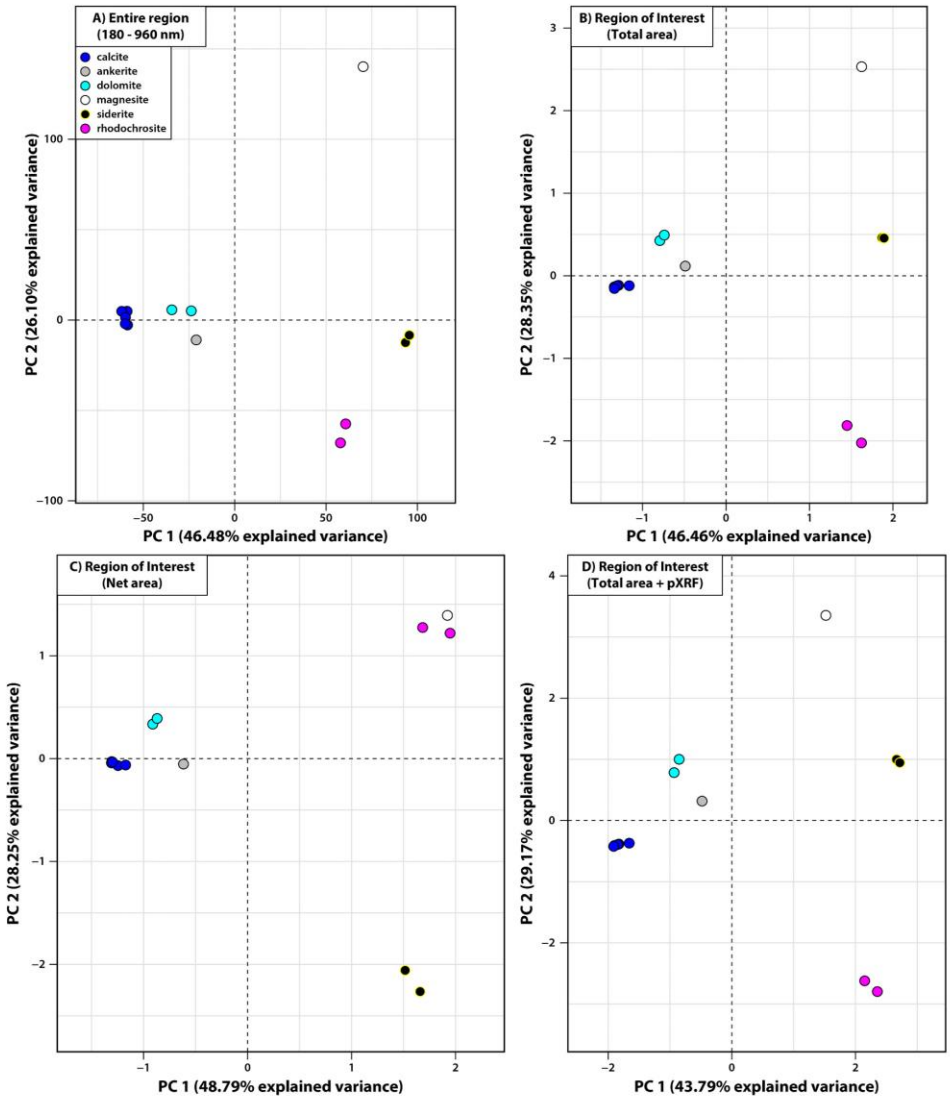

Fig. 14. PCA scores biplot for the natural carbonate standards using LIBS data and/or pXRF data. (A) Entire region of LIBS spectra, (B) Region of interest for the total area of each element, (C) Region of interest for the net area of each element, and D) LIBS total area with pXRF data.

Table 5
Determination coefficients for the region of interest for the total area and the net area from LIBS spectra between primary variables and principal components.

LIBS spectra	Total area				Net area			
	Ca	Mg	Fe	Mn	Ca	Mg	Fe	Mn
PC1	1.00	0.15	0.40	0.31	0.98	0.29	0.28	0.40
PC2	0.00	0.52	0.05	0.57	0.01	0.26	0.71	0.16
PC3	0.00	0.34	0.55	0.11	0.00	0.45	0.01	0.44

magnesite and rhodochrosite; thus, PCA using the net area did not well discriminate carbonate groups nor recognize the content changes in the mixtures. This result suggests that the PCA result of the region of interest from LIBS total area can effectively distinguish both carbonate phases and mixtures by automatically making unknown samples identified against carbonate endmembers.

4. Discussion

4.1. Standard normal variate (SNV) transformation

LIBS spectra are commonly normalized to take into account signal fluctuations and thus obtain enhanced analytical performance. However, normalization in LIBS does not indicate that normalized data always provide better analytical performance than uncorrected ones, thus this is still an open question [10]. Table 6 shows the assessment values comparing the initial spectra used in this study with SNV-corrected

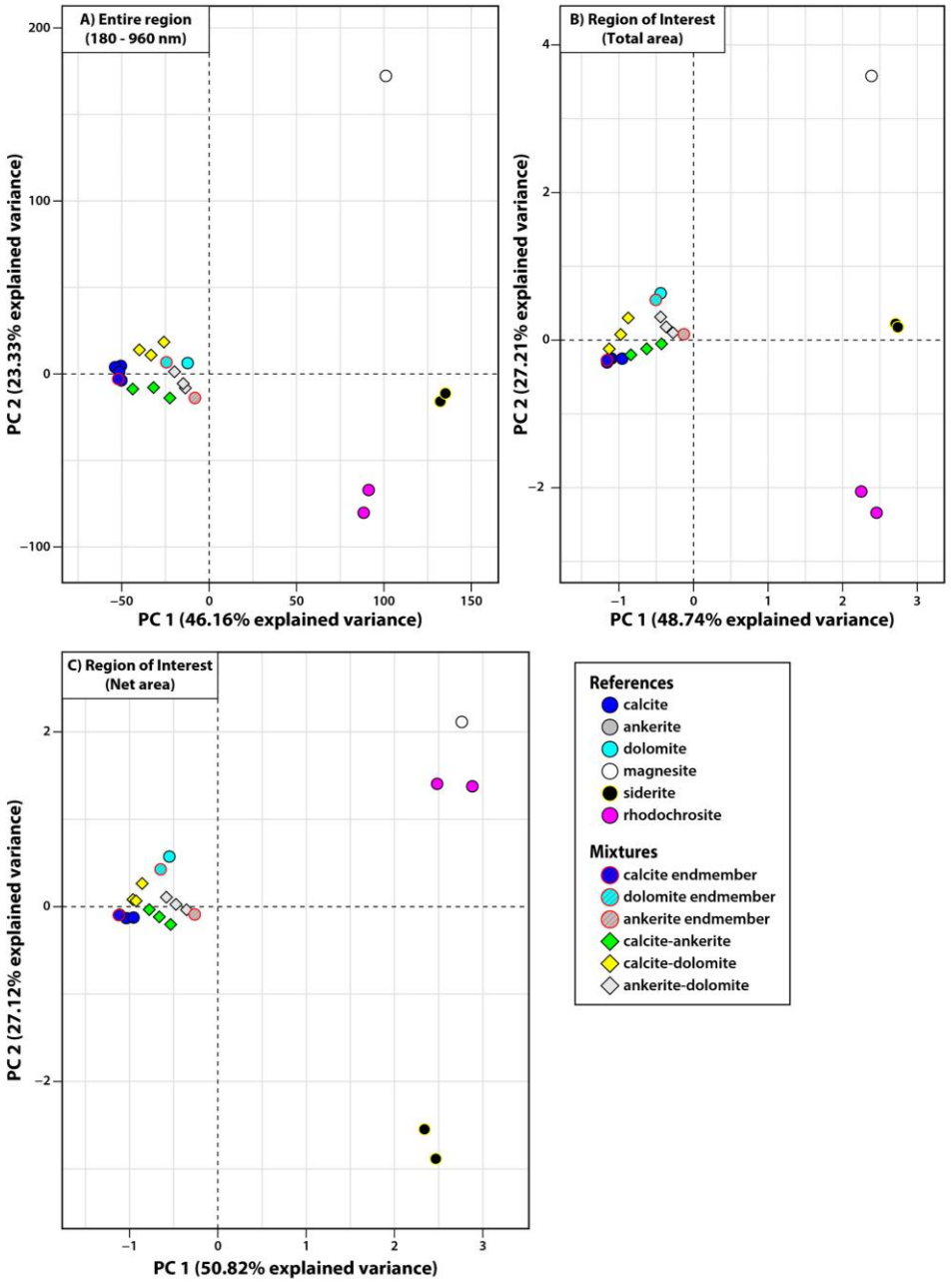

Fig. 15. PCA scores biplot for the natural carbonate standards and the binary mixtures using LIBS data and/or pXRF data.

spectra for the four emission lines of the carbonate standards spectra and the spectral ratios of the carbonate mixtures used in this study. The quantitative models were considered at the intensity and net area parameters of each emission line, and the calibration curve for magnesium excluded the rhodochrosite sample due to spectral interference with manganese emission lines. Since the total area method can be only applied to the spectra having positive values, this method was excluded from the SNV spectra, which have both positive and negative values in the target regions. The initial spectra of the carbonate standards have similar R^2 and RMSE values in Fe and Mn compared to the SNV-corrected spectra. The SNV spectra in Fe shows better MAAPE values than the those of the initial spectra, but the other elements displayed similar prediction abilities in both spectra. In the case of Ca, the calibration models from the initial spectra have better coefficient of

Table 6
Comparison of R^2, RMSE, and MAAPE values between initial spectra and SNV spectra for the elements and the mixtures.

element	emission line (nm)	parameter	Raw spectra			SNV spectra		
			R^2	RMSE	MAAPE	R^2	RMSE	MAAPE
		intensity	0.97	3.01	0.50	0.92	3.98	0.48
Ca	558.9	total area	0.96	3.10	0.50			
		net area	0.97	3.01	0.41	0.94	3.39	0.39
		intensity	0.989	1.67	0.60	0.995	1.16	0.29
Fe	495.8	total area	0.989	1.64	0.58			
		net area	0.995	1.09	0.45	0.993	1.33	0.42
		intensity	0.98	2.45	0.82	0.98	2.58	1.12
Mn	478.3	total area	0.98	2.19	0.80			
		net area	0.98	2.46	0.91	0.97	2.63	1.11
		intensity	0.90	2.57	0.75	0.92	2.25	0.72
Mg*	309.7	total area	0.87	2.92	0.76			
		net area	0.88	2.77	0.69	0.90	2.49	0.69

* Except for rhodochrosite

carbonate mixtures	spectral ratios	parameter	Raw spectra			SNV spectra		
			R^2	RMSE	MAAPE	R^2	RMSE	MAAPE
		intensity	0.995	2.59	0.24	0.996	2.14	0.24
calcite-dolomite	Mg/Ca	total area	0.967	6.42	0.30			
		net area	0.917	10.17	0.36	0.917	10.18	0.36
		intensity	0.988	3.92	0.26	0.996	2.10	0.24
	Mg/Ca	total area	0.977	5.38	0.26			
calcite-ankerite		net area	0.970	6.13	0.30	0.970	6.11	0.30
		intensity	0.997	2.00	0.23	0.998	1.70	0.23
	Fe/Ca	total area	0.992	3.09	0.21			
		net area	0.995	2.40	0.23	0.995	2.41	0.23
		intensity	0.990	3.58	0.26	0.985	4.28	0.27
ankerite-dolomite	Fe/Ca	total area	0.992	3.15	0.25			
		net area	0.967	6.37	0.30	0.967	6.38	0.30

determination and smaller prediction errors. Although Mg emission line shows a good correlation in SNV-corrected spectra, the difference with the initial spectra is not significant. In the case of the models from the carbonate mixtures reported in Table 6, the values of R^2, RMSE, and MAAPE are not significantly different from the initial LIBS data and after SNV transformation. In conclusion, SNV transformation in the carbonate minerals and the mixtures exhibits a better or worse predictive ability than the model built from non-corrected data. This result can be interpreted as fewer matrix effects and signal fluctuations due to the same sample condition prepared as pellets in this study. For this reason, we consider that it is better for studies of this type only to involve results obtained from the initial data.

4.2. Applicability of LIBS portable device in the field

This study was carried out on the flat surface of pelletized monomineralic samples and mixtures consisting of the same carbonate group. However, in the field, diverse mixtures commonly exist, showing various particle sizes and different mineral groups. Previous LIBS studies for mineral identification of heterogeneous mixtures used different methods of chemometrics such as PCA, Singular Value Decomposition (SVD), Partial Least Squares Discriminant Analysis (PLSDA), and Multivariate Curve Resolution – Alternating Least Square (MCR-ALS) [11,13,18]. Assuming that another portable technique can be added, the combination of LIBS-Raman or LIBS-IR analysis is the most appropriate to identify carbonate minerals in the field. A portable Raman and a portable IR analysis are both mineralogical analyses, and they are also effective to recognize the compositional changes for Ca-Mg-Fe-Mn carbonate minerals of calcite structure [20]. The user needs to export the LIBS data from the handheld device, but this method proposed in this study does not need any pre-processing such as normalization and curve-fitting by maximally reducing the data management. After the carbonate group is firstly identified by the above methods, the spectral ratios and the calibration curves in our study will be useful for distinguishing detailed carbonate classification and mixing ratios between carbonate minerals.

5. Conclusion

This quantitative study aimed to compare chemical compositions with LIBS data using natural carbonate endmembers, and two synthetic mixtures of three carbonates in a two-component system. They were used to approach the quantitative relationship between their spectral characteristics and also between their mineralogical proportions. Based on the values of determination coefficient and predictive ability, we demonstrated that all the LIBS parameters for each element, especially the intensity or net area, are linearly correlated with the elemental concentrations acquired from a portable XRF device. Furthermore, the LIBS spectral ratios using Fe#-Mg/Mn and Fe/Ca-Mg/Mn confirmed clear separation of the single carbonate clusters from each other. While the calcite-ankerite mixture displayed a good level of correlation with both the Mg/Ca and the Fe/Ca ratio using the intensity and the total area method, the Mg/Ca ratio using the intensity method showed a higher linear tendency only in the calcite-dolomite mixtures due to low Fe content in both calcite and dolomite endmember. Meanwhile, a significant result was obtained from the Fe/Ca ratio using the intensity and total area method with the different iron content in the ankerite-dolomite mixtures. These quantitative results suggest that the spectral data using the intensity method from handheld LIBS are effectively applied to determine the chemical composition and discrimination of carbonate minerals. The linear correlations in the carbonate mixtures show potential for subsequent quantitative analysis for mineral mixtures in the field. In the future in this NEXT project, this spectral information will be applied to the core samples from the Elvira deposit, providing mineralogical and elemental information for both qualitative and quantitative analysis. The PCA using the region of interest from LIBS data could also be helpful to apply carbonate discrimination and quantification in carbonate mixtures.

Authorship statement

All persons who meet authorship criteria are listed as authors, and all authors certify that they have participated sufficiently in the work to take public responsibility for the content, including participation in the concept, design, analysis, writing, or revision of the manuscript. Furthermore, each author certifies that this material or similar material has not been and will not be submitted to or published in any other publication before its appearance in the Spectrochimica Acta Part B: Atomic Spectroscopy.

Declaration of Competing Interest

The authors declare that they have no known competing financial interests or personal relationships that could have appeared to influence the work reported in this paper.

Acknowledgment

This research is part of the NEXT project, supported by funding from the European Union's Horizon 2020 research and innovation program under Grant Agreement No. 776804 – H2020-SC5-2017. We thank all the anonymous reviewers for their critical reviews and comments.

References

[1] R.J. Barnes, M.S. Dhanoa, S.J. Lister, Standard normal variate transformation and de-trending of near-infrared diffuse reflectance spectra, Appl. Spectrosc. AS 43 (1989) 772–777.
[2] B. Bultel, J.-C. Viennet, F. Poulet, J. Carter, S.C. Werner, Detection of carbonates in martian weathering profiles, J. Geophys. Res. Planets 124 (2019) 989–1007, https://doi.org/10.1029/2018JE005845.
[3] J. Carter, F. Poulet, J.-P. Bibring, N. Mangold, S. Murchie, Hydrous minerals on Mars as seen by the CRISM and OMEGA imaging spectrometers: updated global view, J. Geophys. Res. Planets 118 (2013) 831–858, https://doi.org/10.1029/2012JE004145.
[4] W.A.F.R.S. Deer, R.A. Howie, J. Zussman, An introduction to the rock-forming minerals, Min. Soc. Great Britain Ireland. (2013), https://doi.org/10.1180/DHZ.
[5] D. Díaz Pace, N. Gabriele, M. Garcimuño, C. D'Angelo, G. Bertuccelli, D. Bertuccelli, Analysis of minerals and rocks by laser-induced breakdown spectroscopy, Spectrosc. Lett. 44 (2011) 399–411, https://doi.org/10.1080/00387010.2011.573048.
[6] B. Ehlmann, J. Mustard, S. Murchie, F. Poulet, J. Bishop, A. Brown, W. Calvin, R. Clark, D. Des Marais, R. Milliken, L. Roach, T. Roush, G. Swayze, J. Wray, Orbital Identification of Carbonate-Bearing Rocks on Mars vol. 322, Science (New York, N.Y, 2009, pp. 1828–1832, https://doi.org/10.1126/science.1164759.
[7] C. Fabre, Advances in laser-induced breakdown spectroscopy analysis for geology: a critical review, Spectrochim. Acta B At. Spectrosc. 166 (2020), 105799, https://doi.org/10.1016/j.sab.2020.105799.
[8] Y. Foucaud, C. Fabre, B. Demeusy, I.V. Filippova, L.O. Filippov, Optimisation of fast quantification of fluorine content using handheld laser induced breakdown spectroscopy, Spectrochim. Acta B At. Spectrosc. 158 (2019), 105628, https://doi.org/10.1016/j.sab.2019.05.017.
[9] G. Gisbert, E. Losantos, J.M. Pons, J.C. Videira, F. Tornos, Elvira: A New Shale-Hosted VMS Deposit in the Iberian Pyrite Belt, 2019.
[10] J. Guezenoc, A. Gallet-Budynek, B. Bousquet, Critical review and advices on spectral-based normalization methods for LIBS quantitative analysis, Spectrochim. Acta B At. Spectrosc. 160 (2019), 105688.
[11] J. Haddad, L. Canioni, B. Bousquet, Good practices in LIBS analysis: review and advices, Spectrochim. Acta B At. Spectrosc. 101 (2014) 171–182, https://doi.org/10.1016/j.sab.2014.08.039.
[12] R.S. Harmon, R.R. Hark, C.S. Throckmorton, E.C. Rankey, M.A. Wise, A.M. Somers, L.M. Collins, Geochemical fingerprinting by handheld laser-induced breakdown spectroscopy, Geostand. Geoanal. Res. 41 (2017) 563–584, https://doi.org/10.1111/ggr.12175.
[13] R.S. Harmon, C.J.M. Lawley, J. Watts, C.L. Harraden, A.M. Somers, R.R. Hark, Laser-induced breakdown spectroscopy—an emerging analytical tool for mineral exploration, Minerals 9 (2019) 718, https://doi.org/10.3390/min9120718.
[14] R.S. Harmon, J. Remus, N.J. McMillan, C. McManus, L. Collins, J.L. Gottfried, F. C. DeLucia, A.W. Miziolek, LIBS analysis of geomaterials: geochemical fingerprinting for the rapid analysis and discrimination of minerals, Appl. Geochem. 24 (2009) 1125–1141, https://doi.org/10.1016/j.apgeochem.2009.02.009.
[15] P. Heraud, B.R. Wood, J. Beardall, D. McNaughton, Effects of pre-processing of Raman spectra on in vivo classification of nutrient status of microalgal cells, J. Chemom. 20 (2006) 193–197, https://doi.org/10.1002/cem.990.
[16] Y. Iida, Effects of atmosphere on laser vaporization and excitation processes of solid samples, Spectrochim. Acta B At. Spectrosc. 45 (1990) 1353–1367, https://doi.org/10.1016/0584-8547(90)80188-O.
[17] A. Ismaël, B. Bousquet, K.M.-L. Pierrès, G. Travaillé, L. Canioni, S. Roy, In situ semi-quantitative analysis of polluted soils by laser-induced breakdown spectroscopy (LIBS), Appl. Spectrosc. AS 65 (2011) 467–473.
[18] N. Khajehzadeh, T.K. Kauppinen, Fast mineral identification using elemental LIBS technique, in: IFAC-PapersOnLine, 4th IFAC Workshop on Mining, Mineral and Metal Processing MMM 2015 48, 2015, pp. 119–124, https://doi.org/10.1016/j.ifacol.2015.10.089.
[19] S. Kim, H. Kim, A new metric of absolute percentage error for intermittent demand forecasts, Int. J. Forecast. 32 (2016) 669–679, https://doi.org/10.1016/j.ijforecast.2015.12.003.
[20] Y. Kim, M.-C. Caumon, O. Barres, A. Sall, J. Cauzid, Identification and composition of carbonate minerals of the calcite structure by Raman and infrared spectroscopies using portable devices, Spectrochim. Acta A Mol. Biomol. Spectrosc. 261 (2021), 119980, https://doi.org/10.1016/j.saa.2021.119980.
[21] N.L. Lanza, R.C. Wiens, S.M. Clegg, A.M. Ollila, S.D. Humphries, H.E. Newsom, J. E. Barefield, Calibrating the ChemCam laser-induced breakdown spectroscopy instrument for carbonate minerals on Mars, Appl. Opt. AO 49 (2010) C211–C217, https://doi.org/10.1364/AO.49.00C211.
[22] V. Lazic, A. Fantoni, A. Colao, A. Santagata, A. Moroneb, V. Spizzichino, Quantitative laser induced breakdown spectroscopy analysis of ancient marbles and corrections for the variability of plasma parameters and of ablation rate, J. Anal. At. Spectrom. 19 (2004) 429, https://doi.org/10.1039/b315606k.
[23] S. Lê, J. Josse, F. Husson, FactoMineR: an R package for multivariate analysis, J. Stat. Softw. 25 (2008) 1–18, https://doi.org/10.18637/jss.v025.i01.
[24] N.J. McMillan, R.S. Harmon, F.C. De Lucia, A.M. Miziolek, Laser-induced breakdown spectroscopy analysis of minerals: Carbonates and silicates, in: Spectrochimica Acta Part B: Atomic Spectroscopy, A Collection of Papers Presented at the 4th International Conference on Laser Induced Plasma Spectroscopy and Applications (LIBS 2006) 62, 2007, pp. 1528–1536, https://doi.org/10.1016/j.sab.2007.10.037.
[25] F. Menges, Spectragryph-Optical Spectroscopy Software, Version 1.2. 14, 2020, 2020.
[26] R Core Team, Rf, R: A Language and Environment for Statistical Computing, R foundation for statistical computing Vienna, Austria, 2013.
[27] L.J. Radziemski, D.A. Cremers, Laser-Induced Plasmas and Applications, 1989.
[28] F. Rezaei, G. Cristoforetti, E. Tognoni, S. Legnaioli, V. Palleschi, A. Safi, A review of the current analytical approaches for evaluating, compensating and exploiting self-absorption in laser induced breakdown spectroscopy, Spectrochim. Acta B At. Spectrosc. 169 (2020), 105878.
[29] J.R. Ridley, Ore Deposit Geology, 2013, https://doi.org/10.1017/CBO9781139135528.
[30] Å. Rinnan, F. van den Berg, S.B. Engelsen, Review of the most common pre-processing techniques for near-infrared spectra, TrAC Trends Anal. Chem. 28 (2009) 1201–1222, https://doi.org/10.1016/j.trac.2009.07.007.
[31] A.S. Rivkin, E.L. Volquardsen, B.E. Clark, The surface composition of Ceres: discovery of carbonates and iron-rich clays, Icarus 185 (2006) 563–567, https://doi.org/10.1016/j.icarus.2006.08.022.
[32] S. Romero-Torres, J.D. Pérez-Ramos, K.R. Morris, E.R. Grant, Raman spectroscopy for tablet coating thickness quantification and coating characterization in the presence of strong fluorescent interference, J. Pharm. Biomed. Anal. 41 (2006) 811–819, https://doi.org/10.1016/j.jpba.2006.01.033.
[33] G.S. Senesi, R.S. Harmon, R.R. Hark, Field-portable and handheld laser-induced breakdown spectroscopy: historical review, current status and future prospects, Spectrochim. Acta B At. Spectrosc. 175 (2021), 106013, https://doi.org/10.1016/j.sab.2020.106013.
[34] D. Syvilay, J. Guezenoc, B. Bousquet, Guideline for increasing the analysis quality in laser-induced breakdown spectroscopy, Spectrochim. Acta B At. Spectrosc. 161 (2019), 105696, https://doi.org/10.1016/j.sab.2019.105696.
[35] D. Syvilay, N. Wilkie-Chancellier, B. Trichereau, A. Texier, L. Martinez, S. Serfaty, V. Detalle, Evaluation of the standard normal variate method for laser-induced breakdown spectroscopy data treatment applied to the discrimination of painting layers, Spectrochim. Acta B At. Spectrosc. 114 (2015) 38–45, https://doi.org/10.1016/j.sab.2015.09.022.
[36] Team, Rs, RStudio: integrated development for R. RStudio, Inc., Boston, MA URL http://www. rstudio. com 42, 2015, p. 14.
[37] J. Velasco-Acebes, F. Tornos, A.T. Kidane, M. Wiedenbeck, F. Velasco, A. Delgado, Isotope geochemistry tracks the maturation of submarine massive sulfide mounds (Iberian Pyrite Belt), Mineral. Deposita 54 (2019) 913–934, https://doi.org/10.1007/s00126-018-0853-x.

3. Carbonate discrimination by VNIR-SWIR and pXRD

3.1. VNIR-SWIR spectroscopy

Carbonate minerals have several diagnostic absorption characteristics mainly depending on the amount of Mg, Fe and Mn replacing Ca in the VNIR-SWIR region, showing considerable changes in location and shape based on combination and overtone of the CO_3 fundamentals (Clark et al., 1990; Gaffey, 1985; Laukamp, 2011; Pontual, 2008). Four vibrational modes in the free CO_3^{-2} ion appear in medium infrared: the symmetric stretch, ν_1: 1063 cm^{-1}; the out-of-plane bend, ν_2: 879 cm^{-1}; the asymmetric stretch, ν_3: 1415 cm^{-1}; and the in-plane bend, v4: 680 cm^{-1} (Clark et al., 1990). The main diagnostic absorption feature in the SWIR region is located between 2300 and 2340 nm due to an asymmetric stretch of the CO_3 anion ($3\nu_3CO_3$) with a characteristic left-hand asymmetry (**Fig. 42**). Carbonate discrimination by the SWIR spectroscopy was carried out using pellets of pure carbonate powders from the spectral library in **Chapter II**. The spectral library from USGS and JPL (Jet Propulsion Laboratory) provides only spectral data of carbonate minerals without composition data. Furthermore, no studies have reported a univariate analysis between band shifts and compositional changes among the most common carbonate minerals in the calcite structure. The pure carbonates were prepared as a 13 mm diameter pellet by using a 10 tons hydraulic press. Each spectrum is produced from an average of 20 measurement to represent the overall spectral pattern in the VNIR-SWIR range (350-2500 nm). Prior to its first usage, the instrument is calibrated using a specialized ceramic disk with 99% whiteness. The selection of the absorption position was determined by the wavelength at maximum absorption after removing the convex-hull of the signal by hull quotient installed in the ENVI software (Exelis, 2012).

The absorption bands in the SWIR region are located at near 2300 nm for magnesite, at near 2320 nm for dolomite, at near 2330 nm for ankerite, at near 2332 nm for siderite, and at near 2340 nm for calcite, respectively (**Fig. 42**). Rhodochrosite has longer diagnostic absorption at 2365 nm compared to the other carbonate minerals, and three Mn absorptions of rhodochrosite are additionally observed at 408, 448, and 554 nm in the visible region. Therefore, carbonate minerals without rhodochrosite display the diagnostic absorption band located between 2300 nm and 2340 nm. **Fig. 42** also highlights two weaker, but diagnostic absorption features for recognizing presence and composition of carbonates due to $\nu_1+3\nu_3$ and $2\nu_1+2\nu_3$ in

carbonate minerals (Hunt and Salisbury, 1971). For example, in calcite, the bands are observed at near 1880 and 1990 nm, respectively. These two features appear always as pairs in carbonates and though decreasing in intensity with increasing Mg or Fe content, they display as well a blue-shift with increasing replacement of Ca by Mg and Fe (Laukamp, 2011). Diagnostic ferrous (Fe^{2+}) iron in carbonate minerals produces a broad double absorption band due to Fe^{2+} crystal field in the NIR region between 1000 and 1300 nm (**Fig. 42**, Gaffey, 1985). However, the strength of the Fe^{2+} crystal field has been found to be highly variable, especially when comparing across mineral species (Gaffey, 1985; Hunt and Salisbury, 1971).

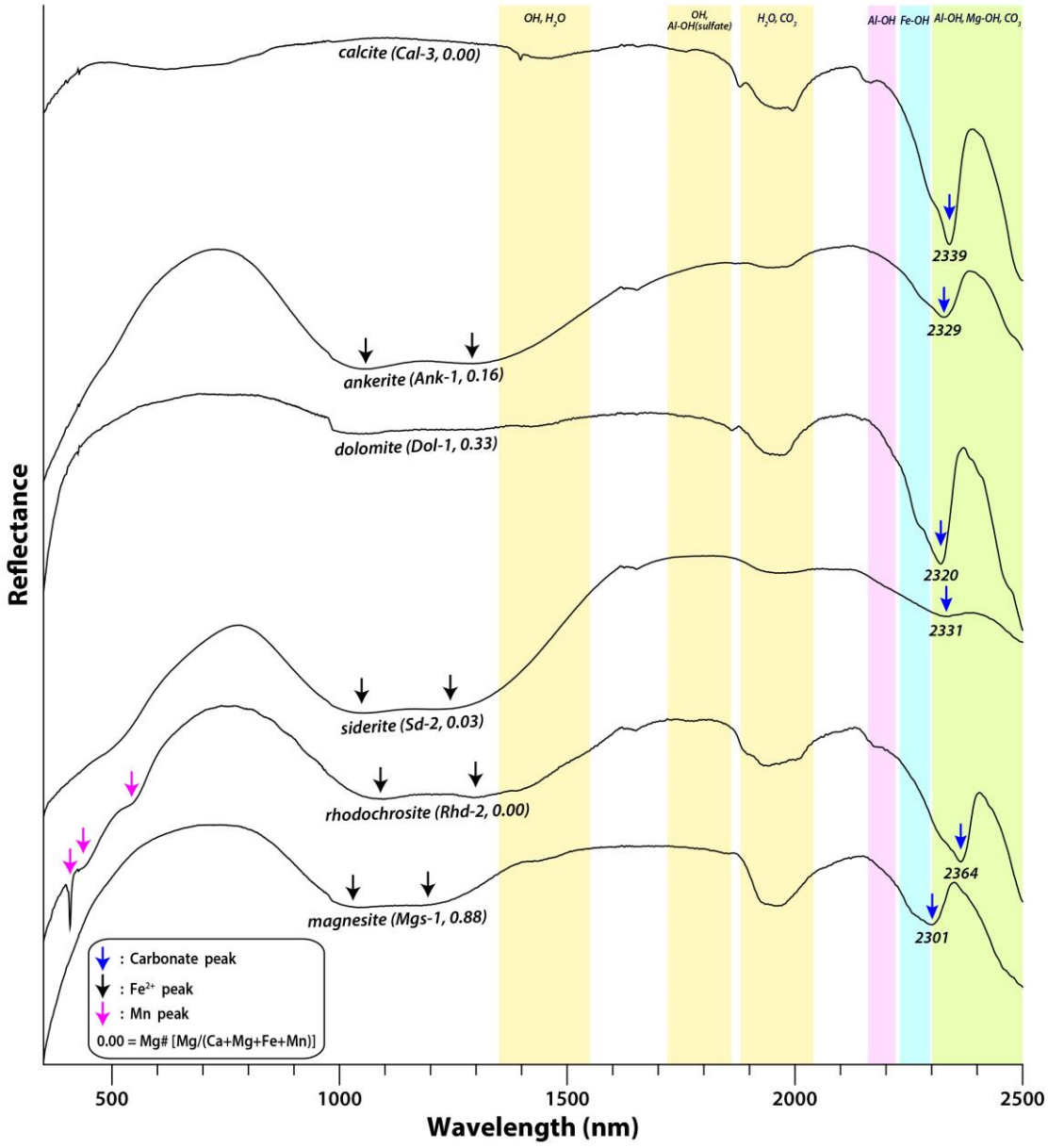

Fig. 42. Representative VNIR-SWIR spectrum of each carbonate mineral.

Fig. 43 exhibits the correlation between Mg# and the absorption position of the carbonate minerals. Two sets of samples were used in this study. The first set is from the spectral library in **Chapter II**, and 21 carbonate samples consisting of 15 calcite, 5 dolomite, and 1 ankerite were added from a previous study to extend the dataset in this study and compare them with the results from our samples (Kim et al., 2017). The most Mg-rich magnesite (0.90 Mg#) has a band position at 2301 nm, and dolomite has lower Mg# values (0.34-0.38) with longer absorption region at 2317-2321 nm (**Fig. 43**). The band position of ankerite occurs at 2329 and 2330 nm, and they yield low Mg# values of 0.20 and 0.11, respectively. Ca-rich calcite (0.00-0.03 Mg#) shows the diagnostic band at 2336-2340 nm, and Fe-rich siderite has absorption positions (2331-2332 nm) and Mg# values (0.08-0.04 Mg#) between those of the ankerite and calcite (**Fig. 43**). Mn-rich rhodochrosite is observed at 2364 nm far from the other carbonates. Therefore, an increase in Mg concentration of carbonate minerals appears to be associated with a band shift from 2340 towards 2300 nm.

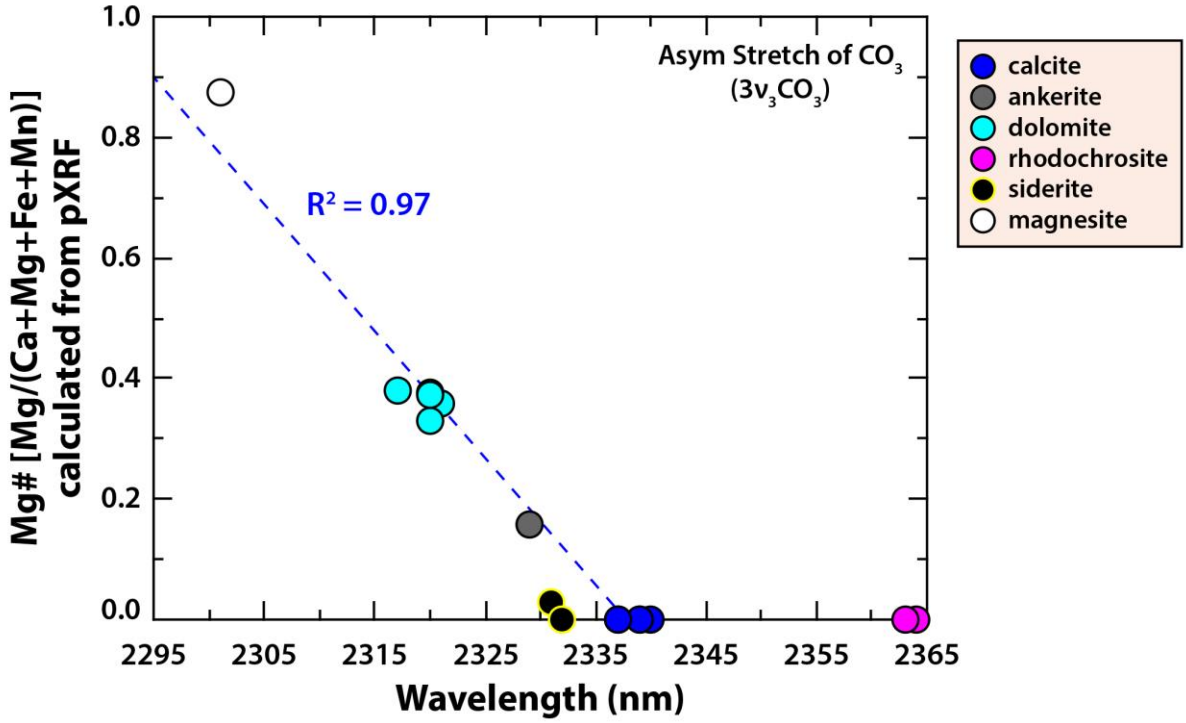

Fig. 43. Correlation between the absorption band and Mg# of carbonate minerals.

3.2. Portable X-ray diffraction (pXRD)

X-ray diffraction is a conventional method for mineralogical research based on crystal constructive interference of monochromatic X-ray and a crystalline sample following the Bragg's Law. XRD technique associated with geology has been well established in the study of hydrothermal system, as it allows for the identification and quantification of mineral assemblages (Jenkins et al., 1997). Nevertheless, XRD analysis has been performed in the laboratory due to several limitations. The most significant factor is the size of the instrument and the measurement condition that ensures stable movement of the detector or the X-ray source with a fixed sample holder. However, the Olympus Terra pXRD instrument used in this study employs a patented Vibrating Sample Holder (VSH) that the sample is moving as suspension, not the parts of the instrument (Sarrazin et al., 2005). This technique made it possible to carry a portable device with the size and weight of a suitcase held in one hand. It is consequently suggested the possibility of on-site analysis for geological application firstly reviewed by Burkett et al. (2015).

The position of the diffraction peak was used as an indicator of the Mg number in carbonate by Solotchina et al. (2009). However, the target minerals are only calcite-dolomite series, and these are analyzed by a laboratory-based instrument. As in the case of carbonate study in VNIR-SWIR analysis, comparison of compositional changes with the positions of the diffraction peaks in the various carbonates has not yet been studied with a portable XRD instrument. In this study, the Olympus Terra pXRD instrument owned by Geological Survey of Finland (GTK) in Rovaniemi was used as a part of the NEXT project.

The carbonate samples were prepared in the form of powder with particles of less than 150 μm, the minimum amount is 15 mg. The portable XRD device operates with CoKα radiation (λ = 1.789), and a data collection range of 5 to 55° 2θ (10.26 to 1.94 Å) with an increment of 0.25°. The number of measurements varies from 75 to 120 depending on the degree of constant background. Furthermore, the RRUFF database were added to extend the dataset in this study and compare them with the results from our samples (Lafuente et al., 2015). Since the samples from the RRUFF database were measured using Cu-Kα radiation (λ = 1.542), each XRD pattern was converted from CuKα to CoKα radiation.

Carbonate minerals in the calcite structure are identified between 34° and 39° 2θ CoKα (3.06 to 2.68 Å) interval based on the position of the most intense reflection (hkl = 104) in the trigonal varieties (**Fig. 44**). The peak reflection of calcite is observed in lower 2θ angles (34.3°, 3.03 Å), while magnesite exhibits the peak reflection in higher 2θ angles (38.1°, 2.74 Å). The 2θ position of the diffraction peak arises from 35.9° (2.90 Å) in ankerite, 36.1° (2.89 Å) in dolomite, 36.6° (2.85 Å) in rhodochrosite, and 37.4° (2.79 Å) in siderite, respectively (**Fig. 44**). The position of the diffraction peak in the carbonates is well scattered among minerals within the peak interval (34°-39°), thus this interval is the best region for carbonate discrimination (**Fig. 45**).

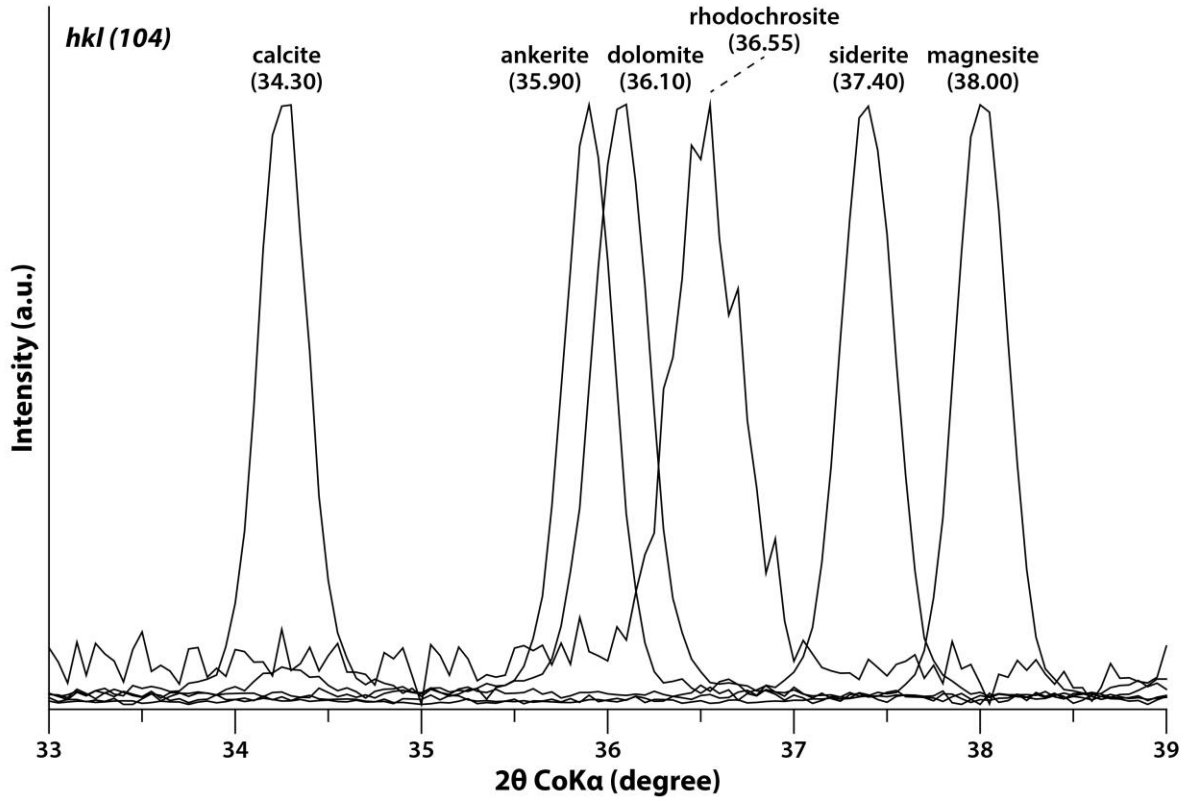

Fig. 44. Representative XRD pattern of each carbonate mineral.

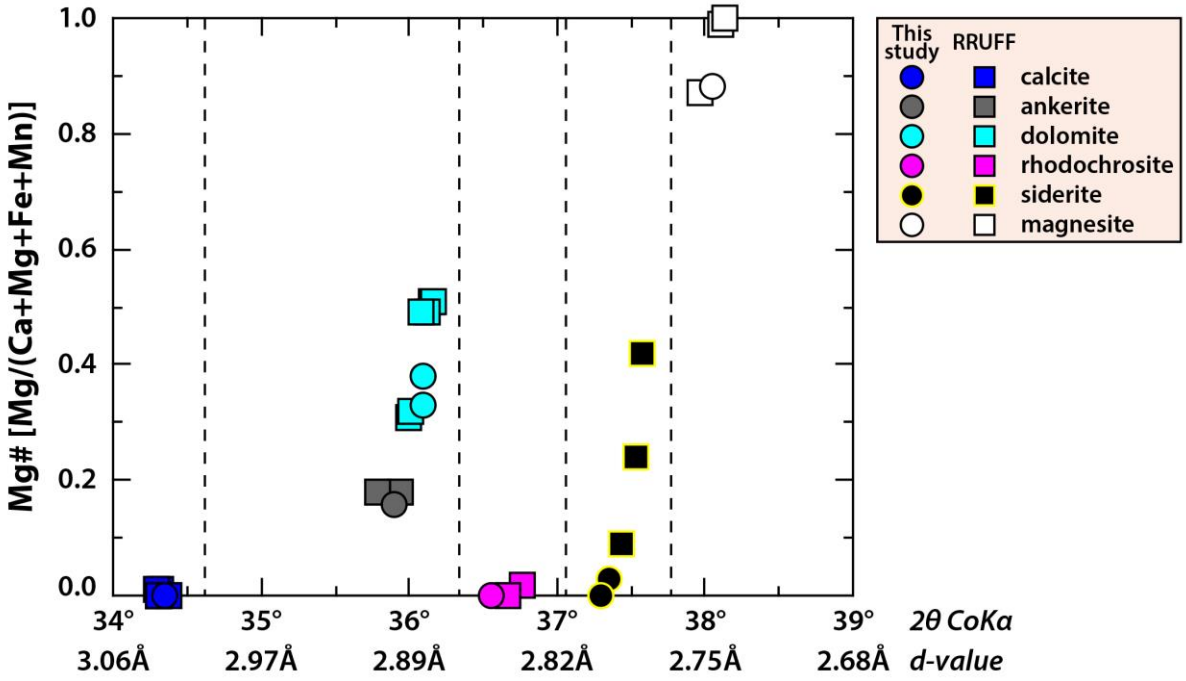

Fig. 45. Correlation between the position of the diffraction peak and Mg# of carbonate minerals.

4. Self-Organizing Map (SOM)

Self-Organizing Maps (SOM) is an unsupervised clustering method that arranges a set of n-dimensional vectors to a usually one to three-dimensional SOM lattice so that similar vectors are located close to one another (Kohonen, 2001). The advantages of SOM are easily interpreted and understood in a 2D map, and capable of handling several types of classification. SOM can be applied to diverse regions, for example, elemental or mineral classification on thin-sections, and mapping SOM data on thin-sections or satellite images. In this study, "GisSOM" software under development by GTK in Kuopio as a part of the NEXT project was tested to investigate how carbonate minerals with different chemical compositions are discriminated against on SOM based on our spectral data. Four different types of portable instruments were used: Raman, XRD and MIR with attenuated total reflectance (ATR) mode. Portable XRF data was used quantified (interpreted) data only, not spectra. 11 pure carbonate minerals from the spectral library in **Chapter II** are used by representing six carbonate groups: calcite, ankerite, dolomite, siderite, rhodochrosite, and magnesite. The experiment progressed using a SOM-network with 10x10 neurons and a toroid map type. The dataset containing all

the four techniques (i.e., parameters) has more than 130 variables, and the location of the data point in the SOM map was investigated in this study.

The experiment procedure was systematically carried out by using spectral data from one to four techniques successively to observe how well the minerals can be distinguished with each combination of different types of spectra. When GisSOM operated, the 11 mineral samples rapidly found their place on the 10x10 SOM and extended their properties to the neighbourhood each time they were represented to the SOM as they spread like drops of aquarelle paint on wet paper. All SOM nodes had learned during the training and represented spectral values similar to the sample minerals or their mixtures in the end. The 100 SOM neurons were further clustered using k-means clustering method implemented in "GisSOM" software to see which minerals each node on the final SOM represent. It was then easy to colour the SOM to show the regions representing similar variable values.

The result showed that the more parameters were applied, the better the different minerals could be distinguished (**Fig. 46**). Dolomite and ankerite, for example, clustered in the same group using the data from three instruments (i.e., XRF, Raman and XRD). However, the two minerals were separated by adding the fourth type of spectral data (MIR) and produced a well-organized SOM. The promising result indicates the possibilities of spectral identification of minerals based on SOM. These mineral spectra example shows the usefulness of SOM for extending the information in the available dataset to data of yet non-existing samples. One can assume that all the cells on SOM that belong to the same k-means cluster represent samples of similar composition. For instance, the entire red region on the SOM in **Fig. 46** represents siderite even though only three siderite samples are available in the dataset, and, thus, only three red SOM nodes are assigned a sample. The spectral values of the rest (17) of the red cells on SOM represent other kinds of spectra typical for siderite samples. In this study, the number of samples and the size of SOM were relatively small, but large enough to distinguish different minerals. The more mineral samples we had, the bigger SOM we could have, and the more details we could reveal about the spectra of pure minerals and possibly also mineral mixtures. There is still a lot to learn and study in this field of research.

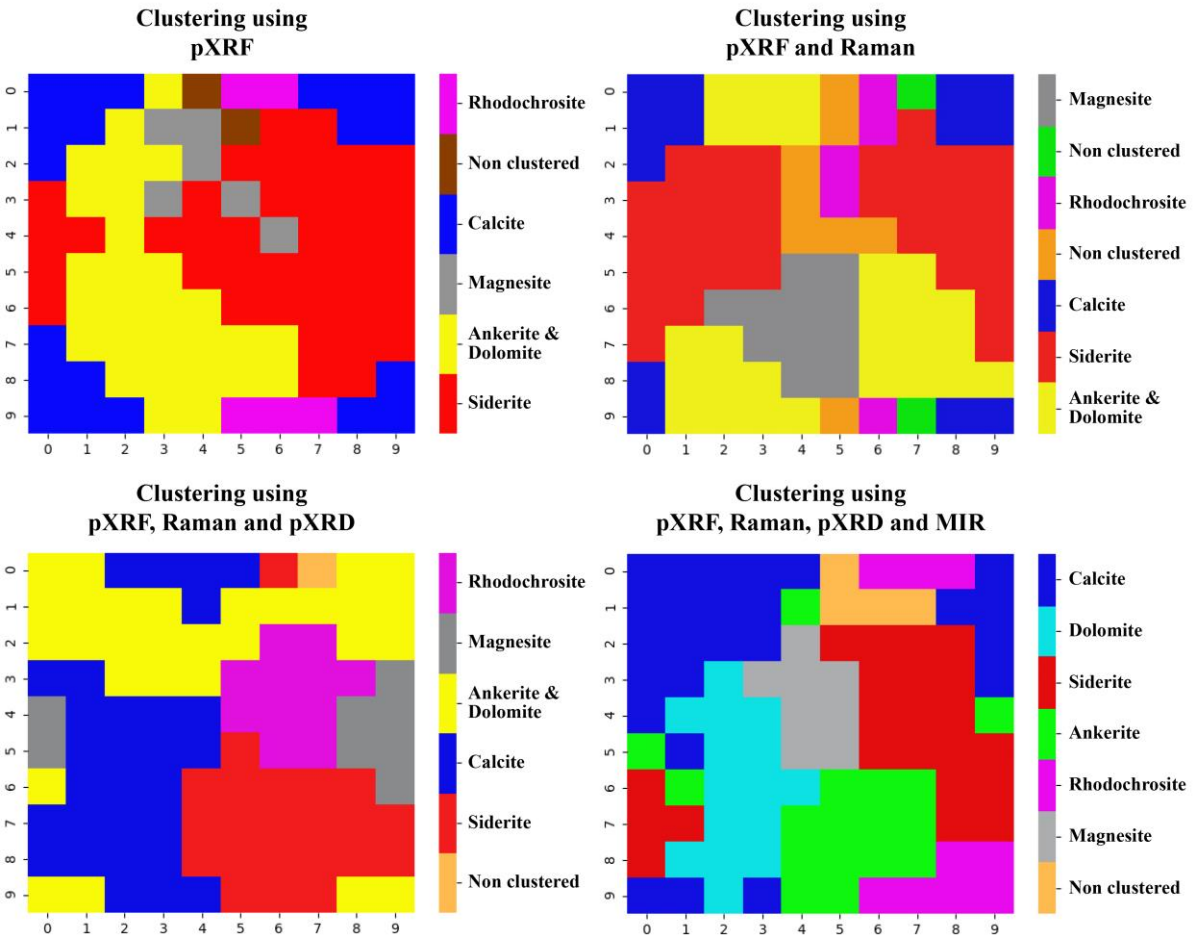

Fig. 46. Clustering results from SOM computed by different parameters using the spectral data of pure carbonate minerals in the NEXT project.

5. Carbonate quantification by Raman, MIR-ATR and pXRD

Carbonate-rich alteration is widely distributed in the IPB and in particular, a systematic mineralogical and textural variation is shown according to depth in the Sotiel-Migollas (Velasco-Acebes et al., 2019). The spatial distribution of the carbonate alteration in the Sotiel-Migollas deposit displayed the gradual change from siderite in the uppermost drillhole to ankerite to dolomite in the deepest parts. Since some carbonates are replaced or crosscut by veinlets of other carbonates with different compositions, quantitative changes among the carbonates are bound to appear with the compositional changes as well. In this study, synthetic mixtures among calcite-ankerite-dolomite are analysed to assess the quantitative relationship between the spectral ratios and the mineral volumes in the two- or three-component systems.

Experiments on the synthetic mixtures are carried out by portable two Raman, MIR-ATR, and XRD instruments. Each pure carbonate mineral is selected from the spectral database in **Chapter II**. The mixtures were prepared by mixing different proportions, weighting 3:1, 1:1, and 1:3 for the two-component system, and 1:1:1 for the three-component system. Since calcite (2.72), ankerite (2.93), and dolomite (2.86) have similar densities, the mixed samples were prepared by applying mass ratios replacing their volume ratios (Deer et al., 2013). The measurement parameters for the mixed samples are the same as those of the sample measurement performed in **Chapter II**.

5.1. Binary mixtures of carbonate minerals

The baseline-corrected Raman spectra obtained from the portable device using a green laser show differences in peak intensity of each carbonate according to the mineral contents of calcite-dolomite, calcite-ankerite, and ankerite-dolomite while the peak position is fixed (**Fig. 47-49**). The carbonate mixtures are quantified by measuring both bands from 150 to 180 cm^{-1} (Region I) and from 275 to 300 cm^{-1} (Region II) due to translational and librational lattice mode, respectively. The spectral ratio calculated by dividing the maximum intensity of the two minerals is compared to the mixing ratio. The spectral ratios calculated from the Raman spectra are highly correlated with the mineral content in both regions (**Fig. 50**). It is confirmed that the slopes obtained from the trend lines decreased as the peak position between the two carbonates approached. In particular, the ankerite-dolomite mixtures exhibit that the spectral ratios in both regions are well reflected in accordance with mineral content by showing determination coefficients higher than 0.97, despite the similar peak position between them.

The other Raman set measured by the portable Raman device with a red-NIR laser consists of average spectra of six spectra per sample. Then, the average spectrum is carried out for quantitative analysis after baseline correction using the peak occurring in the 710-730 cm^{-1} range (**Fig. 51**). Each trend line obtained from the spectral ratio shows a linearly strong correlation (R^2 higher than 0.97) with the mineral content (**Fig. 52**). These Raman results, therefore, show that both portable techniques are effectively applicable to the determination of quantification in carbonate mixtures.

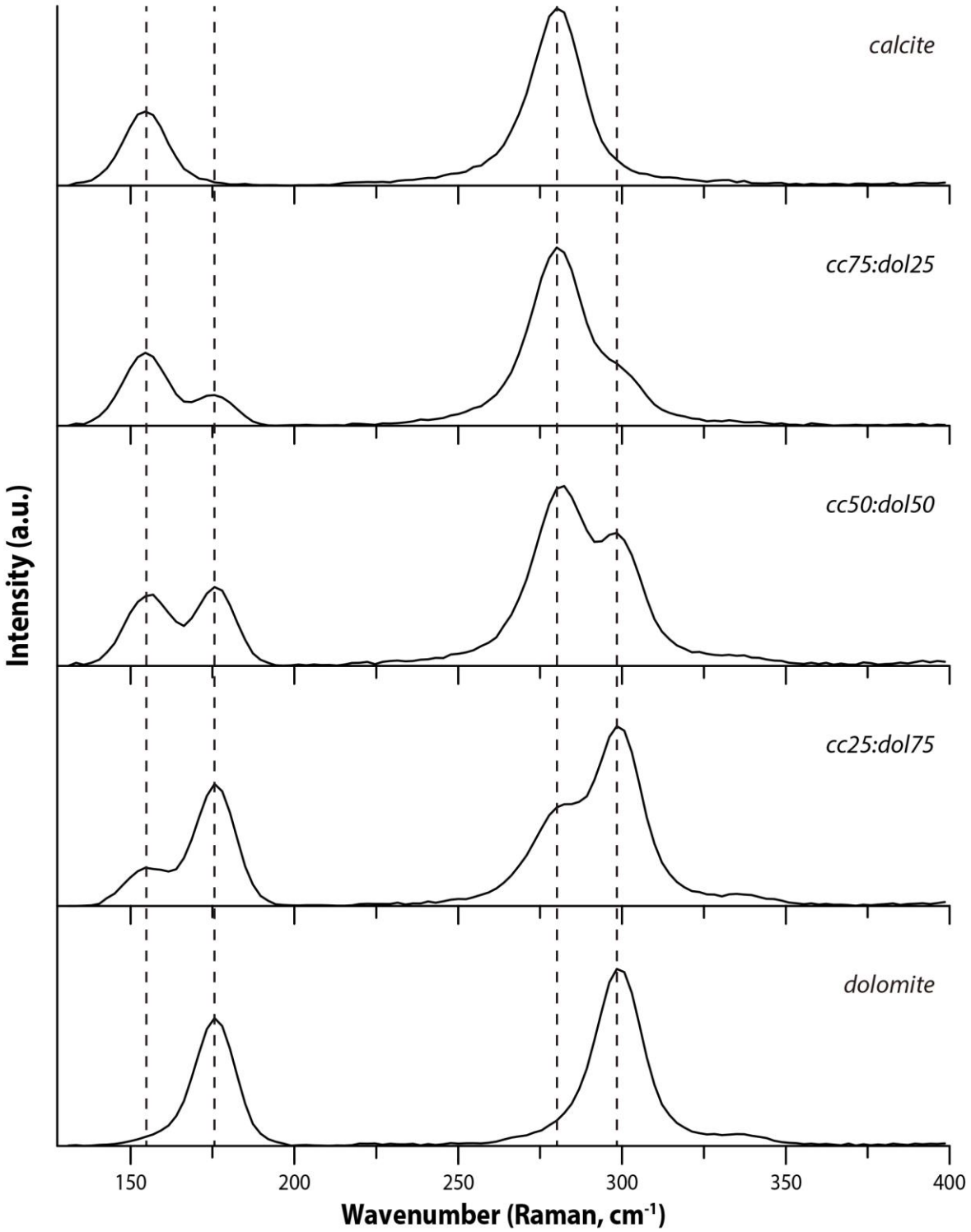

Fig. 47. Raman (green) spectra of the calcite-dolomite mixtures.

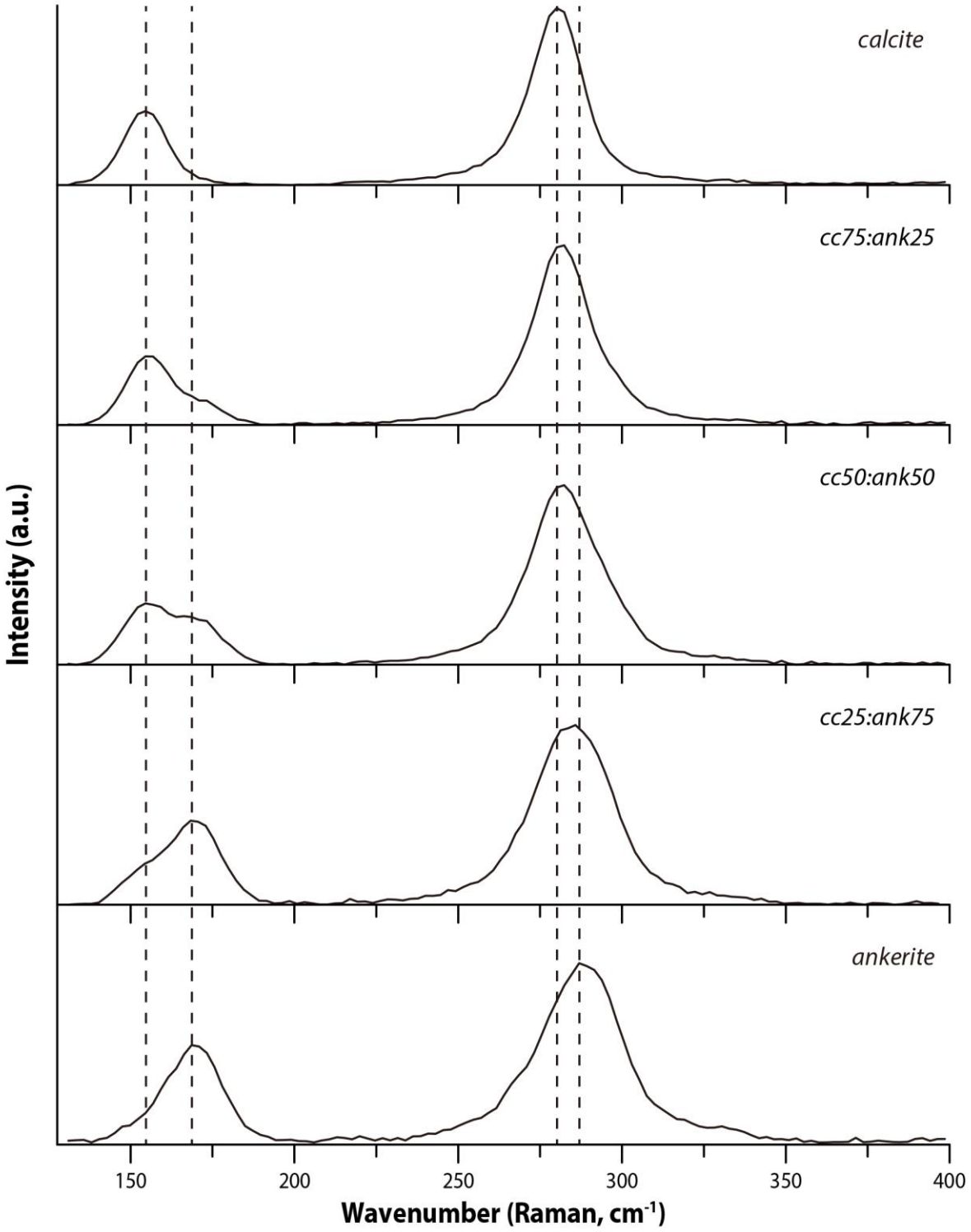

Fig. 48. Raman (green) spectra of the calcite-ankerite mixtures.

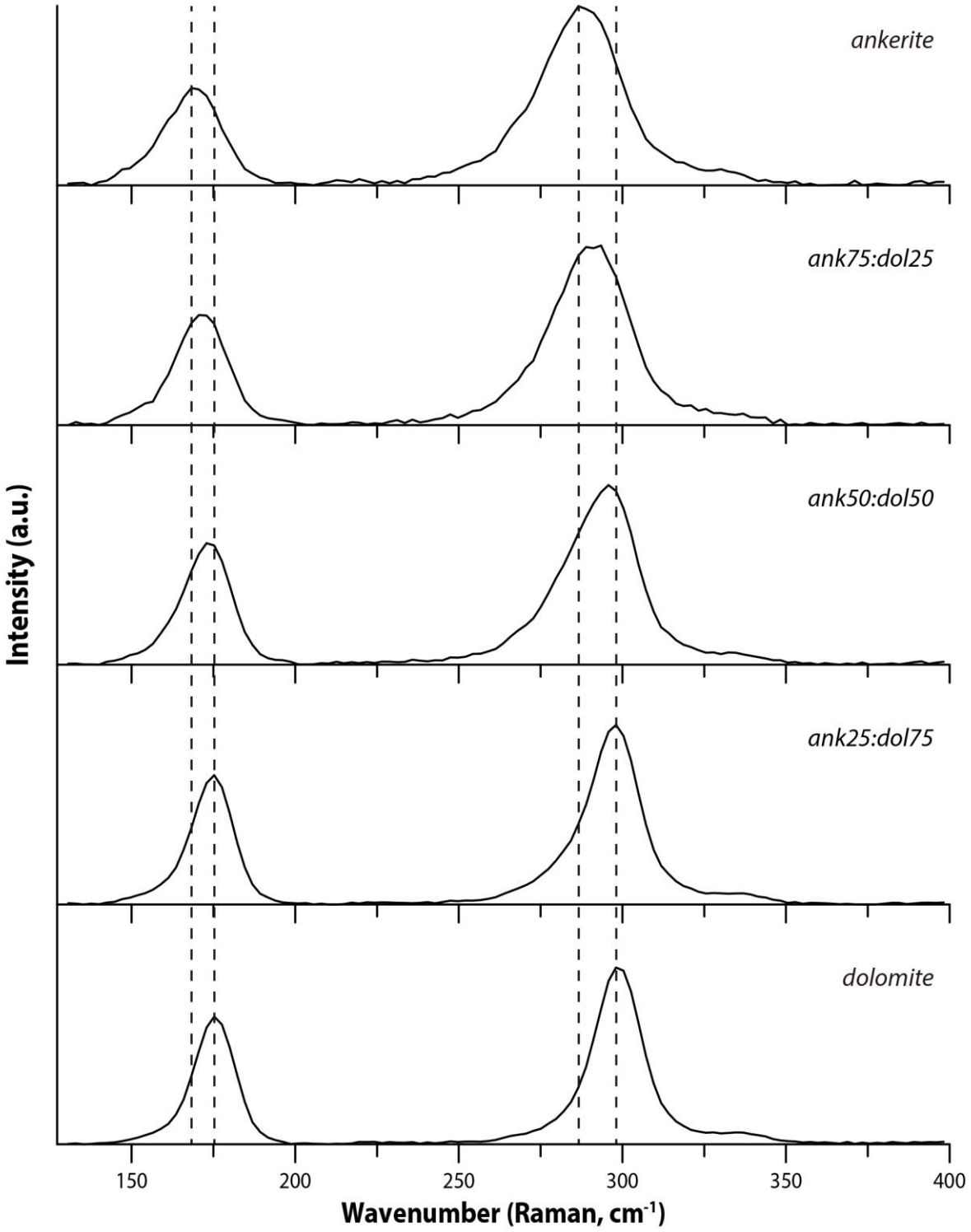

Fig. 49. Raman (green) spectra of the ankerite-dolomite mixtures.

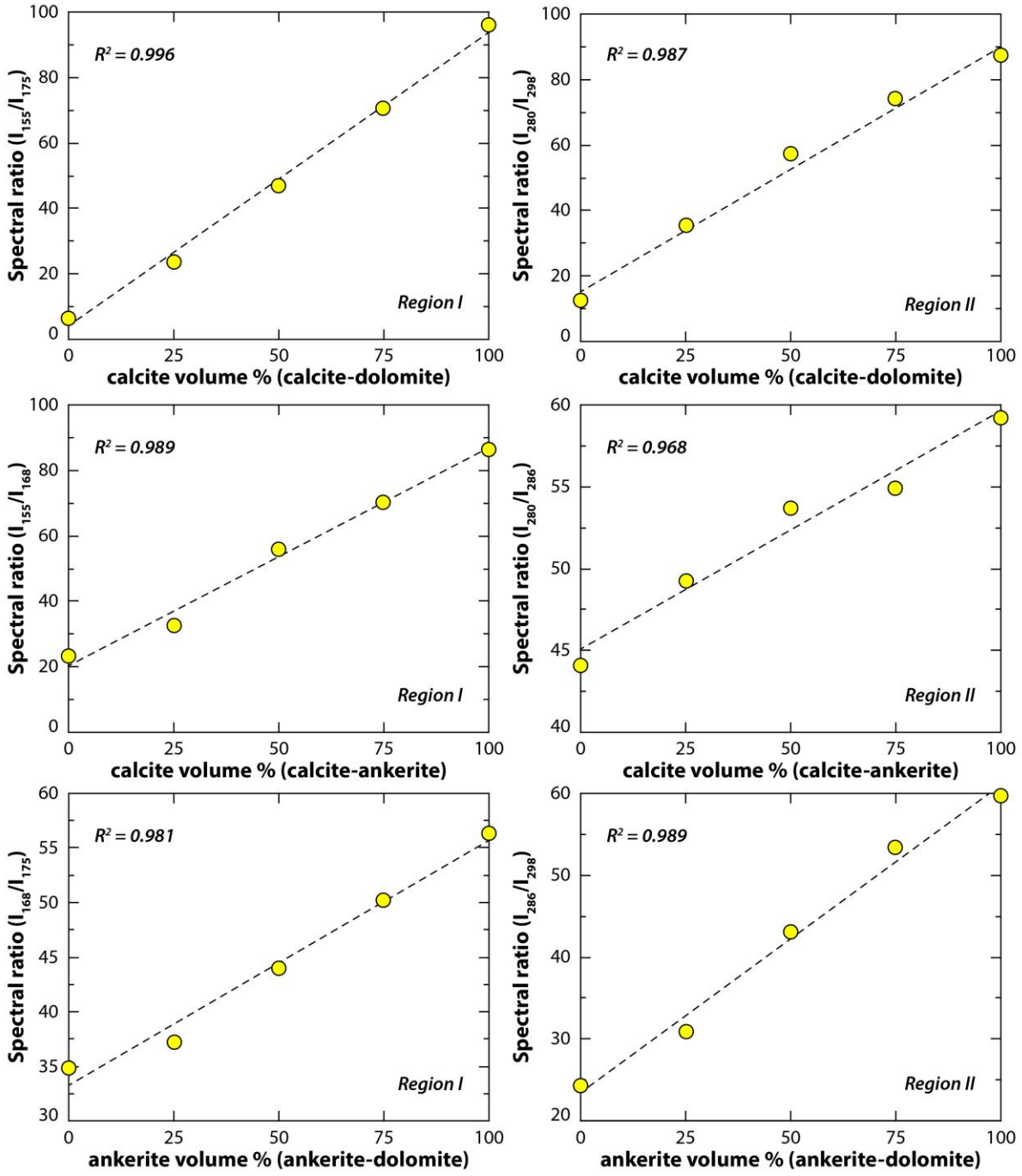

Fig. 50. Correlation between the spectral ratios from Raman (green) and the mixing ratios.

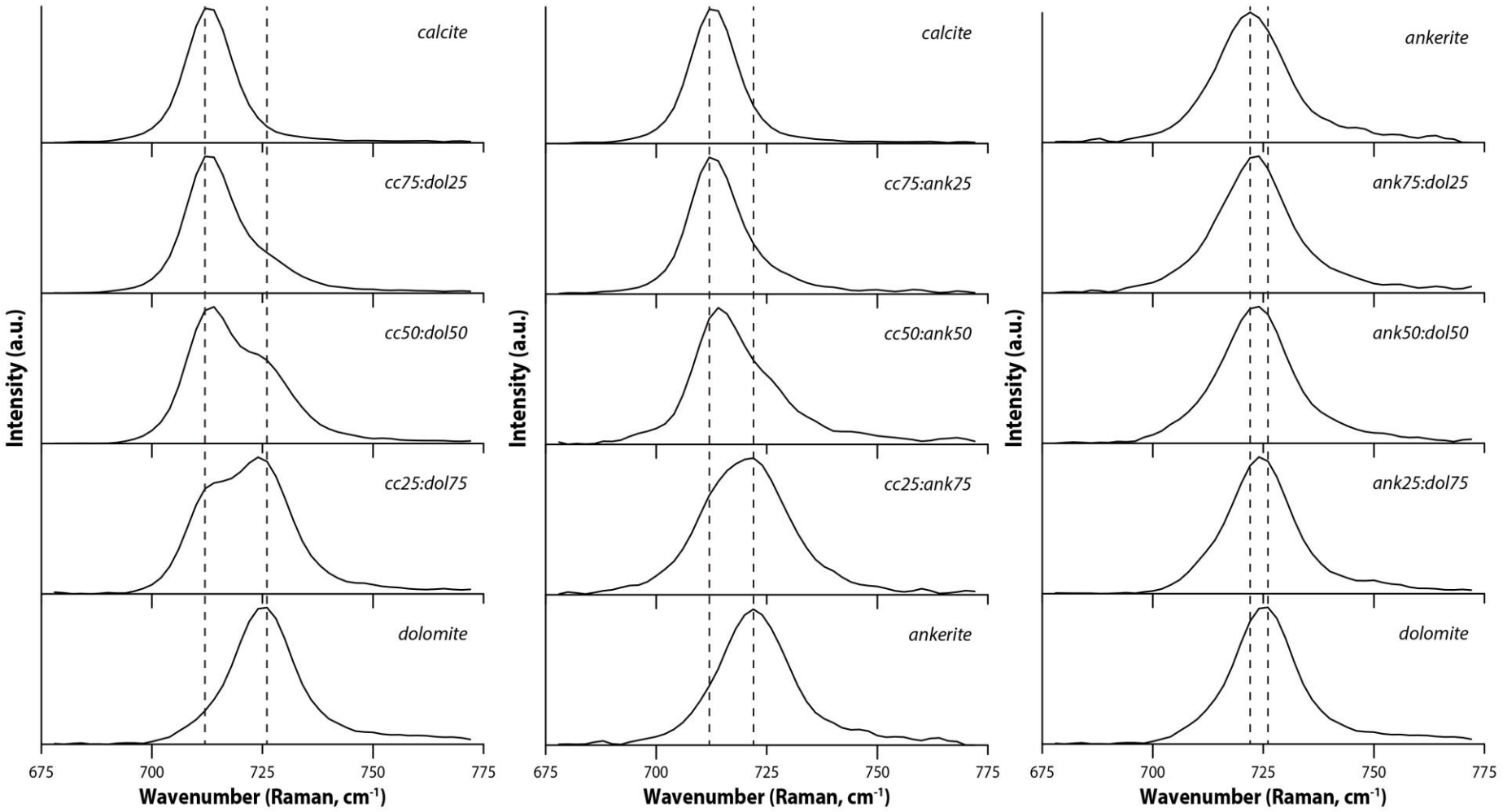

Fig. 51. Raman (red-NIR) spectra among calcite-dolomite, calcite-ankerite, and ankerite-dolomite mixtures.

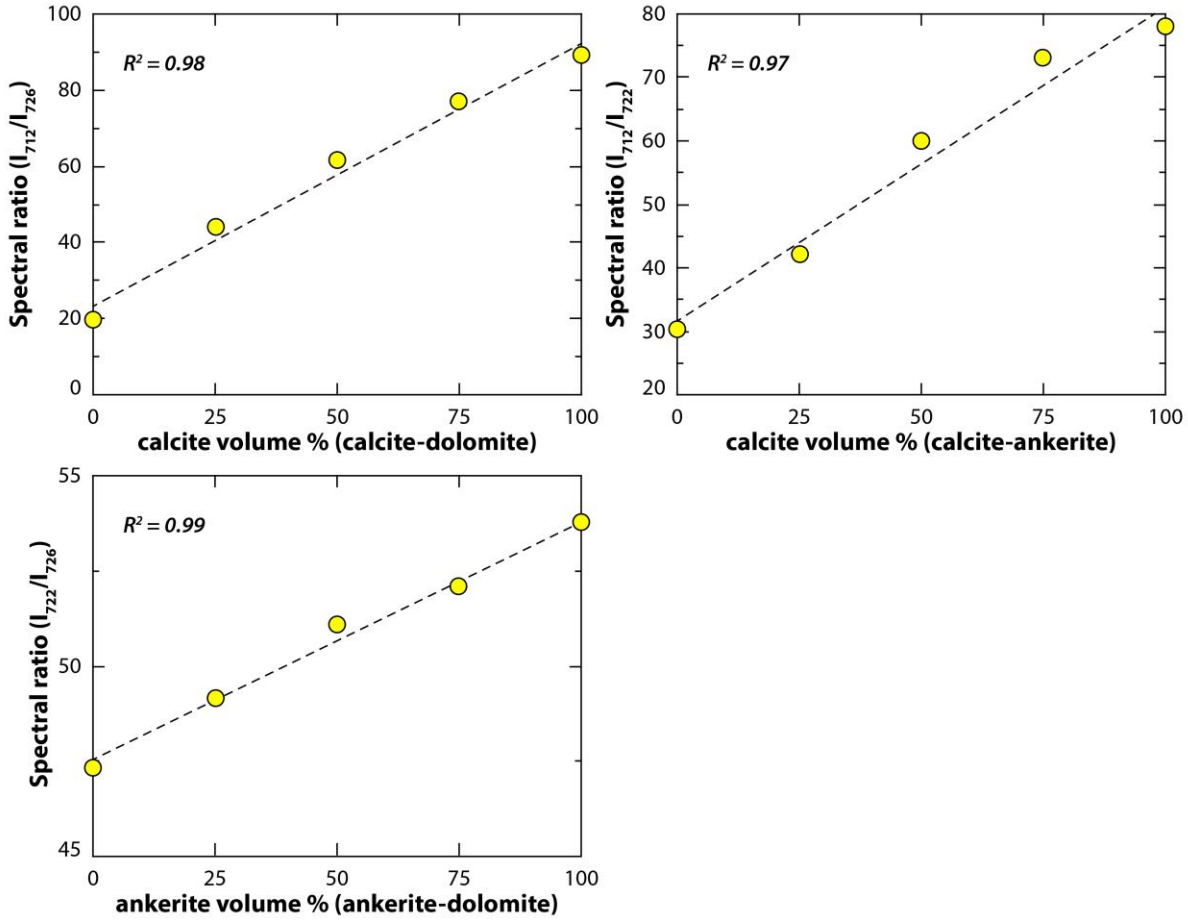

Fig. 52. Correlation between the spectral ratios from Raman (red-NIR) and the mixing ratios.

Spectroscopic variations associated with mixing ratios between the carbonate minerals are observed by MIR-ATR spectroscopy. The MIR-ATR spectra among calcite-dolomite, calcite-ankerite, and ankerite-dolomite mixture are shown in **Fig. 53**. The fingerprint region in the IR spectra ranges from 760 to 660 cm-1 due to symmetric bending vibration of CO_3^{2-} and spectral ratios using band intensity between two carbonates are used as indicators for mineral concentration. As shown in the Raman results, intensity differences are observed between the mixtures in the MIR-ATR spectra. **Fig. 54** shows that the trend line from each carbonate mixture have a strong correlation between the spectral ratio and mineral concentration, displaying R^2 values higher than 0.996. This result suggests that the target mineral content in carbonate mixtures can be estimated by MIR-ATR analysis even though the spectra are acquired on powders with small amount (~10 mg).

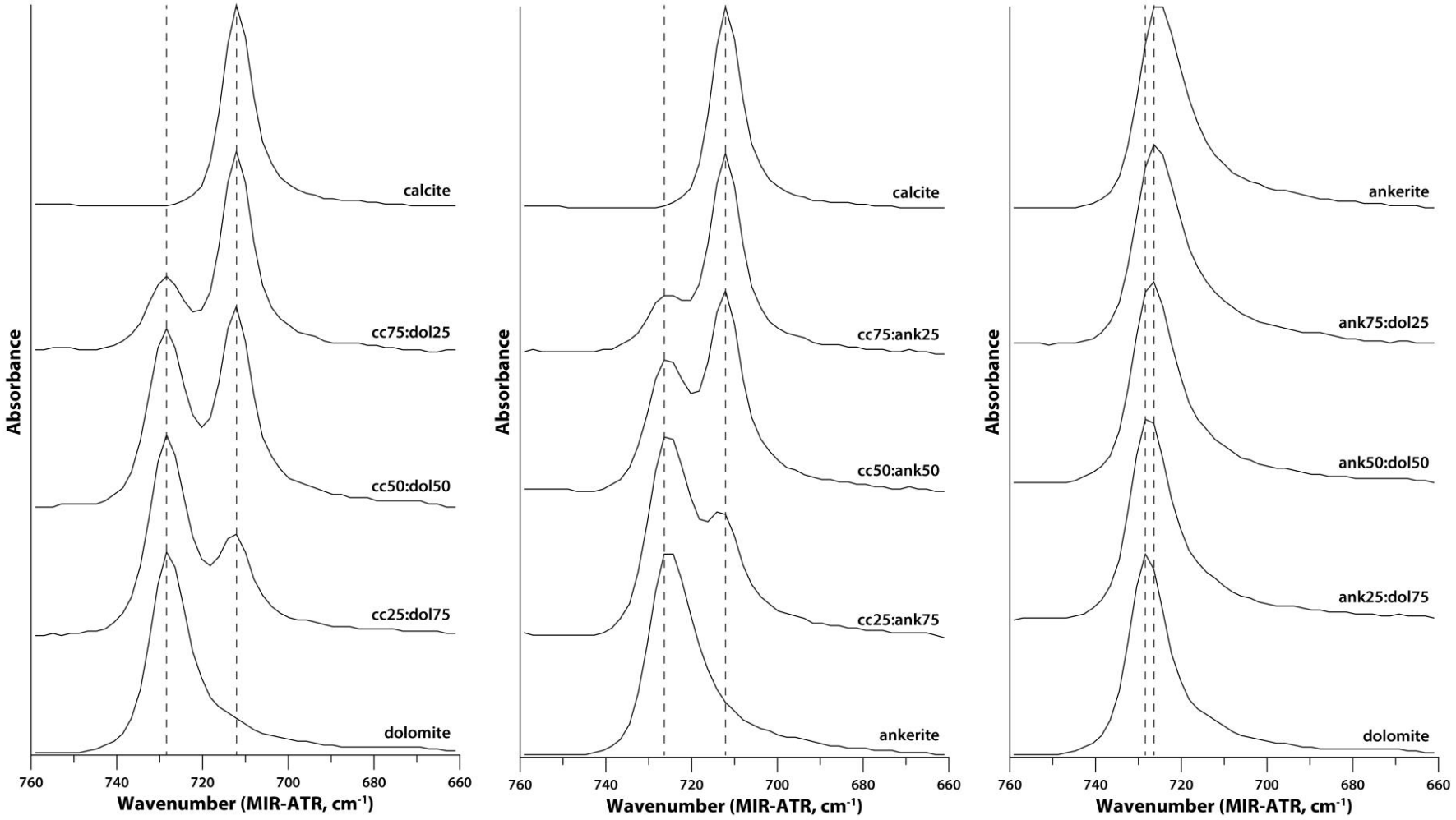

Fig. 53. MIR-ATR spectra among calcite-dolomite, calcite-ankerite, and ankerite-dolomite mixtures.

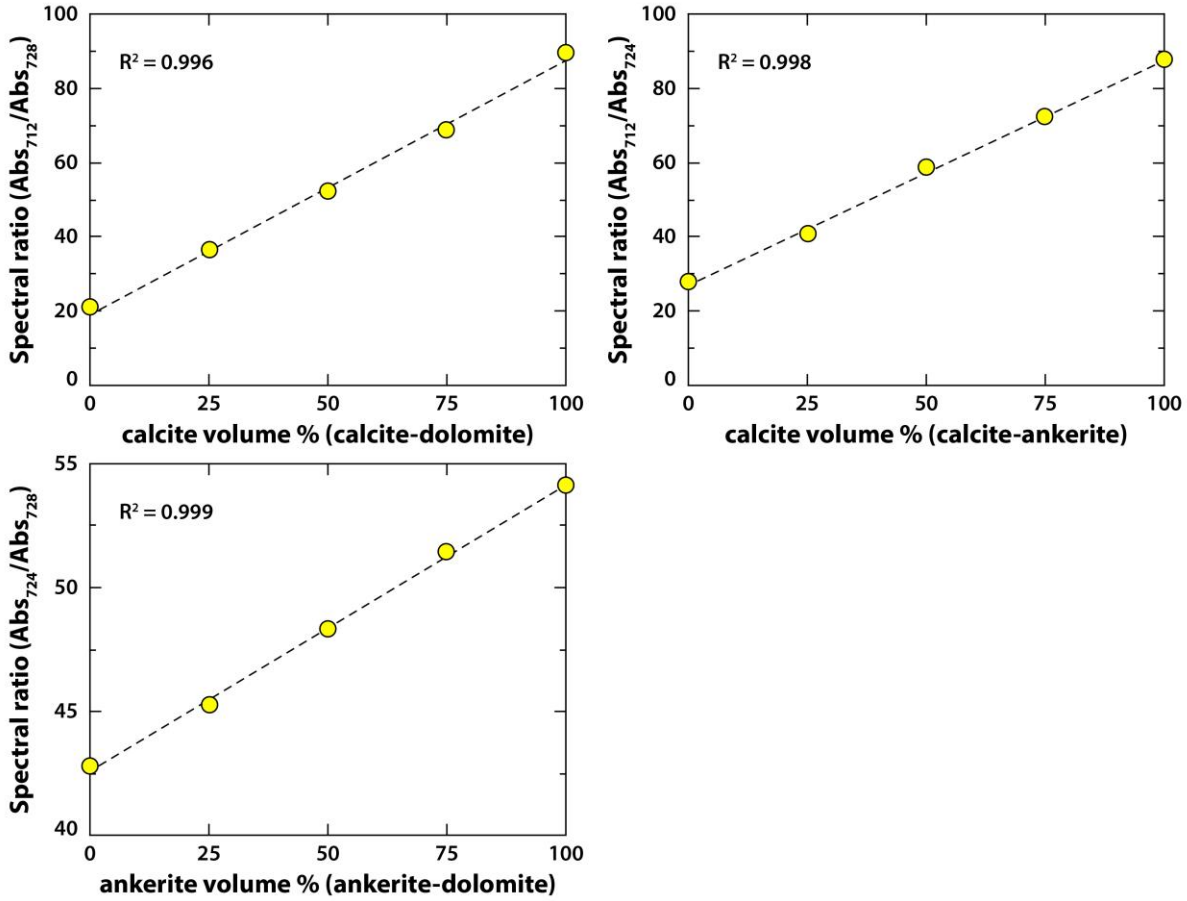

Fig. 54. Correlation between the spectral ratios from MIR-ATR and the mixing ratios.

The XRD patterns of carbonate mixtures are investigated to compare their intensities with the mixing ratios (**Fig. 55**). The distinct intensity differences are observed in accordance with mineral concentration in all the sets of carbonate mixtures. The intensity ratios are used for quantitative analysis, and the determination coefficients are 0.996 or higher (**Fig. 56**). Therefore, pXRD requiring powders as MIR-ATR presents the possibility of quantitative analysis for carbonate mixtures by showing the linear intensity change in the XRD patterns with the mixing ratios.

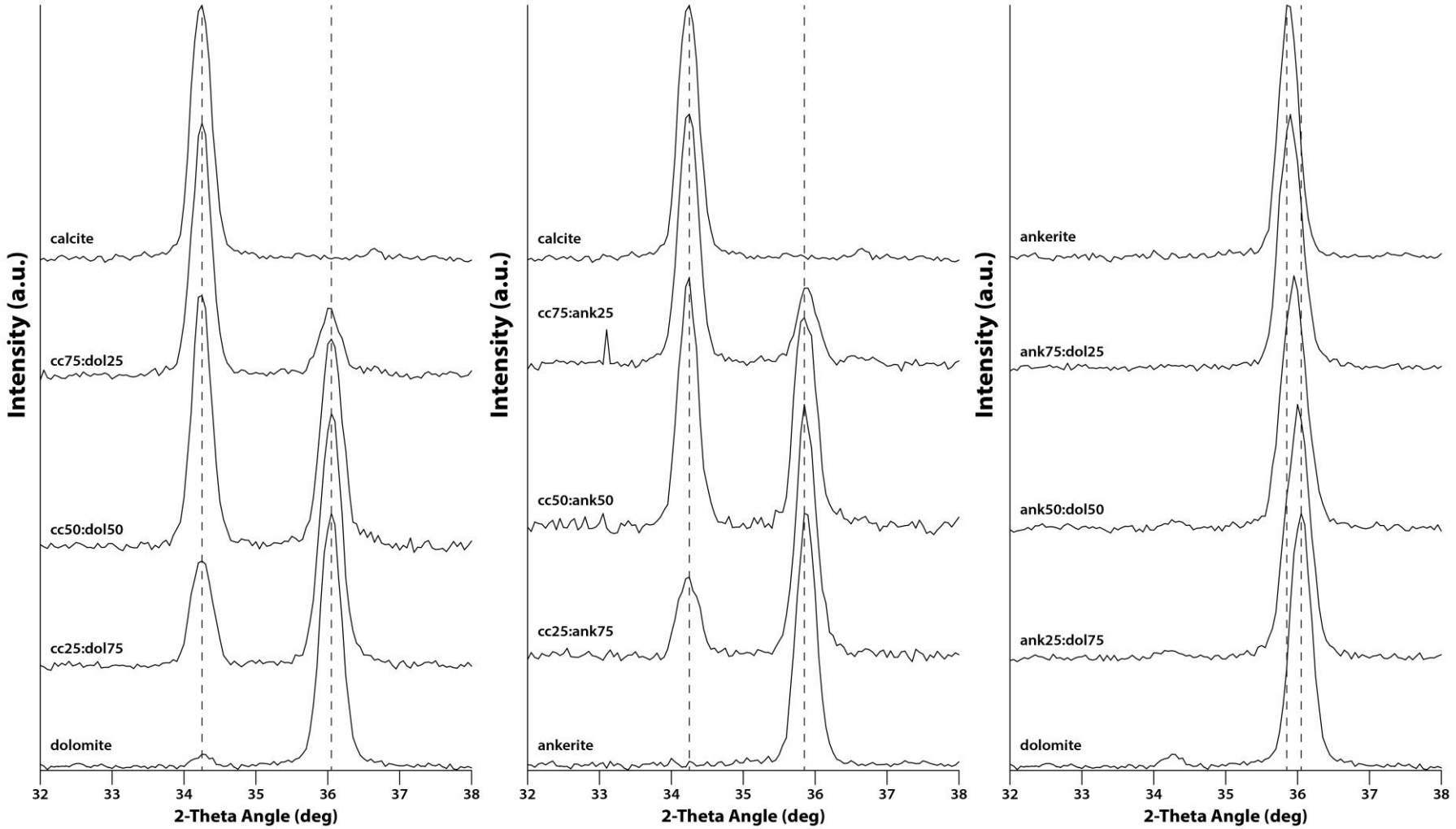

Fig. 55. XRD patterns among calcite-dolomite, calcite-ankerite, and ankerite-dolomite mixtures.

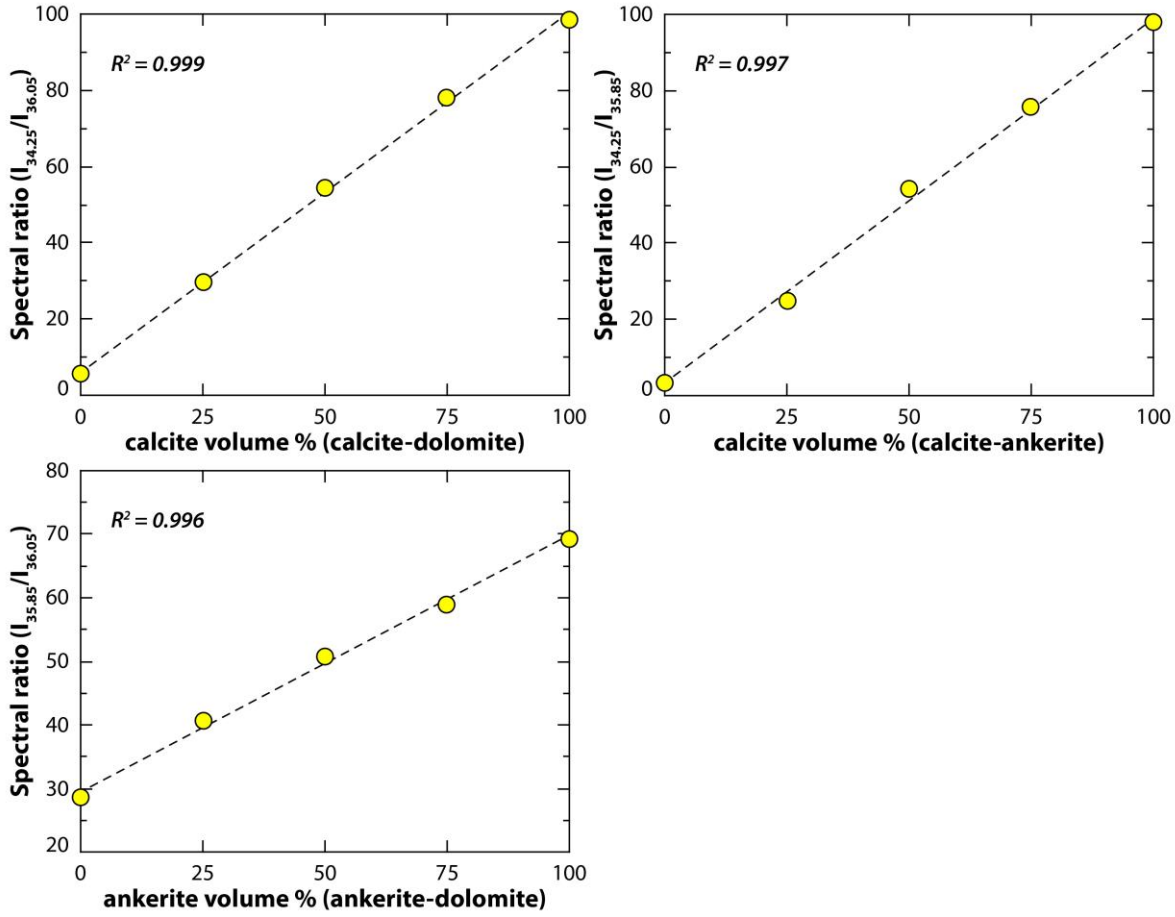

Fig. 56. Correlation between the spectral ratios from pXRD and the mixing ratios.

5.2. Ternary mixtures of carbonate minerals

This study describes quantitative analysis of carbonate minerals in a ternary mixture (1:1:1 mass ratio) containing calcite, ankerite, and dolomite using two Raman, MIR-ATR, and pXRD devices. The mixed sample was prepared and measured following a previously described procedure in the binary mixtures, and the spectral ratio covering all the minerals is used for evaluating carbonate quantification. Each spectrum and XRD pattern from the mixture include low intensity in the single calcite band, and the ankerite and dolomite band appear as shoulder or single band with a wider FWHM (Full width at half maximum) than the individual band (**Fig. 57**). The ankerite and dolomite band have higher intensity than the calcite band, and it can be interpreted as a result of overlapping the two bands due to similar band positions rather than quantitative differences. The maximum error of the Raman spectrum acquired by a green

laser is 16.9% (region I), and 6.2% (region II), respectively. The Raman spectrum measured by a red-NIR laser shows 2.8% maximum error (**Fig. 58**). The maximum error of MIR-ATR and pXRD is 4.0%, thus all the portable techniques can be applied to ternary mixtures in carbonate minerals as quantitative analysis.

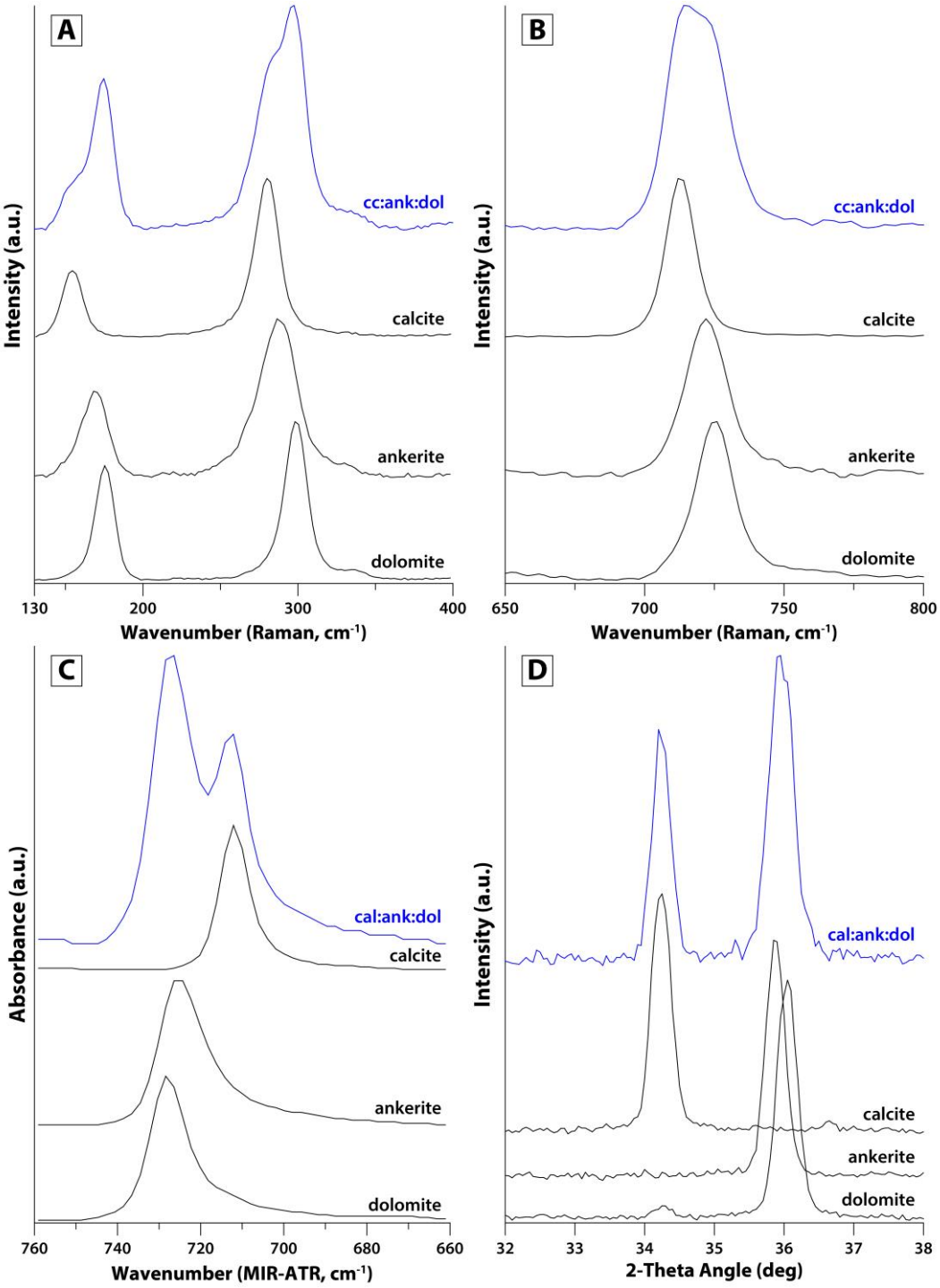

Fig. 57. Raman and MIR-ATR Spectra and XRD pattern of ternary mixtures of carbonates.

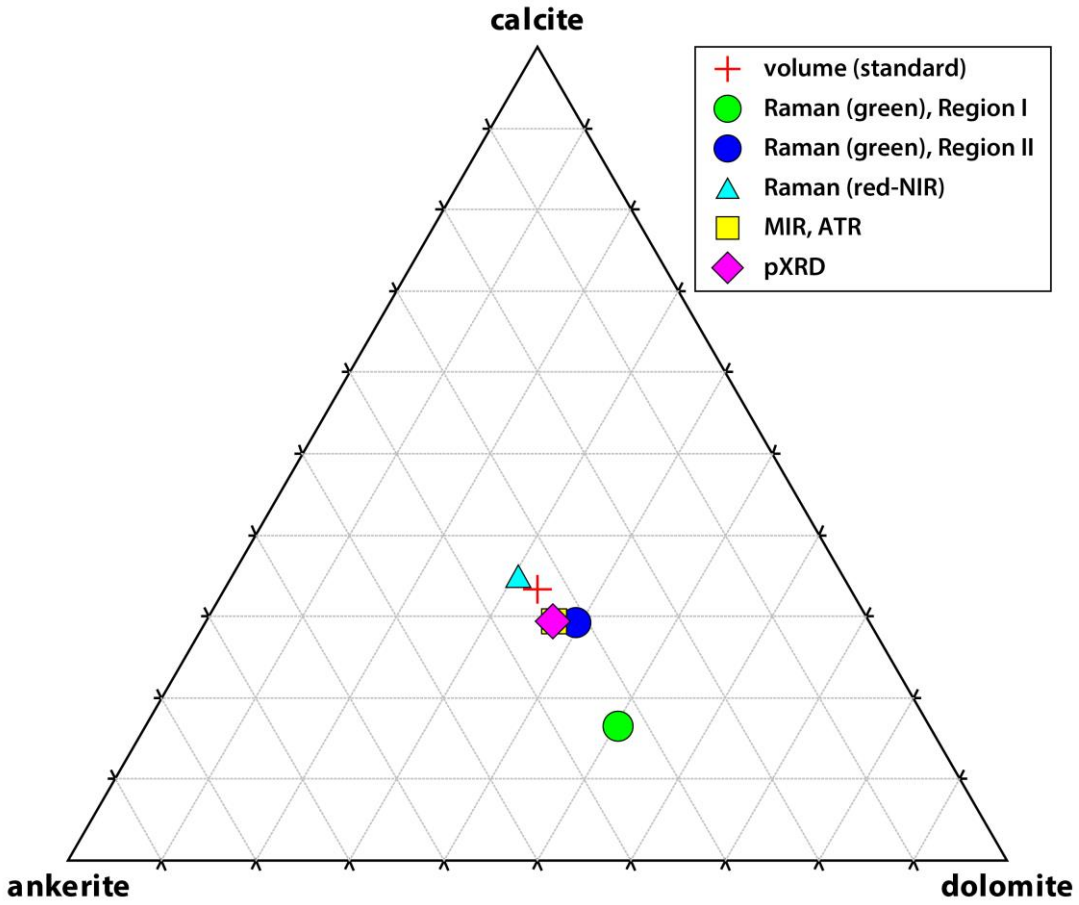

Fig. 58. Ternary diagram calculated for the three-component system in the calcite-ankerite-dolomite mixtures.

5.3. Discussion and conclusion

Curve-fitting is commonly applied in Raman and IR spectroscopy to extract individual band characteristics from overlapping bands in form of a shoulder or a single-like band with broader FWHM in a spectrum. Therefore, the Raman and MIR-ATR spectra of the binary carbonate mixtures are curve-fitted in order to compare the function parameters such as the height or area value of each band with the mineral concentration (**Fig. 59**). OPUS (Bruker) software is used for both baseline correction and curve-fitting in MIR-ATR, and Crystal Sleuth (Lafuente et al., 2015) and LabSpec 6 software (Horiba) for baseline correction and curve-fitting in Raman, respectively. Raman and MIR-ATR bands show a large variety of line shapes, thus mixed Gaussian-Lorentzian profile is applied for both spectroscopic data.

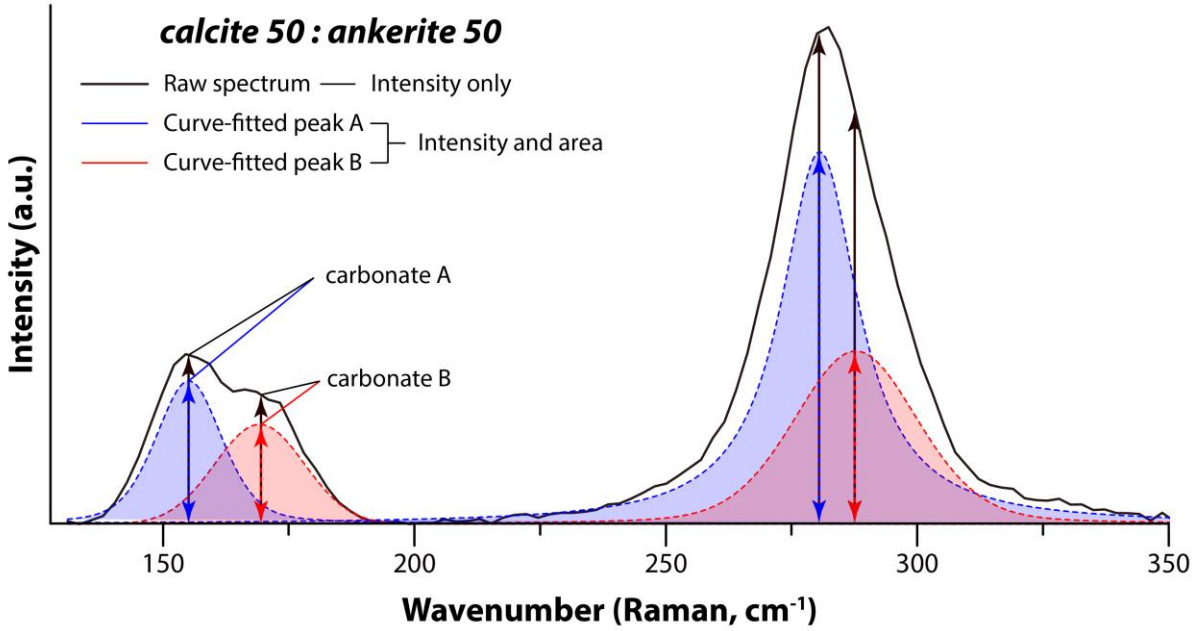

Fig. 59. A spectral ratio using raw spectrum and curve-fitted peaks in Raman spectrum.

Table 10 shows linear correlations between the spectral ratios and mineral content with respect to both raw and decomposed data of the carbonate mixtures. The result from the spectral ratios shows no significant difference between the two sets of spectra, suggesting the applicability of carbonate quantification using intensity ratios directly without the curve-fitting procedure in the field.

Table 10. Determination coefficients in the carbonate mixtures

Mixture	Spectrum	Method	Raman Green (R1)	Raman Green (R2)	Raman Red-NIR	MIR ATR
calcite-dolomite	Raw	Intensity	0.996	0.987	0.983	0.996
	Curve-fitting	Intensity	0.999	0.980	0.981	0.998
		Area	1.000	0.967	0.998	1.000
calcite-ankerite	Raw	Intensity	0.989	0.968	0.973	0.998
	Curve-fitting	Intensity	0.985	0.960	0.980	0.992
		Area	0.989	0.962	0.988	0.993
ankerite-dolomite	Raw	Intensity	0.981	0.989	0.990	0.999
	Curve-fitting	Intensity	0.967	0.986	0.975	0.995
		Area	0.980	0.965	0.983	0.997

Chapter V. Phyllosilicate identification and quantification

Mineral resource exploration aims to predict specific regions of the presence of ore bodies. The ore bodies refer to concentrations of specific mineral aggregates of economic interest in a very small area (Haldar, 2018), and various differentiated techniques are used for exploration in accordance with the genetic model of ore deposits in terms of geological and ore-forming aspects. In particular, the importance of exploring hydrothermal alteration has been emphasized as an indicator of proximity to ore in exploration due to the existence of the target ore bodies at depth as hidden ores (Haldar, 2018). Another reason is that most of the significant exposed ore deposits have been discovered and are being exploited. Since hydrothermal alteration affects a volume of rock many times that of the ore body, it provides a much larger target for detecting and mapping hydrothermal systems than does ore deposits (Ridley, 2013). Alteration minerals are formed based on the seven main variables: temperature, fluid chemistry, concentrations of components in hydrothermal fluids, host rock composition, the kinetics of alteration/mineral deposition, duration of the hydrothermal system, and permeability (Browne, 1978). Alteration facies on the basis of characteristic mineral assemblages formed in specific regions are controlled by a combination of temperature and pressure, fluid composition, host-rock composition, and fluid/rock ratio (Ridley, 2013). Thus, the nature or chemical composition of alteration minerals can help define the alteration halos and therefore have been commonly used as vectors to ore.

Phyllosilicate minerals such as chlorite and micas are often ubiquitous in hydrothermal alteration zones, and phyllosilicate alteration contains a wide range of mineralogical and geochemical characteristics depending on the deposit type. Phyllosilicate geochemistry is commonly investigated for major elements, and variations in such features as Fe/Mg of chlorites and K/Na of white micas can reflect spatial and temporal relationships with respect to the proximity of mineralization in VMS deposits (Soltani Dehnavi et al., 2019). For example, white micas vary systematically in composition from phengite [$K(Al,Mg)_2(Si,Al)_4O_{10}(OH)_2$] at the outer edge of the alteration to sodic muscovite [$NaAl_2(Al,Si_3)O_{10}(F,OH)_2$] proximal to massive sulphides in some VMS deposits (Large et al., 2001b). Nevertheless, there is no universal trend covering all VMS districts and deposits, thus it is essential to investigate subtle changes in the composition of white mica by each deposit.

In the case of chlorites, Fe and Mg contents have been used as geothermometers and useful vectors to ore in VMS deposits. Despite significant changes in chlorite composition, several studies have demonstrated that the variation trend towards the ore may not be systematic. For example, the Mg content of Fe-Mg chlorite commonly increases passing from the margin to the core of the footwall alteration system, but the opposite pattern has been found in some cases (Lentz et al., 1997; Luff et al., 1992; Urabe, 1983). Thus, as the same as white micas, it is also necessary to investigate detailed compositional variations of chlorites in every target area.

As with carbonate minerals described above, the significance of portable spectroscopy has been increasing because it is rarely possible to visually identify the compositional variations within the same mineral group (i.e., chlorite and white mica) in the field. Although Raman and SWIR bands of trioctahedral chlorites and dioctahedral micas have been characterized in a number of spectral studies (Bishop et al., 2008; Cloutier et al., 2021; Gopal et al., 2004; King and Clark, 1989; Li et al., 2011; Post and Noble, 1993; Prieto et al., 1991; Tlili et al., 1989; Wang et al., 2015), no study has provided univariate calibrations that systematically compare changes in band position with compositional variation within the same mineral groups. Therefore, in this study, Raman and VNIR-SWIR spectroscopic analyses are carried out to investigate spectral features of a diverse range of chemical compositions in chlorites and white micas. Then, the band changes are compared with their compositional variations in order to estimate their composition using spectral information in the field.

1. Trioctahedral chlorites discrimination by Raman and VNIR-SWIR

1.1. Mineralogy background

Chlorite is a hydrous phyllosilicate in which the unit structure consists of alternating a negatively charged tetrahedral-octahedral-tetrahedral talc-like 2:1 layer (TOT; $Y_6Z_8O_{20}(OH)_4$) with a positively charged octahedral brucite-like layer (O; $Y_6(OH)_{12}$), where Y and Z represent octahedral and tetrahedral sites respectively (Deer et al., 2013). The simplified formula can be written as

$$[\boldsymbol{R^{2+}, R^{3+}}]^{6}_{12}[\boldsymbol{Si_{8-x}R^{3+}_{x}}]^{4}\boldsymbol{O_{20}(OH)_{16}} \quad (7)$$

where

$$R^{2+} = Mg, Fe, Mn, Ni, Zn;\ R^{3+} = Al, Fe, Cr; and\ x\ (generally) \sim 1-3$$

In most common chlorites there are 12.0 octahedral per $O_{20}(OH)_{16}$, and approximately equivalent amounts of aluminium in tetrahedral and octahedral sites. Such minerals are referred to as trioctahedral chlorites, and Mg↔Fe substitution occurs over a wide range in the chlorite group. Natural trioctahedral chlorites can as a first approximation be expressed as binary combinations of the clinochlore (Mg-rich) and chamosite (Fe-rich) endmembers.

1.2. Materials and methods

Table 11 displays the descriptions and conditions of chlorite samples used in this study. The chlorite samples for Raman analysis used in this study were selected 11 samples, indicating 3 samples from the RRUFF database, 2 samples from previous studies, and 2 samples from our spectral library (Lafuente et al., 2015; Wang et al., 2015). Another 10 chlorite samples for VNIR-SWIR analysis were used in this study, indicating 6 samples from the USGS spectral library, 2 samples from a previous study, and 2 samples from our spectral library (Kokaly et al., 2017; Yang and Huntington, 1996). The spectral data of the two chlorite samples are used from our spectral library in **Chapter II**. The samples are measured in the form of pellets with Raman and VNIR-SWIR portable equipment. Fe# [Fe/(Fe+Mg)] as shown in **Table 11** was calculated by mass converting from oxide. In this study, iron and magnesium contents were used as weight percentages to consider the immediate applicability of elemental data from pXRF in the field.

Raman spectra were collected using a Bravo portable spectrometer equipped with two lasers in the 700-1100 nm range (red to near infrared) at a power lower than 100 mW. The spectral resolution was 10-12 cm^{-1} in the range 300-3200 cm^{-1}. Since all acquisition parameters of this device are fully automatized, six spectra were acquired on each sample and averaged before interpretation. The selection of the peak position was determined by the wavenumber at maximum intensity after an automated background removal which was installed in the Crystal Sleuth software (Laetsch and Downs, 2006). The Raman data measured by a portable device using a 532 nm green laser are excluded due to high noisy by fluorescence effect.

Table 11. Sample information of chlorite minerals for Raman and VNIR-SWIR analysis.

Raman analysis								
Sample	Affiliation	Analysis	SiO_2	Al_2O_3	FeO(T)	MnO	MgO	Fe/(Fe+Mg)
R060188	RRUFF	EPMA	24.91	20.56	27.62	0.26	13.19	0.73
R061080	RRUFF	EPMA	28.46	19.74	20.94	0.73	18.64	0.59
R060725	RRUFF	EPMA	31.51	19.19	2.20	0.05	32.71	0.08
CCa-1*	Wang	AAS**	26.00	20.00	20.80	0.10	17.20	0.61
203	Wang	EPMA	34.11	11.38	4.32	0.04	32.19	0.15
Chl_1	UL	EPMA	29.71	20.48	14.48	0.15	22.90	0.45
Chl_2	UL	ICP-OES	30.89	15.59	6.07	0.02	30.89	0.20
VNIR-SWIR analysis								
Sample	Affiliation	Source	SiO_2	Al_2O_3	FeO(T)	MnO	MgO	Fe/(Fe+Mg)
GDS157	USGS	EPMA	25.20	19.60	22.76	0.11	16.60	0.64
CCa-1*	USGS	AAS**	26.00	20.00	20.80	0.10	17.20	0.61
GDS158	USGS	EPMA	27.50	19.80	12.69	0.13	24.70	0.40
SMR-13	USGS	EPMA	31.00	17.30	7.50	0.12	30.20	0.24
NMNH83369	USGS	EPMA	32.00	16.00	3.38	0.00	33.90	0.11
GDS159	USGS	EPMA	31.30	19.40	1.04	0.02	34.70	0.04
13615	CSIRO	EPMA	21.90	20.83	31.95	0.00	7.25	0.85
13646	CSIRO	EPMA	21.88	19.93	30.15	0.00	8.78	0.82
Chl_1	UL	EPMA	29.71	20.48	14.48	0.15	22.90	0.45
Chl_2	UL	ICP-OES	30.89	15.59	6.07	0.02	30.89	0.20

* Spectral data are used from CCa-1 sample, but the chemical data used a new sample CCa-2 in the same region because the previous data was no longer provided.

** CMS mentions that the chemical data does not mean analytical certification for this sample and is meant to be used as a guideline (see https://www.clays.org/sourceclays_data/).

VNIR-SWIR analysis was carried out by portable SR-6500 spectroradiometer. The spectrum ranges from 350 to 2500 nm with different spectral resolutions based on the region: 1.5 nm at 700 nm, 3.0 nm at 1500 nm, and 3.8 nm at 2100 nm. The spectrometer is connected to a contact probe with an internal light source, which enables stable illumination conditions across the spectral region of interest. Prior to its first usage, the instrument is calibrated using a specialized ceramic disk with 99% whiteness in order to reflect uniformly across the spectrum. Minimum scan speed is 100 milliseconds, and each spectrum is produced from an average of 40 measurement to represent the overall spectral pattern. The selection of the absorption position was determined by the wavelength at maximum absorption after removing the convex-hull of the signal by hull quotient installed in the ENVI (Exelis, 2012).

1.3. Result

1.3.1. Raman characterization of chlorite

Stretching vibrations of hydroxyl groups occurring in the 3400-3700 cm^{-1} interval is the diagnostic spectral range exhibiting spectral patterns of chlorites with wide variations (Prieto et al., 1991; Wang et al., 2015). However, the spectral region (300-3200 cm^{-1}) provided from the portable device is not covered in that region, thus the region within 1300 cm^{-1} in the Raman spectrum is targeted in this study. The peaks within 1300 cm^{-1} spectral range indicate the vibration of the tetrahedral layer of phyllosilicates considered as originating in the pseudo-hexagonal rings (T_2O_5) of the 2:1 layers with a maximum symmetry C_{6v} (Ishii et al., 1967). The representative Raman spectrum of chlorite mineral is presented in **Fig. 60**. The peak at 352 cm^{-1} has been assigned to bending vibration of Si-O group, and The peaks observed at 546, and 678 cm^{-1} have been assigned to symmetric stretching modes of Si-O-Si (Gopal et al., 2004). Prieto et al. (1991) found that the intensity of this peak at 350 cm^{-1} strongly decreased with the Si substitution by Al, and the peak at 550 cm^{-1} results from the substitution of Si by Al or the substitution of Mg by Fe induced a slight decrease in frequency and in width at half height. The peak observed around 680 cm^{-1} shows hydrogen substitution by deuterium, which contains a contribution of OH vibrations (Shirozu, 1985; Shirozu and Ishida, 1982). Furthermore, this vibration is strongly dependent on the composition of the interlayer octahedral sheet followed as i) peak intensity diminishes as tetrahedral aluminium (Al^{IV}) or iron decreases and ii) peak splits into two components if Fe# [Fe/(Fe+Mg)] is greater than 0.5 (Prieto et al., 1991).

Fig. 61 shows the Raman peak positions plotted against Fe# calculated by mass wt.% in order to compare between position changes of the peak and compositional variations. Around 350 cm^{-1}, it is difficult to identify distinct peak position due to weak intensity and high noises, thus this peak is excluded in this study. The peaks observed at 546 and 678 cm^{-1} have been assigned to symmetric stretching modes of Si-O-Si, and their peaks are investigated to determine the most sensitive spectral region with compositional variations. The symmetric stretching mode around 550 cm^{-1} shows a narrower peak interval (9 cm^{-1}) than the same mode around 680 cm^{-1} (16 cm^{-1}) with a wide range of peak dispersion (**Fig. 61**A). However, the Raman peak around 680 cm^{-1} shows the linear peak downshift from 683 cm^{-1} for Mg-rich chlorites to 666 cm^{-1} for Fe-rich ones. Furthermore, this mode displays a well-correlated trend line with high a regression coefficient (R^2) greater than 0.98 (**Fig. 61**B). This result indicates

that the peak region from 660-685 cm^{-1} is the best region for estimating Fe/Mg contents for chlorites in the spectral range of phyllosilicate fundamental vibrations.

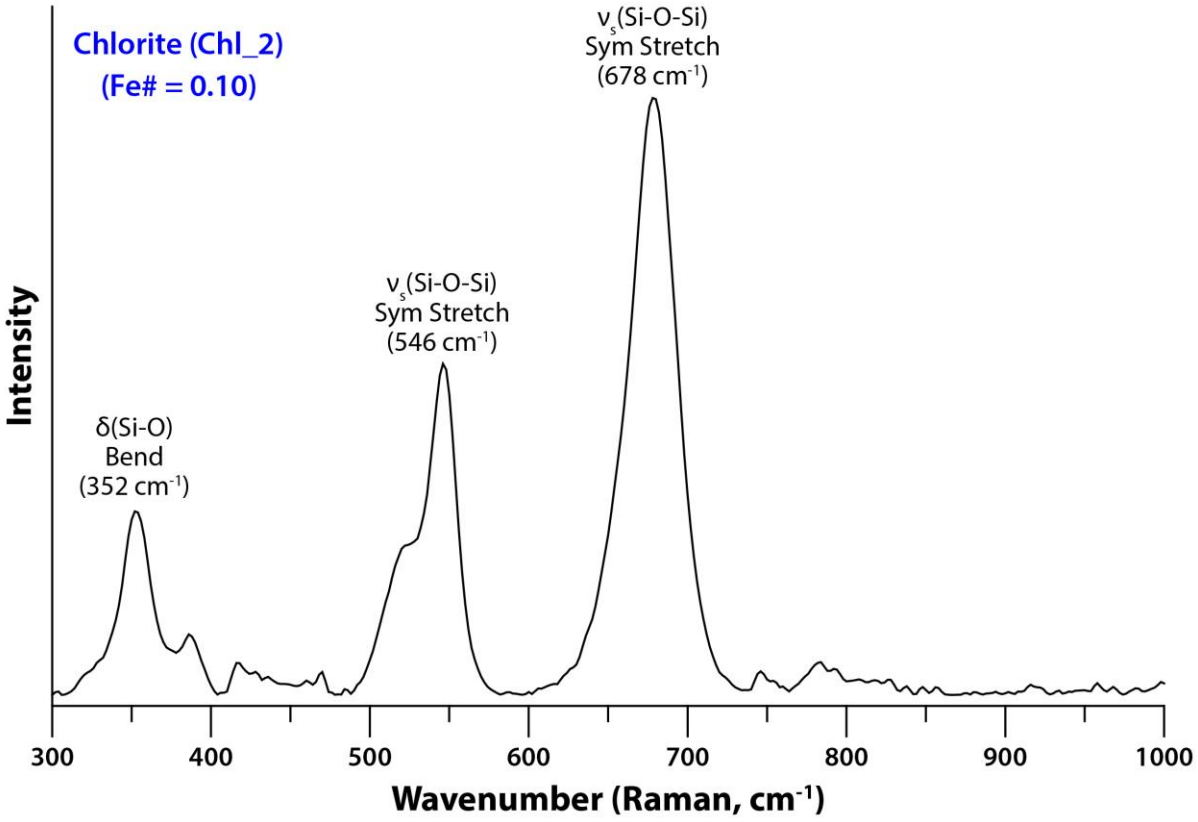

Fig. 60. Representative Raman spectrum of chlorite measured by portable Raman device (Bravo).

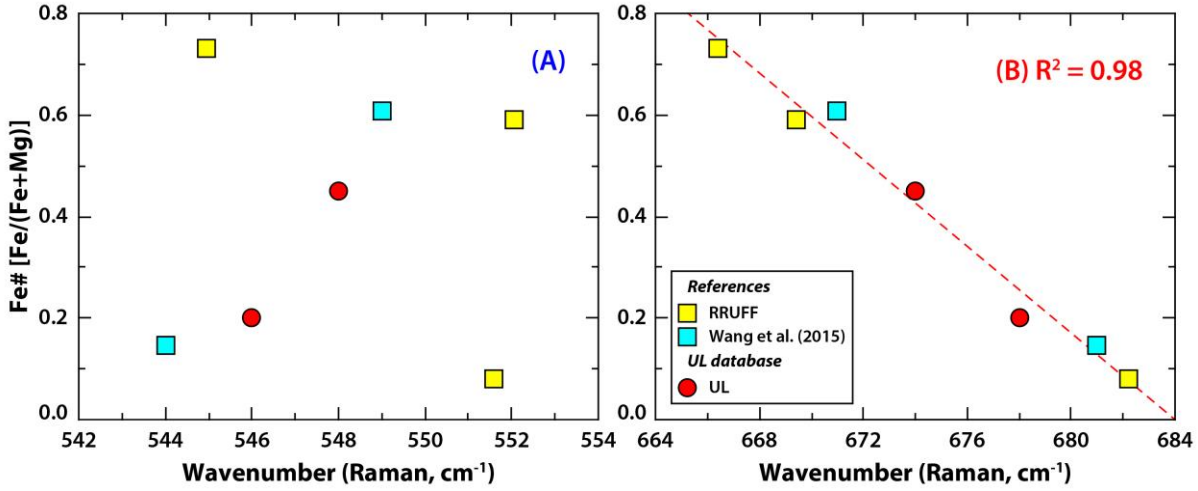

Fig. 61. Correlation between the different peak regions of chlorites in the Raman spectrum and Fe#.

1.3.2. SWIR characterization of chlorite

Trioctahedral chlorites have two diagnostic overtone absorption features around 2250 and 2330 nm, indicating Fe-OH and Mg-OH, respectively (**Fig. 62**). These absorption features arise from bonds in the octahedral sheets, and they are due to combinations of fundamental Al-, Fe- and Mg-OH stretching near 3600 cm^{-1} (2775 nm) with OH librational vibrations near 800 cm^{-1} (12500 nm) for the 2250 nm feature and near 650 cm^{-1} (15385 nm) for the 2330 nm feature (Cloutier et al., 2021). Based on the Mg# of chlorites, $\nu+\delta(Mg,Fe^{2+})_2OH$ (i.e., interlayer OH related brucite-like layer) shifts from about 2240 to 2260 nm, and $\nu+\delta(Mg,Fe^{2+})_3OH$ (i.e., inner OH of 2:1 talc-like layer) shifts from about 2320 to 2360 nm, respectively (Bishop et al., 2008).

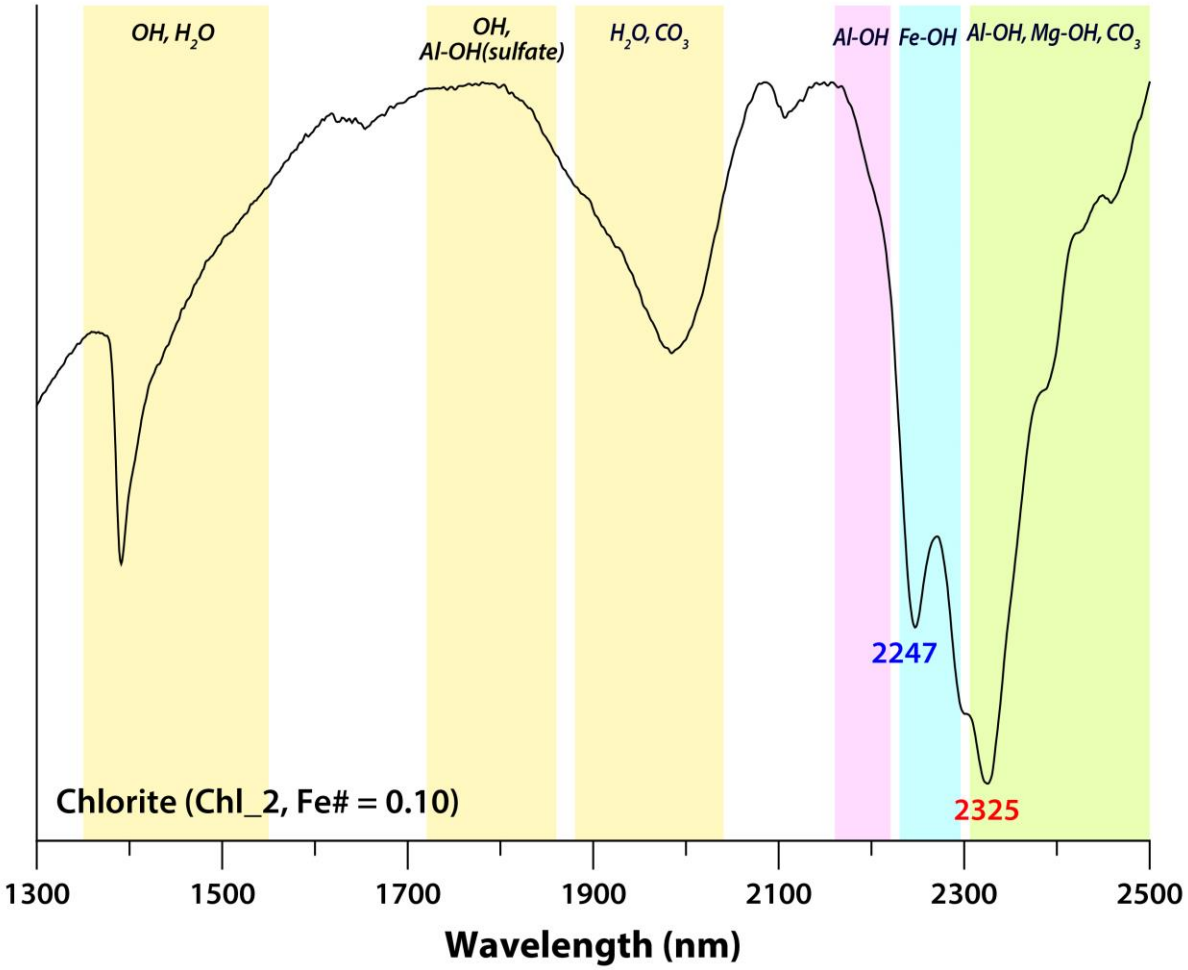

Fig. 62. Representative SWIR spectrum of chlorite.

Fig. 63 shows the correlation between Fe# of chlorites and the position of the absorption feature with respect to Fe-OH and Mg-OH. Since one sample (13646) from the CSIRO report does not provide the absorption position of Mg-OH, nine samples are used to compare between Mg-OH position and Fe# in this study, unlike ten samples used in the Fe-OH region. The Fe-OH and Mg-OH bands are observed from 2245 to 2262 nm and 2325 to 2351 nm, respectively (**Fig. 63**). The position of the 2250 nm and 2340 nm absorption features correlate with their Fe#, wherein a decrease in Fe# shifts the position of the absorption feature to shorter wavelengths. The trend line from Fe-OH has a strong correlation ($R^2 = 0.95$) between the band position and Fe# of chlorites whereas a correlation between Mg-OH position and Fe# shows lower R^2 values of 0.91 (**Fig. 63**). Although the range of the Mg-OH region (26 nm) exhibits wider than the Fe-OH region (17 nm), this region displays not only the spectral feature of chlorites but also the absorption characteristics of carbonate minerals and hydrous silicates such as amphiboles, white micas, biotites, and epidotes. Therefore, it is suggested that the spectral signature of chemical composition for chlorites is focused on the Fe-OH region in order to avoid the possibility of band overlaps.

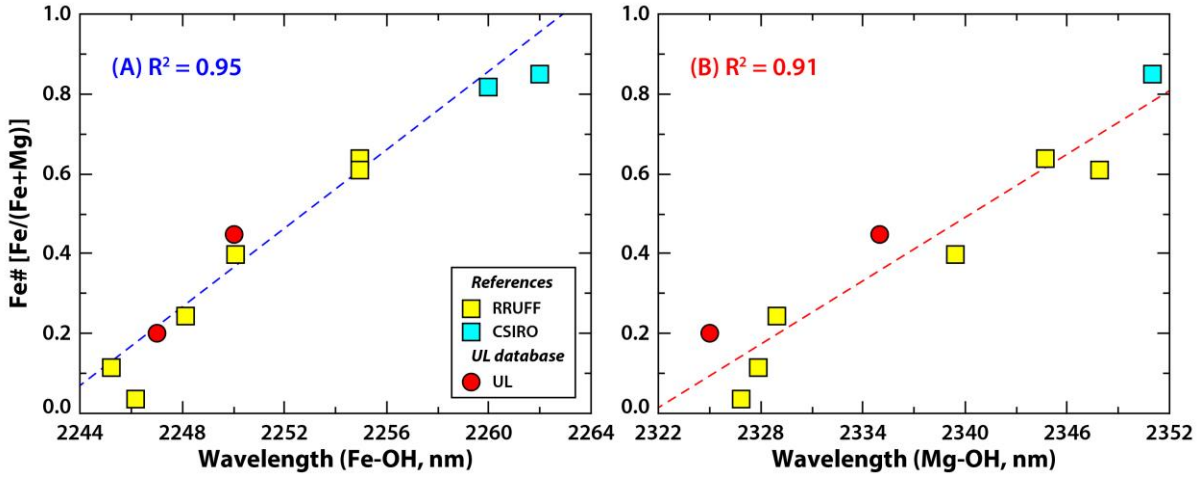

Fig. 63. Correlation between the different band regions of chlorites in the SWIR spectrum and Fe#.

2. Dioctahedral micas discrimination by Raman and VNIR-SWIR

2.1. Mineralogy background

The general formula of micas can be written as

$$\boldsymbol{X_2Y_{4-6}Z_8O_{20}(OH,F)_4} \quad (8)$$

where

X is mainly K, Na or Ca but also Ba, Rb, Cs, etc.

Y is mainly Al, Mg, or Fe but also Mn, Cr, Ti, Li, etc.

Z is mainly Si or Al but perhaps also Fe3+ and Ti.

The basic structure of micas consists of a composite sheet. A layer of octahedrally coordinated Y cations is sandwiched between linked $(Si,Al)O_4$ tetrahedra with large 12-fold coordinated X cations between the tetrahedral sheets (Deer et al., 2013). The micas can be subdivided into tri-octahedral and di-octahedral classes in which the number of Y ions is 6 and 4, respectively. A trioctahedral sheet has the structure of a sheet of the mineral brucite, with magnesium or ferrous iron being the most common cation. A dioctahedral sheet has the structure and the composition of a gibbsite sheet, with aluminium being the cation. Four out of six (OH) ions are replaced by apical oxygens of the tetrahedral layers (two on each side) in the layer. In this study, dioctahedral micas are used for spectroscopic analysis.

In the common dioctahedral micas, X is largely K or Na, representing muscovite (K-rich) and paragonite (Na-rich), respectively. Formation of paragonite might be expected to involve simple replacement of K^+ by Na^+ in the large ion sites. However, in practice, such a reaction involves replacement of equivalent substitution of divalent ions for Al in Y sites (i.e., Tschermak substitution, Eqs (9)). Therefore, the resultant paragonite tends to be more Al rich than the coexisting muscovite (Guidotti, 1984).

$$\boldsymbol{R^{2+}_{oct} + Si^{4+}_{tet} = Al^{3+}_{oct} + Al^{3+}_{tet}} \quad (9)$$

where R^{2+} = divalent cations, usually Fe^{2+} and Mg^{2+}.

Phengite $[K_2Al_3(Fe,Mg)(Si_7Al)O_{20}(OH)_4]$ indicates that the charge balance is maintained within the mica structure by coupling the substitution of divalent ions in octahedral sites with

increased Si^{4+} in the tetrahedral sites. Thus, phengites have lower tetrahedral and octahedral Al than muscovite. This chapter focuses on the spectroscopic properties of K-bearing dioctahedral micas such as muscovite and phengite.

2.2. Materials

Table 12 displays the descriptions and conditions of dioctahedral mica samples used in this study. The samples for Raman analysis used in this study were selected 35 samples, indicating 26 samples from previous studies, 7 samples from the RRUFF database, and 2 samples from our spectral library (Lafuente et al., 2015; Li et al., 2011; Tlili et al., 1989; Wang et al., 2015). VNIR-SWIR analysis was carried out with 11 mica samples, indicating 9 samples from the USGS spectral library and 2 samples from our spectral library (Kokaly et al., 2017). The spectral data of the two muscovite samples are used from our spectral library in **Chapter II**. The samples are measured in the form of pellets with Raman and VNIR-SWIR portable equipment. The Raman and VNIR-SWIR spectra were obtained using the same instruments used in the chlorite samples (i.e., Bravo portable Raman spectrometer and SR-6500 VNIR-SWIR spectroradiometer).

2.3. Results

2.3.1. Raman characterization of dioctahedral mica

Muscovite structure, referred to as the monomineralic C_2 group, has two prominent Raman peaks in the range 300-1000 cm^{-1} (**Fig. 64**). In the spectral range for fundamental vibration between 300 and 1200 cm^{-1}, it is assigned to internal vibrations of the distorted SiO_4 tetrahedron (Loh, 1973). Internal tetrahedral sheet T-O-stretch and T-O-T bend motions appear between 800 and 1200 cm^{-1}, and the modes between 800 and 360 cm^{-1} contain internal tetrahedral sheet motions mixed with K and octahedral Al displacements (McKeown et al., 1999). In particular, the peak observed near 400 cm^{-1} arises from the O-Al-O translation, and the peak near 700 cm^{-1} is assigned to the bending vibration of O-Al-O (Singha and Singh, 2016; Šontevska et al., 2008). Tlili et al. (1989) found a distinct trend for the peak shift around 700 cm^{-1} attributed to Si-O-Si vibration in muscovites and paragonites by the replacement of Si by

Al in the tetrahedra. In addition, Raman shift with octahedral Al content and spectral variation with Si content in the fundamental vibration region were investigated by Li et al. (2011).

Fig. 65A shows that K-bearing dioctahedral mica samples used in this study are on the trend line of the Tschermak substitution by plotting Si+Mg+Fe values and Al values obtained by stoichiometric calculations. It is notable that there is small deviations due to presence of titanium (Ti), or ferric iron (Fe^{3+}), which substitutes for aluminium and/or silicon in the tetrahedral sites (Besson and Drits, 1997). Since the two Raman peaks are associated with aluminium, Al contents are plotted against the Raman peak position around 400 and 700 cm^{-1}, respectively (**Fig. 65**B-D). The Raman peak near 700 cm^{-1} (**Fig. 65**B) does not show a clear trend although there is a negative trend dispersedly. However, another Raman peak near 400 cm^{-1} displays a distinct negative trend with either total Al contents by stoichiometric calculation or by mass (**Fig. 65**C and D). The two trend lines can be highlighted with a high regression coefficient (R^2) of 0.95 and 0.92, respectively. Therefore, the Raman peak shift near 400 cm^{-1} is well-correlated with the corresponding compositional variation of Al in mica. The results enable to perform (semi-) quantitative estimations of Al content for the K-bearing dioctahedral micas by Raman spectroscopy.

2.3.2. VNIR-SWIR characterization of dioctahedral mica

Absorption bands in the SWIR region are mainly related to overtones of stretching vibrations and combinations of stretching and bending vibrations (Laukamp, 2011). Dioctahedral micas have diagnostic overtone absorption features at 2200, 2340, and 2430 nm (**Fig. 66**). In particular, the wavelength position of the 2200 nm feature varies between 2190 and 2225 nm and is the result of overtones between the fundamental OH stretching vibrations of the $OH_{Al\text{-}Al}$, $OH_{Al\text{-}Mg}$, and $OH_{Al\text{-}Fe}$ near 3600 cm^{-1} (2775 nm) and $OH_{Al\text{-}Al}$ librational vibration (δ(OH)) near 915 cm^{-1} (10929 nm). The position of the absorption feature was documented to negatively correlate with the abundance of Al^{VI} in the octahedral layer, which also coincides with an increase in Si and Mg-Fe due to the Tschermak substitution (Eqs (9)).

Table 12. Sample information of dioctahedral micas for Raman and VNIR-SWIR analysis in this study.

Raman analysis									
Sample	Affiliation	Analysis	SiO_2	TiO_2	Al_2O_3	FeO(T)	MgO	Na_2O	K_2O
A115A-2	Li	EPMA	45.89	0.70	35.58	35.58	0.74	1.18	9.36
A115B-2	Li	EPMA	46.14	0.48	35.03	35.03	0.65	1.58	9.02
TH01A-2	Li	EPMA	48.34	0.98	31.29	31.29	2.57	0.76	10.07
D04-64A-1	Li	EPMA	47.57	0.54	27.86	27.86	1.99	0.27	10.76
D04-65A-3	Li	EPMA	48.85	0.42	29.40	29.40	2.10	0.49	10.25
D04-65A-1	Li	EPMA	49.71	0.22	28.71	28.71	2.54	0.49	10.28
QS09B-1	Li	EPMA	50.11	0.22	26.96	26.96	2.94	0.53	10.40
2Q33A-1	Li	EPMA	51.19	0.24	25.94	25.94	3.57	0.33	10.41
TP03B-3	Li	EPMA	51.87	0.23	25.46	25.46	4.08	0.31	10.31
BX12B-2	Li	EPMA	53.33	0.29	24.69	24.69	4.95	0.18	10.71
A117A-1	Li	EPMA	45.82	0.53	37.93	37.93	0.40	1.40	9.33
NJ43B-2	Li	EPMA	46.61	1.01	35.65	35.65	0.84	0.56	10.46
D04-77A-3	Li	EPMA	46.84	0.84	29.02	29.02	1.91	0.29	10.90
TH01B-3	Li	EPMA	48.48	0.80	30.45	30.45	2.73	0.55	10.08
2D78A-2	Li	EPMA	49.66	0.48	31.86	31.86	1.89	0.71	9.22
2Q73A-1	Li	EPMA	49.19	0.21	28.76	28.76	2.23	0.51	10.18
2Q33A-2	Li	EPMA	50.45	0.22	28.27	28.27	3.20	0.73	9.73
TP03A-1	Li	EPMA	51.60	0.28	25.55	25.55	4.23	0.37	10.50
MY01A-3	Li	EPMA	52.32	0.31	26.82	26.82	3.59	0.15	10.15
BX12B-3	Li	EPMA	53.32	0.22	24.47	24.47	4.91	0.23	10.68
N4	Tlili	EPMA	52.80	0.21	21.07	1.83	5.82	0.01	12.29
1131	Tlili	EPMA	51.81	0.72	27.70	2.26	3.45	0.61	11.16
FTS4	Tlili	EPMA	49.10	0.46	31.48	0.54	3.41	0.80	10.58
A58	Tlili	EPMA	46.27	0.33	34.80	1.87	0.51	0.54	11.05
GAL170-39	Tlili	EPMA	44.83	0.53	34.70	1.38	1.62	0.55	11.27
458-11	Wang	EPMA	44.66	0.32	33.78	1.39	0.68	0.70	10.70
R040104	RRUFF	EPMA	47.57	0.47	34.37	3.69	0.86	0.62	9.74
R040108	RRUFF	EPMA	49.74	0.53	29.13	6.32	1.64	0.30	9.89
R050080	RRUFF	EPMA	46.93	0.00	39.09	0.43	0.01	0.43	8.64
R050188	RRUFF	EPMA	47.16	0.22	34.56	4.12	0.54	0.63	9.63
R050198	RRUFF	EPMA	50.01	0.23	26.31	1.90	3.60	0.62	10.41
R060182	RRUFF	EPMA	44.92	0.13	33.17	1.65	0.49	0.65	9.84
R061120	RRUFF	EPMA	45.85	0.01	38.17	0.76	0.02	0.53	10.96
Ms_1	UL	EPMA	47.39	0.16	36.24	1.45	0.42	0.75	10.21
Ms_2	UL	ICP-OES	44.89	0.03	35.44	0.28	0.04	0.80	9.94
VNIR-SWIR analysis									
Sample	Affiliation	Analysis	SiO_2	TiO_2	Al_2O_3	FeO(T)	MgO	Na_2O	K_2O
GDS108	USGS	EPMA	44.00	0.13	35.00	2.24	0.57	9.60	0.72
GDS111	USGS	EPMA	47.87	0.69	28.03	6.48	0.94	10.16	0.00
GDS113	USGS	EPMA	45.89	0.32	35.64	1.78	0.56	10.00	0.78
GDS114	USGS	EPMA	44.93	0.13	33.09	5.06	0.71	10.09	0.70
GDS116	USGS	EPMA	45.90	0.46	31.06	5.33	1.38	10.21	0.43
GDS117	USGS	EPMA	45.28	0.01	35.54	3.01	0.19	9.75	0.19
GDS118	USGS	EPMA	46.05	0.29	31.31	5.81	0.13	10.08	0.34
GDS119	USGS	EPMA	46.28	0.13	33.34	3.46	0.55	9.97	0.64
GDS120	USGS	EPMA	45.89	0.29	35.69	2.10	0.25	9.94	0.47
Ms_1	UL	EPMA	47.39	0.16	36.24	1.45	0.42	0.75	10.21
Ms_2	UL	ICP-OES	44.89	0.03	35.44	0.00	0.04	0.80	9.94

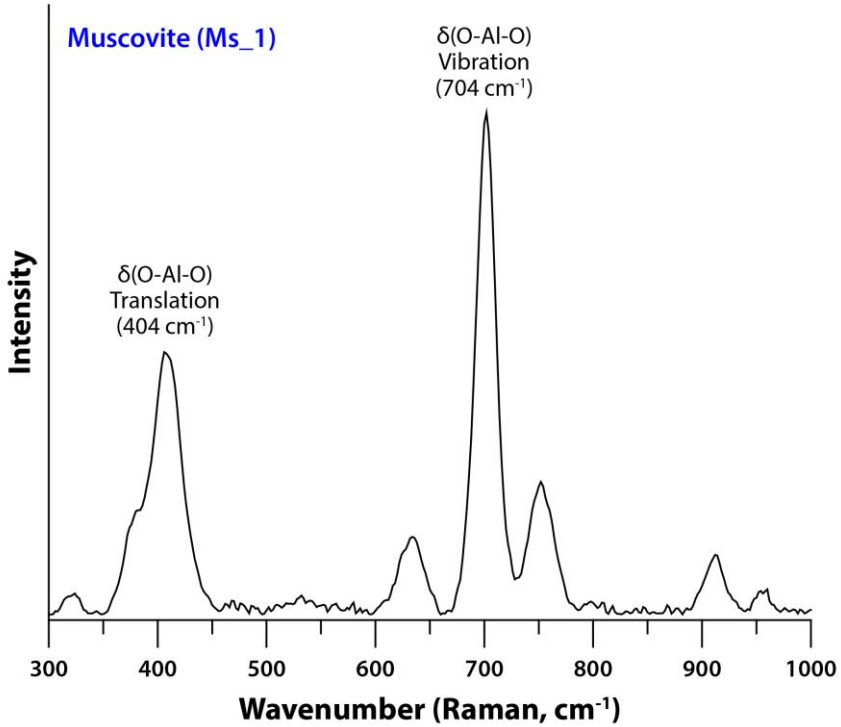

Fig. 64. Representative Raman spectrum of muscovite measured by portable Raman device (Bravo).

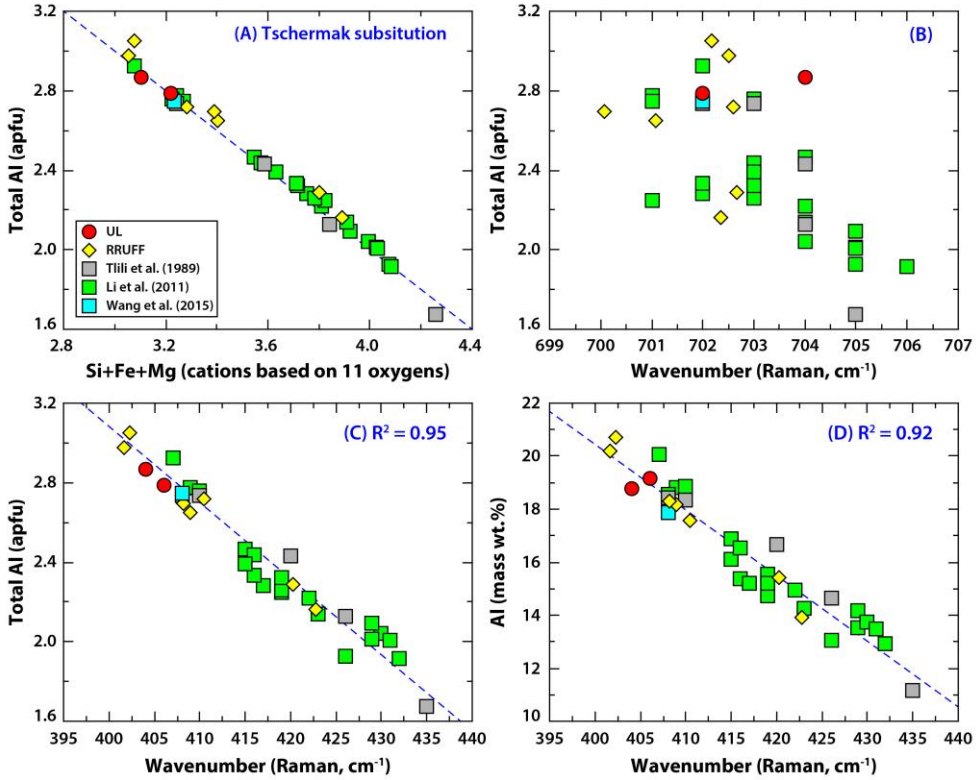

Fig. 65. Scatter plots among cation contents and Raman peaks. (A) Compositional variation in dioctahedral micas due to the Tschermak substitution calculated using 11 oxygens. (B and C) Correlation between the different peak regions of dioctahedral micas in the Raman spectrum and content of total aluminium. (D) Correlation between the peak region around 400 cm^{-1} and aluminium content in mass (wt.%).

The elemental data of each dioctahedral mica plot close to the Tschermak substitution line along which divalent cations substitute for aluminium in the octahedral sites, thereby causing a charge deficiency that allows silicon to enter more tetrahedral sites (**Fig. 67**A). **Fig. 67**B-D shows the band position near 2200 nm of each sample is plotted against compositional combinations: total Al, octahedral Al, and Al in mass. All the results shows that the band position increases from 2194 to 2218 nm as the Al content decreases. Total aluminium and octahedral Al obtained by stoichiometric calculations show negative correlations with the band positions, showing high R^2 values of 0.98 and 0.96, respectively. Al contents in mass, considering the applicability of pXRF data, display a strong linear correlation (R^2 = 0.95). Therefore, this result shows the relationship between the band shift in this region and the corresponding compositional variation based on the Tschermak substitution in dioctahedral micas.

3. Conclusion

This chapter found that trioctahedral chlorite and dioctahedral mica have distinctive Raman and SWIR spectral pattern. Chemical composition in each mineral leads to a shift in the corresponding Raman and SWIR band positions. Fe# [Fe/(Fe+Mg)] in chlorites and Al content (i.e., total Al and octahedral Al) in dioctahedral micas are strongly correlated with the band positions from both Raman and SWIR spectrometers. The compositional variation in chlorites is highly correlated to the spectral regions with respect to O-Si-O mode in Raman spectra and Fe-OH region in the SWIR region. Dioctahedral micas show the changes in the band position with respect to bending O-Al-O mode in Raman spectra and Al-Oh region in the SWIR region. The band shift can be explained by Tschermak substitution, which is substitutions among Al^{VI}, Fe and Mg in octahedral sites. Our detailed mineralogical and spectral study suggests that spectral analysis using portable tools is effectively applicable to the determination of phyllosilicate minerals in the field.

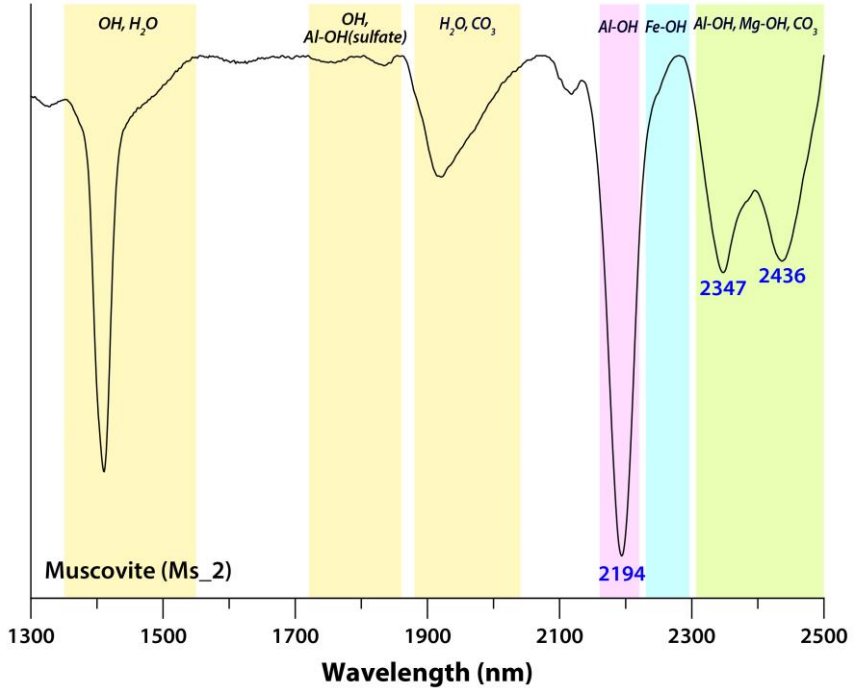

Fig. 66. Representative SWIR spectrum of muscovite.

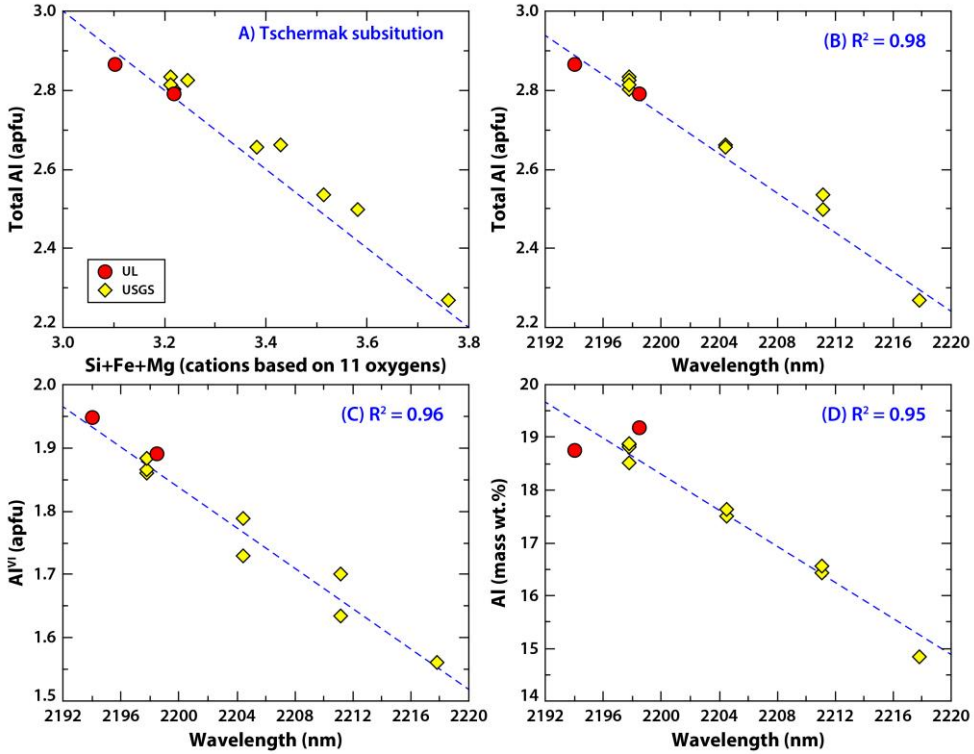

Fig. 67. Scatter plots among cation contents and band shift. (A) Compositional variation in dioctahedral micas due to the Tschermak substitution calculated using 11 oxygens. (B-D) Correlation between the band regions around 2200 nm in the SWIR spectrum and different types of aluminium contents.

4. Phyllosilicate quantification by Raman and VNIR-SWIR

The mineralogical zoning in alteration halos around VMS deposits has long been used as an empirical vectoring tool worldwide (Franklin et al., 2005; Gibson et al., 2007; Large et al., 2001b). Most VMS deposits in the IPB have a stockwork zone enclosed in hydrothermally altered volcanic and sedimentary rocks, dominantly with zoned sericite- and chlorite-rich assemblages. Silica- and carbonate-rich alteration zones are common but have a rather irregular distribution (Velasco-Acebes et al., 2019). Therefore, in this study, synthetic mixtures among ankerite-chlorite-muscovite are analysed to assess the quantitative relationship between the spectral ratios and the mineral volumes in the two-component system.

Experiments on the synthetic mixtures are carried out by portable Raman with a red-NIR laser and VNIR-SWIR instruments. Each pure carbonate mineral is selected from the spectral database in **Chapter II**. The mixtures were prepared by mixing different proportions, weighting 3:1, 1:1, and 1:3 for the two-component system. Since ankerite (2.93), chlorite (2.95) and muscovite (2.82) have similar densities, the mixed samples were prepared by applying mass ratios replacing their volume ratios (Deer et al., 2013). The measurement parameters for the mixed samples are the same as those of the sample measurement performed in **Chapter II**.

4.1. Binary mixtures among carbonates and phyllosilicates

Three sets of the binary mixtures (ankerite-muscovite, ankerite-chlorite, and chlorite-muscovite) are investigated the differentiation between their mineral mixtures in a specific band region in the spectrum. The Raman set measured by the portable Raman device with a red-NIR laser consists of average spectra of six spectra per sample. The hull quotient spectrum in VNIR-SWIR is a corrected spectrum calculated by dividing the reflectance value at the "Hull line" that links the background values of curved shapes in the reflectance spectrum. Therefore, it is effective in minimizing the effects individually affecting the VNIR-SWIR spectrum such as grain size or colour of a sample, and in comparing the tendency of changes in band intensity between minerals.

The mixed samples in the Raman spectra are quantified in the 670-730 cm^{-1} range, where the band characteristics of the three minerals are prominent. VNIR-SWIR analysis focuses on

the SWIR region (1300-2500 nm) showing absorption features in the three minerals due to OH, Al-OH, Fe-OH and CO_3 in the SWIR region. The intensity changes in the Raman spectra of the ankerite-muscovite mixtures are observed in the form of shoulder according to the difference in mineral content. In the SWIR region, the intensity of Al-OH band at 2194 nm with a fixed position becomes stronger as the muscovite content increases (**Fig. 68**). However, the secondary Al-OH absorption position for muscovite is close to the position for ankerite, thus the band shifts are observed as a single band in the 2325-2347 nm. The spectral ratios calculated from both techniques show high correlations with the change in mineral content by showing R^2 of 0.99 and 0.96, respectively (**Fig. 69**A and B).

The chlorite-ankerite mixtures show the intensity change without overlapping the two peaks at 678 cm^{-1} and 722 cm^{-1} for chlorite and ankerite, respectively in the Raman spectra (**Fig. 70**). In the SWIR region, it is observed that the absorption intensities at 1392 nm and 2194 nm, indicating OH and Fe-OH, weaken as the chlorite concentration decreases. However, the absorption position of Mg-OH for the pure chlorite and CO_3 for the pure ankerite is the same, thus the absorption feature at 2325 nm shows strong intensity of the absorption regardless of the mixing ratio (**Fig. 70**). The spectral ratios calculated from the Raman spectra show a high correlation ($R^2 = 0.98$) with the change in mineral content (**Fig. 69**C). In the SWIR region, the intensity change of Fe-OH in the chlorite-ankerite mixtures linearly increases as the chlorite content increase (**Fig. 69**D). However, the spectral ratio between the band intensity of Fe-OH and the one at 2325 nm of Mg-OH and CO_3 does not show any correlation with the mixing ratio (**Fig. 69**E). Instead, the spectral ratio using the absorption intensity at 1392 nm, indicating the absorption feature of OH, shows a high determination coefficient of 0.99 (**Fig. 69**F). Nevertheless, it needs to pay attention to apply this spectral ratio because the absorption feature around 1400 nm by OH appears not only in chlorite but also in other silicates such as phyllosilicates and hydroxylated silicates (Pontual, 2008).

The intensity changes of the chlorite-muscovite mixtures in the Raman spectra are observed in the form of shoulder or single-like peak according to the mixing ratio (**Fig. 71**). The spectral ratio between the intensity of Al-OH at 2194 nm and the one of Fe-OH at 2247 nm are used for quantitative analysis in the SWIR region. The spectral ratios calculated from both techniques show high correlations with the change in mineral content by showing R^2 higher than 0.99 (**Fig. 69**G and H).

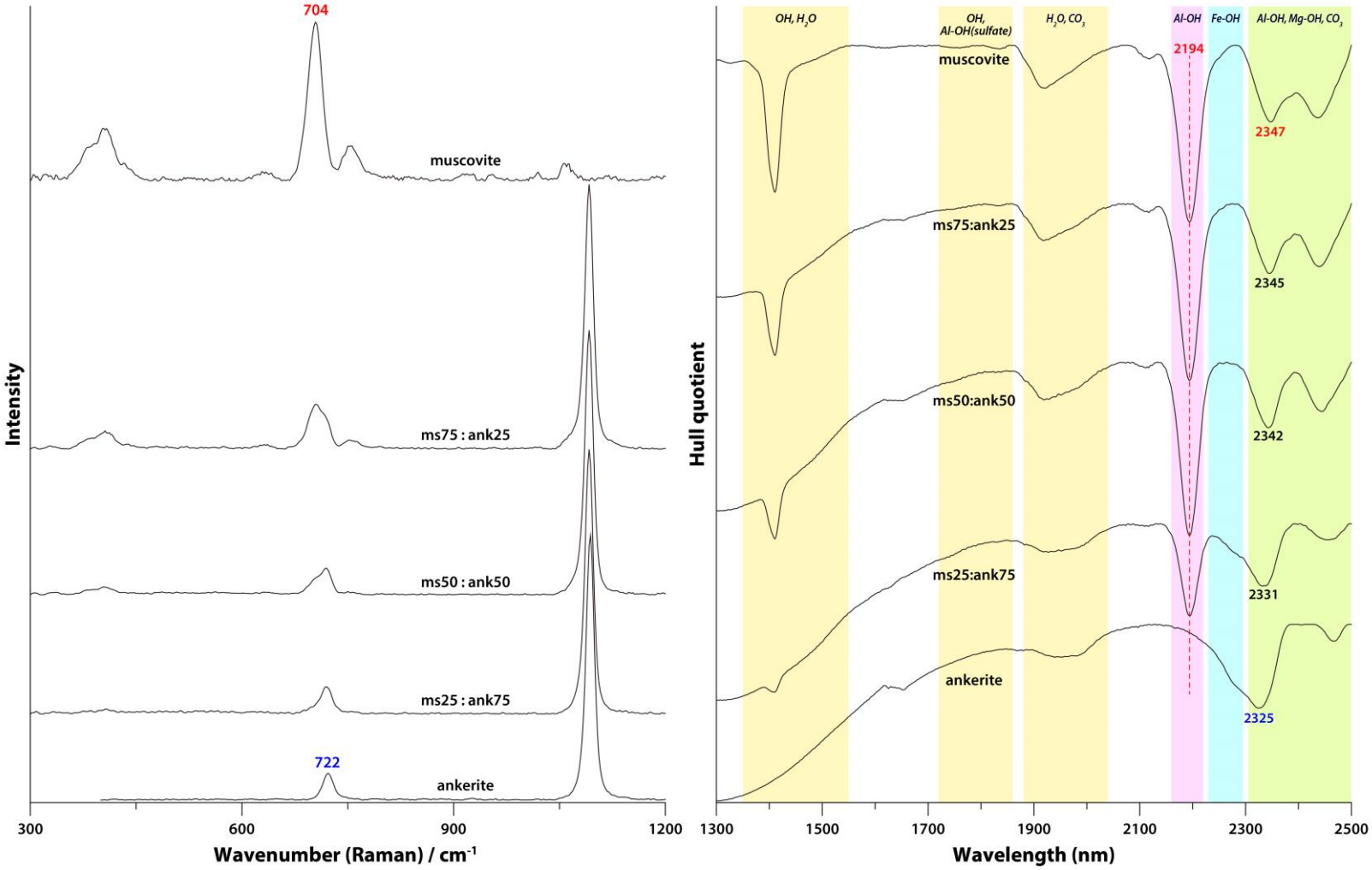

Fig. 68. Raman and SWIR spectra of muscovite-ankerite mixtures.

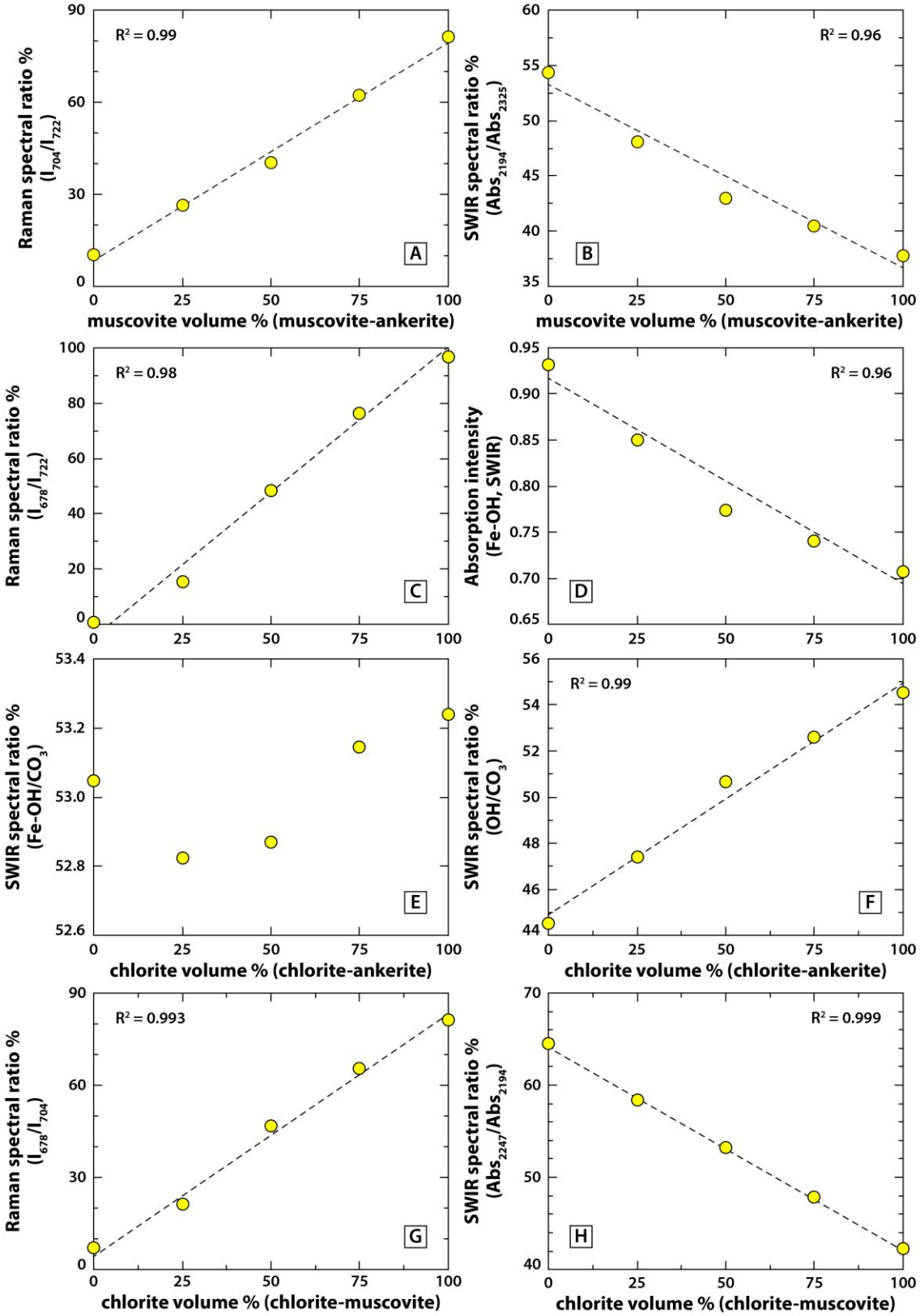

Fig. 69. Correlation between the spectral ratios and the mixing ratios in the muscovite-ankerite mixtures (A and B), the chlorite-ankerite mixtures. (C-F), and the chlorite-muscovite mixtures (E and F).

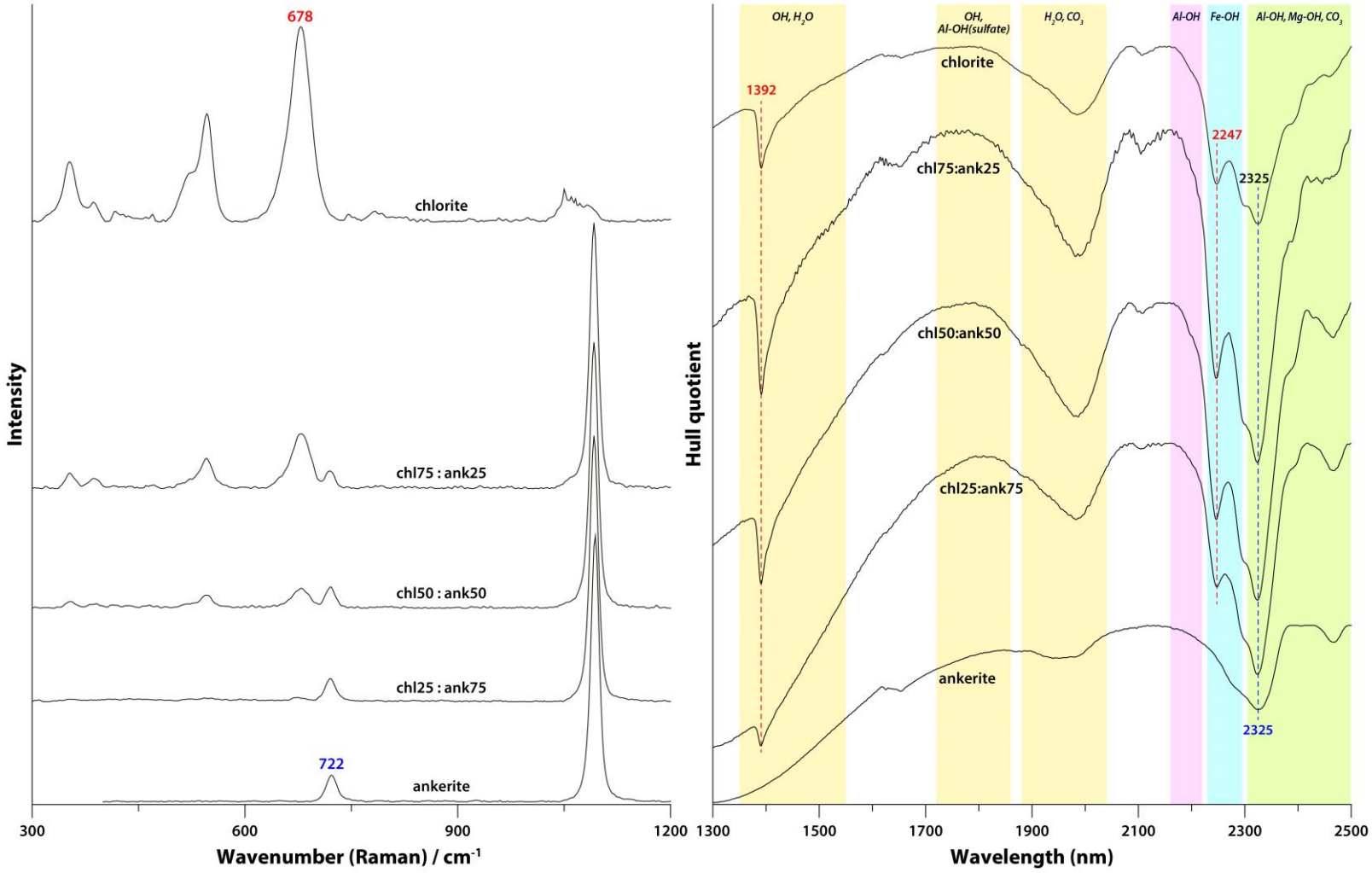

Fig. 70. Raman and SWIR spectra of chlorite-ankerite mixtures.

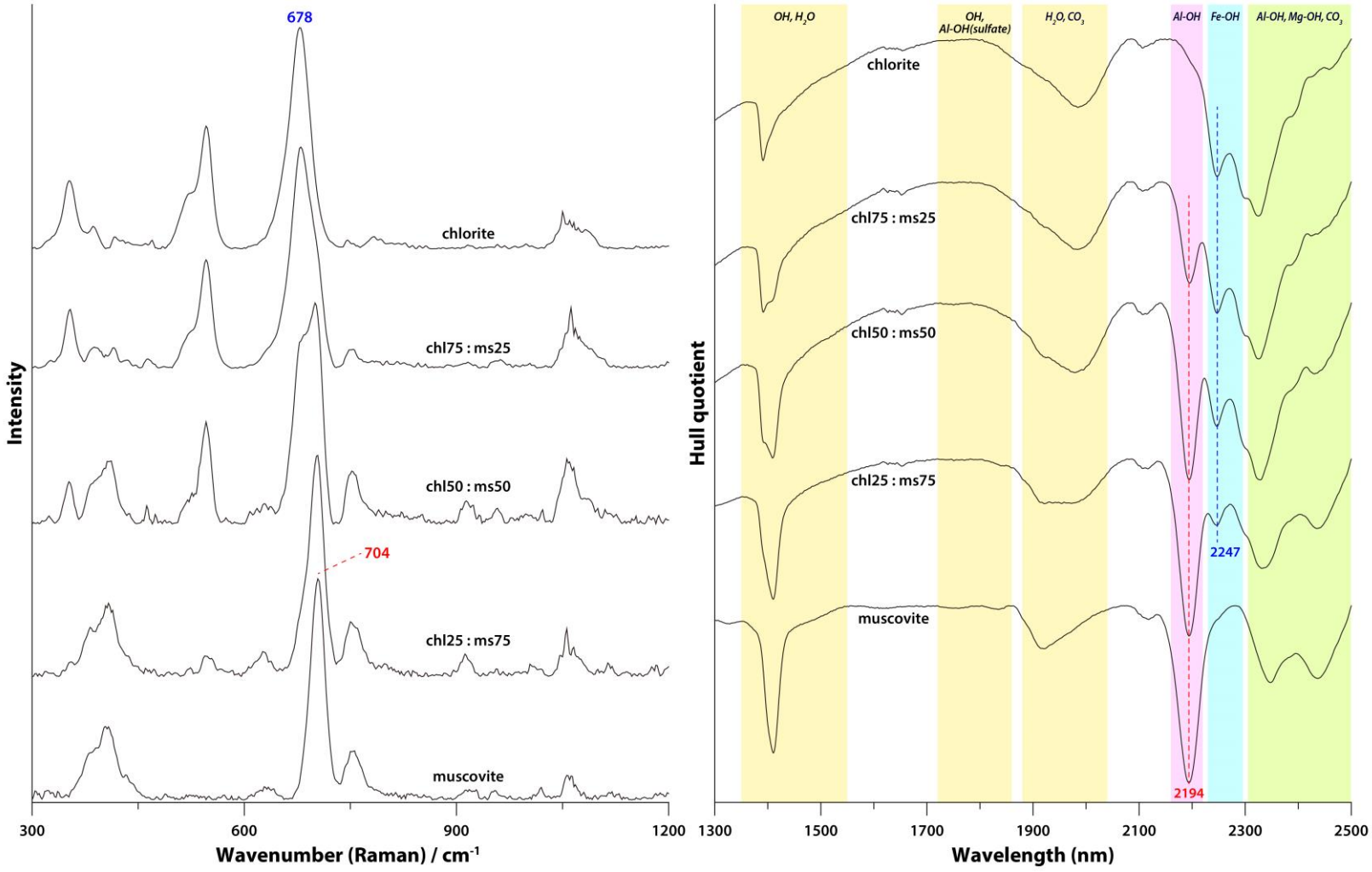

Fig. 71. Raman and SWIR spectra of chlorite-muscovite mixtures.

Chapter VI. Application to the Elvira VMS deposit

1. Introduction

Volcanogenic Massive Sulphide (VMS) deposits are stratabound or sometimes stratiform accumulations of massive sulphide hydrothermal ores that precipitated at or near the sea floor where circulating hydrothermal fluids in spatial, temporal, and genetic association with contemporaneous volcanism and/or plutonism in extensional settings (Franklin et al., 2005; Hannington, 2014; Shanks and Thurston, 2012). VMS deposits contain a significant source of the base (Cu, Pb, Zn), precious (Ag. Au), and other metals (e.g., Co, Sn, In, Cd, Tl, Ga, Se, Sb, Bi) of economic and industrial importance (Franklin et al., 2005; Large et al., 2001b; Tornos et al., 2015). The Iberian Pyrite Belt (IPB) belongs to the southernmost domain of the Variscan Belt in the Iberian Peninsula, holding over 1600 Mt of massive sulphides originally in place and about 250 Mt of stockwork ore in over 90 VMS deposits (Tornos, 2006). This large amount of the ores indicates the IPB is one of the most outstanding ore provinces in Europe and one of the largest concentrations of sulphides in the Earth's crust.

The use of vectors to locate hidden ores focuses on the identification and study of geochemical fingerprints produced by the mineralizing hydrothermal system or by subsequent ore remobilizations within and around ore deposits since the progressive depletion of the shallowest and most easily accessible ore deposits (Ames et al., 2016; Large et al., 2001b; Madeisky and Stanley, 1993). The vectors are potentially able to detect the nearby presence of an ore deposit based on the observation of variation in lithology, geochemistry, mineralogy, and mineral chemistry. Therefore, they do not simply find the location of the ores but also provide the spatial distribution around an ore deposit. Exploration for new sources faces challenges such as exploration in non-conventional settings, as well as an inevitable need for improved efficiency and lower impact in both environmental and social terms. In this chapter, the combined study of VMS mineral systems and the development of new exploration strategies and technologies based on geochemically spectral methods and vectors to ore play a vital role.

The Elvira VMS deposit located in the south-eastern area of the IPB consists of polymetallic (Cu-Zn-Pb) massive sulphides (**Fig. 72**A). A geological model of the Elvira

deposit is currently being developed by the Consejo Superior de Investigaciones Cientificas (CSIC) and the Minas de Aguas Teñidas SAU (MATSA) mining company in the NEXT (New Exploration Technologies) project (G.A. No. 776804), funded by the European Union's Horizon 2020 research and innovation programme. This project aims to develop new geo-models and novel sensitive exploration technologies, and one of the tasks involved focuses on obtaining rapid, reliable, and efficient data in the field within this frame. Although the specific characteristics of the stratigraphic sequence and the style of mineralization associated with the Elvira deposit have not been yet studied in detail, the vectors to the ores can be based on the mineralogical and geochemical variation from the Sotiel-Migollas massive sulphide cluster due to the westward continuation of the Elvira deposit (Gisbert et al., 2019, **Fig. 72**B). Therefore, the lithologic and structural settings observed in the Sotiel-Migollas deposit are expected to be strongly similar to the Elvira deposit. A single massive sulphide lens located 250 to 500 m below the surface of the Elvira deposit is hosted in a shale-dominated sequence, including dark shales both in the footwall and hanging wall (Gisbert et al., 2019, **Fig. 72**C).

Since recent developments of light portable spectroscopic tools have provided practical information in the field, spectroscopic characteristics of indicative minerals such as carbonates, chlorites, and dioctahedral micas present in the Elvira deposit are investigated for the application of portable spectroscopy for rapid analysis of geochemical data generated by Raman and VNIR-SWIR spectrometers. Based on the spectroscopic information of the pure carbonate and phyllosilicate minerals in **Chapter IV** and **Chapter V**, respectively, this chapter shows the application to heterogeneous samples from a whole drill core in the Elvira deposit by identifying the indicative minerals and their compositional changes. Therefore, this result provides that portable spectroscopy can be employed as a new method in resource exploration by developing the optimized methodology.

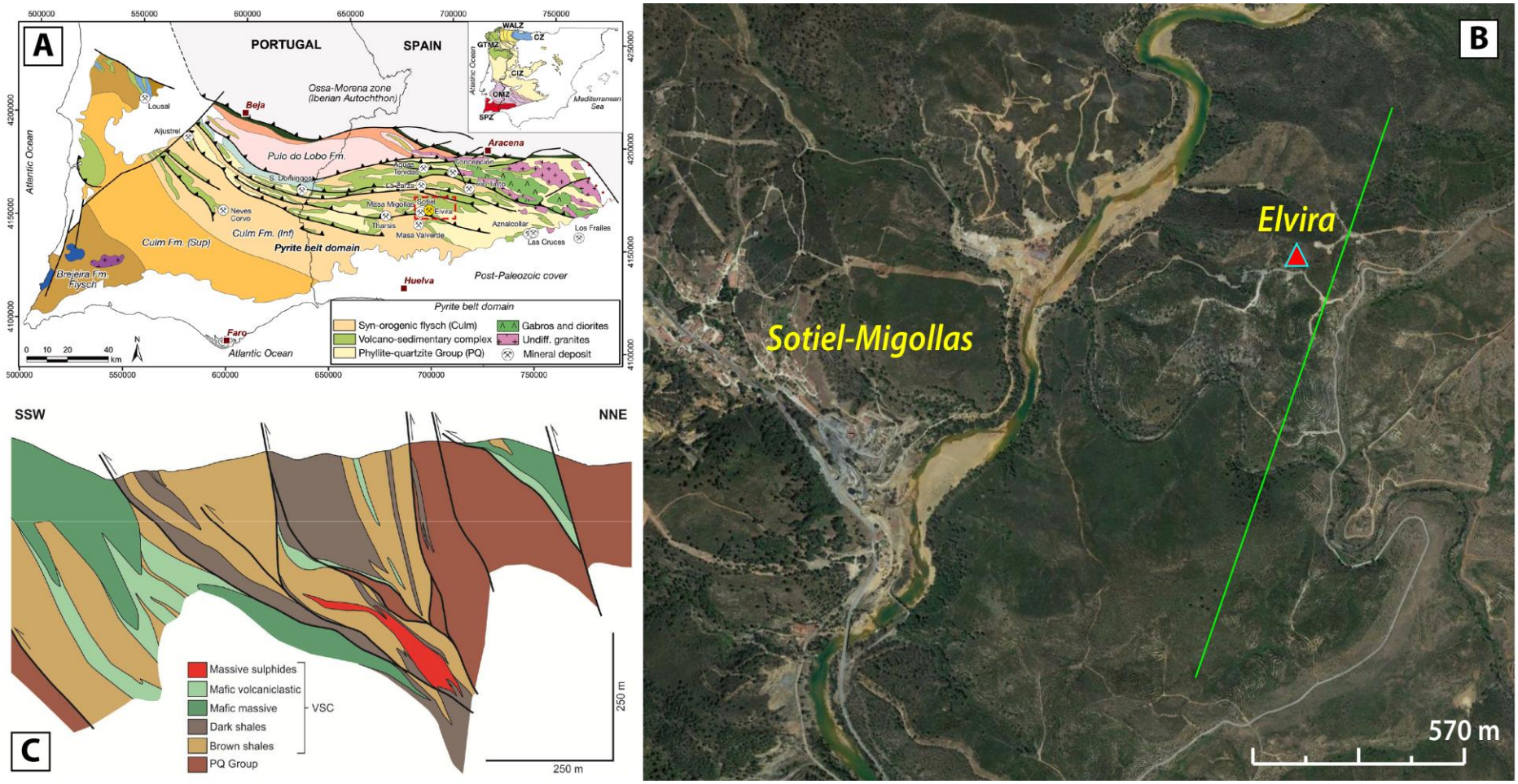

Fig. 72. A) Main stratigraphic units in the Iberian Pyrite Belt modified from De La Rosa et al. (2021); B) Satellite image of the area around the Elvira deposit taken from Google Earth. The green line indicates the position of the cross-section; C) Geological cross-section of the Elvira deposit provided from MATSA.

2. Geologic setting and mineralogy

The Iberian Pyrite Belt (IPB) is an E-W 250 km long by 20-70 km wide VMS district in the southwestern Iberian Peninsula (**Fig. 72**A, Inverno et al., 2015). The original mineralization and depositional setting was strongly modified by Carboniferous Variscan orogeny compressive stage, which in the area produced a thin-skinned foreland fold and thrust belt and regional metamorphism up to the low green schist facies (Bobrowicz, 1995; Inverno et al., 2015; Tornos, 2006). The Elvira deposit represents an eastward continuation of the Sotiel-Migollas massive sulphide deposits cluster, which is located in the south-eastern area of the IPB (**Fig. 72**B, Inverno et al., 2015; Prada et al., 1996; Velasco-Acebes et al., 2019). The Sotiel-Migollas-Elvira is one of the largest clusters of massive sulphide deposits in the IPB, with a tonnage well above 100 Mt (Gisbert et al., 2019). The Elvira deposit consists of a polymetallic (Cu-Zn-Pb) pyrite-rich massive sulphide body with evidence of having been dominantly deposited in a suboxic to anoxic intracontinental basin and rooted on a large stockwork zone during late Devonian to early Carboniferous (Gisbert et al., 2019).

Information retrieved from exploration drill cores of the Elvira deposit show a largely similar stratigraphic and structural setting for the Sotiel-Migollas deposit (Gisbert et al., 2019). The Elvira consists of a single massive sulphide lens hosted in a shale-dominated sequence including black shales both in the footwall and hanging wall to the deposit, and minor fragmental volcanic rocks (**Fig. 72**C). In the sequence footwall, a coherent subvolcanic basaltic sill related to the Volcanic Sedimentary Complex (VSC) has been intersected. In hanging wall position, PQ rocks are thrusted over the VSC sequence. Therefore, the local stratigraphic sequence and the mineralogy part are briefly described by referring to previous research studied by Prada et al. (1996), Velasco-Acebes et al. (2019), and others.

2.1. Local stratigraphic sequence

The stratigraphic sequence in the Sotiel-Migollas-Elvira area is highly tectonized consisting of: (i) a structural footwall of the VSC dominated by felsic dome complexes intruding and interbedded with dark shales in the lower part, (ii) an overlying shale unit hosting the massive sulphides, and (iii) an overthrusted hanging wall of the Phyllite-Quartzite (PQ)

Group, which hosts a well-developed stockwork in the Migollas deposit (**Fig. 73**, Prada et al., 1996; Velasco-Acebes et al., 2019). The contact between the VSC and the PQ Group is interpreted as a major thrust in the inverse limb of a major south-verging fold (Velasco-Acebes et al., 2019). The PQ Group, the oldest rock unit in the IPB, consists of a monotonous sequence of shales and quartz-rich sandstones with only some minor lenses of limestone deposited on a stable continental platform during Middle Devonian (Schermerhorn, 1971; Velasco-Acebes et al., 2019). The VSC is composed of several hundred meters thick of dominantly footwall felsic volcanic rocks and, in its structural hanging wall, a 400 m-thick unit of dark shale overlaying the felsic rocks is host to the massive sulphides. The footwall felsic volcanic rocks are mostly dacites forming dome complexes with a coherent core and large deposits of transported hyaloclasite (Velasco-Acebes et al., 2019).

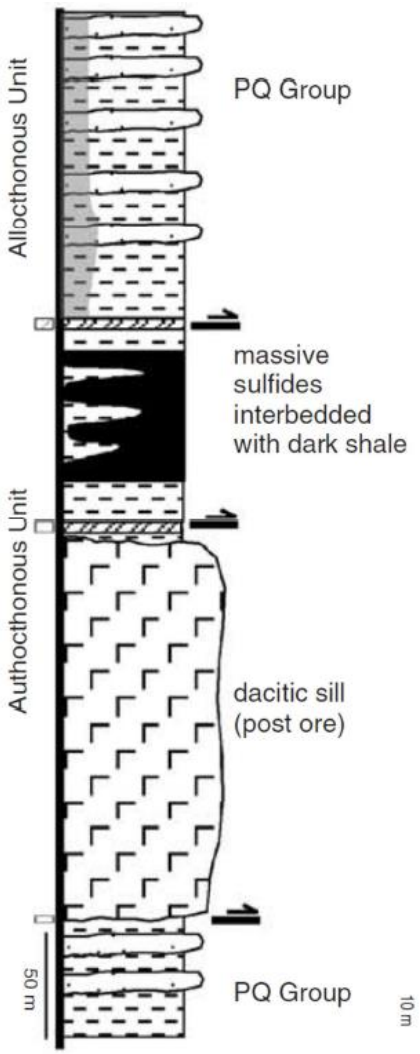

Fig. 73. Schematic stratigraphic sequence of the Sotiel-Migollas deposit from Tornos (2006).

The dark shale is locally carbon-rich, presenting a cm-thick sedimentary layering, sparse levels of volcanoclastic sandstone, some layers of quartz-rich sandstone, and abundant disseminated to stratiform pyrite with local bodies of sedimentary breccias with chloritised fragments supported by an unaltered shale (Velasco-Acebes et al., 2019). Furthermore, in the direct structural footwall to the massive sulphide, the shale hosts a discontinuous layer of black limestone with organic matter and disseminated pyrite. The sequence of massive sulphide hosting shales is capped by discontinuous lenses of glass-rich breccias which are interpreted as pumice breccia (Velasco-Acebes et al., 2019). The immediate footwall to the shale unit is represented by a dacitic sill which was interpreted to postdate the mineralizing event since it does not host any stockwork and, instead, includes pyrite-bearing peperites (Tornos, 2006). The contact between PQ and VSC rocks hosts abundant mylonitic bands with lenses of mixed lithologies from both groups that show widespread chlorite and carbonate alteration (Velasco-Acebes et al., 2019). This surface was interpreted to have favoured the widespread remobilization of the sulphides, showing abundant thin sulphide-rich veins parallel to the foliation and massive chalcopyrite concentrated along shear zones (Velasco-Acebes et al., 2019).

2.2. Ore and alteration mineralogy

Most of the shale-hosted VMS deposits in the IPB do not display either clear metal zonation or zones of major base metal enrichment, and in Sotiel-Migollas, Cu and Zn–Pb rich zones are common, but these do not show a well-defined distribution, and neither does Elvira (Prada et al., 1996; Tornos, 2006). The style of mineralization of Sotiel-Migollas has been observed to vary between the individual orebodies by Velasco-Acebes et al. (2019). The mineralization at Sotiel and Sotiel-Este is banded and dominated by alternating layers of massive sulphides and hydrothermally altered shale. On the other hand, the mineralization at Migollas, the deposit closest to Elvira, is mostly massive and with no interbedded shale and is dominated by a siderite-rich massive sulphide. The style of mineralization in Elvira is yet to be studied in detail, but exhalative massive sulphides, and dark shale interbedding is locally observed (Gisbert et al., 2019). The mineral assemblage of massive sulphides in the Sotiel-Migollas-Elvira is dominated by massive pyrite with variable amounts of chalcopyrite,

sphalerite and galena, lesser amounts of arsenopyrite, pyrrhotite, magnetite and tetrahedrite-tennantite, as well as trace amounts of sulfosalts (boulangerite, bournonite, jaskolkiite and meneghinite), cassiterite, native bismuth and electrum (Velasco-Acebes et al., 2019).

The massive sulphides in the southern IPB are hosted by dark shales with variable hydrothermal alteration (Velasco-Acebes et al., 2019). The alteration is conspicuous in the footwall, less pervasive and irregular adjacent to the mineralization and almost non-existent above it, and mostly produces shale chloritization (chlorite ± quartz). Alteration characteristics in the Sotiel-Migollas area show that the less hydrothermally altered shale mainly consists of a foliated groundmass of fine-grained illite ± muscovite, sparse pyrite, disperse grains of anhedral quartz, carbonates, ilmenite (altered to rutile), and zircon (Velasco-Acebes et al., 2019). In areas affected by hydrothermal alteration, chloritic alteration is closely associated with zones of brecciation or veinlets of carbonates and sulphides ± quartz (Gisbert et al., 2019). Primary shale layering was lost during chloritization, and the illite was replaced by massive chlorite. The resulting mineral assemblage contains clinochlore ± chamosite, variable amounts of carbonates, abundant anhedral pyrite (10-30%), and small amounts of disseminated sphalerite, chalcopyrite, galena, monazite and a significant amount of hydrothermal zircon. In the Migollas area, the shale between the individual lenses and lateral to the mineralization shows irregular chloritization and a subtle carbonate-rich alteration.

3. Materials and methods

3.1. Sample materials

The investigation of geochemical vectoring tools at the Elvira deposit has been performed through the study of samples collected from a representative drill core (ELV44) provided by MATSA mining company. The ELV44 drill core with a total 358m length intersects the very margin of the massive sulphide orebody by its southern margin. Starting at the surface, it proceeds through 324m of VSC shale consisting of black shales and grey/dark shales, only 2m of massive sulphides, and 14 m of carbonate-rich stockwork whose base is defined by a fault zone (**Fig. 74**). It is noted that the carbonate stockworks likely formed after the genesis of the geochemical halos around the deposit since they are depleted in Tl but not Sb relative to the

surrounding halo concentrations (Gisbert et al. 2021b). This drilling was chosen to study the petrological and geochemical characteristics of the shales in the VSC and their variations with increasing stratigraphic or structural distance (along the core) to the ore, as well as the stockwork system of this deposit.

According to CSIC, the VSC shales in the ELV44 drill core are divided into two groups based on whole rock geochemistry: i) "regular" dark grey to black shales, and ii) "special" black shales. Regular black shales are characterized by low MgO, FeO, and SiO2 with lower total organic carbon (TOC), and special black shales have low P and high V, Ba, U, and Si with higher TOC. As V and U are redox-sensitive elements, their higher contents in the special black shales indicate less oxidized conditions of deposition compared to the regular shales. The regular shales occur in discrete horizons along the stratigraphic sequence, separated from the massive sulphide stratigraphic level. The special black shales are located immediately above the massive sulphides or within the VSC footwall in the ELV44, and they belong to the stratigraphic horizon of the massive sulphides. Furthermore, the black shales between the massive sulphides and the carbonate stockworks are highly chloritised related to hydrothermal fluids, and their chemical characteristics are analogous to the regular shales (**Fig. 74**).

In this study, 56 samples were intensively collected from ca. 245m depth to the bottom in the ELV44 drill core according to diverse lithologies at the bottom of the core (**Fig. 74**). The 56 thin sections are investigated for mineral assemblages under microscopic observation and mineral chemistry by SEM-EDS. Then, 30 thin sections among them were selected to acquire precise mineral chemistry by EPMA, and the counterparts of the thin sections are measured by portable Raman and VNIR-SWIR devices. Phyllosilicate minerals observed from the ELV44 drill core are fine-grained and dispersed with smaller amounts compared to other minerals such as quartz, carbonate, and graphite. Furthermore, fluorescence interference was confirmed in the Raman spectra of the drill core measured by the portable Raman device with a green laser (RaPort). Therefore, Micro-Raman analysis using a green laser in a laboratory are additionally carried out to identify the spectral characteristics associated with the mineral composition. Micro-Raman analysis can be out of the objective of this study, which focuses on spectroscopic applications using portable instruments. However, it attempts to investigate the uncertainty of the calibration curves presented in **Chapter V** by showing how consistently the minerals from the "real" rock samples plot against the calibration curves.

The previous research plan was to distinguish minerals from the spectra on the core and recognise the compositional variation in the indicative minerals for identifying the Elvira deposit footprint. However, the CSIC team confirmed that the Elvira deposit does not have pathfinders for the indicative minerals (i.e., phyllosilicates and carbonates) contrary to the presence of representative indicators shown in the VMS system (Gisbert et al., 2021). Therefore, this chapter aims at identifying the possibility of lithology classification from the spectrum of each lithology in the ELV44 drill core. For that, the applicability of the calibration curves to estimate chemical composition with respect to major elements of the indicative minerals built from **Chapter IV and V** was investigated on the actual core samples.

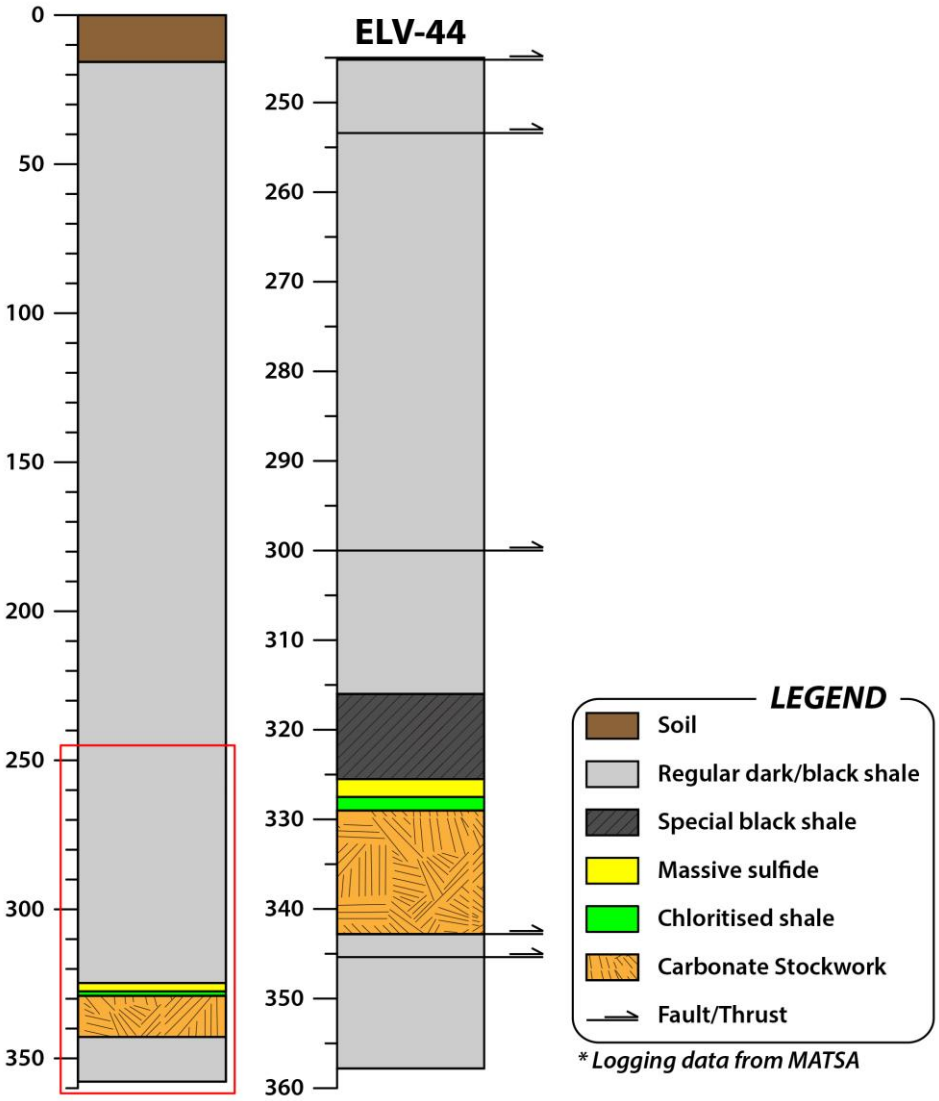

Fig. 74. Schematic stratigraphic columns of the main studied drill core (ELV44) at Elvira deposit. Depth along the core in metre. Logging data provided from MATSA.

3.2. Experimental methods

Chemical compositions were determined with a CAMECA SXFive TACTIS electron microprobe (EPMA) at the Service Commun de Microscopie Electronique et de Microanalyse X (SCMEM) of the GeoRessources laboratory (Vandœuvre-lès-Nancy, France). Analyses were carried out in spot mode using 15 kV accelerating voltage, 10 nA beam current and a 10s on-peak acquisition time with respect to both carbonates and phyllosilicates.

VNIR-SWIR spectral measurements were carried out by the SR-6500 spectroradiometer (Spectral Evolution), and the instrument was corrected using a calibrated ceramic disk that uniformly reflected 99% whiteness across the spectrum. The specimens were measured using a contact probe with 10 mm spot size, and each spectrum was produced from an average of 40 measurements to represent the overall spectral pattern. The selection of the absorption position was determined by the wavelength at maximum absorption after removing the convex-hull of the signal by hull quotient installed in the ENVI software (Exelis, 2012).

Raman spectra were collected by a portable and laboratory-based spectrometers, respectively. Bravo portable spectrometer (Bruker) is equipped with dual excitation lasers at expected 785 nm and 1064 nm, respectively. The maximum output power is 30 mW, and the minimum spot size is around 15 µm. The spectral range is 300-3200 cm^{-1} at a spectral resolution of 10-12 cm^{-1}. Spectrum acquisition, basic data visualization and management, and baseline subtraction are automatically controlled by OPUS software of the device itself. Additionally, an automated background removal installed in the Crystal Sleuth software is carried out (Laetsch and Downs, 2006). LabRAM HR micro-Raman spectrometer (Horiba Jobin Yvon) in GeoRessources are used for phyllosilicates and carbonates in the ELV44 drill core, which are fine-grained, or show fluorescence interference with the portable Raman with a green laser (RaPort). The laboratory-based Raman instrument works with a 514.53 nm laser excitation (green) at a power of 200 mW. The spectra were acquired at 25% and 50% of maximum power with respect to phyllosilicates (i.e., chlorites and dioctahedral micas) and carbonates, respectively. The acquisition time is 10 seconds with 10 accumulations. Peak positions are identified after the subtraction of a straight baseline using LabSpec 6 software (Horiba Jobin Yvon). In order to consider the possibility of peak shift, the Raman peak position of Argon laser at 919 cm^{-1} was regularly confirmed.

4. Results

4.1. Carbonate minerals

Fig. 75A displays four types of carbonate minerals with the compositional changes in the ELV44 drill core by Ca-Mg-Fe+Mn ternary diagram using the cation composition of carbonate minerals by the microprobe analysis. Calcite, which is not related to the ore-forming event, is only observed in veins in the regular/special shales. Ankerite-dolomite solid solution and siderite appear in all the lithology groups and magnesite is additionally found in the carbonate-rich stockwork. According to the cations of carbonates in the Elvira (i.e., Ca, Mg, and Fe) at depth, calcite only appears in the upper part of the shales, and ankerite-dolomite solid solution is found in all the lithology groups (**Fig. 75**B). Siderite appears among the regular shales, the carbonate-rich stockwork, and the massive sulphide. In the carbonate-rich stockworks, one sample has iron-rich magnesite around 335m. In Sotiel-Migollas, the hydrothermal carbonates associated with the ores show a systematic variability according to depth with a predominance of dolomite in the deepest part under the ore, which is gradually replaced by ferroan dolomite in the intermediate zone to ankerite and even siderite in the shallowest part (Velasco-Acebes et al., 2019). However, types or compositional changes of carbonate minerals in the ELV44 drill core do not show any tendency to depth or proximity to the massive sulphides.

VNIR-SWIR spectroscopy is able to recognize the presence and also the composition of carbonate minerals in the regular shales and the carbonate-rich stockworks in the Elvira samples despite diverse carbonate clusters (**Fig. 76**). However, it is difficult to distinguish the absorption characteristics of carbonates in the VNIR-SWIR region in the other lithology groups due to small amount of carbonates in the chloritised shales or extremely low reflectance in the special black shales and the massive sulphides. Some samples from the veins and the regular shales contain calcite and ankerite positioned at 2336 nm and around 2327 nm, respectively (**Table 13**). The absorption position of most carbonate-rich stockwork samples indicates ankerite-dolomite solid solution close to the dolomite area (Mg# = 0.28-0.33). One Mg-rich dolomite sample (Mg# = 0.43) has the shorter absorption (2321 nm) with a large compositional variation (Mg# = 0.28-0.82) than the other stockwork samples. The large standard deviation is due to the presence of two carbonate minerals analysed by electron microprobe (**Fig. 76**).

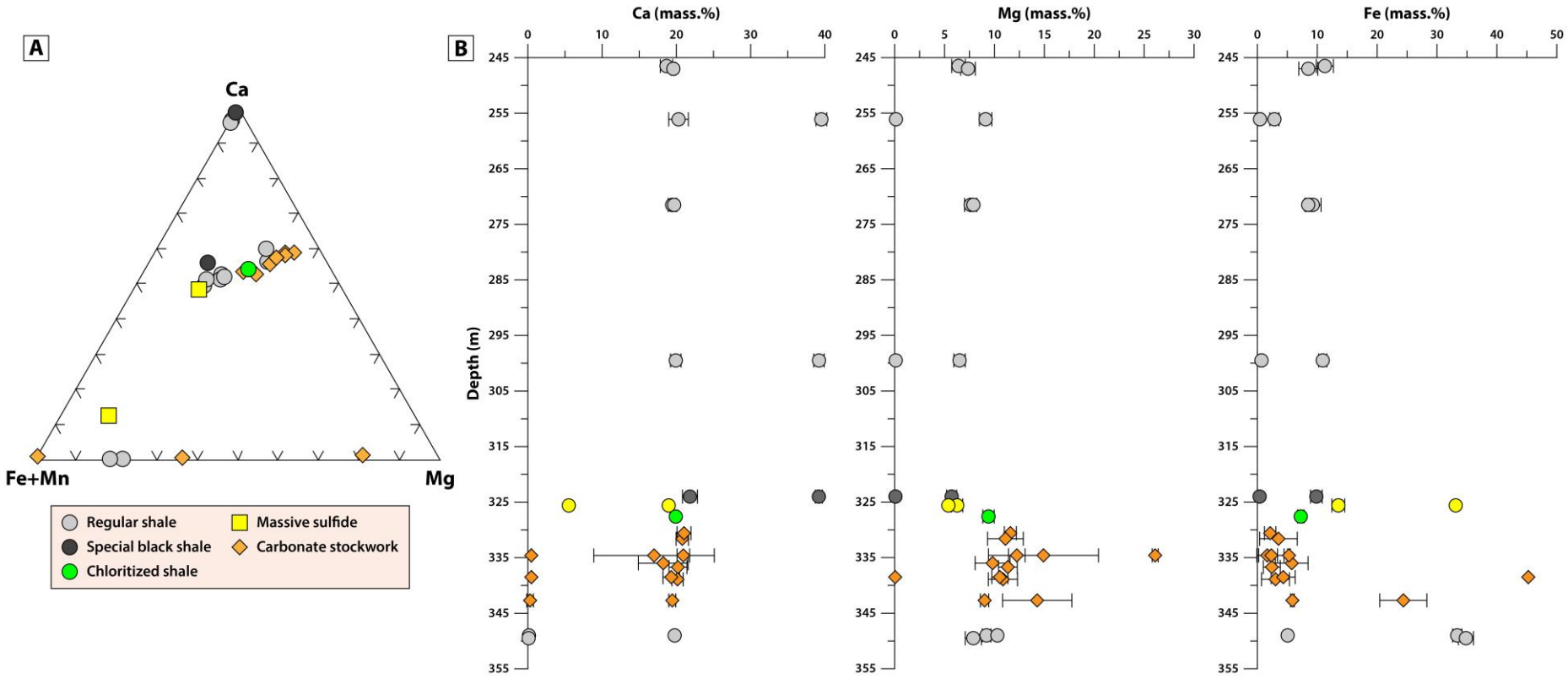

Fig. 75. A) Chemical composition of carbonate minerals in the ELV44 drill core plotted in the Ca-Mg-Fe+Mn ternary diagram; B) Ca, Mg, and Fe profiles in the carbonates along the ELV44 drill core in meter.

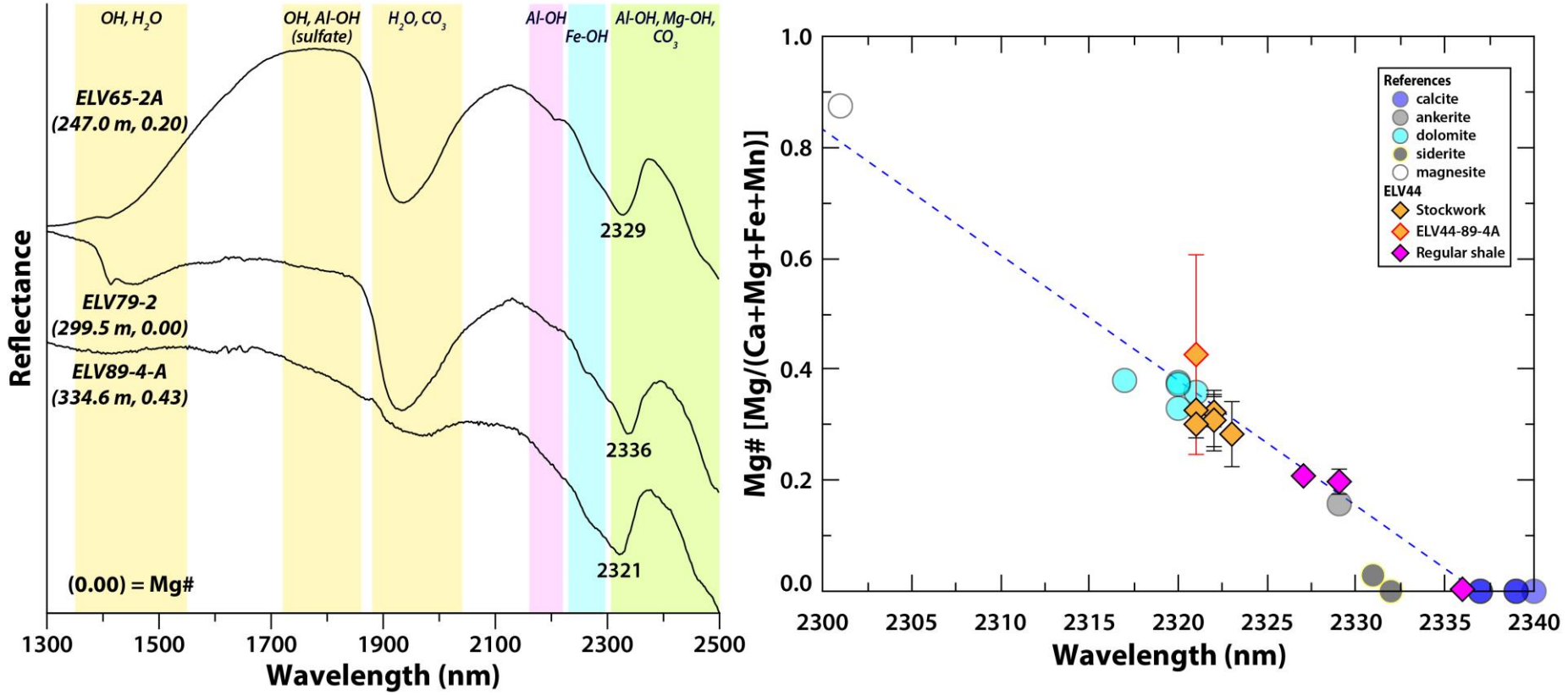

Fig. 76. Correlation between the absorption position in the SWIR region and Mg# of carbonate.

Table 13. The result of carbonate mineral composition from electron microprobe and band position in the SWIR region from the regular shales and stockworks.

Sample	Lithology	Depth (m)	SWIR (nm)	N	Mg		Ca		Mn		Fe		Mg#
					Avg	S.D.	Avg	S.D.	Avg	S.D.	Avg	S.D.	
ELV44-72-1B	Regular shale	271.5	2327	10	7.89	0.32	19.70	0.33	1.86	0.12	8.49	0.39	0.21
ELV44-79-2	Regular shale	299.5	2336	12	0.11	0.04	39.21	0.70	0.87	0.24	0.69	0.27	0.00
ELV44-88-3	Stockwork	330.6	2322	7	11.59	0.60	21.03	0.94	1.04	0.27	2.14	0.96	0.32
ELV44-88-4B	Stockwork	331.6	2324	17	11.10	1.79	20.80	0.83	0.71	0.33	3.53	3.14	0.31
ELV44-89-4A	Stockwork	334.6	2321	26	14.91	5.51	17.00	8.11	0.69	0.41	2.34	2.11	0.43
ELV44-90-2	Stockwork	336.0	2323	19	9.81	1.75	18.23	3.35	0.83	0.29	5.74	2.73	0.28
ELV44-90-3B	Stockwork	336.7	2321	33	11.34	0.94	20.21	1.21	0.81	0.28	2.41	1.42	0.33
ELV44-90-4C	Stockwork	338.5	2321	11	10.54	0.81	19.31	1.11	0.61	0.23	4.32	2.00	0.30
ELV44-91-1	Stockwork	338.9	2322	20	10.85	1.46	20.16	0.75	1.11	0.57	3.03	2.33	0.31

N = Number of spot analyses by electron microprobe; S.D. = Standard deviation.

Grey carbonates indicate dolomite composition (A, 0.34 Mg#) and magnesite in the milky white region (B, 0.80 Mg#) (**Fig. 77**). In order to investigate mineral discrimination between the two carbonates, the distinct grey part was additionally measured by VNIR-SWIR portable device. The SWIR result shows that the absorption band is shifted to the shorter wavelength from the grey to white milky carbonate showing well-reflected chemical composition (**Fig. 77**). Therefore, the absorption position at A point can be interpreted as the average spectrum between dolomite and magnesite because of the large spot size (10 mm) of the VNIR-SWIR device.

The spectral results by both micro-Raman and portable Raman analyses support the SWIR result from the carbonate mixture in the Elvira sample (ELV44-89-4) (**Fig. 78**). The Raman spectrum measured by the portable Raman spectrometer using a green laser does not show spectral characteristics due to fluorescence effects, thus the peak identification in the T mode below 210 cm^{-1} is investigated by micro-Raman spectroscopy. The symmetric bending vibration (ν_4) around 710 cm^{-1} is confirmed by the portable spectrometer using red and near infrared laser.

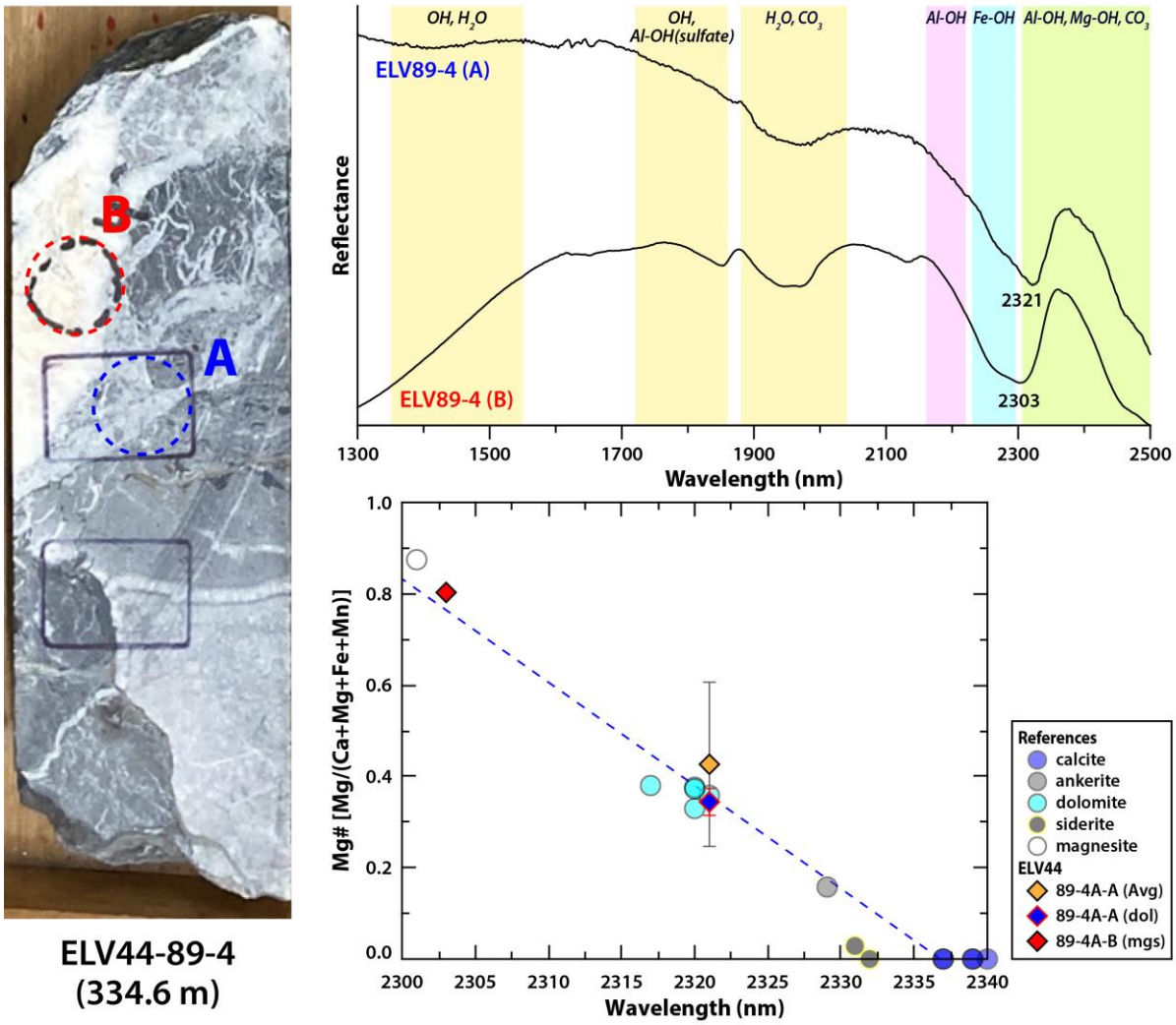

Fig. 77. SWIR spectra and Mg# of region A and B in the ELV44-89-4 sample. A region covers both grey and white carbonates and B region covers white carbonate only.

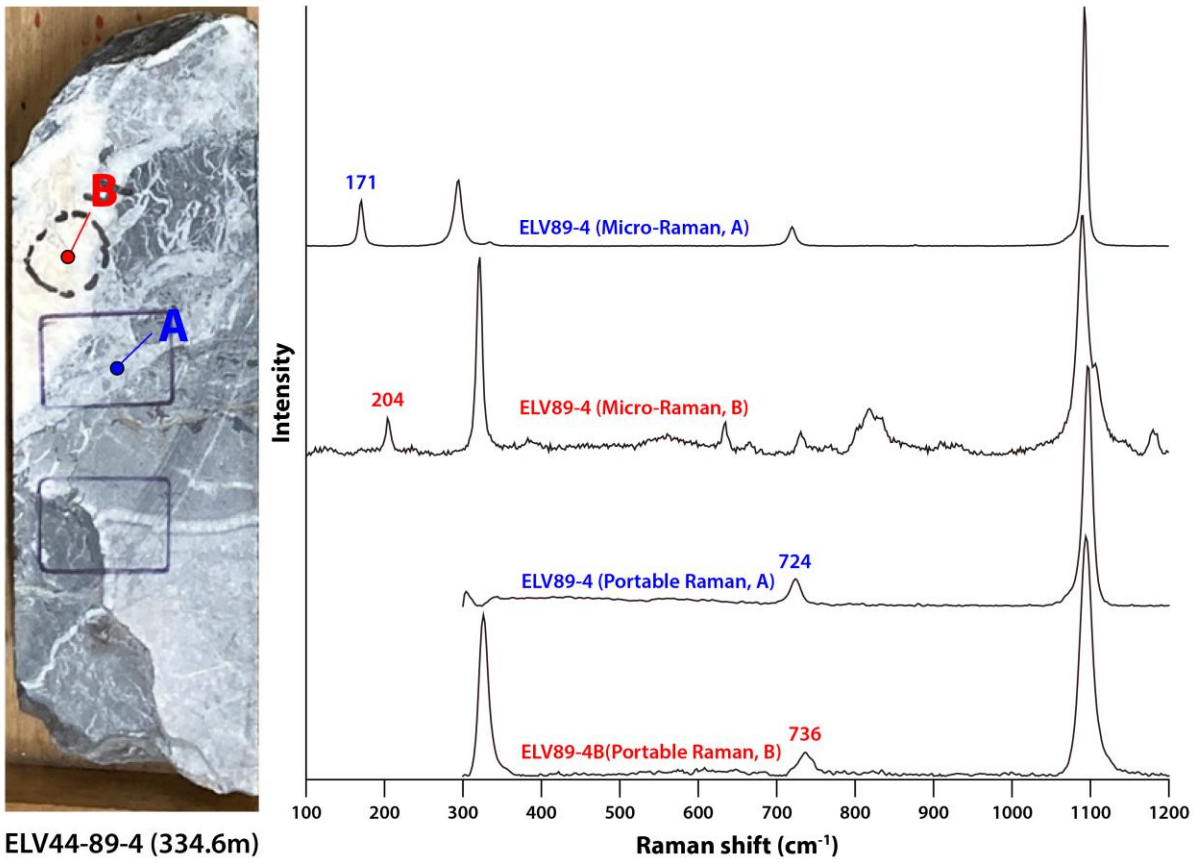

Fig. 78. Raman spectra of region A and B in the ELV44-89-4 sample acquired by the micro-Raman and the portable Raman (Bravo) devices.

Fig. 79 shows that both carbonate minerals from the Elvira sample are on the correlation curves established in **Chapter IV** of each mode (T and v_4 mode), indicating ankerite-dolomite solid solution and magnesite, respectively. Furthermore, a small amount of siderite in the regular shales is identified by micro-Raman analysis. Since a Micro-Raman spectrometer is able to obtain a Raman spectrum while being observed under a microscope, it is possible to measure the Raman spectrum at the exact location analysed by an electron microprobe. However, measurement with the exact location cannot be carried out with the portable devices. Therefore, portable spectrometers face somewhat difficulties in measuring fine-grained carbonates in heterogeneous shales, and absorption features of other minerals, which occupy a large volume in the sample such as quartz and graphite, are prominent in the Raman spectra.

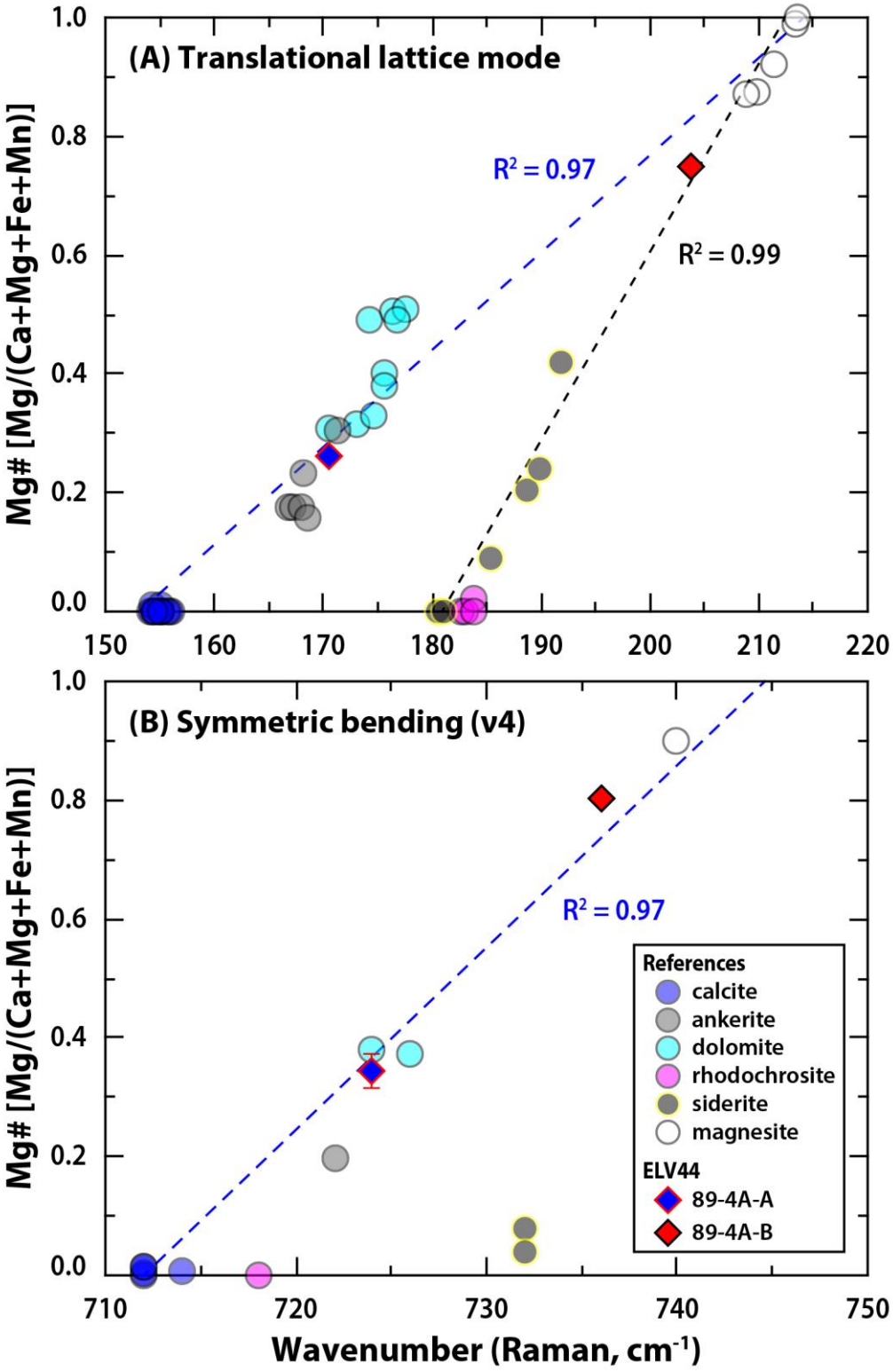

Fig. 79. Correlation between the different peak regions and Mg#. For the Elvira samples, the peak position in the T mode (A) and the ν4 mode (B) were obtained from the micro-Raman and the portable Raman devices, respectively.

4.2. Trioctahedral chlorites

In the shale-hosted VMS deposits in the southern IPB, the shale was pervasively hydrothermally altered near the ore body and especially beneath it. Chloritic alteration is closely associated to zones of brecciation or veinlets of carbonates and sulphides ± quartz (Velasco-Acebes et al., 2019). During chloritization, the rock lost its primary layering and the illite was replaced by both massive Mg-rich and Fe-rich chlorites.

Chlorites from the regular and special shales in the ELV44 drill core display brown to deep blue in XPL images with high Fe# ranging from 0.7 to 0.9 (**Fig. 80**). The Fe# corresponds to the average value of all chlorite data acquired from each thin section analysed by EPMA. Blue chlorites are normally observed in the shales, but the brown chlorites slightly lower Fe# than the blue chlorites are found in the press shadows of metamorphic process (**Fig. 80**). The chloritised shale has the intermediate Fe# between the shales and the carbonate-rich stockwork. In that region, there are diverse compositions from 0.5 to 0.8 in Fe# showing different interference colours from grey to blue. In the carbonate-rich stockwork region, pale grey chlorites are commonly observed with very low Fe# (0.2-0.5) with large standard deviations.

VNIR-SWIR analysis is appropriate for chlorite, which is one of the hydroxylated phyllosilicates active in that region. According to the SWIR result in **Chapter IV**, the absorption for Fe-OH appears in the longer wavelength as iron content increases. In order to identify the composition of chlorites in the SWIR region, the absorption band for Fe-OH around 2255 nm was selected because the other region for Mg-OH around 2340 nm can be overlapped with the other indicative minerals such as dioctahedral micas and carbonate minerals. Few samples only show absorption feature of chlorite in the visible to SWIR region because most dark/black shales have excessively low reflectance to rarely recognize the diagnostic absorption of chlorite. Furthermore, I confirmed that the chlorites in the drill core have much smaller amounts than other minerals such as quartz, graphite, and carbonate under the microscopic observation. The absorption position of the regular, special and chloritised shales is well located on the calibration curve provided in **Chapter IV** (**Fig. 81**). The regular and special shales have similarly high Fe# of chlorites while the chloritised shale shows lower Fe# of chlorites than the other shales with a large compositional variation. This result shows that the Fe-OH absorption position effectively reflects the compositional changes in chlorites.

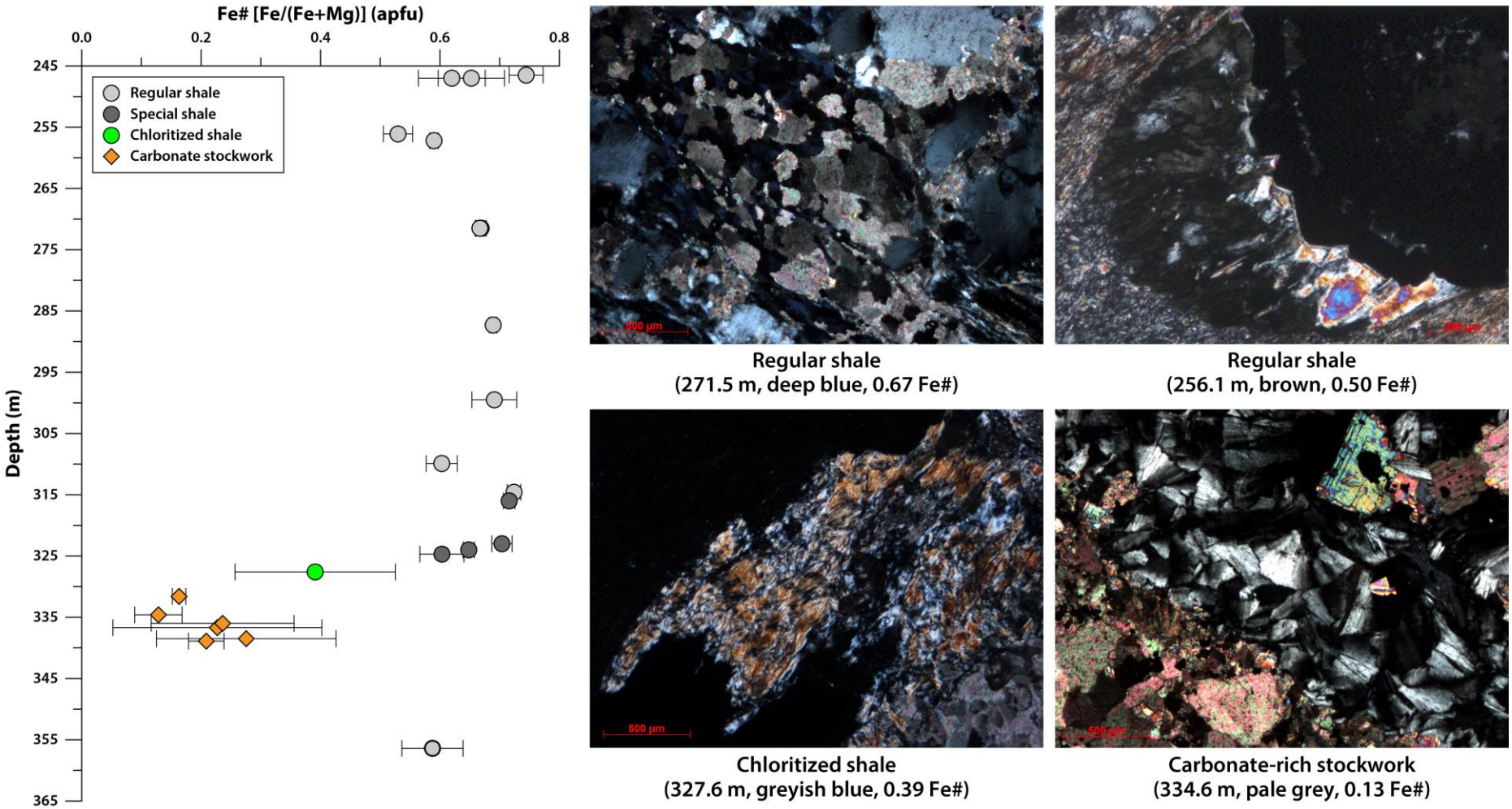

Fig. 80. Fe# profiles in the chlorites along the ELV44 drill core in meter.

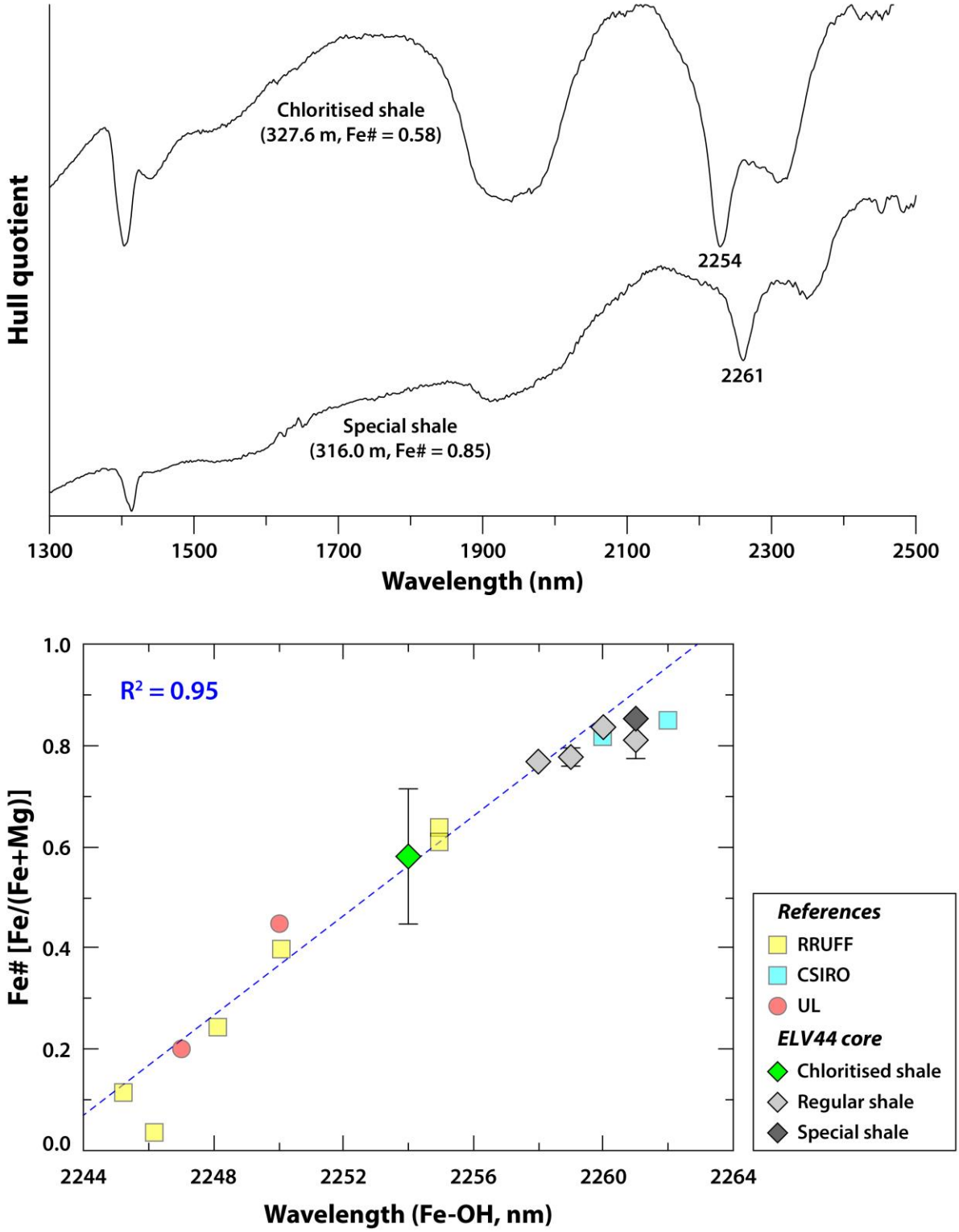

Fig. 81. SWIR spectra and correlation between the absorption position for Fe-OH and Fe# of the chloritised and special shale in the ELV44 drill core.

Chlorites in the Elvira deposit accounts for smaller amounts than other major minerals such as quartz, graphite, and carbonate through microscopic observation. Raman spectroscopy can detect most mineral groups according to **Chapter III**, thus it is difficult to identify fine-grained chlorites in the ELV44 samples by the portable Raman device. Therefore, chlorites are identified by micro-Raman analysis on the thin section under microscopic observation instead of portable Raman spectroscopy. Based on the Raman result in **Chapter V**, the Raman peak shift with compositional changes is evident from 650 to 700 wavenumber. This result is consistent with the chlorites in the Elvira samples. Iron-rich chlorites in the regular/special shales have peaks in shorter wavenumber, whereas magnesium-rich chlorites in the carbonate stockworks have peaks in longer wavenumber (**Fig. 82**). The peak position of the Elvira samples is well located on the linear trend line established in **Chapter V**, and the iron-rich chlorites from the shales expand the curve showing linear correlation (**Fig. 83**).

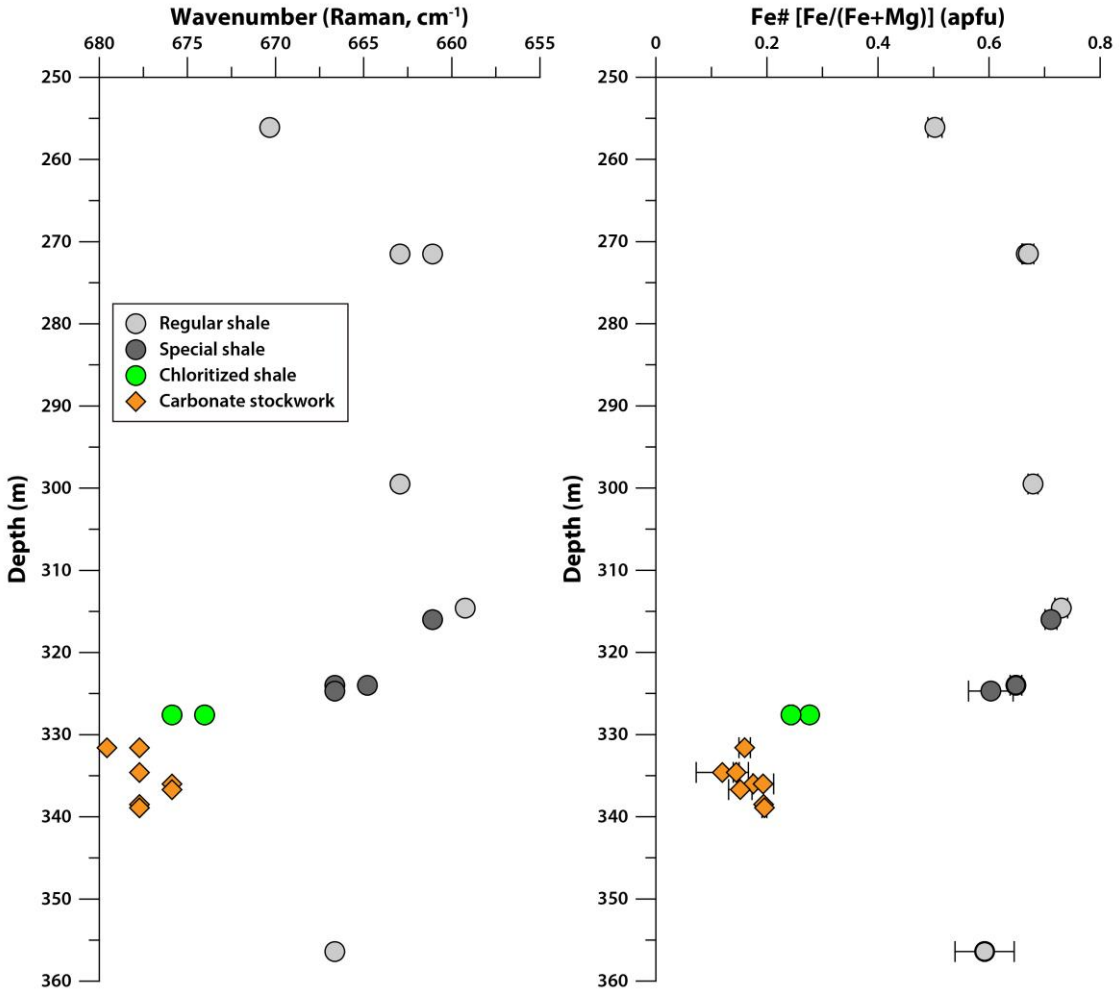

Fig. 82. Raman peak profiles in the chlorites along the ELV44 drill core

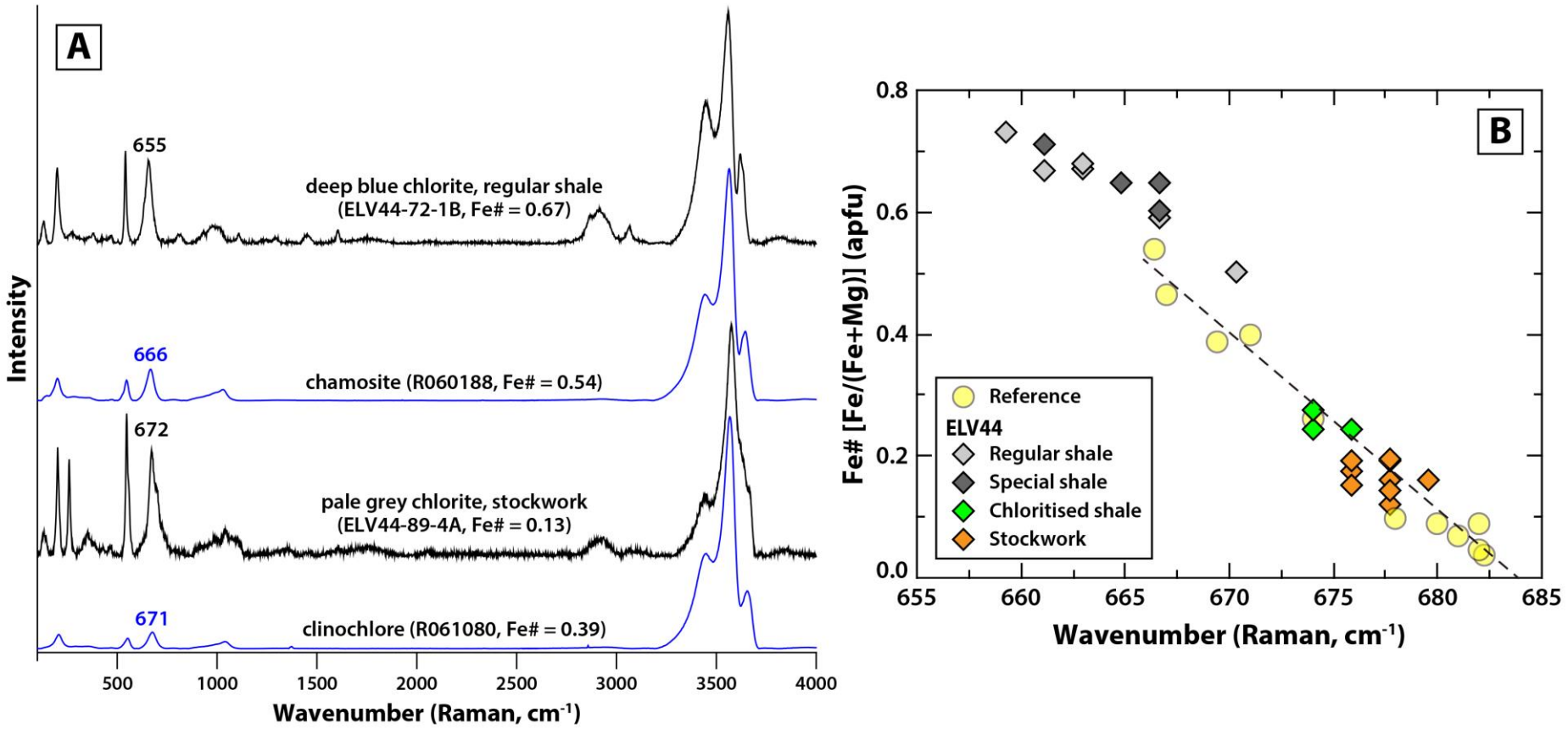

Fig. 83. A) Raman spectra of chlorites of the references from the RRUFF database and of the Elvira samples; B) Correlation between the peak position and Fe# in the ELV44 drill core.

4.3. Dioctahedral micas

Dioctahedral mica is generally regarded as one of the most useful vectoring phases in the VMS system (Gisbert et al., 2021). Solid solutions between muscovite and phengite are the dominant phase with respect to alteration halos because of the common and extensive mineral phase related to hydrothermal alteration (Large et al., 2001b). Typical major element chemical vectors include variations related to Tschermak substitution (Fe-Mg + Si ↔ Al; phengicity), and substitutions between K, Na and Ba.

In the case of the ELV 44 drill core, dioctahedral micas have constant muscovitic composition among the regular, special, and chloritised shales (**Fig. 84**). The white micas in the Elvira samples have high contents of Si and Al indicating muscovite. The muscovite samples at the lower part of the regular shales have lower potassium number [K# = K/(K+Na)] values (**Fig. 84**). The diverse potassium contents affecting potassic and sodic contents in the white micas in that region can be interpreted as the replacement by dickite. VNIR-SWIR and Raman showed band characteristics mainly around 2200 nm and 404 cm^{-1}, respectively (**Fig. 85**). Therefore, both spectroscopic analyses indicated the same result of the uniform muscovitic composition for the dioctahedral micas in the Elvira samples.

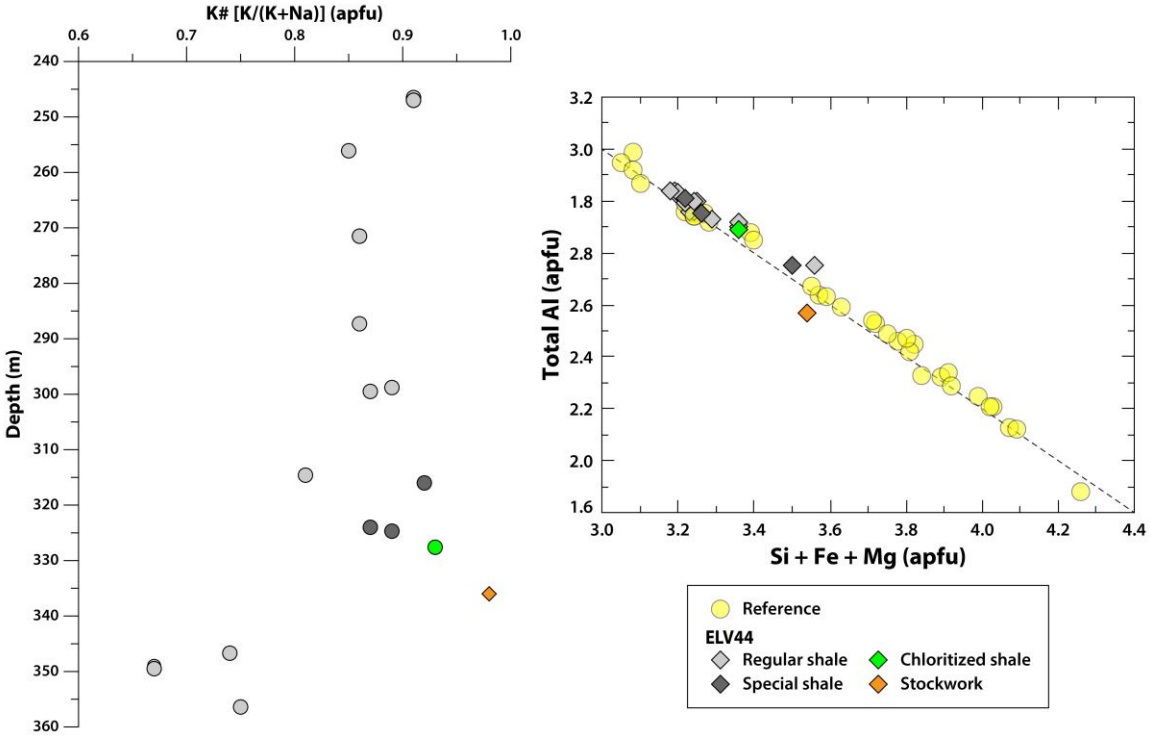

Fig. 84. K# profiles in the white micas along the ELV44 drill core and chemical variations.

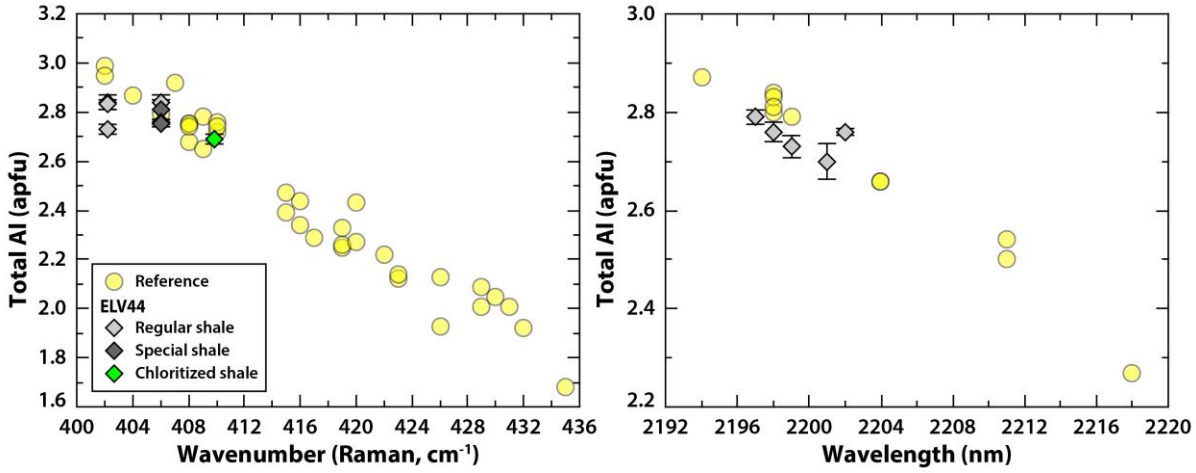

Fig. 85. Relationship between Al total contents with the absorption position for Al-OH in the SWIR region and the peak position in the Raman spectra, respectively.

4.4. Other accessory minerals

4.4.1. Dickite

Dickite was observed in a specific area, which is the contact between the carbonate stockwork and the shales (i.e., 325-350m depth) in the ELV44 drill core. Greyish blue minerals in XPL images similar to the interference colour of iron-rich chlorites were identified between the carbonate-rich stockwork and the lower part of the regular shales (**Fig. 86**). According to the optical properties, and the mineral chemistry analysed by an electron microprobe, the minerals indicate the kaolinite group, which has high Si and Al values without Fe nor Mg. The kaolinite group [$Al_2Si_2O_5(OH)_4$] is a 1:1-layer dioctahedral phyllosilicate comprising two sheets: one being linked SiO4 tetrahedra in hexagonal array and the other being a gibbsite-type layer with Al and OH (Deer et al., 2013). There are theoretically 28 polytypes with only 3 observed in nature (nacrite, dickite and kaolinite) resulting from the different location of their vacant octahedral site (Cudahy, 1997). Kaolinite is the most common member of the kaolinite group, and dickite and nacrite are rarer polymorphs. Kaolinite has a single-layered triclinic unit cell whereas dickite and nacrite has a two-layered and a six-layered monoclinic cell, respectively (Deer et al., 2013). Especially, kaolinite and dickite are one of the important indicative minerals reflecting physical-chemical condition, such as pressure, temperature and pH, in a hydrothermal system (Corbett and Leach, 1998).

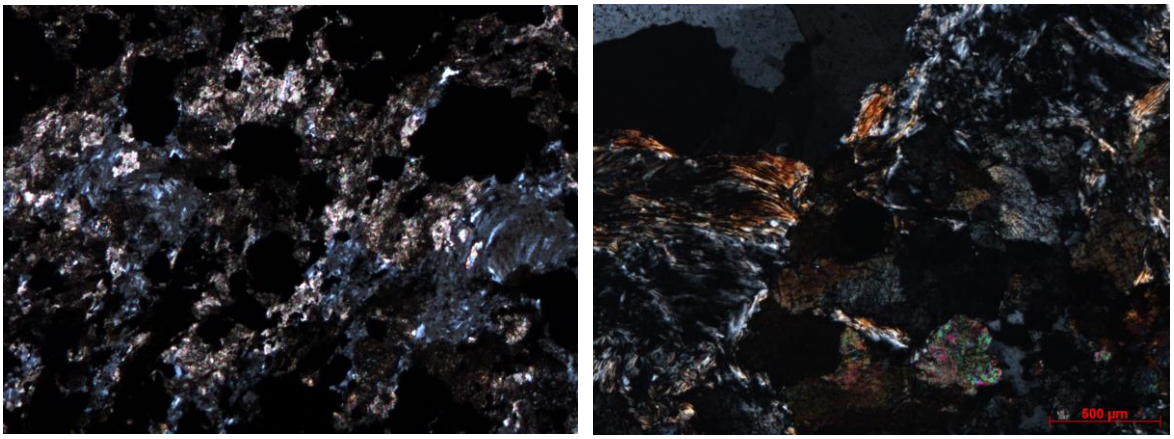

Fig. 86. Photomicrographs of dickite (greyish blue in cross-polarized light) from the ELV44 samples.

The SWIR spectroscopy of the kaolinite group has been studied with attention given to those wavelengths affected by overtones of the stretches and combination tones of the fundamental bends and stretches. The absorption characteristics of the kaolinite group appear in the form of doublets near 1400 nm and 2205 nm in the SWIR region, respectively (**Fig. 87**). The doublet near 1400 nm is due to the Al_2-OH stretching overtone, and the doublet near 2205 nm is due to the OH stretching and Al-OH bending combination vibrations (Bishop et al., 2008; Clark et al., 1990; Cudahy, 1997). Kaolinite and dickite show a similar feature centred at 2205 nm related to the inner hydroxyl absorption, but the absorption related to the surface hydroxyls show significant differences. Thus, kaolinite is recognized by absorption at 2162 nm and dickite by a feature at 2178 nm. Additionally, previous studies demonstrated that well crystalline kaolinite differs from poorly crystalline kaolinite by a sharper and shorter wavelength to the absorption near 2165 nm (Cudahy, 1997; Pontual, 2008). The absorption wavelength of the ELV44 sample in the regular shales is almost the same as dickite (**Fig. 87**). In the Elvira spectrum, the absorption depth near 1410 nm and 2200 nm is deeper than the pure dickite because the absorption features of white mica are overlapped.

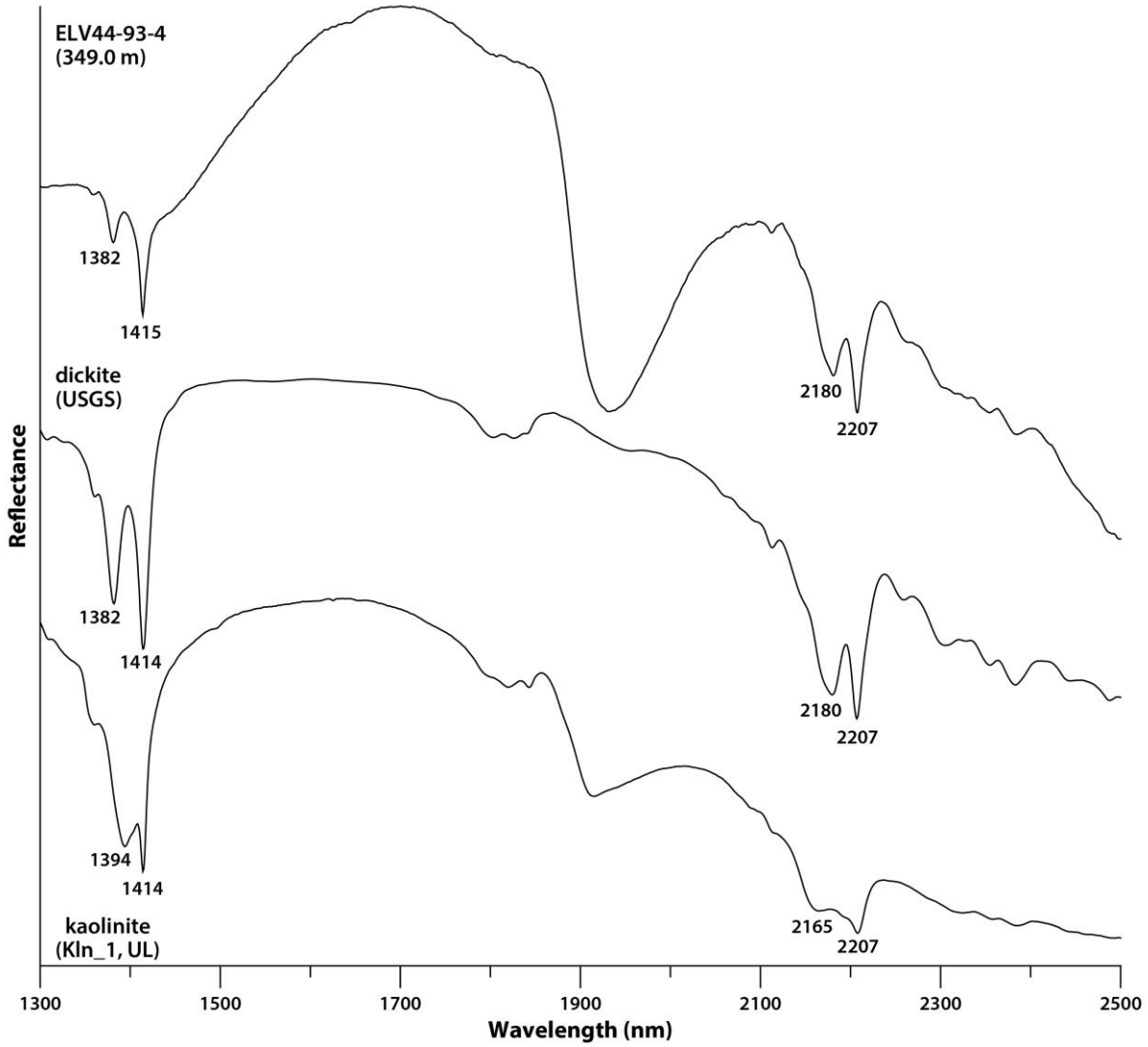

Fig. 87. SWIR reflectance spectrum of dickite in the regular shale from the ELV44 drill core.

Hydroxyl groups in phyllosilicates have well-defined crystallographic sites in the structure, thus they produce sharp Raman peaks in the H_2O/OH spectral range (3000-3700 cm^{-1}) (Wang et al., 2015). The Raman spectrum of the kaolinite group displays four bands corresponding to the four distinct crystallographic sites of OH groups that coordinate with Al^{3+} in octahedral sites of the kaolinite structure (Bish and Von Dreele, 1989). The Raman peaks for kaolinite and dickite appear in the same spectral regions, but their positions differ between them. The Raman band observed near 3620 cm^{-1} for both kaolinite and dickite has been assigned to the stretching vibration of the inner OH [$\nu(Al_2OH)_I$] (**Fig. 88**, Theo Kloprogge, 2017).

The Raman bands of kaolinite appear at 3650, 3667, 3686, and 3695 cm-1 related to the stretching vibrations of the inner surface OH[$\nu(Al_2OH)_{IS}$]. However, the Raman spectra of dickite reveal only three bands near 3639, 3652 and 3700 cm-1 related to the inner surface OH groups (Frost, 1997). As a result of micro-Raman analysis for the Elvira samples based on comparing pure dickite Raman spectra from the RRUFF library and previous studies, the Elvira samples consist of dickite. The Raman result is consistent with the SWIR result that the silicate minerals indicate dickite.

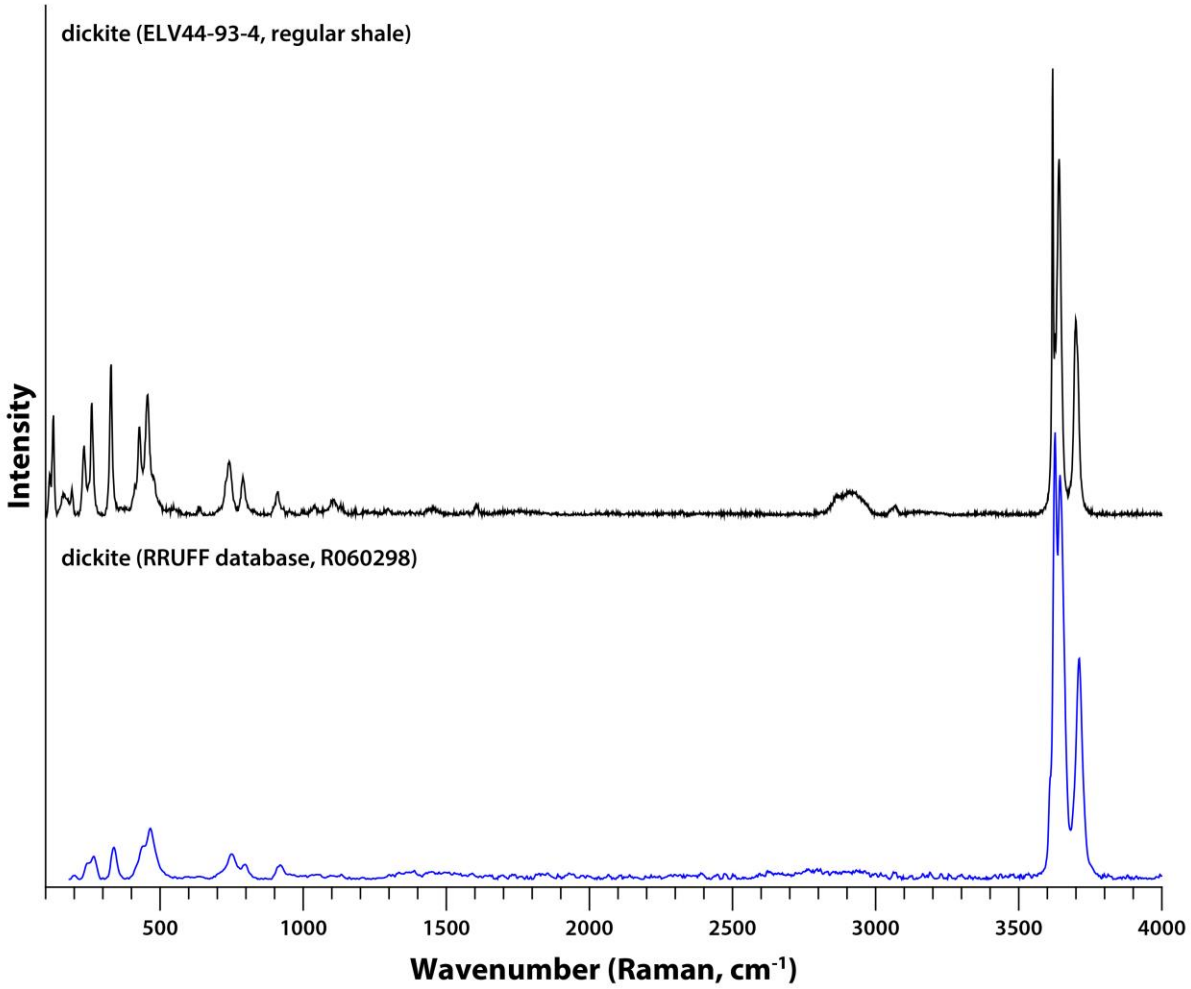

Fig. 88. Raman spectrum of dickite from the ELV44 drill core and the RRUFF spectral library (Lafuente et al., 2015).

4.4.2. Graphite

After Tuinstra and Koenig (1970) firstly reported the Raman spectra of single crystals of graphite and other graphite materials, Raman spectroscopy has commonly been used to identify organic matter as rapid and non-destructive determination for the thermal alteration (maturity) (Henry et al., 2019). The Raman spectrum of the pure graphite from the spectral library in **Chapter II** is composed of two main peaks: the disordered (D) band around 1300 cm^{-1} and the graphite (G) band around 1600 cm^{-1} (**Fig. 89**). The G-band is associated with the in-plane vibration of carbon atoms in graphene sheets, and the D-band is related to structural defects and heteroatoms (Beny-Bassez and Rouzaud, 1985; Jehlička and Beny, 1999; Tuinstra and Koenig, 1970). Different Raman parameters have been used for three main applications: (i) hydrocarbon exploration; (ii) metamorphic studies; (iii) estimating maximum heating along fault planes (Henry et al., 2019).

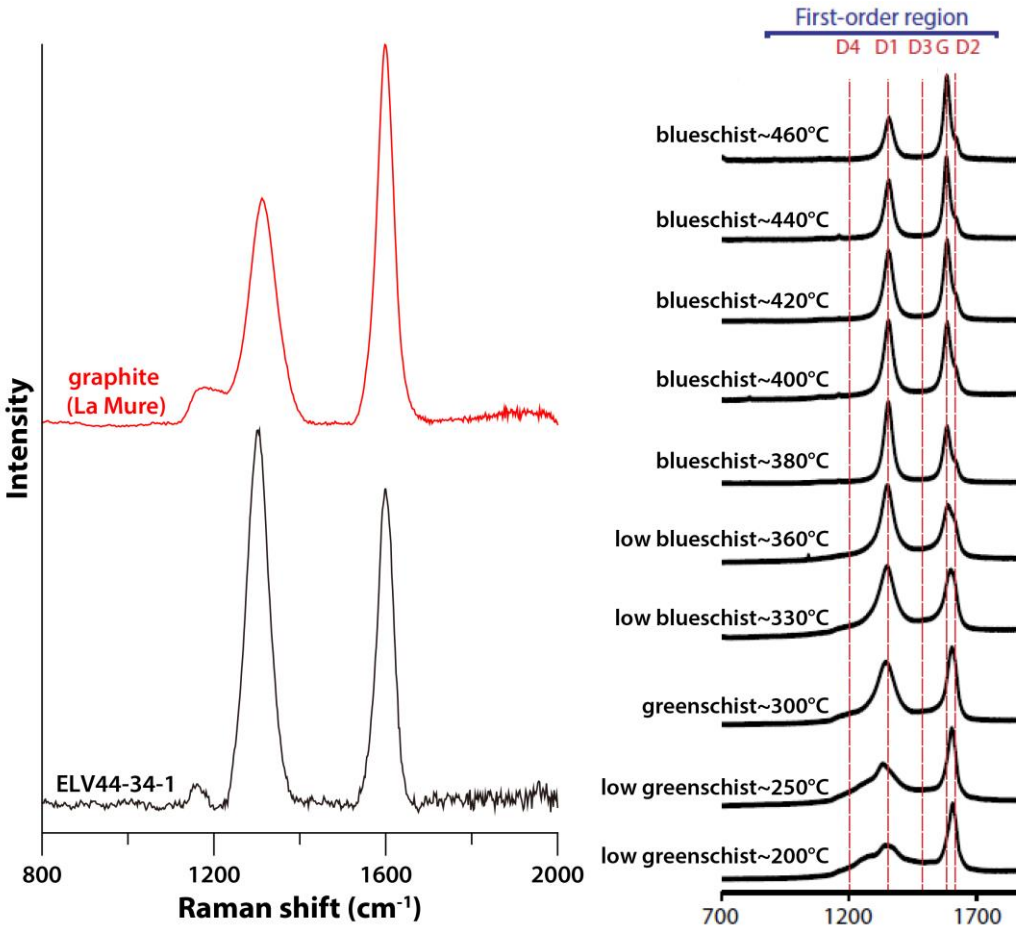

Fig. 89. Raman spectra of graphite from the spectral library and the ELV44 drill core, and correlation between the Raman peak and metamorphic facies from Buseck and Beyssac (2014).

Fig. 89 shows a general summary of how the Raman spectrum of OM and Raman parameters change with increasing metamorphism. The peak difference between the D-band and the G-band represents the degree of metamorphism. According to the **Fig. 89**, as the intensity of the disordered band becomes stronger, metamorphic facies change from eclogite to blueschist facies (Buseck and Beyssac, 2014). In addition, as the full width at half maximum (FWHM) in the D band becomes larger, the degree of metamorphism changes to greenschist facies. When comparing these parameters to our data, the pure graphite from La Mure indicates low greenschist facies and graphites from the ELV44 drill core correspond to blueschist to greenschist facies. The estimations are consistent with the previous studies that a very low-grade regional metamorphism up to lower greenschist facies in IPB (Velasco-Acebes et al., 2019) and lower green schist facies in La Mure area (Goffé and Bousquet, 2004).

5. Geochemical data reconciliation

5.1. The elemental to mineral composition relationship

The elemental concentration in the analysed area is associated with the mineralogical concentration and the elemental concentration of each mineral. Based on this relationship, the reconciliation of mineralogical and elemental data corresponds to the resolution of the following matrix (**Fig. 90**).

$$\begin{bmatrix} C_R(E_1) \\ C_R(E_i) \\ C_R(E_k) \end{bmatrix} = \begin{bmatrix} C_{M^1}(E_1) & \dots & C_{M^j}(E_1) & \dots & C_{M^l}(E_1) \\ C_{M^1}(E_i) & \dots & C_{M^j}(E_i) & \dots & C_{M^l}(E_i) \\ C_{M^1}(E_k) & \dots & C_{M^j}(E_k) & \dots & C_{M^l}(E_k) \end{bmatrix} \times \begin{bmatrix} C_R(M^1) \\ C_R(M^j) \\ C_R(M^l) \end{bmatrix}$$

Fig. 90. Matrix product for geochemical data reconciliation.

When the matrix is applied to our portable devices, the elemental concentration in a spot ($C_R(E)$) can be easily acquired by portable XRF. However, the matrix (Elemental composition of each mineral, $C_M(E)$) and the column vector (Mineralogical concentration in a spot, $C_R(M)$)

on the right-hand side should be processed based on the results studied in this thesis. The matrix, $C_M(E)$, can be provided by representative chemical composition with respect to minerals having distinct composition with little compositional changes such as quartz and pyrite. The mineral composition database in **Chapter II** provides the elemental concentration of these minerals chosen from literatures about the VMS deposits. However, in the case of solid solutions such as carbonates and phyllosilicates, additional information is required to estimate a wide range of compositions. **Chapter IV and V** provide the calibration curves established by univariate analysis from compositional changes of carbonates and phyllosilicates (i.e., chlorites and white micas), respectively. Therefore, the composition of each solid solution can be estimated using the band position from a spectrum, which does not provide elemental information.

The column vector, $C_R(M)$, has to be inverted to obtain the mineralogical concentration since both matrices (i.e., $C_R(E)$ and $C_M(E)$) are finally become known variables. However, task 4.3 team in the NEXT project found that inversion is not a solution since the measurements obtained by the portable tools have errors. Furthermore, when dealing with mineralogical data is that the concentration in a rock of a single mineral does not follow a normal distribution. It however may not follow an even distribution either. Its distribution is unknown. It was hence necessary to implement a Monte-Carlo approach finding the vector of mineralogical concentration who maximise the likelihood function. Except for the information related to the mineralogical concentration, the list of expected minerals from spectra on the analysed area can be provided from the column vector. For that, a decision tree, **Chapter III**, was built by identifying the diagnostic bands of each mineral from each technique. Based on the reconciled spectral data established in this study, the task 4.3 team in the NEXT project focuses on conceiving a software solution utilizing them as a computing code. A coding staff was hired in charge of converting the spectral data in this study into a python code in order to develop the software which immediately processes spectral reconciliation in near-real time by simply inputting various spectral data into the software.

5.2. Specific case: comparison with SEM-EDS mapping

One thin section from the ELV44 drill core was selected to compare the result from the

reconciliation software with the result of mineralogical mapping analysed by SEM-EDS (**Fig. 91**). The mineralogical concentration was classified by the python library, MARCIA (masking spectroscopic datacube), provided on GitHub (https://github.com/hameye/MARCIA).

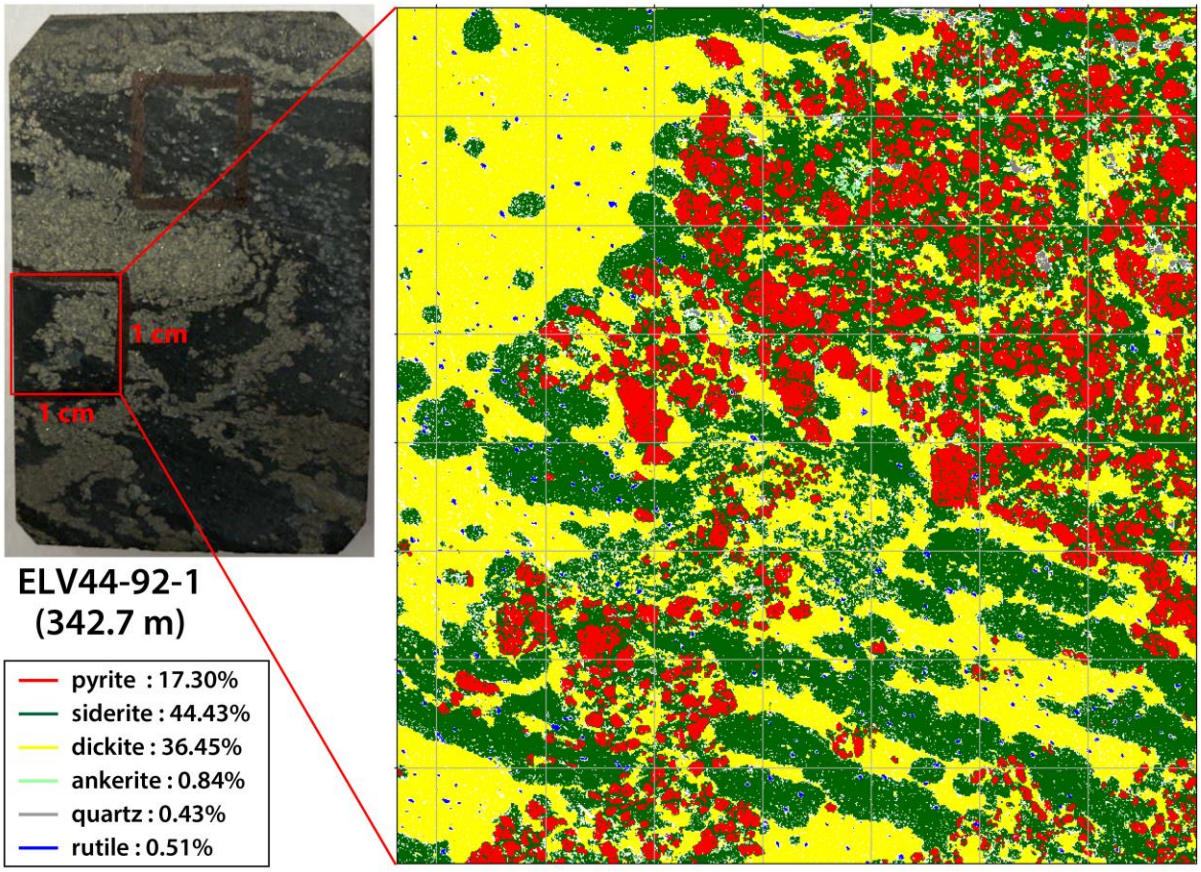

Fig. 91. SEM-EDS mineral map of the carbonate stockwork sample with massive sulphites with mineralogical concentration.

The sample, ELV44-92-1, is the carbonate stockwork with massive sulphides consisting of mainly siderite, pyrite, and dickite. The analysed area is 1x1 cm taking a few hours for SEM-EDS mapping. On the other hand, the reconciliation software can process much faster less than one minute and the analysed area in this case is 8 mm diameter measured by pXRF. The expected minerals such as pyrite, carbonate, dickite, and graphite are identified by the portable Raman device using a red-NIR laser. The carbonate composition was unable to estimate from the Raman spectra due to noises and overlapping with dickite. Therefore, considering that dolomite is mainly identified in the carbonate stockworks, dolomite composition was

arbitrarily applied to the software. **Table 14** shows that the mineralogical concentration is significantly different with the mapping result. Due to the input of the wrong carbonate composition, the iron content from pXRF induced the overestimation of pyrite contents and the presence of chlorite, which did not actually exist. This result emphasises the importance of accurate composition input. In order to confirm this, the actual carbonate composition analysed by EPMA was input into the software instead of dolomite composition. As a result, the mineralogical concentration is similar with the SEM-EDS mapping showing only 7% of the maximum error from siderite contents (**Table 14**). These errors can be explained for the following reasons apart from the different elemental concentrations between SEM-EDS and pXRF: i) different units of mineralogical concentration (volume% vs. mass%) and ii) different analysed areas (1x1 cm vs. 8 mm). Nevertheless, the software showed the high accuracy of the quantitative result from reconciled geochemical data. Therefore, any type of geochemical data can be applied to the software regardless of laboratory-based or portable spectroscopic devices.

Table 14. Comparison of mineralogical concentrations among three different dataset.

SEM-EDS mapping		**Reconciliation software**				
		XRF-Raman		**XRF-EPMA-Raman**		
Mineral	Vol.%	Mineral	Mass.%	Mineral	Mass.%	Error (%)*
pyrite	17.30	pyrite	28.24	pyrite	21.57	4.27
siderite	44.43	dolomite	1.66	siderite	51.66	7.23
dickite	36.45	dickite	12.17	dickite	32.04	4.41
ankerite	0.84	chlorite	33.40			
quartz	0.43	quartz	0.00	quartz	0.03	0.4
rutile	0.51					

* Percentage error compared to the SEM-EDS mapping.

6. Discussion and Conclusion

Portable Raman and VNIR-SWIR spectroscopy effectively identified the presence of the indicative and accessory minerals as well as compositional changes in the indicative minerals from heterogeneous drill core. Nevertheless, limitations of portable spectroscopy were also confirmed based on the device itself and the geological environment in the Elvira deposit. Since the band intensity in the spectrum is associated with the mineral content, mineral identification using spectral signatures can be a significant challenge if the mineral is small and dispersed.

For example, in this study, small amounts of chlorites and dioctahedral micas were not detected by the portable Raman and VNIR-SWIR devices. This can be interpreted as follow: i) the large spot size (10 mm) of the VNIR-SWIR device may cover these minerals, but their contents may not be above the detection limit. Furthermore, black shales mainly have low reflectance to recognize spectral absorptions in the VNIR-SWIR region. ii) the small spot size (15 μm) of the Raman device (Bravo), on the contrary, may miss the minerals in the analysed area. Moreover, fluorescence interference was confirmed in the Raman spectra of the drill core measured by the portable Raman devices. The Elvira deposit in the case of ELV44 drill core, does not display distinct alteration zones nor significant variations in the indicative minerals around the ore. Chlorite in the chloritised shales is the only detectable mineral linked to the ore, but the thin shale was observed only nearby the ore. However, if the chloritization of the shales appeared on a larger lateral extension than the ore deposit or the carbonates showed a systematic variability according to the depth as shown in Sotiel-Migollas next to the Elvira deposit, portable spectroscopy could effectively help fast decision-making support while drilling on site.

Elvira polymetallic (Cu-Zn-Pb) massive sulphide deposit is located in the south-eastern region of the Iberian Pyrite Belt (IPB). The shale-hosted VMS deposit represents an eastward continuation of the Sotiel-Migollas massive sulphide deposits cluster. Systematic comparison between spectral characteristics and chemical composition in carbonates, chlorites, and dioctahedral micas in the ELV44 drill core, which intersects the very margin of the massive sulphides, are mainly investigated by spectroscopic analyses as vectoring tools to ore. Various types of carbonate minerals are found in all the lithology groups in the ELV44 drill core, and they are well discriminated by the Raman and SWIR analysis indicating the continuous changes in composition. Chlorites in the regular and special shales are iron-rich, and the chlorites in the carbonate-rich stockwork have magnesium-rich. The composition in the chloritised shales is in the middle of the shales and the carbonate-rich stockwork. The dioctahedral micas in the Elvira have a constant muscovitic composition regardless of the shale types. As an accessory mineral, the kaolinite group is able to be distinguished by SWIR and Raman analysis, and the Elvira samples are distinguished as dickite. Graphite has two diagnostic peaks in the Raman spectrum, and the intensity difference between the disordered (D) band and the graphite (G) band reflects the degree of metamorphism. The reconciliation software calculates a mineralogical composition from a series of spectral measurements. The strength of this software is that each

spectroscopic technique can be applied from any commercially available instruments, whether they are laboratory-based or portable. In addition, the mineralogical composition of the sample is complemented with extra information that are of interest for geologists.

Conclusion and perspectives

1. Conclusion

This study aims at reconciling geochemical data acquired from portable spectroscopic devices in the field to determine the best geochemical information from each technique applied by combining the mineralogical and elemental information. The reconciled multi-spectral data focuses on “vectors” providing the quantitative relationship between elemental concentration and mineralogy in the hydrothermally altered minerals from the distal margin to the high-grade ores. According to the technological development of portable instruments, spectroscopic analysis in the field requires the discrimination and quantification of minerals in rocks, which are heterogeneous mixtures, and even the chemical composition of minerals present in the rocks. To achieve this, step-by-step procedures consisting of six chapters in this thesis were carried out, and the compositional change and quantification of minerals which can be present in the VMS system were investigated by the various spectroscopic techniques. The spectral data are provided by six portable devices: (i) elemental analyses such as XRF and LIBS, and (ii) mineralogical analyses such as Raman, VNIR-SWIR, MIR, and XRD.

To assist rapid mineral recognition with respect to unknown materials and support the spectral reconciliation for diverse types of spectral data, a spectral database, which is the beginning and the fundamental source of this dissertation, was established. The total number of mineral phases is 27 consisting of 52 samples, and the mineral groups are composed of silicates, carbonates, sulphides, sulphates, and graphite. Since the reconciliation procedure is considered the elemental composition of all detected minerals, a series of EPMA analyses were conducted to recognize the average composition and variability of these composition for all the minerals as a mineralogical composition database. Based on diagnostic bands from the spectral data with respect to mineralogical analyses, a decision tree provides the proper order for the presence, absence, and ranking of minerals by combining the diverse spectroscopic data. It consequently classifies band areas based on the mineral groups and determines the representative band areas of minerals. Spectral identification and quantification of carbonates, trioctahedral chlorites, and dioctahedral micas considered as the indicative minerals in the VMS system are investigated for identifying presence of the minerals and also observing

compositional variations in each mineral. Building calibration curves for all the indicative minerals has been done using spectral variations observed among the end-members of these solid solutions. Finally, the multi-spectral parameters were applied to the "real" samples from a drill core in the Elvira VMS deposit to identify vectors to the ore. Several limitations of portable spectroscopy were confirmed based on the device itself and the geological environment in the Elvira deposit. Portable spectroscopy is effective in identifying the presence and compositional changes of various minerals from heterogeneous rock samples, thus spectroscopic analysis on-site can be one of the vectoring tools to determine the implication for ore mineralization in hidden ore explorations.

All the mineralogical and elemental data studied in this thesis, which corresponds to the reconciliation of the geochemical data, were translated into a software by the coding staff in the task 4.3 team in the NEXT project to automatically execute this reconciliation method. The software could provide mineralogical concentrations in a minute after exporting spectral data from the portable devices to the user computer. Despite the interchangeable data reconciliation between portable equipment and/or laboratory instrument, there has been a problem with the full automation of the software. The VNIR-SWIR region still requires a spectroscopist's eye for mineral identification due to the overlap among minerals that may occur in narrow spectral regions. In the case of Raman, the device itself has a small spot size with a longer operation time which cannot be configured by the user. In addition, fluorescence effect is another obstacle to identifying characteristics of Raman peaks. In these reasons, geochemical data reconciliation using the software in the field is still difficult to be feasible. Since the expected mineral list should be prepared prior to software execution, the study area has to be a geologically well-known area.

2. Perspectives

Three perspectives on improvement will be further developed after the end of the thesis. Spectral data acquisition on the core sample ELV44 from the Elvira deposit has been finished by a master student. 200 points have been measured with 6 portable devices (i.e., XRF, LIBS, MIR-SR, VNIR-SWIR, and two Raman using a green and a red-NIR laser, respectively). Another application targets on the San Finx Sn-W mine and surrounding, and the whole dataset

has been formatted and is ready for applying the reconciliation software.

To optimize the treatment of the large amount of LIBS data acquired and identify geochemical variation not only in the rock but within mineral phases, a chemometric analysis using artificial neural networks (ANN) supervised algorithm aims at identifying and classifying the LIBS signal (net elemental intensities) of specific minerals based on predetermined data extracted from reference LIBS spectra. Then, the variation of composition from a specific mineral could be observed as a function of the distance to the ore. That trial could provide two pieces of information: (i) The composition of a mineral can be qualitatively followed using LIBS. That means that an indicator to the ore consisting of elemental variations in a specific mineral mixed with several others can be followed without sample preparation. (ii) The list of minerals can also be extracted from the LIBS data.

In order to enhance the software, reworking pXRF data will be additionally carried out except for the reconciliation procedure. pXRF is the only technique providing truly quantitative results by default and without extensive work from an expert. However, in some geological contexts, the quantitative results from the pXRF may not be adapted to the reconciliation. That may arise from several issues: (i) The device may not provide results for a specific element, detectable but not included in the pXRF program, (ii) The device may provide results biased by an interference between an element of interest and another element not included in the pXRF program, and (iii) The device may provide results biased by an interference between an element of interest and another element, included in the pXRF program but at concentrations that do not correspond to the concentrations for which the interference can be properly solved. The XRF data reworking relies on the spectral decomposition of the spectrum into mathematical functions (Gaussian or pseudo-Voigt) while existing XRF analyses evaluate the intensities on the integration of the signal in spectral windows, followed by multilinear correction for compensating inter-elemental interferences. These perspectives will be expected to further enhancement in Le Laboratoire d'Excellence RESSOURCES21 (LabEx R21) project on Beauvoir in France in near future.

References

Ames, D.E., Galley, A.G., Kjarsgaard, I.M., Tardif, N., Taylor, B.T., 2016. Hanging-wall vectoring for buried volcanogenic massive sulfide deposits, Paleoproterozoic Flin Flon mining camp, Manitoba, Canada. Economic Geology 111, 963–1000.

Atkins, P.W., Friedman, R.S., 2011. Molecular quantum mechanics. Oxford university press.

Baldridge, A.M., Hook, S.J., Grove, C.I., Rivera, G., 2009. The ASTER spectral library version 2.0. Remote Sensing of Environment 113, 711–715. https://doi.org/10.1016/j.rse.2008.11.007

Barnes, R.J., Dhanoa, M.S., Lister, S.J., 1989. Standard Normal Variate Transformation and De-trending of Near-Infrared Diffuse Reflectance Spectra. Appl. Spectrosc., AS 43, 772–777.

Beny-Bassez, C., Rouzaud, J.N., 1985. Characterization of carbonaceous materials by correlated electron and optical microscopy and Raman microspectroscopy. Scanning electron microscopy 1, 119–132.

Bertin, E.P., 1975. Principles and Practice of X-Ray Spectrometric Analysis. Springer US. https://doi.org/10.1007/978-1-4613-4416-2

Besson, G., Drits, V.A., 1997. Refined relationships between chemical composition of dioctahedral fine-grained mica minerals and their infrared spectra within the OH stretching region. Part I: Identification of the OH stretching bands. Clays and Clay Minerals 45, 158–169.

Bish, D.L., Von Dreele, R.B., 1989. Rietveld refinement of non-hydrogen atomic positions in kaolinite. Clays and Clay Minerals 37, 289–296.

Bishop, J., Murad, E., Dyar, M.D., 2002. The influence of octahedral and tetrahedral cation substitution on the structure of smectites and serpentines as observed through infrared spectroscopy. Clay Minerals 37, 617–628.

Bishop, J.L., Lane, M.D., Dyar, M.D., Brown, A.J., 2008. Reflectance and emission spectroscopy study of four groups of phyllosilicates: smectites, kaolinite-serpentines, chlorites and micas. Clay minerals 43, 35–54.

Blake, D., Vaniman, D., Achilles, C., Anderson, R., Bish, D., Bristow, T., Chen, C., Chipera, S., Crisp, J., Des Marais, D., 2012. Characterization and calibration of the CheMin mineralogical instrument on Mars Science Laboratory. Space Science Reviews 170, 341–399.

Bobrowicz, G.L., 1995. Mineralogy, geochemistry and alteration as exploration guides at Aguas Tenidas Este, Pyrite Belt, Spain. Unpublished PhD Thesis, Birmingham University.

Bohr, N., 1914. On the spectrum of hydrogen. Fysisk Tidsskrift 12, 97.

Browne, P.R.L., 1978. Hydrothermal alteration in active geothermal fields. Annual review of earth and planetary sciences 6, 229–248.

Bultel, B., Viennet, J.-C., Poulet, F., Carter, J., Werner, S.C., 2019. Detection of Carbonates in Martian Weathering Profiles. Journal of Geophysical Research: Planets 124, 989–1007. https://doi.org/10.1029/2018JE005845

Burkett, D.A., Graham, I.T., Ward, C.R., 2015. THE APPLICATION OF PORTABLE X-RAY DIFFRACTION TO QUANTITATIVE MINERALOGICAL ANALYSIS OF HYDROTHERMAL SYSTEMSTHE CANADIAN MINERALOGIST. The Canadian Mineralogist 53, 429–454. https://doi.org/10.3749/canmin.1400099

Buseck, P.R., Beyssac, O., 2014. From organic matter to graphite: Graphitization. Elements 10,

421–426.
Calas, G., Hawthorne, F., 1988. Introduction to Spectroscopic Methods. Rev. Miner. 18, 1–9.
Carter, J., Poulet, F., Bibring, J.-P., Mangold, N., Murchie, S., 2013. Hydrous minerals on Mars as seen by the CRISM and OMEGA imaging spectrometers: Updated global view. Journal of Geophysical Research: Planets 118, 831–858. https://doi.org/10.1029/2012JE004145
Clark, R.N., King, T.V., Klejwa, M., Swayze, G.A., Vergo, N., 1990. High spectral resolution reflectance spectroscopy of minerals. Journal of Geophysical Research: Solid Earth 95, 12653–12680.
Cloutier, J., Piercey, S.J., Huntington, J., 2021. Mineralogy, Mineral Chemistry and SWIR Spectral Reflectance of Chlorite and White Mica. Minerals 11, 471.
Commission, E., 2020. Critical raw materials resilience: Charting a path towards greater security and sustainability.
Corbett, G.J., Leach, T.M., 1998. Southwest Pacific Rim gold-copper systems: structure, alteration, and mineralization. Society of Economic Geologists Littleton, Colorado.
Cremers, D.A., Radziemski, L.J., 2013. Handbook of laser-induced breakdown spectroscopy. John Wiley & Sons.
Crocombe, R.A., 2018. Portable spectroscopy. Applied Spectroscopy 72, 1701–1751.
Crocombe, R.A., Leary, P.E., Kammrath, B.W., 2021a. Portable Spectroscopy and Spectrometry, Applications. John Wiley & Sons.
Crocombe, R.A., Leary, P.E., Kammrath, B.W., 2021b. The Role of Applications in Portable Spectroscopy. Portable Spectroscopy and Spectrometry 1: Applications 2, 1–17.
Cudahy, T.J., 1997. Pima-II spectral characteristics of natural kaolins, in: CSIRO Exploration and Mining Report 420R.
Cullity, B.D., 1956. Elements of X-ray Diffraction. Addison-Wesley Publishing.
De Graef, M., McHenry, M.E., 2012. Structure of materials: an introduction to crystallography, diffraction and symmetry. Cambridge University Press.
De La Rosa, R., Khodadadzadeh, M., Tusa, L., Kirsch, M., Gisbert, G., Tornos, F., Tolosana-Delgado, R., Gloaguen, R., 2021. Mineral quantification at deposit scale using drill-core hyperspectral data: A case study in the Iberian Pyrite Belt. Ore Geology Reviews 139, 104514.
Deer, W.A., FRS, Howie, R.A., Zussman, J., 2013. An Introduction to the Rock-Forming Minerals. Mineralogical Society of Great Britain and Ireland. https://doi.org/10.1180/DHZ
Dehnavi, A.S., Lentz, D.R., McFarlane, C.R., Walker, J.A., 2018. Quantification of fluid-mobile elements in white mica by LA-ICP-MS: From chemical composition to a potential micro-chemical vectoring tool in VMS exploration. Journal of Geochemical Exploration 188, 290–307.
Downs, R.T., Hall-Wallace, M., 2003. The American Mineralogist crystal structure database. American Mineralogist 88, 247–250.
Dubessy, J., Caumon, M.-C., Rull, F., Sharma, S., 2012. Instrumentation in Raman spectroscopy: elementary theory and practice. Raman spectroscopy applied to Earth sciences and cultural heritage 12, 83–172.
Edwards, H.G.M., Jehlička, J., Culka, A., 2021. Portable Raman Spectroscopy in Field Geology and Astrobiology Applications. Portable Spectroscopy and Spectrometry 1: Applications 2, 377–400.
Ehlmann, B., Mustard, J., Murchie, S., Poulet, F., Bishop, J., Brown, A., Calvin, W., Clark, R.,

Des Marais, D., Milliken, R., Roach, L., Roush, T., Swayze, G., Wray, J., 2009. Orbital Identification of Carbonate-Bearing Rocks on Mars. Science (New York, N.Y.) 322, 1828–32. https://doi.org/10.1126/science.1164759

Einstein, A., 1905. Über einen die Erzeugung und Verwandlung des Lichtes betreffenden heuristischen Gesichtspunkt. Annalen der Physik 322, 132–148. https://doi.org/10.1002/andp.19053220607

Exelis, E., 2012. Exelis Visual Information Solutions: Boulder. CO, USA.

Fabre, C., 2020. Advances in Laser-Induced Breakdown Spectroscopy analysis for geology: A critical review. Spectrochimica Acta Part B: Atomic Spectroscopy 166, 105799. https://doi.org/10.1016/j.sab.2020.105799

Fabre, C., Ourti, N.E., Mercadier, J., Cardoso-Fernandes, J., Dias, F., Perrotta, M., Koerting, F., Lima, A., Kaestner, F., Koellner, N., Linnen, R., Benn, D., Martins, T., Cauzid, J., 2021. Analyses of Li-Rich Minerals Using Handheld LIBS Tool. Data 6, 68. https://doi.org/10.3390/data6060068

Foucaud, Y., Fabre, C., Demeusy, B., Filippova, I.V., Filippov, L.O., 2019. Optimisation of fast quantification of fluorine content using handheld laser induced breakdown spectroscopy. Spectrochimica Acta Part B: Atomic Spectroscopy 158, 105628. https://doi.org/10.1016/j.sab.2019.05.017

Franklin, J.M., Gibson, H.L., Jonasson, I.R., Galley, A.G., 2005. Volcanogenic massive sulfide deposits. Economic Geology 100th anniversary volume 98, 523–560.

Frost, R.L., 1997. The structure of the kaolinite minerals—a FT-Raman study. Clay Minerals 32, 65–77.

Fultz, B., Howe, J.M., 2012. Transmission electron microscopy and diffractometry of materials. Springer Science & Business Media.

Gaffey, S.J., 1985. Reflectance spectroscopy in the visible and near-infrared (0.35–2.55 μm): Applications in carbonate petrology. Geology 13, 270–273. https://doi.org/10.1130/0091-7613(1985)13<270:RSITVA>2.0.CO;2

Gates, W., 2005. Infrared spectroscopy and the chemistry of dioctahedral smectites. The Application of Vibrational Spectroscopy to Clay Minerals and Layered Double Hydroxides 126–168.

Gazley, M., Fisher, L., 2014. A review of the reliability and validity of portable X-ray fluorescence spectrometry (pXRF) data. pp. 69–82.

Geiger, C., 2004. An Introduction to Spectroscopic Methods in the Mineral Sciences and Geochemistry. pp. 1–42.

Gibson, H.L., Allen, R.L., Riverin, G., Lane, T.E., 2007. The VMS model: Advances and application to exploration targeting, in: Proceedings of Exploration. pp. 713–730.

Gisbert, G., Losantos, E., Pons, J.M., Videira, J.C., Tornos, F., 2019. Elvira: a new shale-hosted VMS deposit in the Iberian Pyrite Belt.

Gisbert, G., Tornos, F., Losantos, E., Pons, J.M., Videira, J.C., 2021. Vectors to ore in replacive VMS deposits of the northern Iberian Pyrite Belt: mineral zoning, whole rock geochemistry, and use of portable XRF. Solid Earth Discussions 1–41.

Goetz, A.F.H., Billingsley, F.C., Elston, D., Lucchitta, I., Shoemaker, E.M., Abrams, M.J., Gillespie, A.R., Squires, R., 1975. Portable field reflectance spectrometer. Applications of ERTS Images and Image Processing to Regional Geological Problems and Geologic Mapping of Northern Arizona, JPL Tech. Rep 32, 1567.

Goffé, B., Bousquet, R., 2004. Metamorphic structure of the Alps: Western and Ligurian Alps. Nature 387, 586–589.

Gopal, N.O., Narasimhulu, K.V., Rao, J.L., 2004. Optical absorption, EPR, infrared and Raman spectral studies of clinochlore mineral. Journal of Physics and Chemistry of Solids 65, 1887–1893.

Gosson, G., 2018. CIM Mineral Exploration Best Practice Guidelines 17.

Griffiths, P.R., De Haseth, J.A., 2007. Fourier transform infrared spectrometry. John Wiley & Sons.

Guezenoc, J., Gallet-Budynek, A., Bousquet, B., 2019. Critical review and advices on spectral-based normalization methods for LIBS quantitative analysis. Spectrochimica Acta Part B: Atomic Spectroscopy 160, 105688.

Guidotti, C.V., 1984. Micas in metamorphic rocks. Reviews in Mineralogy and Geochemistry 13, 357–467.

Guinier, A., 1994. X-ray diffraction in crystals, imperfect crystals, and amorphous bodies. Courier Corporation.

Haddad, J., Canioni, L., Bousquet, B., 2014. Good practices in LIBS analysis: Review and advices. Spectrochimica Acta Part B: Atomic Spectroscopy 101, 171–182. https://doi.org/10.1016/j.sab.2014.08.039

Haldar, S.K., 2018. Mineral exploration: principles and applications. Elsevier.

Hall, G., Buchar, A., Bonham-Carter, G., 2011. Quality control assessment of portable XRF analysers: development of standard operating procedures, performance on variable media and recommended uses. CAMIRO Project 10E01 report.

Hall, G.E.M., Bonham-Carter, G.F., Buchar, A., 2014. Evaluation of portable X-ray fluorescence (pXRF) in exploration and mining: Phase 1, control reference materials. Geochemistry: Exploration, Environment, Analysis 14, 99–123. https://doi.org/10.1144/geochem2013-241

Hammond, C., Hammond, C., 2001. The basics of cristallography and diffraction. Oxford.

Hannington, M.D., 2014. Volcanogenic massive sulfide deposits.

Harmon, R.S., Hark, R.R., Throckmorton, C.S., Rankey, E.C., Wise, M.A., Somers, A.M., Collins, L.M., 2017. Geochemical Fingerprinting by Handheld Laser-Induced Breakdown Spectroscopy. Geostandards and Geoanalytical Research 41, 563–584. https://doi.org/10.1111/ggr.12175

Harmon, R.S., Lawley, C.J.M., Watts, J., Harraden, C.L., Somers, A.M., Hark, R.R., 2019. Laser-Induced Breakdown Spectroscopy—An Emerging Analytical Tool for Mineral Exploration. Minerals 9, 718. https://doi.org/10.3390/min9120718

Harmon, R.S., Remus, J., McMillan, N.J., McManus, C., Collins, L., Gottfried, J.L., DeLucia, F.C., Miziolek, A.W., 2009. LIBS analysis of geomaterials: Geochemical fingerprinting for the rapid analysis and discrimination of minerals. Applied Geochemistry 24, 1125–1141. https://doi.org/10.1016/j.apgeochem.2009.02.009

Harris, D.C., Bertolucci, M.D., 1989. Symmetry and spectroscopy: an introduction to vibrational and electronic spectroscopy. Courier Corporation.

Hauff, P., 2008. An overview of VIS-NIR-SWIR field spectroscopy as applied to precious metals exploration. Spectral International Inc. 80001.

Henry, D.G., Jarvis, I., Gillmore, G., Stephenson, M., 2019. Raman spectroscopy as a tool to determine the thermal maturity of organic matter: Application to sedimentary, metamorphic and structural geology. Earth-Science Reviews 198, 102936. https://doi.org/10.1016/j.earscirev.2019.102936

Heraud, P., Wood, B.R., Beardall, J., McNaughton, D., 2006. Effects of pre-processing of Raman spectra on in vivo classification of nutrient status of microalgal cells. Journal of

Chemometrics 20, 193–197. https://doi.org/10.1002/cem.990
Hertz, H., 1888. Ueber die Ausbreitungsgeschwindigkeit der electrodynamischen Wirkungen. Annalen der Physik 270, 551–569. https://doi.org/10.1002/andp.18882700708
Horta, A., Malone, B., Stockmann, U., Minasny, B., Bishop, T.F.A., McBratney, A.B., Pallasser, R., Pozza, L., 2015. Potential of integrated field spectroscopy and spatial analysis for enhanced assessment of soil contamination: a prospective review. Geoderma 241, 180–209.
Hunt, G.R., 1977. Spectral signatures of particulate minerals in the visible and near infrared. Geophysics 42, 501–513.
Hunt, G.R., Salisbury, J.W., 1971. Visible and near infrared spectra of minerals and rocks. II. Carbonates. Modern Geology 2, 23–30.
Iida, Y., 1990. Effects of atmosphere on laser vaporization and excitation processes of solid samples. Spectrochimica Acta Part B: Atomic Spectroscopy 45, 1353–1367. https://doi.org/10.1016/0584-8547(90)80188-O
Inverno, C., Díez-Montes, A., Rosa, C., García-Crespo, J., Matos, J., García-Lobón, J.L., Carvalho, J., Bellido, F., Castello-Branco, J.M., Ayala, C., 2015. Introduction and geological setting of the Iberian Pyrite Belt, in: 3D, 4D and Predictive Modelling of Major Mineral Belts in Europe. Springer, pp. 191–208.
Ishii, M., Shimanouchi, T., Nakahira, M., 1967. Far infra-red absorption spectra of layer silicates. Inorganica Chimica Acta 1, 387–392.
Ismaël, A., Bousquet, B., Pierrès, K.M.-L., Travaillé, G., Canioni, L., Roy, S., 2011. In Situ Semi-Quantitative Analysis of Polluted Soils by Laser-Induced Breakdown Spectroscopy (LIBS). Appl. Spectrosc., AS 65, 467–473.
Jehlička, J., Beny, C., 1999. First and second order Raman spectra of natural highly carbonified organic compounds from metamorphic rocks. Journal of Molecular Structure 480, 541–545.
Jehlička, J., Vítek, P., Edwards, H.G.M., Heagraves, M., Čapoun, T., 2009. Application of portable Raman instruments for fast and non-destructive detection of minerals on outcrops. Spectrochimica Acta Part A: Molecular and Biomolecular Spectroscopy, Raman Spectroscopy Applied to the Earth Sciences - Sensu Latu 73, 410–419. https://doi.org/10.1016/j.saa.2008.09.004
Jenkins, R., 2008. X-ray fluorescence spectrometry. Handbook of Analytical Techniques.
Jenkins, R., Snyder, R.L., Cernik, R.J., 1997. X-ray Powder Diffractometry, Introduction. Angewandte Chemie-English Edition 36, 1128–1128.
Kerr, A., Rafuse, H., Sparkes, G., Hinchey, J., Sandeman, H., 2011. Visible/infrared spectroscopy (VIRS) as a research tool in economic geology: background and pilot studies from Newfoundland and Labrador. Geological Survey, Report 11, 145–166.
Khajehzadeh, N., Kauppinen, T.K., 2015. Fast mineral identification using elemental LIBS technique. IFAC-PapersOnLine, 4th IFAC Workshop on Mining, Mineral and Metal Processing MMM 2015 48, 119–124. https://doi.org/10.1016/j.ifacol.2015.10.089
Khoshhesab, Z.M., 2012. Reflectance IR spectroscopy. Infrared spectroscopy—materials science, engineering and technology 11, 233–244.
Kim, C.S., Kim, Y., Choi, S.-G., Ko, K.-B., Han, K., 2017. Mineral Identification and Field Application by Short Wave Infrared (SWIR) Spectroscopy. Economic and Environmental Geology 50, 1–14. https://doi.org/10.9719/eeg.2017.50.1.1
Kim, S., Kim, H., 2016. A new metric of absolute percentage error for intermittent demand forecasts. International Journal of Forecasting 32, 669–679.

https://doi.org/10.1016/j.ijforecast.2015.12.003
Kim, Y., Caumon, M.-C., Barres, O., Sall, A., Cauzid, J., 2021. Identification and composition of carbonate minerals of the calcite structure by Raman and infrared spectroscopies using portable devices. Spectrochimica Acta Part A: Molecular and Biomolecular Spectroscopy 261, 119980. https://doi.org/10.1016/j.saa.2021.119980
King, T.V., Clark, R.N., 1989. Spectral characteristics of chlorites and Mg-serpentines using high-resolution reflectance spectroscopy. Journal of Geophysical Research: Solid Earth 94, 13997–14008.
Kohonen, T., 2001. Self-Organizing Maps, 3rd ed, Springer Series in Information Sciences. Springer-Verlag, Berlin Heidelberg. https://doi.org/10.1007/978-3-642-56927-2
Kokaly, R.F., Clark, R.N., Swayze, G.A., Livo, K.E., Hoefen, T.M., Pearson, N.C., Wise, R.A., Benzel, W.M., Lowers, H.A., Driscoll, R.L., Klein, A.J., 2017. USGS Spectral Library Version 7 (USGS Numbered Series No. 1035), USGS Spectral Library Version 7, Data Series. U.S. Geological Survey, Reston, VA. https://doi.org/10.3133/ds1035
Laetsch, T., Downs, R., 2006. Software for identification and refinement of cell parameters from powder diffraction data of minerals using the RUFF Project and american mineralogist crystal structure databases. Abstracts from the 19th General Meeting of the International Mineralogical Association 23–28.
Lafuente, B., Downs, R.T., Yang, H., Stone, N., 2016. The power of databases: The RRUFF project. Highlights in Mineralogical Crystallography 1–29. https://doi.org/10.1515/9783110417104-003
Lafuente, B., Downs, R.T., Yang, H., Stone, N., 2015. The power of databases: the RRUFF project. in "Highlights in mineralogical crystallography", Armbruster, T. & Danisi, RM, eds. W. De Gruyter, Berlin, Germany 1, 30.
Lanza, N.L., Wiens, R.C., Clegg, S.M., Ollila, A.M., Humphries, S.D., Newsom, H.E., Barefield, J.E., 2010. Calibrating the ChemCam laser-induced breakdown spectroscopy instrument for carbonate minerals on Mars. Appl. Opt., AO 49, C211–C217. https://doi.org/10.1364/AO.49.00C211
Laperche, V., Lemière, B., 2021. Possible Pitfalls in the Analysis of Minerals and Loose Materials by Portable XRF, and How to Overcome Them. Minerals 11, 33. https://doi.org/10.3390/min11010033
Large, R.R., Allen, R.L., Blake, M.D., Herrmann, W., 2001a. Hydrothermal alteration and volatile element halos for the Rosebery K lens volcanic-hosted massive sulfide deposit, western Tasmania. Economic Geology 96, 1055–1072.
Large, R.R., McPhie, J., Gemmell, J.B., Herrmann, W., Davidson, G.J., 2001b. The spectrum of ore deposit types, volcanic environments, alteration halos, and related exploration vectors in submarine volcanic successions: Some examples from Australia. Economic Geology 96, 913–938.
Laukamp, C., 2011. Short Wave Infrared Functional Groups of Rock-forming Minerals. Report number EP115222, CSIRO Earth Science and Resource Engineering, Australia.
Lazic, V., Fantoni, a, Colao, a, Santagata, A., Moroneb, A., Spizzichino, V., 2004. Quantitative laser induced breakdown spectroscopy analysis of ancient marbles and corrections for the variability of plasma parameters and of ablation rate. Journal of Analytical Atomic Spectrometry 19, 429. https://doi.org/10.1039/b315606k
Lê, S., Josse, J., Husson, F., 2008. FactoMineR: An R Package for Multivariate Analysis. Journal of Statistical Software 25, 1–18. https://doi.org/10.18637/jss.v025.i01
Leary, P.E., Crocombe, R.A., Kammrath, B.W., 2021. Introduction to Portable Spectroscopy.

Portable Spectroscopy and Spectrometry 1: Technologies and Instrumentation 1, 1–13.
Lemière, B., Harmon, R.S., 2021. XRF and LIBS for Field Geology. Portable Spectroscopy and Spectrometry 1: Applications 2, 455–497.
Lemière, B., Uvarova, Y.A., 2020. New developments in field-portable geochemical techniques and on-site technologies and their place in mineral exploration. Geochemistry: Exploration, Environment, Analysis 20, 205–216.
Lentz, D.R., Hall, D.C., Hoy, L.D., 1997. Chemostratigraphic, alteration, and oxygen isotopic trends in a profile through the stratigraphic sequence hosting the Health Steele B zone massive sulfide deposit, New Brunswick. The Canadian Mineralogist 35, 841–874.
Levine, I.N., Busch, D.H., Shull, H., 2009. Quantum chemistry. Pearson Prentice Hall Upper Saddle River, NJ.
Lewis, I.R., Edwards, H., 2001. Handbook of Raman spectroscopy: from the research laboratory to the process line. CRC press.
Li, H., Zhang, L., Christy, A.G., 2011. The correlation between Raman spectra and the mineral composition of muscovite and phengite, in: Ultrahigh-Pressure Metamorphism. Elsevier, pp. 187–212.
Lindon, J.C., Tranter, G.E., Koppenaal, D., 2016. Encyclopedia of spectroscopy and spectrometry. Academic Press.
Loh, E., 1973. Optical vibrations in sheet silicates. Journal of Physics C: Solid State Physics 6, 1091.
Longshaw, T.G., 1974. Field spectroscopy for multispectral remote sensing: an analytical approach. Applied optics 13, 1487–1493.
Luff, W.M., Goodfellow, W.D., Juras, S.J., 1992. Evidence for a feeder pipe and associated alteration at Brunswick No. 12 massive-sulfide deposit. Exploration and Mining Geology 1, 167–185.
Lydon, J., 1988. Ore deposit models# 14. Volcanogenic massive sulphide deposits Part 2: Genetic models. Geoscience Canada 15, 43–65.
Madeisky, H.E., Stanley, C.R., 1993. Lithogeochemical exploration of metasomatic zones associated with volcanic-hosted massive sulfide deposits using Pearce element ratio analysis. International Geology Review 35, 1121–1148.
Madejová, J., 2003. FTIR techniques in clay mineral studies. Vibrational spectroscopy 31, 1–10.
Maxwell, J.C., 1865. VIII. A dynamical theory of the electromagnetic field. Philosophical Transactions of the Royal Society of London 155, 459–512. https://doi.org/10.1098/rstl.1865.0008
McKeown, D.A., Bell, M.I., Etz, E.S., 1999. Vibrational analysis of the dioctahedral mica: 2M1 muscovite. American Mineralogist 84, 1041–1048.
McMillan, N.J., Harmon, R.S., De Lucia, F.C., Miziolek, A.M., 2007. Laser-induced breakdown spectroscopy analysis of minerals: Carbonates and silicates. Spectrochimica Acta Part B: Atomic Spectroscopy, A Collection of Papers Presented at the 4th International Conference on Laser Induced Plasma Spectroscopy and Applications (LIBS 2006) 62, 1528–1536. https://doi.org/10.1016/j.sab.2007.10.037
Menges, F., 2020. Spectragryph-optical spectroscopy software, Version 1.2. 14, 2020.
Merkt, F., Quack, M., 2011. Molecular Quantum Mechanics and Molecular Spectra, Molecular Symmetry, and Interaction of Matter with Radiation. Handbook of High-resolution Spectroscopy. Fundamentals and Theory 1, 1–55. https://doi.org/10.3929/ethz-a-010782758

Mermet, J.-M., 2010. Calibration in atomic spectrometry: A tutorial review dealing with quality criteria, weighting procedures and possible curvatures. Spectrochimica Acta Part B: Atomic Spectroscopy 65, 509–523.

Milton, E.J., 2004. Field spectroscopy. Geoinformatics, Encyclopaedia of Life Support Systems (EOLSS). Oxford, UK: EOLSS Publishers.

Milton, E.J., Schaepman, M.E., Anderson, K., Kneubühler, M., Fox, N., 2009. Progress in field spectroscopy. Remote Sensing of Environment 113, S92–S109.

Moudgil, H.K., 2010. Textbook of physical chemistry. PHI Learning Pvt. Ltd.

Nesse, W.D., 2012. Introduction to mineralogy.

Neuendorf, K.K., 2005. Glossary of geology. Springer Science & Business Media.

Nickel, E.H., Grice, J.D., 1998. The IMA Commission on New Minerals and Mineral Names: procedures and guidelines on mineral nomenclature, 1998. Mineralogy and Petrology 64, 237–263.

Pirajno, F., 2009. Metalliferous Sediments and Sedimentary Rock-Hosted Stratiform and/or Stratabound Hydrothermal Mineral Systems, in: Pirajno, F. (Ed.), Hydrothermal Processes and Mineral Systems. Springer Netherlands, Dordrecht, pp. 727–883. https://doi.org/10.1007/978-1-4020-8613-7_8

Planck, M., 1901. Ueber das Gesetz der Energieverteilung im Normalspectrum. Annalen der Physik 309, 553–563. https://doi.org/10.1002/andp.19013090310

Pontual, S., 2008. GMEX spectral analysis guides for mineral exploration.

Post, J.L., Noble, P.N., 1993. The near-infrared combination band frequencies of dioctahedral smectites, micas, and illites. Clays and clay minerals 41, 639–644.

Prada, J.M., Caballero, B., Santos, A., 1996. Descripción geológica de los yacimientos de Sotiel Coronada. Boletín geológico y minero 107, 31–38.

Prieto, A.C., Dubessy, J., Cathelineau, M., 1991. Structure composition relationships in trioctahedral chlorites: a vibrational spectroscopy study. Clays and Clay Minerals 39, 531–539.

R Core Team, Rf., 2013. R: A language and environment for statistical computing. R foundation for statistical computing Vienna, Austria.

Radziemski, L.J., Cremers, D.A., 1989. Laser-induced plasmas and applications.

Raman, C.V., Krishnan, K.S., 1928. A new type of secondary radiation. Nature 121, 501–502.

Ravansari, R., Wilson, S.C., Tighe, M., 2020. Portable X-ray fluorescence for environmental assessment of soils: Not just a point and shoot method. Environment international 134, 105250.

Rayleigh, Lord, 1899. XXXIV. On the transmission of light through an atmosphere containing small particles in suspension, and on the origin of the blue of the sky. The London, Edinburgh, and Dublin Philosophical Magazine and Journal of Science 47, 375–384.

Rezaei, F., Cristoforetti, G., Tognoni, E., Legnaioli, S., Palleschi, V., Safi, A., 2020. A review of the current analytical approaches for evaluating, compensating and exploiting self-absorption in Laser Induced Breakdown Spectroscopy. Spectrochimica Acta Part B: Atomic Spectroscopy 169, 105878.

Ricci, C., Miliani, C., Brunetti, B.G., Sgamellotti, A., 2006. Non-invasive identification of surface materials on marble artifacts with fiber optic mid-FTIR reflectance spectroscopy. Talanta 69, 1221–1226. https://doi.org/10.1016/j.talanta.2005.12.054

Ridley, J.R., 2013. Ore Deposit Geology. https://doi.org/10.1017/CBO9781139135528

Rinnan, Å., Berg, F. van den, Engelsen, S.B., 2009. Review of the most common pre-processing techniques for near-infrared spectra. TrAC Trends in Analytical Chemistry 28, 1201–

1222. https://doi.org/10.1016/j.trac.2009.07.007
Rivkin, A.S., Volquardsen, E.L., Clark, B.E., 2006. The surface composition of Ceres: Discovery of carbonates and iron-rich clays. Icarus 185, 563–567. https://doi.org/10.1016/j.icarus.2006.08.022
Romero-Torres, S., Pérez-Ramos, J.D., Morris, K.R., Grant, E.R., 2006. Raman spectroscopy for tablet coating thickness quantification and coating characterization in the presence of strong fluorescent interference. Journal of Pharmaceutical and Biomedical Analysis 41, 811–819. https://doi.org/10.1016/j.jpba.2006.01.033
Rull, F., Dubessy, J., Caumon, M.C., 2012. The Raman effect and the vibrational dynamics of molecules and crystalline solids. Raman Spectroscopy applied to Earth Sciences and Cultural Heritage 1–60.
Sakurai, J.J., Commins, E.D., 1995. Modern quantum mechanics, revised edition. American Association of Physics Teachers.
Sarala, P., 2016. Comparison of different portable XRF methods for determining till geochemistry. Geochemistry: Exploration, Environment, Analysis 16, 181–192. https://doi.org/10.1144/geochem2012-162
Sarala, P., Koskinen, H., 2018. Application of the portable X-Ray Diffraction (pXRD) analyser in surficial geological exploration 11.
Sarala, P., Taivalkoski, A., Valkama, J., 2015. Portable XRF: An advanced onsite analysis method in till geochemical exploration. Special Paper - Geological Survey of Finland 57, 63–86.
Sarkar, A., Alamelu, D., Aggarwal, S.K., 2012. Gallium quantification in solution by LIBS in the presence of bulk uranium. Optics & Laser Technology 44, 30–34.
Sarrazin, P., Blake, D., Feldman, S., Chipera, S., Vaniman, D., Bish, D., 2005. Field deployment of a portable X-ray diffraction/X-ray flourescence instrument on Mars analog terrain. Powder Diffraction 20, 128–133.
SCHERMERHORN, L.J.G., 1971. An outline stratigraphy of the Iberian Pyrite Belt. Bolet. Geol. Minero 82, 239–268.
Schodde, R., 2019. Role of technology and innovation for identifying and growing economic resources, in: Proceedings of the AMIRA International's 12th Biennial Exploration Managers Conference, Hunter Valley, Australia. pp. 26–29.
Schramm, R., 2017. 8. Use of X-ray Fluorescence Analysis for the Determination of Rare Earth Elements. Handbook of Rare Earth Elements 231–252.
Senesi, G.S., Harmon, R.S., Hark, R.R., 2021. Field-portable and handheld laser-induced breakdown spectroscopy: Historical review, current status and future prospects. Spectrochimica Acta Part B: Atomic Spectroscopy 175, 106013. https://doi.org/10.1016/j.sab.2020.106013
Shanks, W.C., Thurston, R., 2012. Volcanogenic massive sulfide occurrence model. US Department of the Interior, US Geological Survey.
Shirozu, H., 1985. Infrared spectra of trioctahedral chlorites in relation to chemical composition. Clay Science 6, 167–176.
Shirozu, H., Ishida, K., 1982. Infrared study of some 7 Å and 14 Å layer silicates by deuteration. Mineralogical Journal 11, 161–171.
Singh, J.P., Almirall, J.R., Sabsabi, M., Miziolek, A.W., 2011. Laser-induced breakdown spectroscopy (LIBS). Anal Bioanal Chem 400, 3191–3192. https://doi.org/10.1007/s00216-011-5073-5
Singha, M., Singh, L., 2016. Vibrational spectroscopic study of muscovite and biotite layered

phyllosilicates.
Solotchina, E.P., Prokopenko, A.A., Kuzmin, M.I., Solotchin, P.A., Zhdanova, A.N., 2009. Climate signals in sediment mineralogy of Lake Baikal and Lake Hovsgol during the LGM-Holocene transition and the 1-Ma carbonate record from the HDP-04 drill core. Quaternary International 205, 38–52.
Soltani Dehnavi, A., McFarlane, C.R., Lentz, D.R., McClenaghan, S.H., Walker, J.A., 2019. Chlorite-white mica pairs' composition as a micro-chemical guide to fingerprint massive sulfide deposits of the Bathurst mining camp, Canada. Minerals 9, 125.
Šontevska, V., Jovanovski, G., Makreski, P., Raškovska, A., Šoptrajanova, B., 2008. Minerals From Macedonia. XXI. Vibrational Spectroscopy as Identificational Tool for Some Phyllosilicate Minerals. Acta Chimica Slovenica 55.
Syvilay, D., Guezenoc, J., Bousquet, B., 2019. Guideline for increasing the analysis quality in laser-induced breakdown spectroscopy. Spectrochimica Acta Part B: Atomic Spectroscopy 161, 105696. https://doi.org/10.1016/j.sab.2019.105696
Syvilay, D., Wilkie-Chancellier, N., Trichereau, B., Texier, A., Martinez, L., Serfaty, S., Detalle, V., 2015. Evaluation of the standard normal variate method for Laser-Induced Breakdown Spectroscopy data treatment applied to the discrimination of painting layers. Spectrochimica Acta Part B: Atomic Spectroscopy 114, 38–45. https://doi.org/10.1016/j.sab.2015.09.022
Taylor, J.K., 2018. Quality assurance of chemical measurements. Routledge.
Team, Rs., 2015. RStudio: integrated development for R. RStudio, Inc., Boston, MA URL http://www. rstudio. com 42, 14.
Theo Kloprogge, J., 2017. Infrared and Raman Spectroscopy of Minerals and Inorganic Materials, in: Lindon, J.C., Tranter, G.E., Koppenaal, D.W. (Eds.), Encyclopedia of Spectroscopy and Spectrometry (Third Edition). Academic Press, Oxford, pp. 267–281. https://doi.org/10.1016/B978-0-12-409547-2.12154-7
Thomas, L.E., 1985. Light-element analysis with electrons and X-rays in a high-resolution STEM. Ultramicroscopy 18, 173–184.
Thompson, A.J.B., Thompson, J.F.H., Dunne, K.P.E., 1996. Atlas of alteration: a field and petrographic guide to hydrothermal alteration minerals. Geological Association of Canada. Mineral Deposits Division 120.
Tlili, A., Smith, D.C., Beny, J.-M., Boyer, H., 1989. A Raman microprobe study of natural micas. Mineralogical Magazine 53, 165–179.
Tornos, F., 2006. Environment of formation and styles of volcanogenic massive sulfides: The Iberian Pyrite Belt. Ore Geology Reviews 28, 259–307. https://doi.org/10.1016/j.oregeorev.2004.12.005
Tornos, F., Peter, J.M., Allen, R., Conde, C., 2015. Controls on the siting and style of volcanogenic massive sulphide deposits. Ore Geology Reviews 68, 142–163.
Tuinstra, F., Koenig, J.L., 1970. Raman spectrum of graphite. The Journal of chemical physics 53, 1126–1130.
Urabe, T., 1983. A comparison of footwall-rock alteration and geothermal systems beneath some Japanese and Canadian volcanogenic massive sulfide deposits. Econ. Geol. Monogr. 5, 345–364.
Velasco-Acebes, J., Tornos, F., Kidane, A.T., Wiedenbeck, M., Velasco, F., Delgado, A., 2019. Isotope geochemistry tracks the maturation of submarine massive sulfide mounds (Iberian Pyrite Belt). Miner Deposita 54, 913–934. https://doi.org/10.1007/s00126-018-0853-x

Wang, A., Freeman, J.J., Jolliff, B.L., 2015. Understanding the Raman spectral features of phyllosilicates. Journal of Raman Spectroscopy 46, 829–845.

Warren, B.E., 1990. X-ray Diffraction. Courier Corporation.

Weber, W.H., Merlin, R., 2013. Raman scattering in materials science. Springer Science & Business Media.

Whitney, D.L., Evans, B.W., 2010. Abbreviations for names of rock-forming minerals. American Mineralogist 95, 185–187. https://doi.org/10.2138/am.2010.3371

Yang, K., Huntington, J.F., 1996. Spectral signatures of hydrothermal alteration in the metasediments at Dead Bullock Soak, Tanami Desert, Northern Territory. Aus. J. Earth Sci 25, 257.

Yi, C., Lv, Y., Xiao, H., Ke, K., Yu, X., 2017. A novel baseline correction method using convex optimization framework in laser-induced breakdown spectroscopy quantitative analysis. Spectrochimica Acta Part B: Atomic Spectroscopy 138, 72–80.

Zaffino, C., Guglielmi, V., Faraone, S., Vinaccia, A., Bruni, S., 2015. Exploiting external reflection FTIR spectroscopy for the in-situ identification of pigments and binders in illuminated manuscripts. Brochantite and posnjakite as a case study. Spectrochimica Acta Part A: Molecular and Biomolecular Spectroscopy 136, 1076–1085.

Zaini, N., Van der Meer, F., Van der Werff, H., 2012. Effect of Grain Size and Mineral Mixing on Carbonate Absorption Features in the SWIR and TIR Wavelength Regions. Remote Sensing 4, 987–1003. https://doi.org/10.3390/rs4040987

List of figures

List of tables